Advanced Studies on the Thermoelectric Properties of Cu_2Se Based Nanostructures

Thesis submitted to the
University of Calicut, Kerala, for the partial fulfillment of the requirements for the award of the degree of

DOCTOR OF PHILOSOPHY IN PHYSICS
Under the Faculty of Science

By
PARVATHY. T

Under the guidance of
Prof. (Dr.) P.P. Pradyumnan
Senior Professor

DEPARTMENT OF PHYSICS
UNIVERSITY OF CALICUT
KERALA 673635 - INDIA

MARCH 2025

Advanced Studies on the Thermoelectric Properties of Cu_2Se Based Nanostructures

Ph.D. thesis in Physics

Author:

Parvathy. T
Department of Physics,
University of Calicut.
Calicut University (PO) - 673635, Kerala, India.
Email: parvathysivadass@gmail.com

Under the guidance of

Prof.(Dr).P.P.Pradyumnan
Senior Professor
Department of Physics
University of Calicut
Calicut University (PO) - 673635,
Kerala, India.
Email : ppp@uoc.ac.in
March 2025

DEPARTMENT OF PHYSICS
UNIVERSITY OF CALICUT
KERALA 673635 - INDIA

Grams: UNICAL
91-0494- 2401144,415,416
Fax- (0494) 2400 269
Residence: +09895961751
e-mail: drpradyumnan@gmail.com
Kerala, India. 673 635

Prof.(Dr.)P.P.Pradyumnan
Senior Professor

28th March 2025

CERTIFICATE

Certified that the work presented in this thesis entitled "**Advanced Studies on the Thermoelectric Properties of Cu_2Se Based Nanostructures**" submitted to the University of Calicut for the award of the degree of Doctor of Philosophy is based on the authentic record of research carried out by Ms. Parvathy. T under my guidance and supervision in the Department of Physics, University of Calicut, and this work has not been included in any other thesis submitted previously for the award of any degree.

Calicut University

Dr. P.P.Pradyumnan

Prof.(Dr.) P.P. PRADYUMNAN
Senior Professor
Department of Physics
University of Calicut
Kerala - 673 635, India

DEPARTMENT OF PHYSICS
UNIVERSITY OF CALICUT
KERALA 673635 - INDIA

Grams: UNICAL
91-0494- 2401144,415,416
Fax- (0494) 2400 269
Residence: +09895961751
e-mail: drpradyumnan@gmail.com
Kerala, India. 673 635

Prof.(Dr.)P.P.Pradyumnan
Senior Professor

28th July 2025

CERTIFICATE

Certified that all the corrections/suggestions recommended by the adjudicators have been incorporated in the thesis entitled "**Advanced Studies on the Thermoelectric Properties of Cu_2Se Based Nanostructures**" submitted to the University of Calicut for the award of the degree of Doctor of Philosophy in Physics by Ms. Parvathy. T, Department of Physics, University of Calicut, and content in this thesis and the soft copy are one and same.

Calicut University

Dr. P.P.Pradyumnan
Prof.(Dr.) P.P. PRADYUMNAN
Senior Professor
Department of Physics
University of Calicut
Kerala - 673 635, India

DECLARATION

Certified that the work presented in this thesis entitled "**Advanced Studies on the Thermoelectric Properties of Cu_2Se Based Nanostructures**" submitted to the University of Calicut for the award of the degree of Doctor of Philosophy is based on the original research work done by me under the supervision and guidance of Dr. P.P.Pradyumnan, Senior Professor, Department of Physics, University of Calicut, Calicut University P.O, Kerala- 673635 and has not been included in any other thesis submitted previously for the award of any degree. I declare that the thesis has undergone plagiarism check using iThenticate software at CHMK Library, University of Calicut and the similarity index is found within the permissible limit. I also declare that the thesis is free from AI generated contents.

Parvathy. T

Calicut University
28th March 2025

Dr. P.P.Pradyumnan
Senior Professor
Department of Physics
University of Calicut

ACKNOWLEDGEMENT

This thesis has been a journey filled with challenges and achievements, and I am truly thankful to everyone who has contributed to its success, whether directly or indirectly. The guidance, support, and encouragement I received throughout this process have been incredibly valuable. I would like to take this opportunity to acknowledge all those who have played a part in making this achievement possible. The unwavering support, motivation, and teamwork from friends, colleagues, family and well-wishers have been a constant source of strength during this journey. No words can fully express my gratitude to everyone who made this journey a truly fulfilling and memorable experience.

I would first and foremost like to express my sincere thanks and gratitude to my research supervisor, Dr.P.P.Pradyumnan, for his invaluable guidance, support, constant encouragement, understanding, and patience. Despite his busy schedule, administrative responsibilities, and academic commitments, he always made time for me and ensured his availability whenever I needed assistance. His trust in granting me the freedom to explore my ideas, combined with his insightful guidance and genial nature, kept me on the right track throughout my research journey. For all of this, I am truly thankful.

Apart from my supervisors, I would like to express my gratitude to Dr. Mohammed Shahin Thayyil, Head of the Department of Physics, and all the former Heads of the Department, including Dr. C.D. Ravikumar and Dr. A.M. Vinodkumar, for providing the facilities in the department to carry out my research work. I am also pleased to extend my sincere thanks to all the faculty members of the Physics Department, including Dr. M.M. Musthafa, Dr. Libu K. Alexander, Zuhail K.P, Dr. Drisya K, Dr. Antony Joseph and Dr. K.P.Santhosh for their valuable advice and support throughout this period. I also extend my sincere gratitude to all the non-teaching staff of the Department of Physics for their invaluable assistance and support throughout this journey. Moreover, I sincerely thank all my teachers, from school to

the present, for laying the foundation of my knowledge, nurturing my curiosity, and guiding me with their wisdom, support, and encouragement throughout my academic journey.

I am deeply grateful to my senior, Dr. Muhammed Sabeer N.A., for his invaluable guidance during the early stages of my academic journey. His teachings on research discipline and proper use of instruments have been incredibly helpful in shaping my academic development. I would also like to extend my sincere thanks to Dr. Anju Paulson, Dr. Jumanath E C, and Dr. Shyni P for their support, encouragement, and insightful advice, which greatly contributed to my research and overall growth during this period.

The encouragement and teamwork within my research environment have played a vital role in making this journey both fulfilling and enjoyable. I am truly thankful to my senior co researchers Dr. Vineetha V S, Dr. Soumya C, and my lab mates Nabeela K.V, Hisna P A, Hashir P, Midhun shah, and Jamsheena Sanam for their constant encouragement, support, and friendship. Their teamwork and shared enthusiasm made overcoming challenges easier and celebrating successes more meaningful. This experience would not have been the same without their contributions, and for that, I am deeply grateful.

To my best friend, Aruna Unnikrishnan, this journey would have been incomplete without you. From the very beginning, we walked this path together, facing challenges, celebrating achievements, and growing side by side. Your constant support, encouragement, and faith in me have been my greatest source of strength. Thank you for being my partner in this adventure, for never being judgmental, and for making every step memorable. I'm truly grateful for your friendship and the bond we share.

I am truly blessed to have had two incredible people by my side throughout this journey. Swapna Balakrishnan, who has been more than just a friend, she has been like a sister to me. Sharing a room with her throughout this journey has been a truly meaningful experience, filled with moments of support, understanding, and companionship. Her constant encouragement, kindness, and patience have been a

source of strength, especially during difficult times. She has always been there to listen, uplift me, and stand by my side, making even the toughest days easier to endure. Her unwavering support has made even the toughest times more manageable. Equally, my heartfelt gratitude goes to my best friend, Dinto Sebastian, whose constant support and friendship have meant so much to me. His encouragement, positivity, and willingness to stand by me during both the highs and lows have been truly invaluable. I am truly grateful for his companionship and the enduring support he has provided throughout this journey.

I feel truly fortunate to acknowledge the support of some special individuals. With heartfelt gratitude, I sincerely thank my dear friends Aminabi T, Baheeja C, Sravandas P, Anju K, Vishnu C V, Vinod K T, Ummukulsu and Nicemon Thomas, for their care, love, and support throughout my journey.

I am also grateful to those who have made this journey even more memorable. My deepest thanks go to Shaima Akbar for her constant support and understanding. Even with her busy schedule, she always found time to be there for me, offering comfort, guidance, and encouragement. Her presence has been a source of strength, and I am truly grateful for her kindness and support throughout this journey. I also extend my heartfelt gratitude to Mohammed Riyas, Nihal Mohammed, Nived K, Vishnu Sathyan, Anjali, Aneena Mohan, Akhil Ramesh, Shana Sherin, Jinu K V, Saroop C P, Vafiya Thaslim, Faheema, Ashifa M S, and Farha for their support, kindness, and the wonderful moments we shared along the way. Each of you has added so much richness and meaning to this journey, and I feel truly blessed to have had your presence and support by my side.

The past five years have been a journey filled with challenges, growth, and resilience, shaping me in ways I never imagined. Through every hardship and difficult moment, I have been blessed with the unwavering support of my family, who stood by me with love and strength. I am forever indebted to my beloved Achan and Amma, who have sacrificed their dreams and comforts to shape my future. Their love, endless sacrifices, and belief in me have made me who I am today. Every achievement of mine is a reflection of their dedication, and I stand with immense

pride as their daughter, knowing that their trust and guidance have been the foundation of my journey. I am also deeply grateful to my dear brother Appu, who has always treated me like his daughter. His support and boundless affection have been a constant source of comfort and strength throughout my journey. Through every challenge and hardship, he has stood by my side with immense patience, unconditional love, and unwavering care. His presence has been a source of strength and reassurance, making even the most difficult times easier to bear. I am truly blessed to have him as my brother, mentor, and guardian. I am so thankful to my dear Ammamma, whose endless love, prayers, and belief in me have been my greatest support. Her happiness and excitement for my dreams keep me going every day, and her constant wish to see me submit my thesis and earn this degree has been my biggest motivation. I feel truly blessed and thank God for giving me such a wonderful family, whose love and support have been my greatest treasures.

Above all, I thank God for granting me the perseverance, wisdom, and strength to complete this journey, transforming challenges into stepping stones.

Parvathy. T

Dedicated to

Achan, Amma and Appu

For their endless love, support, and encouragement

LIST OF PUBLICATIONS

1. **T Parvathy**, P.P. Pradyumnan, Thermal energy management through thermoelectric generation using Ni, Zn co-doped Cu_2Se nanocrystallites, Emergent Mater. (2025). https://doi.org/10.1007/s42247-025-00999-9.

2. **T Parvathy**, P.P. Pradyumnan, Impact of mobility and effective mass on the thermoelectric performance of Ni doped Cu_2Se, J. Alloys Compd. 970 (2024). https://doi.org/10.1016/j.jallcom.2023.172615.

3. **T Parvathy**, K. V. Nabeela, P.P. Pradyumnan, Raman structural transition studies and optical band calculation on the multiphase of tin selenides, Mater. Chem. Phys. 301 (2023). https://doi.org/10.1016/j.matchemphys. 2023.127622.

4. **T Parvathy**, N.A. Muhammed Sabeer, N. Mohan, P.P. Pradyumnan, Effect of dopant gas pressure on the growth of magnetron sputtered CuO thin films for electrical and optical applications, Opt. Mater. (Amst). 125 (2022). https://doi.org/10.1016/j.optmat.2022.112031.

5. P.P. Pradyumnan, **T Parvathy**, Thermoelectric nanomaterials for temperature gradient sensing (heat nose), in: R.K. Gupta, T.A. Nguyen, M. Bilal, M. Ahmadi (Eds.), Nanotechnology-Based E-Noses, Elsevier, 2023. https://doi.org/10.1016/B978-0-323-91157-3.00009-X.

6. Hashir P, **Parvathy T**, A.F. Wani, K. Kaur, P.P. Pradyumnan, Advancement in the thermoelectric performance of bulk SnSe: GGA+U approach for band gap calculation and strain induced thermal conductivity, Mater. Res. Bull. 182 (2025). http://dx.doi.org/10.2139/ssrn.4872068.

7. K. V. Nabeela, **T Parvathy**, P.P. Pradyumnan, Realizing the thermoelectric performance in cobalt doped p-CuO semiconductor by valance band flattening and effective phonon scattering approach, Phys. B Condens. Matter. 665 (2023). https://doi.org/10.1016/j.physb.2023.415047.

International Journals (Communicated):

1. Parvathy T, P.P.Pradyumnan, Thermoelectric properties of band engineered Cu_2Se-MgO nanocrystals for thermal energy management, Journal of the Taiwan institute of chemical engineers (submitted).

2. Parvathy T, P.P.Pradyumnan, Cu_2Se-ZnSe nanocomposites for thermal energy wastages into electrical energy, Energy and environmental science (submitted).

Papers presented in International/National conferences

1. Nanofest 2024, International conference celebrating nano day organized by School of Nanoscience and Nanotechnology held at MG University Kottayam on October 9-10, 2024.

2. International conference on advanced materials for sustainability (ICAMS 2023) organized by University of Calicut on December 21-23, 2023.

3. World conference on thermoelectrics and materials (WCT-2023) organized by Jaipur National University, Jaipur, Rajasthan on March 14-18, 2023.

4. 7th International conference on nanoscience and nanotechnology (ICONN-2023), organized by SRM institute of science and technology Kattankulathur, Tamil Nadu, on March 27 – 29, 2023.

5. International conference on advanced materials and mechanical characterization (ICAMMC-2021) organised by SRM institute of science and technology Kattankulathur, Tamil Nadu, India on December 2-4, 2021.

Awards

- **Best Poster Paper Award:** Enhancement in the thermoelectric properties of Cu_2Se through ZnSe nanoinclusions, Parvathy T, P.P.Pradyumnan, Nanofest 2024, International conference celebrating Nano Day, MG University Kottayam on October 9-10,2024.

- **Best Poster Paper Award:** Enhanced thermoelectric performance of Cu_2Se/ZnSe composites through band convergence and carrier optimization, Parvathy T, P.P.Pradyumnan, International conference on advanced materials for sustainability (ICAMS 2023), University of Calicut, December 21-23, 2023.

- **Best Poster Paper Award:** Enhancement in the Thermoelectric properties of Cu_2Se through Zn Doping, Parvathy T, P.P.Pradyumnan, 7th International conference on nanoscience and nanotechnology (ICONN-2023), SRM institute of science and technology, March 27 - 29, 2023.

- **Third best paper Award:** Impact of electronic defects on the thermoelectric properties of Ni doped Cu_2Se, Parvathy T, P.P.Pradyumnan ,World conference on thermoelectric and materials, (WCT), March 2023, Jaipur National university, Jaipur.

CONTENTS

LIST OF FIGURES

LIST OF TABLES

ABBREVIATIONS

TE	:	Thermoelectricity
DOS	:	Density of states
PGEC	:	Phonon glass electron crystal
PLEC	:	Phonon liquid electron crystal
VBM	:	Valence band maximum
PF	:	Power factor
RT	:	Room temperature
PXRD	:	Powder X-ray diffraction
FWHM	:	Full width at half maximum
ICDD	:	International centre for diffraction data
FESEM	:	Field emission scanning electron microscopy
EDS	:	Energy dispersive spectroscopy
TEM	:	Transmission electron microscopy
HRTEM	:	High resolution transmission electron microscopy
SAED	:	Selected area electron diffraction

SYMBOLS USED

S	:	Seebeck coefficient
T	:	Temperature
T_h	:	Hot junction temperature
T_c	:	Cold junction temperature
Π	:	Peltier coefficient
Q	:	Heat energy
C	:	Thomson coefficient
ZT	:	Figure of merit
η	:	Efficiency
σ	:	Electrical conductivity
κ	:	Total thermal conductivity
κ_l	:	lattice thermal conductivity
κ_e	:	Electronic thermal conductivity
m*	:	Effective mass of carriers
μ	:	Carrier mobility
k_B	:	Boltzmann constant
τ	:	Phonon relaxation time
n	:	Carrier concentration
E_f	:	Fermi energy
f_0	:	Fermi distribution function
N_v	:	Valley degeneracy
ε	:	Microstrain
δ	:	Dislocation density
D	:	Crystallite size
α	:	Absorption coefficient
E_g	:	Optical band gap energy
ω	:	Raman frequency

PREFACE

The global energy sector is undergoing a critical transformation driven by the depletion of non-renewable resources, increasing electricity demand, and the pressing environmental challenges of climate change and greenhouse gas emissions. Fossil fuels, which currently account for the majority of power generation, are being exhausted at an alarming rate, necessitating an urgent shift to renewable energy sources. According to the Institute of Sustainable Energy Policies, by 2050, only 33% of non-renewable energy will remain available for power generation, underscoring the urgent need for innovative energy strategies. Scientists and industries around the world are striving to create innovative technologies that minimize reliance on traditional energy sources while tackling environmental challenges. Significant advancements have been made in improving energy efficiency, utilizing renewable resources, and enhancing energy conversion techniques paving the way for a cleaner and more resilient energy future. Among these, the vast amounts of waste heat generated from industrial processes and power plants remain a largely untapped resource, offering a substantial opportunity for energy recovery. Thermoelectric materials, which directly convert temperature differences into electricity, have emerged as a viable technology for harnessing both waste heat and renewable energy, contributing to a more sustainable energy future. However, its practical implementation is hindered by challenges such as high material costs, limited operational temperature ranges, and the difficulty of simultaneously optimizing electrical and thermal transport properties. This has driven growing interest in developing advanced thermoelectric materials and improving the conversion efficiency of existing ones through innovative material design and optimization strategies. Among various thermoelectric materials, copper selenide (Cu_2Se) a p-type semiconductor that exhibits outstanding thermoelectric performance, due its unique phonon-liquid electron-crystal behaviour. To fully harness its potential, further enhancement of its thermoelectric properties through strategies such as nanostructuring and band engineering is essential. This thesis

focuses on enhancing the thermoelectric properties of Cu_2Se nanostructures by optimizing both electronic and thermal transport properties.

The thesis, titled *"Advanced Studies on the Thermoelectric Properties of Cu_2Se Based Nanostructures",* presents a comprehensive investigation into strategies aimed at enhancing the thermoelectric performance of Cu_2Se based systems. The study focuses on doping and nanoinclusion approaches as key methods for optimizing both electrical and thermal transport properties, which are critical for improving energy conversion efficiency. By systematically incorporating dopants and secondary phases, the research explores how modifications at the nanoscale influence the structural, morphological, and electronic properties of Cu_2Se. A significant emphasis is given to nanostructuring, band engineering, and defect modulation which are the keys to optimizing charge carrier dynamics and phonon scattering mechanisms, that directly influence the thermoelectric efficiency. This thesis is structured into eight chapters, with the contents outlined as follows.

Chapter 1 provides a comprehensive introduction to thermoelectricity, detailing the fundamental principles that influence the performance of thermoelectric materials. It explores various strategies used to enhance the thermoelectric properties, including doping, nanostructuring, band engineering, the incorporation of a secondary phase etc. The chapter also introduces Cu_2Se as a promising thermoelectric material, highlighting its unique phonon-liquid electron-crystal behaviour and recent advancements in performance enhancement. Additionally, it outlines the research motivation, scope, and objectives of the thesis, focusing on doping and nanoinclusion strategies to achieve specific improvements in Cu_2Se based systems.

Chapter 2 outlines the synthesis method and characterization techniques utilized in this study. It details the approaches used to synthesize Cu_2Se based nanostructures and provides an overview of the analytical techniques employed to examine the structural, morphological, electrical, optical and thermoelectric properties of the synthesized materials. Techniques such as X-ray diffraction (XRD), Raman spectroscopy, scanning electron microscopy (SEM), transmission electron microscopy (TEM), UV-visible spectroscopy, thermoelectric and thermal

conductivity measurements are discussed, highlighting their crucial role in assessing the performance of grown materials.

Chapter 3 investigates the doping strategy implemented to enhance the thermoelectric properties of Cu_2Se, with a specific focus on Ni doping and its impact on the structural, morphological, and transport properties of the synthesized samples. The incorporation of Ni into the Cu_2Se lattice, synthesized via the hydrothermal route, significantly influences its electronic and thermal transport properties. This study emphasizes band structure modification to optimize carrier transport by maintaining a balance between carrier mobility and effective mass. Band sharpening induced by Ni doping tailors the carrier's effective mass, leading to enhanced carrier mobility without reducing carrier concentration. Additionally, the presence of Ni at interstitial sites results in a simultaneous increase in both carrier mobility and carrier concentration, contributing to improved thermoelectric performance. These results highlight Ni as an effective dopant capable of improving Cu_2Se's thermoelectric features through defect and band engineering.

Chapter 4 explores the dual doping strategy as a means to further enhance the thermoelectric properties of Cu_2Se. This study presents a novel approach by simultaneously optimizing electronic and thermal transport through Ni and Zn co-doping, a method that has not been previously explored. The incorporation of both dopants into the Cu_2Se lattice via a low-temperature hydrothermal route effectively modifies electrical and thermal properties by improving carrier mobility and enhancing phonon scattering through lattice defects. These defects intensify scattering mechanisms, reducing phonon relaxation time and significantly lowering the thermal conductivity. The combined effect of reduced thermal conductivity and enhanced power factor results in the highest thermoelectric efficiency in the co-doped samples.

Chapters 5 examine the impact of nanoinclusions on the thermoelectric properties of Cu_2Se, utilizing the physical method through planetary ball milling techniques to introduce secondary phases at the nanoscale. This approach modifies the microstructure of Cu_2Se, enhancing phonon scattering and reducing thermal

conductivity while maintaining favourable electrical transport properties. The chapter focuses on the incorporation of ZnSe nanoinclusions to decouple the interdependency of transport parameters. ZnSe alloying modifies the band structure of Cu_2Se by converging the energies of the light and heavy valence bands, thus improving charge carrier transport. Moreover, ZnSe additions fine-tune the Fermi level, facilitate valence band convergence, and increase the density of states, optimizing p-type charge carriers. These modifications result in improved electrical conductivity and Seebeck coefficient due to enhanced carrier concentration and variation in the effective mass of the charge carriers. The controlled incorporation of ZnSe nanoinclusions not only improves electrical conductivity and the Seebeck coefficient but also reduces thermal conductivity, leading to a significant improvement in the thermoelectric figure of merit of the materials.

Chapter 6 explores the impact of nanoinclusions of MgO on the thermoelectric properties of Cu_2Se, focusing on their role in modifying electronic and thermal transport behaviour. The incorporation of MgO using planetary ball milling introduces heterointerfaces, which act as energy filtering barriers, selectively scattering low-energy carriers while allowing high-energy carriers to enhance electrical transport. This energy filtering effect significantly improves the Seebeck coefficient without severely affecting electrical conductivity. Moreover, MgO nanoinclusions introduce strong phonon scattering, which effectively reduces thermal conductivity, thereby enhancing the overall thermoelectric efficiency. This nanoinclusion strategy, combined with alloying induced valence band convergence and interface energy filtering, results in a significant improvement in the value of the thermoelectric figure of merit.

Chapter 7 provides a general summary and conclusions of the study, consolidating the key findings from the doping and nanoinclusions strategies employed to enhance the thermoelectric properties of Cu_2Se. It outlines the most effective methods for optimizing both electrical and thermal transport properties and delves into the underlying mechanisms responsible for these improvements. The chapter reviews the impacts of Ni doping, dual Ni-Zn co-doping, ZnSe and MgO nanoinclusions on

the transport properties of Cu_2Se, focusing on the strategies that most effectively boost its performance. Through these investigations, the study accomplishes its objectives of enhancing Cu_2Se's thermoelectric efficiency by tuning its electronic and phonon transport properties. Ultimately, this chapter underscores the potential of these strategies in advancing high-performance thermoelectric materials for sustainable energy applications.

Finally, chapter 8 presents the future scope and recommendations for further enhancing Cu_2Se based thermoelectric materials. While significant improvements have been achieved through doping, dual doping, and nanoinclusion engineering, additional research is needed to fully optimize Cu_2Se for energy conversion applications. Exploring advanced material design strategies and scalable fabrication methods will be crucial for applying these developments to practical thermoelectric devices. Future research could optimize thermoelectric properties with additional dopants, explore thin films for lower thermal conductivity, and develop n-type counterparts for efficient the fabrication of p-n modules.

Chapter-1

Introduction to thermoelectricity: fundamentals and innovations

This chapter provides an overview of the fundamental principles of thermoelectricity, highlighting the key concepts that govern thermoelectric materials. It discusses various innovations and strategies to enhance thermoelectric properties and to optimize material performance. The goal is to establish a comprehensive foundation for understanding the thermoelectric properties of materials and the approaches used to tune them for practical applications. Moreover, the chapter discusses the research motivation and the objectives to attain the specific output.

1.1.Introduction

Globalization has intensified the scientific community's emphasis on green energy, driven by the growing demand for energy in daily life, which largely relies on depleting fossil fuel resources such as coal, petroleum, and natural gas. These limited resources are not only depleting but also adversely affecting the ongoing deterioration of air and water quality. Conventional carbon-based fossil energy sources emit greenhouse gases and fail to meet the growing demands of higher living standards and advanced industrialization. It's worth noting that only 30–40% of the energy produced from fossil fuel combustion is efficiently utilized, while the remaining 60–70% is lost as waste heat [1]. An analysis of industrial waste heat shows that 80% of it is released as hot gas, with temperatures ranging from 373 to 573 K. Efficient heat removal is often critical in cooling systems for electronics, data centers, and air conditioning [2]. Air conditioning, in particular, accounts for a significant portion of energy consumption approximately 10% across Europe. Similarly, refrigeration is a major energy drain, with chillers consuming about 29% of the energy in a typical hypermarket [3]. Roughly 30% of the energy supplied to an internal combustion engine is lost in the exhaust as waste heat. Recovering approximately 6% of this heat from the exhaust could satisfy an automobile's electrical requirements and potentially reduce fuel consumption by around 10% [4]. However, the effectiveness of such recovery systems is often hindered by the limitations of current power generation and conversion technologies, which operate well below the theoretical Carnot efficiency. Capturing and converting this waste heat into usable electrical energy offers significant potential for improving overall energy efficiency and provides a promising approach to sustainably meet rising energy demands. Traditional methods for converting heat energy rely on rotating machinery operating on the Rankine cycle, such as pumps or turbines [5]. While effective in certain applications, these systems present challenges in scaling efficiently for compact or distributed setups and often demand substantial ongoing maintenance, limiting their practicality in some scenarios [5].

The release of waste heat into the environment, along with emissions of carbonaceous compounds such as CO_2 exacerbates the rise in environmental temperatures and amplifies the greenhouse effect [6]. This process disrupts local climates, contributes to global warming, intensifies extreme weather events, and threatens ecosystems. Inefficiencies in energy use across industrial and technological processes further compound the problem by dissipating residual heat, which elevates environmental temperatures and increases greenhouse gas emissions. These inefficiencies result in the unnecessary emission of additional greenhouse gases, particularly in sectors reliant on high energy consumption. Consequently, waste heat and inefficient cooling systems create a cycle of environmental harm by simultaneously increasing temperatures and intensifying greenhouse gas emissions. While some energy loss is unavoidable due to the need to maintain non-zero heat flow, optimizing energy efficiency and implementing waste heat recovery systems are critical for mitigating these adverse impacts. Achieving net zero, which involves balancing greenhouse gas emissions and removals from the environment, has emerged as a crucial objective [7]. Countries like the UK, Sweden, and France are striving to reach net zero by 2050, but progress has been slow. To overcome these challenges and accelerate the transition to a net zero future, technological advancements are crucial. The growing demand for substantial contributions to the global primary energy supply, combined with the urgent need to mitigate climate change by eliminating additional greenhouse gas emissions, frames today's energy challenge. This challenge entails searching for new, clean, and renewable energy resources to meet global energy needs sustainably [8]. Thermoelectric (TE) devices play a crucial role in capturing waste heat and directly converting it into electrical power, making them essential for energy scavenging and green energy harvesting. While they are currently used in specialized applications, their potential impact extends far beyond these niches. Enhancing their efficiency and sustainability is vital for their wider adoption, as these advancements could significantly contribute to achieving global net zero emissions targets.

Thermoelectric materials, which convert temperature differences into electricity, are crucial for advancing energy technology. Their inherent advantages, including

safety, high reliability, compact size, no moving parts, and lack of pollution make them promising solutions in the search for sustainable energy sources [9]. Their effective use relies on carefully designed electrical circuits to manage the generated electricity and on optimizing thermal coupling with both hot and cold sources through thermal resistances. This integrated approach not only enhances the efficiency of energy extraction from heat sources but also supports sustainable energy practices by harnessing unused waste heat, thereby minimizing the overall environmental impact. Thermoelectric generators hold significant potential for harnessing the liberated waste heat to generate electricity, a concept already demonstrated in small-scale applications like charging devices with heat from portable stoves while camping [10]. However, their impact could be much broader. In many human activities, from industrial processes to air conditioning, vast amounts of heat are produced and then lost without being utilized. For instance, in gasoline-powered vehicles, only about one-third of the energy is used for its working, while the remaining two-thirds is wasted in the form of heat energy. By capturing this lost heat with thermoelectric devices, we could greatly improve fuel efficiency and reduce energy waste in the form of heat. Implementing such systems in factories and other heat intensive environments could play a crucial role in achieving our net-zero emissions target by 2050 [11].

1.2. Thermoelectricity: An overview

Thermoelectric is a domain within thermal energy harvesting that has a rich history spanning nearly two centuries [12]. Its development has been marked by a series of groundbreaking concepts and innovations, driven by ongoing research and advancements in the field. The history of thermoelectric dates back to the late 18th century, rooted in the exploration of electrical phenomena in living organisms. Luigi Galvani, a physiologist at the University of Bologna, was among the first to observe the connection between electricity and muscle contractions in frogs, leading to the concept of "galvanism." Galvani observed that when he connected the nerves of a dissected frog to a conductor linked to an electric machine, the frog's muscles would twitch violently. He also noticed that these contractions were even stronger when the

conductor was made from two different metals, like iron and copper. This led Galvani to hypothesize that electricity was somehow inherent in the animal's body, flowing from the nerves to the muscles in a manner similar to how a Leyden jar discharges electricity [12,13]. Galvani's work intrigued Alessandro Volta, another prominent Italian physicist and chemist, who extended these experiments. He further demonstrated this by setting up an experiment where the frog's hind legs were placed in water at one temperature and its back in water at another, connected by a metallic arc. Volta noticed that the muscle contractions only occurred when there was a temperature difference between the two water baths. This led him to conclude that the temperature difference generated an electrical current between the metals a phenomenon we now recognize as the thermoelectric effect. These early experiments by Galvani and Volta were pivotal in the discovery of thermoelectricity, marking the beginning of a field that explores the direct conversion of thermal energy into electrical energy.

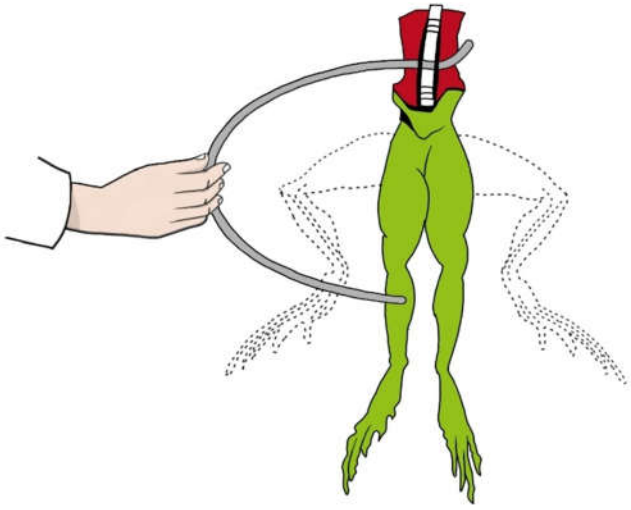

Fig.1.1 Luigi Galvani observed that touching a frog's nerves with a bimetallic arc caused convulsive muscle contractions, revealing the electrical nature of nerve signals.

1.3. Thermoelectric coefficients

1.3.1. Discovery of Johann Seebeck

Thomas Johann Seebeck, a German physicist, made a pivotal contribution to science with his discovery of the thermoelectric effect in 1821 [14]. After being inspired by

Hans Christian Oersted's work on electromagnetism, Seebeck explored the relationship between temperature and electrical currents. He observed that a compass needle would shift when placed near a closed circuit composed of two different metals, provided there was a temperature gradient between the metal junctions. This phenomenon later termed the Seebeck effect, occurs because a temperature gradient causes charge carriers (electrons or holes) to move from the hotter side to the cooler side, generating an electric current through the circuit. Seebeck initially believed that the temperature difference created magnetism, possibly due to the Earth's magnetic field. Later, it was discovered that the "thermoelectric force" generated an electric current, which caused the magnet to move in accordance with Ampère's law [8,15]. In 1851, Gustav Magnus demonstrated that the Seebeck voltage, which arises due to the temperature difference in a thermoelectric material, is unaffected by how the temperature is distributed along the length of the metals between the junctions. This discovery established that thermopower is a thermodynamic state function, meaning it depends only on the properties at the junctions and not on the temperature variations in between. This principle is fundamental to the operation of thermocouples, which are widely used for accurate temperature measurements in various applications. The voltage difference V generated across the terminals of an open circuit consisting of two dissimilar metals, A and B shown in Fig.1.2 is directly proportional to the temperature difference between the hot (T_h) and cold junctions (T_c).

$$V \alpha (T_h - T_c) \quad \text{.....(1.1)}$$

or

$$V = S(T_h - T_c) \quad \text{.....(1.2)}$$

where the proportionality constant S is known as the Seebeck coefficient is expressed in volts per kelvin (V/K)**.** This relationship forms the basis of the Seebeck effect, where the thermoelectric voltage arises due to the temperature gradient between the junctions of the metals. The Seebeck effect is commonly used to measure temperature with thermocouples, which consist of two different metals or alloys, like copper and constantan, with a differential Seebeck coefficient. To

measure temperature, one junction must be maintained at a known reference temperature, such as 0 °C in an ice bath [16].

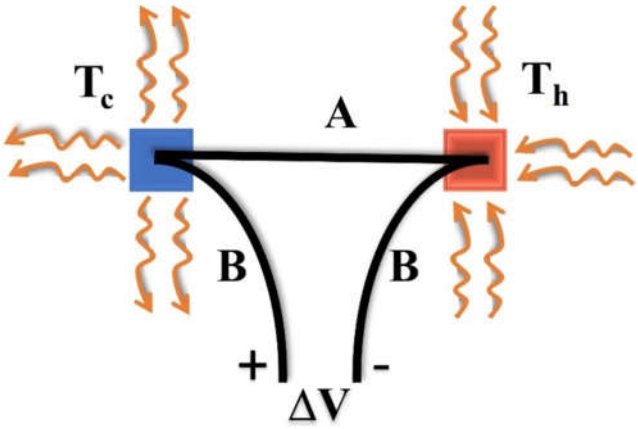

Fig.1.2 Schematic of the Seebeck effect in a thermocouple with metals A and B, where a temperature difference (T_h−T_c) generates a voltage (ΔV).

The thermoelectric effects that form the basis of thermoelectric energy conversion can be illustrated using the schematic of a thermocouple, as shown in Fig.1.3. A thermocouple consists of a circuit formed by two dissimilar conductors, labeled as A and B. These conductors, also known as thermocouple legs, arms, thermoelements, or simply elements (sometimes referred to as pellets by device manufacturers), are electrically connected in series but thermally connected in parallel [17]. When one end of the thermocouple is heated, the electrons in the hotter region move faster than those in the colder region, leading to the migration of electrons from the hot end to the cold end. This results in an accumulation of electrons at the cold end and positive ions at the hot end, generating a charge separation and an electric field, which in turn creates a voltage across the material. The magnitude of this voltage is described by the Seebeck coefficient between the two junctions, A and B, denoted as (S_{AB}). The Seebeck coefficient (S_{AB}), measures the magnitude of the thermoelectric effect and is determined by the ratio of the induced electric potential difference (V_{AB}) appear between two ends to the temperature difference (ΔT) across a thermoelectric material ie.,

$$S_{AB} = \frac{V_{AB}}{\Delta T} \quad \text{.....(1.3)}$$

The net electron flow is influenced by the Fermi functions of the hot and cold regions and the material's density of states. At the hot end, more electrons exist above the Fermi energy level compared to the cold end, and the difference between the Fermi functions is positive above the Fermi level and negative below it. This difference, together with the material's density of states, dictates the direction of electron flow and the sign of the Seebeck coefficient. In n-type materials, where electrons are the main charge carriers, the Seebeck coefficient is negative, while in p-type materials, where holes are the primary carriers, the coefficient is positive [18].

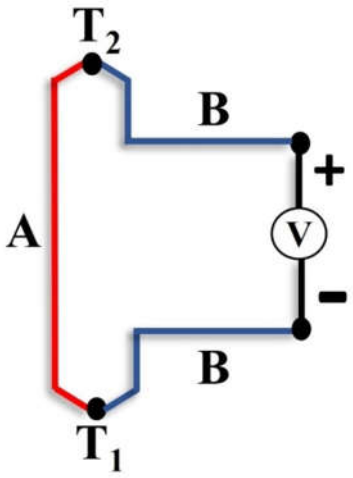

Fig.1.3 Seebeck effect.

1.3.2. The Peltier and Thomson effects

The Seebeck effect underpins thermoelectric power generation devices, the Peltier effect forms the basis of many modern thermoelectric refrigeration technologies. In 1834, the French watchmaker and physicist Jean Charles Athanase Peltier discovered the phenomenon now referred to as the Peltier effect. He observed that when an electric current flows across the junction of two different materials, heat is either absorbed or released at that point, as illustrated in Fig.1.4. At the subatomic level, the effect results from the differences in energy levels between n-type and p-type materials. When electrons move from a p-type material to an n-type material

due to an electric current, they move to a higher energy state, absorbing heat from the surrounding environment. Conversely, when electrons move from an n-type material to a p-type material, they drop to a lower energy state, releasing heat into the surroundings. This heat exchange, driven by the movement of electrons between materials with different energy levels, forms the basis of the Peltier effect [19]. This phenomenon is determined by the Seebeck coefficients of the materials, which indicate their capacity to produce a voltage difference when exposed to a temperature gradient. The Peltier effect is reversible ie, changing the direction of the electric current will reverse the direction of heat transfer at the junction [1,20].

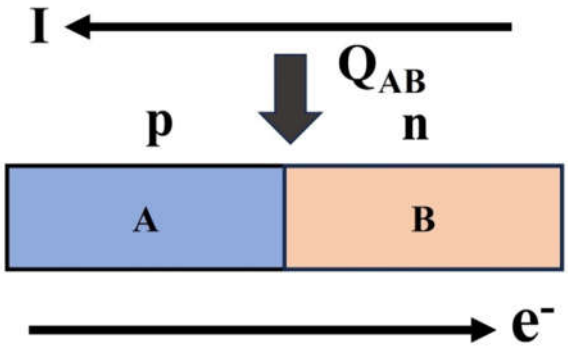

Fig.1.4 Peltier effect.

The Peltier coefficient (Π_{AB}) describes how the heat absorbed or released at the junction of two different semiconductors is related to the amount of current passing through it given by

$$\Pi_{AB}(T) = \frac{\Delta Q_{AB}}{I} \quad \text{.....(1.4)}$$

where ΔQ_{AB} is the heat absorbed or released, T is the temperature and I is the current. A Peltier cooler, or electronic refrigerator, uses thermoelectric energy conversion based on the Peltier effect. When an electric current flows through a thermoelectric material, it generates heat, creating a temperature gradient: heat is absorbed on the cold side, transferred through the material, and expelled at the hot side. When current flows through the junction, it creates either a forward or reverse bias, generating a temperature gradient. By efficiently dissipating heat from the hot

side, the temperature of the cold side can be significantly lowered, often by several tens of degrees, enabling effective cooling [21]. The innovative concept of thermoelectric self-cooling, which involves cooling and temperature regulation of a device using thermoelectric technology without consuming electricity, was explored by Martinez, Astrain, and Rodriguez in 2011. This principle is widely used in medicine, where thermoelectric cooling helps preserve vaccines and syringes at low temperatures to maintain their potency [22]. While liquid nitrogen is commonly used for such purposes, its application in hospitals is limited due to storage challenges. Conventional cooling systems are also bulky and prone to temperature regulation issues that may cause damage. Thermoelectric cooling offers a promising alternative, providing several advantages over traditional thermal methods. Although Peltier coolers have lower cooling power compared to traditional compressor-based refrigerators, they are valuable in niche applications like infrared detectors, CPU coolers, beverage storage units, etc.

In 1854, William Thomson discovered that when an electric current passes through a conductor that has a temperature difference between two points, heat is either absorbed or released, depending on the type of material and the direction of the current. This phenomenon called the Thomson effect, demonstrates the dual characteristics of thermoelectric materials as they can either generate electricity when exposed to a temperature gradient or produce heat when an electric current is applied [18, 23]. The Thomson effect arises from the interaction between the flow of electrical carriers and a temperature gradient within a conductor. Charge carriers moving against the thermal gradient absorb heat, increasing their potential energy, while those moving with the thermal gradient release heat, reducing their potential energy. Unlike the Seebeck and Peltier coefficients, which are determined by the characteristics of a junction between two different materials, the Thomson coefficient is a property of a single conductor [24].

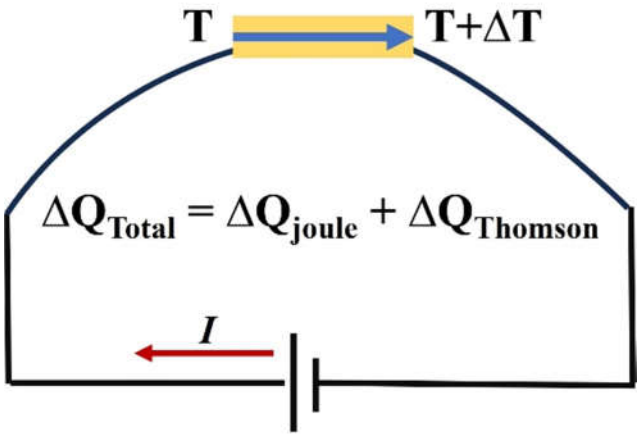

Fig.1.5 Schematic diagram of Thomson effect.

When a current passes through a single conductor with a temperature gradient, the heat transfer is given by the Thomson effect equation,

$$\frac{dQ}{dx} = C\,I\left(\frac{dT}{dx}\right). \quad \text{.....(1.5)}$$

The Thomson coefficient (C) describes how the rate of heating per unit length $\frac{dQ}{dx}$, the electric current (I), and the temperature gradient $\left(\frac{dT}{dx}\right)$ relate to each other. By applying the first and second laws of thermodynamics, the correlation between the Seebeck and Peltier coefficients can be derived as follows,

$$\Pi_{AB} = S_{AB}\,T \quad \text{.....(1.6)}$$

Using equations 1.4 and 1.5, equation 1.6 is related to Thomson coefficient C, given by

$$C_A - C_B = T\,\frac{dS_{AB}}{dT} \quad \text{.....(1.7)}$$

These are called the Kelvin relation. For a single conductor, the equation 1.7 can be rewritten as

$$C = T\,\frac{dS}{dT} \quad \text{.....(1.8)}$$

This relationship demonstrates the interconnection among the three thermoelectric

effects, highlighting the thermal and electrical characteristics of conductive materials. This formula applies to most metals and semiconductors, providing a robust theoretical basis for modern thermoelectric energy conversion technology.

1.4. Thermoelectric generation and the figure of merit (ZT)

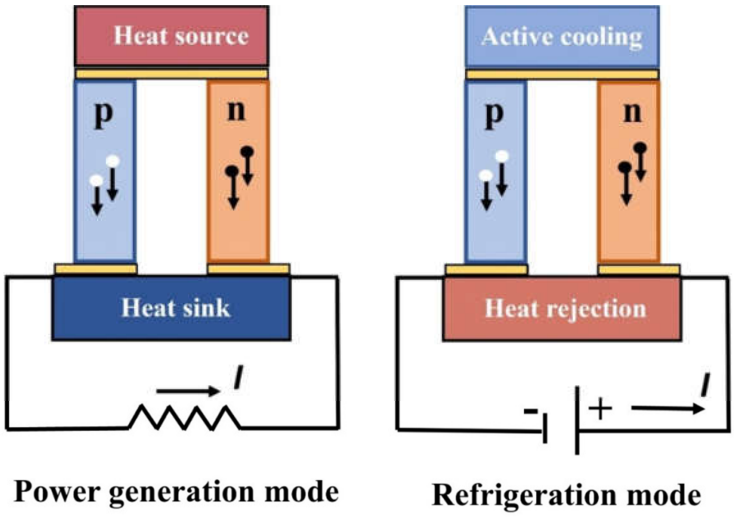

Fig.1.6 Power generation and cooling in thermoelectric materials.

Thermoelectric materials have the potential to directly convert heat into electricity or vice versa. The thermoelectric performance, whether for power generation or cooling as shown in Fig.1.6, relies on the material's efficiency in converting heat into electricity. As a type of heat engine, a thermoelectric converter follows the laws of thermodynamics, with its maximum theoretical efficiency represented by the Carnot engine efficiency. However, in practice, most energy generation systems operate at efficiencies well below this ideal. For an ideal thermoelectric converter with no heat losses, its efficiency is defined as the ratio of the electrical power output to the heat absorbed at the hot junction [17]. Despite theoretical limits, real-world devices must account for factors such as material properties, thermal conductance, and electrical resistance, which impact their overall performance. The maximum efficiency of a thermoelectric generator was initially calculated using a constant property model by Altenkirch in 1909. This formula was refined over time, and since Ioffe established the optimal conditions for achieving maximum efficiency in 1957, it has been commonly utilized given by [25]

$$\eta_{max} = \frac{\Delta T}{T_h} \frac{\sqrt{1+ZT_{avg}}-1}{\sqrt{1+ZT_{avg}}+\frac{T_c}{T_h}} \quad (1.9)$$

where ΔT and T_{avg} denote their temperature difference ($T_h - T_c$) and average ($T_h + T_c$)/2 respectively. The thermoelectric conversion efficiency, as outlined in equation 1.9, is determined by multiplying the Carnot efficiency $\frac{\Delta T}{T_h}$ by a reduction factor that depends on the material's figure of merit $S^2\sigma/\kappa$. In this equation S is the Seebeck coefficient, σ is the electrical conductivity, and κ represents the thermal conductivity. The dimensionless figure of merit (ZT) integrates these parameters to assess the material's efficiency in thermoelectric applications. It is defined as

$$ZT = \frac{S^2\sigma}{\kappa} T \quad (1.10)$$

The figure of merit ZT(T) is generally a temperature dependent property derived from the temperature-dependent material properties S(T), σ (T), and κ(T). The total thermal conductivity (κ) is the sum of the lattice and electronic contributions, expressed as ($\kappa = \kappa_l + \kappa_e$). For a thermoelectric generator to be efficient, it must function across a finite temperature difference ($\Delta T = T_h - T_c$), resulting in variations in material properties between the hot and cold ends [26]. The combined parameter $S^2\sigma$ known as the power factor (PF), is used to assess the conversion efficiency of TE materials.

1.5. Thermoelectric materials

The thermoelectric performance of devices is largely determined by the materials used and their key properties, including the Seebeck coefficient, electrical conductivity, thermal conductivity, and thermal stability. These properties collectively determine how efficiently a material can convert heat into electricity or vice versa [27]. Materials are often classified based on their electrical conductivity. Metals have high electrical conductivity, while insulators have very low conductivity, often considered zero under normal conditions, and semiconductors fall between these two extremes [17]. However, metals lack the necessary characteristics to achieve a high figure of merit (ZT) for thermoelectric applications

because modifying one property, such as electrical conductivity, typically affects others, like thermal conductivity, making it challenging to optimize them for thermoelectric efficiency [28]. In contrast, semiconductors are better suited for achieving a high figure of merit due to their intermediate carrier concentrations, which offer a more favourable balance between electrical conductivity and thermal properties.

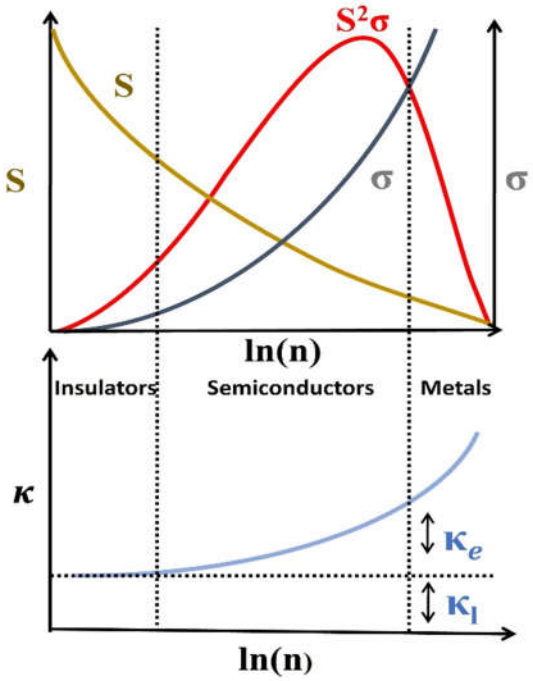

Fig.1.7 Variation of Seebeck coefficient (S), electrical conductivity (σ), power factor ($S^2\sigma$), and thermal conductivity (κ) with carrier concentration (n).

The primary challenge in designing a highly efficient thermoelectric material lies in managing the interdependence of the Seebeck coefficient, electrical conductivity, and thermal conductivity with the carrier concentration. Both the Seebeck coefficient and electrical conductivity are heavily influenced by the Fermi level, which itself is dependent on the carrier concentration, the effective mass of the carriers, and temperature. The Seebeck coefficient and electrical conductivity of a material are intrinsically related to the carrier concentration (n), making it crucial to find an optimal balance among these parameters to enhance thermoelectric performance. The Seebeck coefficient (S), electrical conductivity (σ), and carrier

concentration (n) of a material are related through the Mott relation, which is expressed as:

$$S = \frac{8\Pi^2 k_B{}^2}{3eh^2} m^* T \left(\frac{\Pi}{3n}\right)^{2/3} \quad (1.11)$$

where

$$\sigma = ne\mu \quad (1.12)$$

$$\mu = \frac{e<\tau>}{m^*} \quad (1.13)$$

where m* is the effective mass of holes (electrons), μ is the mobility of the charge carriers, k_B is the Boltzmann constant, e is the electronic charge = 1.6×10^{-19}C, h is the Planck's constant = 6.626×10^{-34} J Hz^{-1}, $\langle\tau\rangle$ is the average relaxation time and T is temperature. Since electrical conductivity depends on charge carrier concentration and mobility, an increase in carrier concentration generally leads to a decrease in the Seebeck coefficient. Consequently, the power factor ($S^2\sigma$) reaches its maximum when the carrier concentration is within an optimal range, striking a balance between electrical conductivity and the Seebeck coefficient. Heavily doped degenerate semiconductors, with carrier concentrations in the range of 10^{19} to 10^{21} cm^{-3}, are widely regarded as efficient thermoelectric materials [29]. These semiconductors are particularly suitable due to their appropriate bandgap, optimal carrier concentration, and negligible electronic contribution to thermal conductivity, making them highly effective for thermoelectric applications. Ideal thermoelectric materials do not occur naturally, so the focus of thermoelectric research is on developing materials that are both efficient and cost-effective. The goal is to enable large-scale production and widespread use, all while minimizing resource consumption. The majority of bulk thermoelectric materials are semiconductors, and the distribution of free charge carriers is described by the Fermi-Dirac function [30].

1.6. Metrics for assessing thermoelectric performance

1.6.1. Seebeck coefficient

The Seebeck coefficient is a crucial parameter for assessing the performance of thermoelectric materials and serves as one of the primary criteria for evaluating their effectiveness in thermoelectric power generation and refrigeration applications [31]. Equation 1.10 indicates that the ZT of a material is directly proportional to the

square of its Seebeck coefficient, highlighting the importance of enhancing the Seebeck coefficient to optimize the ZT of thermoelectric materials [32]. The Bethe-Sommerfeld expansion for the Seebeck coefficient is given by [27]

$$S = \frac{\Pi^2 {k_B}^2 T}{3e} \left(\frac{1}{n}\frac{dn(E)}{dE} + \frac{1}{\mu}\frac{d\mu(E)}{dE}\right)_{E=E_f} \quad \text{..... (1.14)}$$

where n(E) represents the carrier density at energy E, μ(E) denotes the mobility at energy E, E_f is the Fermi energy, and e is the electronic charge. The Seebeck coefficient is influenced by several factors that can be optimized to enhance thermoelectric performance. Since S is directly proportional to the effective mass of charge carriers (m^*) and inversely proportional to the carrier concentration (n), increasing m^* while reducing n can effectively improve S [32]. Additionally, the Seebeck coefficient is dependent on the asymmetry of the electronic density of states (DOS), n(E) around the Fermi level (E_f) and the asymmetry in the energy-dependent mobility of charge carriers. Therefore, strategies to enhance S involve (i) increasing the energy dependence of the mean free path through a scattering mechanism that significantly affects the charge carriers and (ii) locally increasing the density of states (DOS) to amplify the energy dependence of the carrier density n(E) [33].

According to Boltzmann transport theory, the Seebeck coefficient S for a material conducting with a single type of carrier (either electrons or holes) is given by:

$$S = \frac{1}{T}\frac{\int_0^\infty g(E)\,\tau_e E\,(E-E_f)\frac{df_0(E)}{dE}\,dE}{e\int_0^\infty g(E)\,\tau_e E\frac{df_0(E)}{dE}\,dE} \quad \text{..... (1.15)}$$

Where E_f, f_0, e, and τ_e denote the Fermi level, the Fermi distribution function, the electron charge, and the relaxation time for charge carriers. The Seebeck coefficient's sign and magnitude are primarily determined by the numerator of the equation 1.15, while the denominator represents electrical conductivity [34]. Here, − and + denote contributions from electrons ($E > E_f$) and holes ($E < E_f$), respectively. Fig.1.8 shows schematic plots of the integrand function $g(E)\,\tau_e E\,(E - E_f)\,\frac{df_0(E)}{dE}$ from the numerator of equation 1.15, plotted against the Fermi energy. It illustrates

that the contributions to the Seebeck coefficient from carriers with energy above and below the Fermi level (denoted as S1 and S2) have opposite signs.

$$S_1 = g(E)\,\tau_e E\,(E - E_f)\,\frac{df_0(E)}{dE}\,dE > 0 \quad \text{.....(1.16)}$$

$$S_2 = g(E)\,\tau_e E\,(E - E_f)\,\frac{df_0(E)}{dE}\,dE < 0 \quad \text{.....(1.17)}$$

Using the reduced Fermi energy $\eta = E/k_B T$, equation 1.15 can be simplified into a form that involves Fermi–Dirac integrals, applicable for charge transport in a parabolic band. The simplified expression is given by:

$$S(\eta) = \pm\frac{k_B}{e}\left[\frac{(r+5/2)\,F_{(r+3/2)}(\eta)}{(r+3/2)\,F_{(r+1/2)}(\eta} - \eta\right] \quad \text{.....(1.18)}$$

The scattering parameter r in this context is the exponent that relates the relaxation time τ_e to energy in the form $\tau_0 E^r$, where τ_0 is the relaxation time for non-degenerate carriers. This indicates that the Seebeck coefficient S depends solely on the reduced chemical potential for a specific type of scattering. Since acoustic phonon scattering predominantly influences carrier behavior in most high-performing thermoelectrics (which corresponds to a high ZT), a key observation in thermoelectric is that the Seebeck coefficient S tends to decrease with increasing carrier concentration (which corresponds to a higher η) at a constant temperature. Conversely, S tends to increase as the temperature rises at a fixed carrier concentration (which corresponds to a lower η).

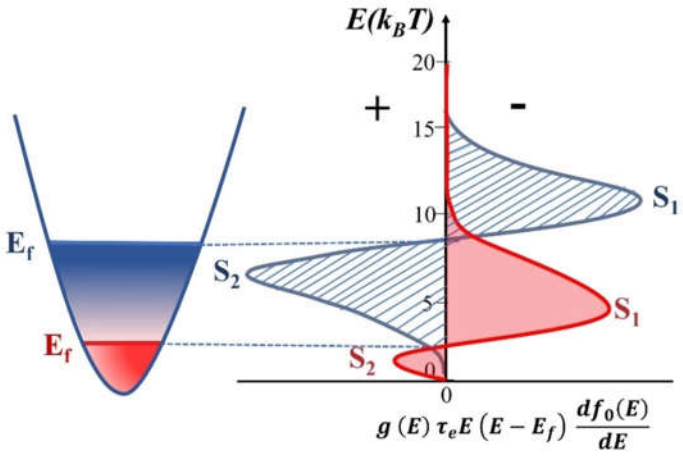

Fig.1.8 Schematic of the integrand in equation 1.15 vs reduced Fermi energy. Shaded areas (S1 and S2) show opposite contributions to the Seebeck coefficient from carriers above and below the Fermi level.

1.6.2. Electrical conductivity

The electrical conductivity (σ) be derived by solving the Boltzmann transport equation under the relaxation time approximation given by

$$\sigma = \frac{2q^2}{3m^*}\int_0^\infty g\,(E)\,\tau(E)E\frac{df_0(E)}{dE}\,dE \qquad (1.19)$$

where
$$g(E) = N(E)\upsilon^2(E)\tau(E) \qquad (1.20)$$

where N(E), υ(E), and τ(E) represent the density of states, Fermi velocity, and scattering time, respectively [35]. The term g(E), encompassing these factors, is known as the transport distribution function, which describes how carriers at different energy states contribute to electrical conductivity. Accordingly, σ(E) indicates the contribution of electrons at a given energy E to the total conductivity. σ(E) is influenced by two energy-dependent components: (i) the band structure, which determines g(E) and related parameters, and (ii) the scattering time τ(E), which depends on factors beyond the band structure itself such as phonon scattering, impurity scattering, and electron-electron interaction [36]. The mobility of charge carriers is directly proportional to the average relaxation time (τ) and inversely proportional to the effective mass (m^*) of the carriers, meaning that longer relaxation times and smaller effective masses result in higher mobility [37]. Since the average relaxation time is determined by these scattering mechanisms, it is crucial to consider its value when calculating the carrier mobility. Understanding the scattering processes that affect τ(E) is essential for optimizing the mobility and thus the overall conductivity of materials. Since electrical conductivity is strongly influenced by carrier behaviour, optimizing key parameters such as carrier concentration and mobility becomes essential for achieving high thermoelectric performance. The carrier concentration directly affects the position of the Fermi level, which in most high-performance thermoelectric materials typically falls within the range of ~10^{19} to 10^{21} cm^{-3}, with the Fermi level near the edge of the valence (conduction band) [38]. Carrier mobility which offers insights into the transport properties of the carriers, as its temperature dependence reveals the dominant scattering mechanisms that affect the material's overall conductivity. Furthermore, mobility is intimately

linked to the relaxation time (τ), determined as the reciprocal sum of contributions from various scattering processes [39]. Thus, both carrier concentration and mobility play interconnected roles in shaping the transport and thermoelectric properties of materials.

1.6.3. Electronic band structure

The electronic band structure, representing energy as a function of momentum, including energy bands and gaps, is fundamental to the thermoelectric properties of materials. Band theory provides essential insights into σ, S, and n which are key to understanding thermoelectric properties [40]. Thermoelectric performance hinges on both electronic and lattice structures: the former dictates carrier concentration and effective mass, while the latter influences electron and phonon scattering. Equations (1.11) – (1.13) emphasize the inherent trade-off between electrical conductivity and the Seebeck coefficient, driven largely by carrier concentration and effective mass, where enhancing one often compromises the other [41]. Therefore, strategies for improving thermoelectric performance focus on optimizing either carrier concentration or effective mass with minimal impact on the counterpart property. These strategies fall into two primary approaches: electronic structure modification and carrier scattering management, with our emphasis here on electronic structure modifications.

Before diving into specific modifications, it is essential to identify the electronic structure characteristics that best support high thermoelectric performance. Foundational work by Mahan and Sofo has greatly informed our understanding of these ideal features [42]. Studying a material's electronic structure not only offers insight into its electrical properties but also reveals valuable information about its thermal behaviour, such as bonding characteristics and lattice anharmonicity, both critical for achieving efficient thermoelectric material. Using Boltzmann transport theory, the electrical conductivity (σ) and the Seebeck coefficient (S) can be expressed as:

$$\sigma = \int_{-\infty}^{+\infty} \sigma(\epsilon, T)\left[-\frac{\partial f_0}{\partial \epsilon}\right] d\epsilon \quad \text{.....(1.21)}$$

$$S\sigma T = \frac{1}{e}\int_{-\infty}^{+\infty} \sigma(\epsilon, T)(\epsilon - \mu_0)\left[-\frac{\partial f_0}{\partial \epsilon}\right] d\epsilon \quad \text{.....(1.22)}$$

In these equations, ε represents the reduced energy, μ_0 denotes the chemical potential, and σ(ε) is the spectral conductivity. These equations highlight the importance of tailoring the electronic structure to maximize thermoelectric performance. At finite temperatures, the Fermi-Dirac distribution function dictates that only electrons near the Fermi energy E_f contribute to conduction. The Fermi window factor, $-\frac{\partial f_0}{\partial \epsilon}$, is a bell-shaped curve centered around E_f with a width of k_B. [36]. The 'effective' electronic structures that govern electrical transport lie within a narrow energy range defined by this factor [42]. This shape reflects the fact that only electrons within this thermal energy range are accessible for conduction, as those further from E_f are either fully occupied or empty and cannot contribute effectively [43]. Consequently, a rapid variation in the transport distribution function near E_f becomes essential for achieving a large Seebeck coefficient. This behavior depends on the asymmetry of the density of states (DOS) and the relaxation time (τ) around E_f, emphasizing the importance of tailoring the electronic band structure to optimize thermoelectric performance.

Fig.1.9 illustrates the critical role of band structure in governing electronic transport properties, with a focus on the DOS and scattering time (τ) near E_f. In Fig.1.9 (a), the DOS (g(E)) represents the number of electronic states available for conduction and interacts with the energy-dependent derivative of the Fermi-Dirac distribution function ($-\frac{\partial f_0}{\partial \epsilon}$), which defines the energy range where electrons contribute most to transport. Fig.1.9 (b) emphasizes the scattering time (τ(E)), which describes how frequently electrons scatter as a function of energy. In both figures, the red curve represents $-\frac{\partial f_0}{\partial \epsilon}$, peaking near the Fermi level, which indicates that electronic transport is dominated by states close to E_f. The dashed red lines show the effective energy range for transport contributions. Together, the figure underscores that the band structure shapes electronic transport by governing the DOS and scattering time, both of which play pivotal roles in determining the efficiency of charge carrier movement in thermoelectric materials.

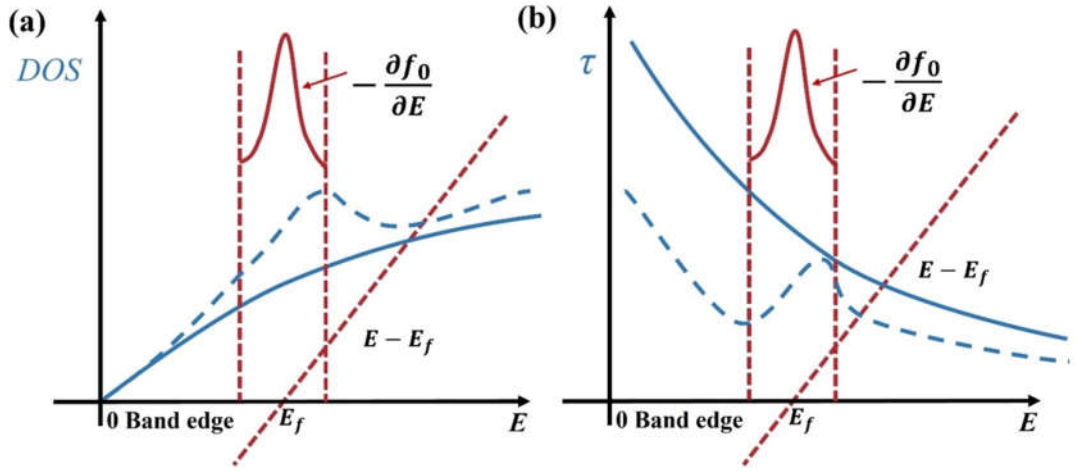

Fig.1.9 Schematic representation of (a) band engineering through modifications in the density of states (DOS) and (b) scattering engineering via changes in relaxation time (τ).

1.6.4. Effective mass of charge carriers

The effective mass (m^*) in thermoelectric materials indicates the curvature of the energy band and can be altered by strategies like doping and nanostructuring. It serves as a crucial parameter in parabolic band models used to analyze the electronic structure and transport properties of these materials [30]. Using a classical statistical approximation, Ioffe proposed that [44]

$$n^* = (m^*T)^{3/2} \quad \text{..... (1.23)}$$

Where the density of state effective mass,

$$m^* = N_v^{2/3} m_b^* \text{.....(1.24)}$$

For semiconductors with a valley degeneracy of N_v and an average effective mass m_b^* of the charge carrier per valley. At a fixed carrier concentration, a larger effective mass leads to a higher density of states in the energy band, which increases the Seebeck coefficient by enhancing the energy difference between carriers [42]. This is especially true in materials with flat, narrow bands that have a high density of states near the Fermi level (E_f). However, since the effective mass is also associated with the inertial mass, heavier carriers move more slowly, resulting in lower mobility [45]. This reduction in mobility decreases electrical conductivity,

which can negatively impact the overall thermoelectric efficiency. Therefore, optimizing thermoelectric materials requires a careful balance between enhancing the effective mass and preserving sufficient electrical conductivity. The inertial effective mass can be mathematically determined by calculating the inverse of the curvature of the band structure responsible for electronic transport. In low band gap materials, the interaction between the valence and conduction bands induces non-parabolicity, often characterized by the Kane band model [46]. Within this framework, the dispersion E(k) and the carrier effective mass (m^*) are linked to the band gap (E_g).

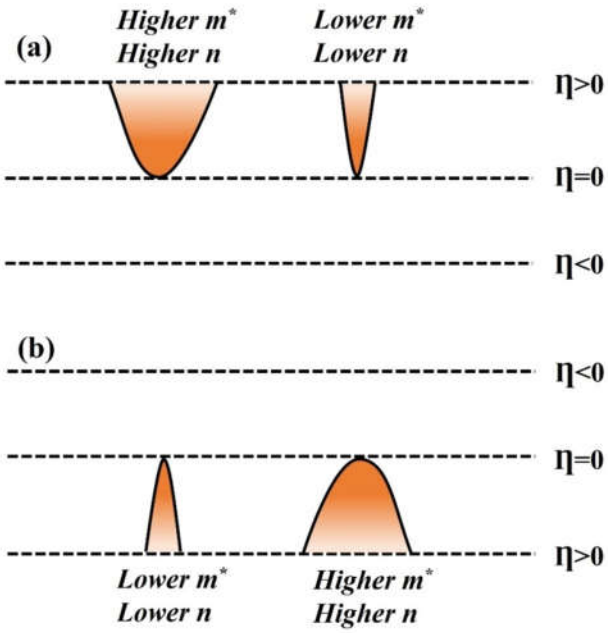

Fig.1.10 Schematic of reduced Fermi levels for (a) conduction and (b) valence bands showing carrier distribution changes.

For degenerate semiconductors exhibiting Kane-type band dispersion, the effective mass (m^*) is directly proportional to the band gap (E_g) through the relationship [47],

$$\frac{\hbar^2 k^2}{2m^*} = E\left(1 + \frac{E}{E_g}\right) \quad \text{(1.25)}$$

where ħ is the reduced Planck's constant, k is the crystal momentum, and E is the energy of electron states. This relationship underscores the intricate connection between the band structure and carrier dynamics in thermoelectric materials. By

modifying the band gap and shaping the band curvature, the effective mass can be tuned to enhance the power factor, a critical parameter for thermoelectric performance. However, this optimization demands a delicate balance, as excessively increasing the effective mass may reduce mobility and, in turn, lower electrical conductivity. Strategies such as controlled doping or exploiting quantum confinement effects are often employed to fine-tune the effective mass and achieve an optimal combination of thermoelectric properties for practical applications.

1.6.5. Thermal conductivity

Thermal conductivity is a key factor that influences the conversion efficiency of thermoelectric materials. For optimal efficiency, the material should exhibit a high power factor while maintaining low thermal conductivity. However, achieving both simultaneously is challenging due to the inherent interdependence between these parameters. Thermal conductivity is defined as.

$$\kappa_T = \kappa_e + \kappa_{l,} \quad (1.26)$$

which is influenced by both electrons and phonons. According to the Wiedemann-Franz law, the electronic component of thermal conductivity is directly related to electrical conductivity as follows

$$\kappa_e = L_0 \sigma T \quad (1.27)$$

where L_0 is a constant known as Lorentz's number, with a value of 2.4×10^{-8} J^2 K^{-2} C^{-2}. Therefore, the electron contribution to thermal conductivity can be reduced by decreasing electrical conductivity, as S, σ, and κ_e are all linked to carrier concentration and effective mass. The primary goal is to lower the thermal conductivity by minimizing the lattice contribution, as it is an independent thermoelectric parameter. In the process of lattice vibration energy transfer, the energy spreads out diffusively through collisions instead of moving in a direct path. Lattice thermal conductivity results from the diffusion of phonons. Based on the kinetic theory of heat conduction, lattice thermal conductivity can be described by the following equation [41]

$$\kappa_l = v_s C_v L_{ph} \quad \text{.....(1.28)}$$

where v_s is the sound velocity, C_v is the specific heat capacity at constant volume, and L_{ph} is the mean free path of phonons. These parameters generally depend on temperature and the material's properties, such as the Debye temperature, mean phonon velocity, and other material-specific factors like average crystalline size, defect density at different length scales, and three-phonon scattering parameters [48]. Specific heat capacity is an intrinsic property of the material, while the mean free path of phonons depends on scattering mechanisms. Lattice thermal conductivity is linked to phonon transport and is not directly influenced by electrical conductivity or the Seebeck coefficient, allowing it to be independently controlled. To reduce thermal conductivity, it is essential to enhance scattering centers, such as point defects, dislocations, boundary scattering, and phonon-phonon Umklapp scattering. The electronic component of thermal conductivity (κ_e) is primarily influenced by carrier concentration (n), while the lattice component (κ_l) is controlled by impurities and various phonon scattering mechanisms. The strategies for lowering thermal conductivity involve reducing the mean free path (MFP) of phonons by increasing the phonon scattering rate [49]. An alternative approach is to explore materials with intrinsically low thermal conductivity to achieve a reduced thermal conductivity value.

1.7. Cu_2Se based thermoelectric materials

Metal chalcogenides, composed of metal elements and chalcogens (S, Se, Te), have gained significant attention for their potential in a wide range of energy applications, including solar cells, light-emitting diodes, sensors, batteries, supercapacitors, and thermoelectric devices [50]. Unlike oxides, metal-chalcogenide-based TE materials exhibit a higher power factor due to their weaker covalent bonding, which results from their lower electronegativity. Additionally, their relatively high atomic weight, compared to certain other thermoelectric materials, aids in minimizing thermal conductivity [51]. Transition metal chalcogenides, subgroups of these compounds, are formed by combining one or more transition metals with chalcogen elements. These compounds feature a stable chalcogenide structure formed by the interaction

between d-block transition metals and p-block group-16 elements [52]. This combination primarily enables the tuning of the material's band gap, which in turn provides enhanced flexibility in tailoring its electronic structure. The tunable electrical transport properties of metal chalcogenide compounds are due to their band structures, which can be easily modified through doping or by forming solid solutions [53]. As a result, these materials have become attractive for thermoelectric applications because of their high power factor values. The "phonon-glass electron-crystal" (PGEC) concept, proposed by Slack, further underscores their potential. This concept envisions an ideal thermoelectric material as one that facilitates free electron movement while impeding heat-carrying phonons, achieving a balance of high electrical conductivity and low thermal conductivity [54]. In PGEC materials, the crystal structure consists of two sublattices: one provides the electrically conductive pathway, while the other functions as a thermal barrier and sometimes as a charge reservoir. This dual-sublattice design has positioned Cu-based chalcogenides as promising candidates for power generation applications.

Copper chalcogenides, including $Cu_{2-x}X$ (where X can be S, Se, or Te), are gaining considerable attention as promising thermoelectric materials because of their exceptional properties [55]. Cu_2Se has emerged as a leading candidate in this category, achieving a peak thermoelectric figure of merit (ZT) > 2, due to its crystal structure that imparts an ultralow thermal conductivity similar to that of a liquid. This impressive performance is complemented by its ecofriendly nature, enhancing its appeal for sustainable energy applications [56]. Cu_2Se is a p-type semiconductor with a bandgap of approximately 2.1-2.3 eV, and it is composed of abundant, inexpensive, and non-toxic elements [57]. Cu_2Se is known as a phase-transition material, existing in a monoclinic phase at lower temperatures, but transitioning to an antifluorite structure in the temperature range 350-400 K. In its fluorite phase, Cu_2Se crystallizes in the cubic $Fm\bar{3}m$ space group, where each Cu^{1+} ion is bonded to four equivalent Se^{2-} ions, forming a combination of edge and corner sharing $CuSe_4$ tetrahedra with uniform Cu-Se bond lengths of 2.51 Å. The Se^{2-} ions adopt a body-centered cubic arrangement, each bonded to eight equivalent Cu^{1+} ions. It is possible to reverse such a phase transition by heating or cooling processes [55].

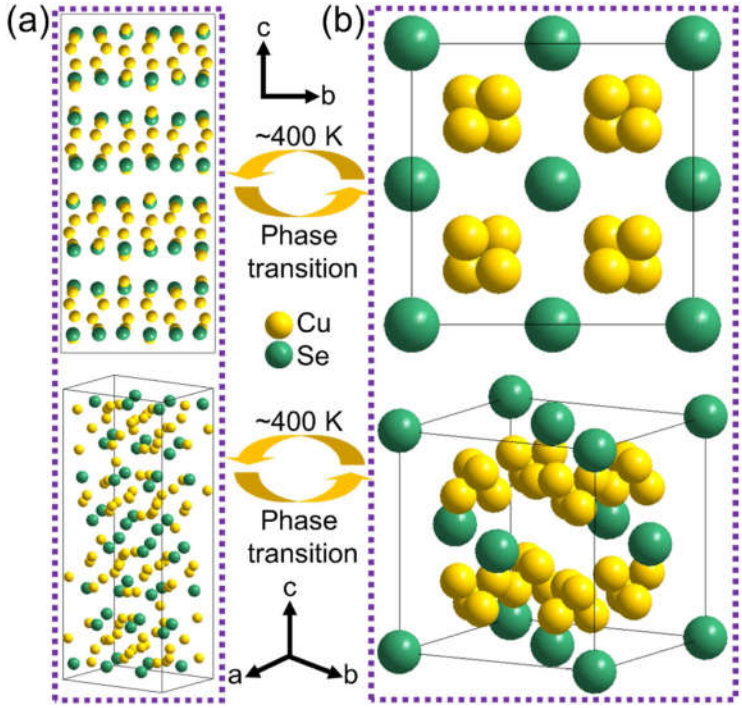

Fig.1.11 Schematic representations of the crystal structures for (a) low-temperature monoclinic Cu_2Se and (b) high-temperature antifluorite Cu_2Se, highlighting the reversible phase transition occurring around ~400 K [58].

The average crystal structure of α-Cu_2Se was determined to have a trigonal symmetry [59]. It exhibits a layered structure with alternating copper-deficient and copper-rich layers along the c-axis, a structural characteristic that is typical of many previously reported materials. Upon heating, Cu ions migrate from the copper-rich layer to the copper-deficient layer, characterized by a space group of Fmm and a lattice parameter of a = 5.74 Å. This process eventually leads to the formation of the high-temperature β-phase [60]. Generally, Cu_2Se in its β-phase exhibits remarkable thermoelectric performance at mid to high temperatures, which is closely linked to its intricate superionic structure [61]. As shown in Fig.1.11, β-Cu_2Se features an antifluorite cubic structure with two distinct sublattices: a rigid face-centered cubic sublattice made up of Se atoms, and a disordered Cu sublattice where Cu ions are randomly distributed across tetrahedral (8c) and trigonal (32f) sites. This transition involves a reorganization of Cu and Se atoms, leading to notable changes in both its crystal structure and properties [58]. As the temperature increases, the disordered copper atoms in Cu_2Se tend to become superionic throughout the crystalline structure while Se atoms create a stable sublattice that offers pathways for carrier

transport. The cation sublattice, exhibiting liquid like behavior, efficiently scatters heat carrying phonons and suppresses certain transverse vibrational modes, resulting in exceptionally low lattice thermal conductivity [62]. As a result, Cu_2Se exhibits the "phonon-liquid, electron-crystal" characteristic, making it a highly promising thermoelectric material for medium temperature power generation [63].

To develop high-performance thermoelectric materials, it's crucial to understand how parameters like effective mass, symmetry, and atomic arrangements affect transport properties. These factors are tied to the material's electronic structure, which is determined by its crystal structure [64]. According to the PLEC concept, Cu_2Se-based thermoelectric materials are known for their low intrinsic thermal conductivity, which contributes to their high energy conversion efficiency owing to their unique stoichiometric frameworks [65]. The thermoelectric properties of Cu_2Se can be significantly modified by varying the concentration of copper vacancies within its crystal structure. The β-phase of Cu_2Se exhibits a complex superstructure, which is highly sensitive to both the composition and preparation methods of the samples [59]. Despite its potential, challenges such as structural instability, lower conversion efficiency, and reduced thermoelectric performance have constrained the broader application of these materials in recent years [65]. To overcome these limitations and harness the promising attributes of Cu_2Se, it is crucial to explore and implement innovative strategies aimed at enhancing its thermoelectric performance. Various approaches, including optimizing dopant levels, incorporating nanostructures, and refining synthesis techniques, offer potential pathways to improve the material's efficiency and stability. The following section discusses some of these adopted strategies that can be implemented to further enhance the performance of Cu_2Se.

1.8. Approaches to maximize thermoelectric potential

1.8.1. Nanostructuring

Nanomaterials, with at least one dimension spanning from 1 to 100 nm, are highly valued for their unique properties. The advancement of different nanostructures provides remedies for many of the limitations associated with conventional

thermoelectric materials. When the dimensions of a material fall within the nanometer range, its surface to volume ratio increases significantly, leading to drastic changes in its properties. Hicks and Dresselhaus showed through theoretical calculations that low dimensional nanostructured materials exhibit far superior thermoelectric properties compared to their bulk counterparts [66]. In these devices, the final properties depend on both the individual nanoparticles and how they are assembled at a macroscopic scale in thin films or bulk materials [67].

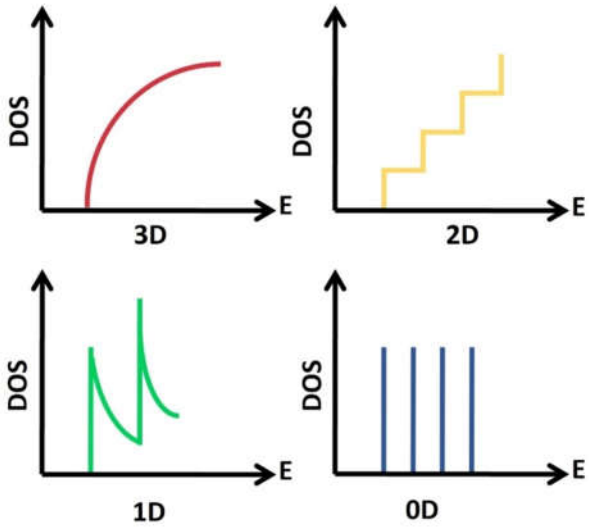

Fig.1.12 DOS vs. energy for materials of various dimensionalities: 3D, 2D, 1D, and 0D.

Nanostructured materials such as bulk nanostructures (3D), quantum wells (2D), quantum wires (1D), and quantum dots (0D) with nanosized inclusions alter the power factor and ZT by modifying the electronic density of states (DOS) [68]. Reducing dimensionality alters the DOS near the Fermi level in nanomaterials through quantum confinement effects that increase the Seebeck coefficient [32]. The quantum confinement and energy filtering effects become prominent when the system size approaches the electron mean free path or wavelength. Under these conditions, the DOS increases, which enhances the Seebeck coefficient [33]. Simultaneously, thermal conductivity decreases due to phonon scattering at nanostructured surfaces or interfaces. In heavily doped semiconductors, electrons have a much shorter mean free path (mfp) compared to phonons. Nanostructuring

introduces numerous interfaces that can scatter phonons of different mfp more efficiently. This process effectively lowers the lattice thermal conductivity while maintaining good carrier mobility and electronic conduction [69]. To optimize this effect, nanostructures should be designed with dimensions smaller than the phonon mfp but larger than the electron mfp [70]. Traditionally, nanostructured TE materials are commonly prepared using many methods, which include methods like ball milling, co-precipitation, hydrothermal method, sol gel method, etc [48].

1.8.2. Doping

Most effective thermoelectric materials are heavily doped semiconductors with carrier concentrations in the range of 10^{18} to 10^{20} cm^{-3} [36]. To enhance the thermoelectric performance dopants must fulfill certain criteria: (i) increase the Seebeck coefficient, (ii) improve electrical conductivity, and (iii) reduce thermal conductivity. A high level of doping is essential to achieve the high density of charge carriers required for efficient electrical conduction. Generally, electrical conductivity can be significantly improved by introducing p-type or n-type impurities. However, this improvement in conductivity often comes at the cost of decreased carrier mobility due to the scattering effects introduced by the impurities [71]. In semiconductors, a modulation doping mechanism has been introduced to separate charge carriers from ionized dopants, thereby reducing carrier scattering. This approach enhances the mobility of charge carriers, which in turn improves the electrical conductivity of the material. In the superionic antifluorite Cu_2Se, which features a stable Se sublattice and a mobile Cu sublattice, point defects caused by vacancies or doping at different sites impact thermoelectric properties in different ways [58]. The high thermoelectric performance is primarily due to dopants creating point defects and dislocations, inducing mass and strain fluctuations in the lattice, and altering microstructures, all of which significantly scatter phonons and carriers, reducing thermal conductivity below the glassy limit [72]. The impact of point defects at the Cu site on the thermoelectric performance of Cu_2Se is closely linked to the homogeneity of doping, which, in turn, depends on the material preparation

method. Therefore, exploring new dopants and optimizing existing ones is crucial for further enhancing thermoelectric performance.

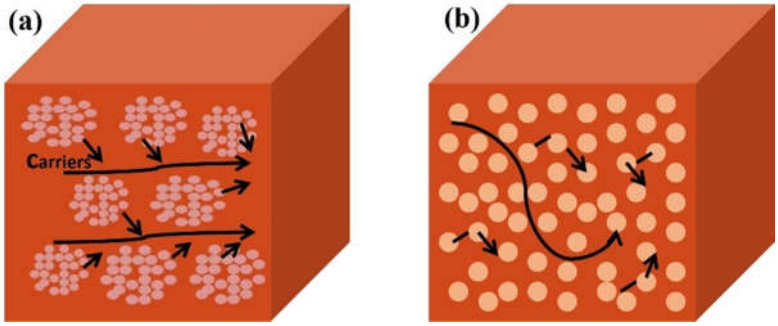

Fig.1.13 Diagram illustrating the techniques of (a) modulation doping and (b) uniform doping.

1.8.3. Composite engineering

Composite engineering has emerged as a transformative strategy to enhance the performance of TE materials by combining multiple components to create synergistic effects that surpass the capabilities of individual constituents [73]. A key aspect of this approach is nanostructuring, where nanometer-scale features such as polycrystals and interfaces are integrated into bulk materials. This design significantly increases phonon scattering, effectively reducing lattice thermal conductivity and enhancing thermoelectric efficiency [69]. The incorporation of nanoparticles, nanoinclusions, or secondary phases into the nanostructured host material further optimizes these properties, offering precise control over scattering characteristics through tunable factors such as size, shape, composition, and arrangement of the nanoscale features [55,74]. These synergistic effects have positioned composite engineering as a pivotal approach for advancing thermoelectric technologies, offering significant improvements in efficiency and performance.

Nanocomposites, a prime example of this approach, offer unique advantages in thermoelectric applications. They enhance electrical conductivity by creating new electron transport channels or improving carrier mobility via modified band structures. Additionally, nanocomposites provide superior mechanical stability compared to single-component materials, making them ideal for environments with

thermal gradients and mechanical stress [42]. Quantum confinement effects in nanocomposites alter the electronic band structure, thereby increasing the Seebeck coefficient and improving thermoelectric sensitivity. Mechanisms such as band alignment and carrier energy filtering further refine charge carrier transport, contributing to the overall enhancement of thermoelectric performance [75].

A defining feature of nanocomposites is their high density of interfaces between nanoscale domains. These interfaces play a critical role in determining transport properties by influencing carrier scattering. Abrupt changes in scattering rates and the density of states near the Fermi level enhance the Seebeck coefficient, while boundary scattering of phonons at the interfaces reduces thermal conductivity. This dual optimization of electron and phonon transport makes nanocomposites a highly promising solution for advancing thermoelectric technologies, offering a balance of improved efficiency, mechanical stability, and sensitivity to thermal gradient.

1.8.4. Carrier energy filtering

Interfaces or grain boundaries are the defects formed at the crystal lattice that scatter the charge carriers and affect conductivity. The minority carriers and the charge carriers with lower energies are more scattered than the majority carriers and high energy charge carriers. This can be overcome by introducing energy barriers that allow the higher energy charge carriers to pass through and block the diffusion of low-energy carriers (blue circles). This is known as carrier energy filtering. This energy filtering effect increases the Seebeck coefficient with a negligible impact on electrical conductivity. Under quasi-equilibrium conditions with diffusive electron transport, the Seebeck coefficient (S) is approximately proportional to the mean excess energy $\langle E - E_f \rangle$, as outlined in equation 1.15. This means that for a fixed carrier concentration, an increase in $\langle E - E_f \rangle$ leads to a higher Seebeck coefficient. To achieve a high power factor, it is crucial to maintain a significant and energy-asymmetric differential conductivity, $\sigma(E)$, within the Fermi energy window. This principle underpins the carrier energy filtering approach [73]. As shown in equations 1.15 and 1.19, energy filtering selectively allows carriers with higher mean excess energy to contribute, thus boosting the Seebeck coefficient. However, this process

also reduces carrier concentration, which can lower electrical conductivity, creating a trade-off that impacts overall performance. Therefore, the reduction in conductivity should be offset by the increase in the Seebeck coefficient, ultimately enhancing the power factor [76]. This can be achieved by introducing tall barriers either in the valence band of p-type materials or the conduction band of n-type materials [77]. Thus, charge carriers selectively get transmitted through the barriers, and the Seebeck coefficient increases, therefore the height of the barrier is an important factor for effective energy filtering.

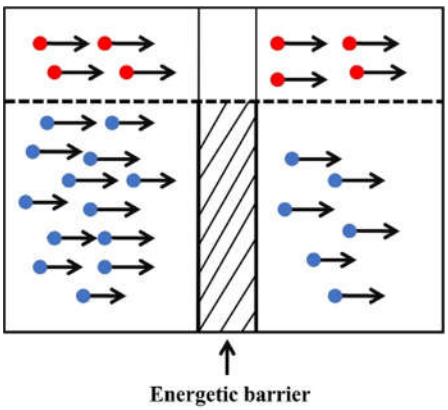

Fig.1.14 Schematic representation of the carrier energy filtering mechanism.

1.8.5. Valence band convergence

Band convergence plays a crucial role in improving thermoelectric performance by increasing charge carrier density at a given Fermi level, typically enhancing electrical conductivity without significantly affecting the Seebeck coefficient [77]. This strategy involves aligning the valence or conduction bands to achieve greater valley degeneracy, resulting in a simultaneous increase in both the Seebeck coefficient and electrical conductivity [40]. Band convergence occurs when separate energy bands are engineered to align at the same energy level, which can be achieved by adjusting the energy of a band at specific symmetry points, such as the Γ point in the Brillouin zone, to match the energies of nearby bands at different symmetry points, often through alloying or doping [78]. When two energy bands are closely spaced, their band multiplicity combines, leading to a higher density of states. The density of state effective mass (m^*_{DOS}) quantifies the density of states at a

given Fermi level [43]. A higher DOS effective mass indicates more states per energy level, which increases the Seebeck coefficient, as described by the Mott formula.

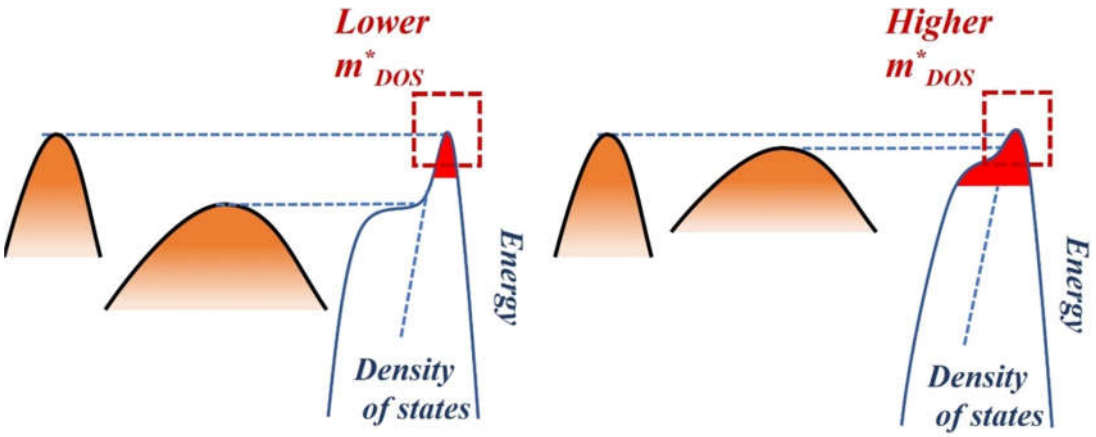

Fig.1.15 Impact of band convergence on m^*_{DOS}, boosting the Seebeck coefficient without sacrificing conductivity.

However, as the density of states increases, the band structure may distort, resulting in a higher effective mass (m*), which can reduce carrier mobility and thermopower. To mitigate this, introducing multiple valleys in semiconductors can offset the reduction in mobility. Mahan demonstrated that multivalley semiconductors with low inertial mass can enhance the density of state effective mass (m^*_{DOS}) without significantly decreasing mobility, provided intervalley scattering is minimized [18].

The density of state effective mass is equal to

$$m^*_{DOS} = N_v{}^{2/3}(m_1 m_2 m_3)^{1/3} \quad \text{.....(1.29)}$$

where N_v is the number of equivalent valleys and m_{123} is inertial masses in each direction. This indicates that semiconductors with multiple valleys and low inertial mass can achieve higher carrier mobility. Therefore, optimizing the Seebeck coefficient in these materials can lead to greater thermopower. Increasing the number of valleys near the energy band edge enhances the power factor, making high-degeneracy band structures advantageous for improving thermoelectric performance. Cu_2Se has a valence band maximum (VBM) at the Γ point with low

degeneracy (3) and a secondary VBM at the L point with higher degeneracy (8) as shown in Fig.1.16. This band structure suggests a potential for band engineering to increase degenerate bands, which is desirable for enhancing thermoelectric performance [79,80].

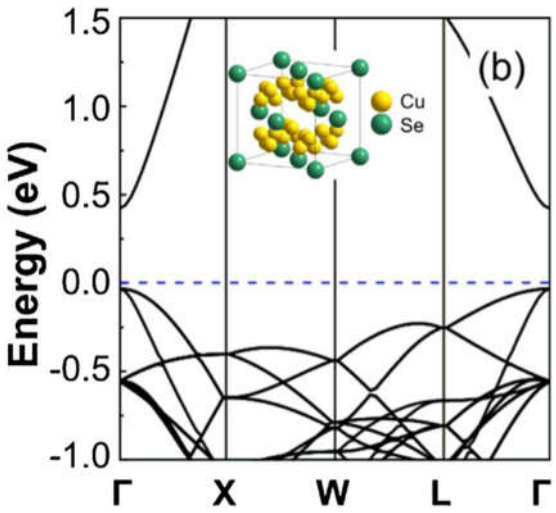

Fig.1.16 Electronic band structure of Cu_2Se [Adapted from 58].

1.8.6. Band Sharpening

The carrier effective mass is typically influenced by the electronic band structure and is connected to the shape of the band and the degree of valley degeneracy. This effective mass plays a significant role in determining carrier mobility, with larger effective masses generally leading to lower mobility, while smaller effective masses result in higher mobility [81]. Although a large carrier effective mass can increase the Seebeck coefficient, it typically reduces electrical conductivity due to the inverse relationship between effective mass and mobility of charge carriers. Band sharpening balances the conflicting relationship between effective mass and carrier mobility, helping to maintain optimal carrier transport properties. Therefore, optimizing the carrier effective mass is crucial to achieving a balance between electrical conductivity and the Seebeck coefficient [82]. One key strategy for enhancing thermoelectric properties is through the manipulation of the band shape to optimize the carrier effective mass [83]. Band sharpening is an effective method for tuning the carrier effective mass, as it reduces the single band effective mass by

modifying the band shape. This process involves converting a broad, flat band with a large effective mass (m*) into a sharper, narrower band with a smaller effective mass (m*), thereby increasing carrier mobility. This strategy has been successfully applied to enhance mobility and thereby improve electrical conductivity in various chalcogenide-based thermoelectric materials [84].

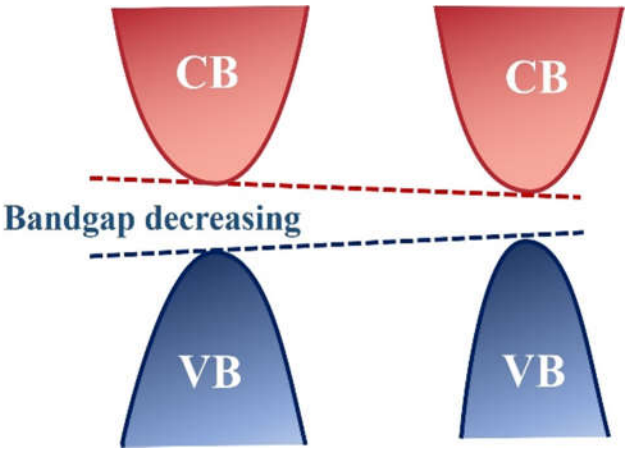

Fig.1.17 Bandgap narrowing shown through shifting conduction (CB) and valence band (VB) edges.

1.9. Motivation and objective of the thesis

Thermoelectricity presents a transformative opportunity to harness waste heat and convert it into usable electrical energy, yet its practical implementation faces significant challenges due to the limitations of current materials. The traditional thermoelectric materials such as telluride-based alloys for room temperature applications and silicon germanium for high-temperature scenarios, both present limitations such as high costs and specific operational temperature ranges. Notably, several thermoelectric materials, including lead and tin based chalcogenides like PbSe, PbS, SnTe, and SnSe, exhibit exceptional performance at elevated temperatures, often exceeding 773 K. However, there is a growing interest in developing materials that perform efficiently at medium temperatures, particularly for waste heat recovery, as many industrial processes and power plants generate waste heat in this temperature range, making its effective utilization crucial for improving energy efficiency. Achieving high thermoelectric efficiency, as measured by the figure of merit (ZT), requires a delicate balance between maximizing the

power factor (PF) and minimizing thermal conductivity (κ), both of which are influenced by carrier concentration and electronic structure. This interdependence makes it challenging to optimize these parameters simultaneously, as improving one often detrimentally impacts the others. The motivation to explore Cu_2Se as a thermoelectric material lies in its potential to overcome these challenges. Cu_2Se is one of the copper based binary chalcogenides that has garnered a lot of attention recently because of its ecofriendly composition, affordability, and potential thermoelectric performance at medium temperature. The diverse structure of Cu_2Se, featuring disordered Cu ions and tightly packed Se atoms, presents the substantial potential for improving thermoelectric performance through its high mobility traits, which induce superionic behavior and phonon liquid like behavior, offer a promising pathway to decouple electron and phonon transport, allowing for simultaneous optimization of electrical and thermal properties. The high mobility of Cu ions within the matrix enhances electrical properties while suppressing thermal conductivity, offering a unique opportunity to achieve a high figure of merit. The research shows that by examining systems where a crystalline sublattice exists for electronic conduction and is surrounded by liquid-like ions, a new strategy and approach for developing high-efficiency thermoelectric materials has become conceivable. In this context, the Cu_2Se matrix stands out as a versatile platform for further enhancements. Its structure allows for modifications such as doping and nanostructuring, which can significantly improve thermoelectric performance. By introducing dopants or designing composite structures, the carrier concentration and electronic structure can be precisely tailored to maximize the power factor while minimizing thermal conductivity. These modifications not only enhance efficiency but also address stability and durability concerns, making the material more practical for real-world applications. By exploring new doping strategies and material modifications, Cu_2Se presents an exciting opportunity to advance thermoelectric performance beyond the constraints of traditional materials, making it a highly promising candidate for more efficient and cost-effective thermoelectric generators.

The objective of this thesis is to synthesize Cu_2Se nanostructures and systematically enhance their thermoelectric properties through a series of strategic approaches. This

study aims to improve the thermoelectric performance of Cu_2Se through nanostructuring and band engineering techniques, which synergistically regulate charge carrier dynamics and phonon transport. By facilitating the decoupling of electrical and thermal properties via mechanisms such as energy filtering, band convergence, and enhanced phonon scattering, these strategies contribute to a significant enhancement in the figure of merit. The thesis aims to synthesize Cu_2Se nanostructures using hydrothermal and planetary ball milling techniques, which will enable controlled nanostructuring and optimization of transport properties. It investigates the effect of Ni doping on the thermoelectric properties of Cu_2Se, particularly its influence on carrier concentration, effective mass, and electrical conductivity. Additionally, the thesis explores a novel approach to enhance the thermoelectric properties of Cu_2Se by simultaneously optimizing electronic and thermal transport through co-doping with Ni and Zn, a method that has not been previously explored. By carefully tuning the dopant concentration within the crystalline matrix, the research aims to optimize the electronic band structure, thereby improving carrier transport and significantly boosting the material's overall thermoelectric efficiency. Furthermore, the strategy of introducing nanoinclusions into the Cu_2Se matrix is also explored as a potential method to reduce thermal conductivity and enhance electrical transport properties, demonstrating a promising synergy for achieving superior thermoelectric efficiency. This is achieved through composite engineering, utilizing a planetary ball mill to facilitate the uniform dispersion of nanoinclusions within the Cu_2Se matrix. This approach provides a pathway to further boost the thermoelectric performance by simultaneously improving carrier transport and reducing thermal conductivity, ultimately enhancing the overall power factor and efficiency.

References

[1] R. Singh, S. Dogra, S. Dixit, N.I. Vatin, R. Bhardwaj, A.K. Sundramoorthy, H.C.S. Perera, S.P. Patole, R.K. Mishra, S. Arya, Advancements in thermoelectric materials for efficient waste heat recovery and renewable energy generation, Hybrid Adv. 5 (2024) 100176. https://doi.org/10.1016/j.hybadv.2024.100176.

[2] A.R. Dhumal, A.P. Kulkarni, N.H. Ambhore, A comprehensive review on thermal management of electronic devices, J. Eng. Appl. Sci. 70 (2023) 1–18. https://doi.org/10.1186/s44147-023-00309-2.

[3] R. Freer, A. V. Powell, Realising the potential of thermoelectric technology: A roadmap, J. Mater. Chem. C. 8 (2020) 441–463. https://doi.org/10.1039/c9tc05710b.

[4] C.R. Kumar, A. Sonthalia, R. Goel, Experimental study on waste heat recovery from an internal combustion engine using thermoelectric technology, Therm. Sci. 15 (2011) 1011–1022. https://doi.org/10.2298/TSCI100518053K.

[5] O. Badr, S. Naik, P.W. O'Callaghan, S.D. Probert, Expansion machine for a low power-output steam Rankine-cycle engine, Appl. Energy. 39 (1991) 93–116. https://doi.org/10.1016/0306-2619(91)90024-R.

[6] Q. Bian, Waste heat : the dominating root cause of current global warming, Environ. Syst. Res. (2020) 8. https://doi.org/10.1186/s40068-020-00169-2.

[7] P.A. Finn, C. Asker, K. Wan, E. Bilotti, O. Fenwick, C.B. Nielsen, Thermoelectric materials: current status and future challenges, Front. Electron. Mater. 1 (2021) 1–13. https://doi.org/10.3389/femat.2021.677845.

[8] G. Magnus, History of thermoelectrics brief history of thermoelectrics, (2013) 1–5.

[9] Z. Xiao, Y. Du, Q. Meng, L. Wang, Thermoelectric characteristics of flexible reduced graphene oxide/silver selenide nanowire composites prepared by a facile vacuum filtration process, Chinese Phys. B. 31 (2022) 028103. https://doi.org/-10.1088/1674-1056/ac447e.

[10] H.B. Gao, G.H. Huang, H.J. Li, Z.G. Qu, Y.J. Zhang, Development of stove-powered thermoelectric generators: A review, (2016) 297-310. https://doi.org/10.10-16/j.applthermaleng.2015.11.032.

[11] C.T. Lo, Thermoelectric technologies can help power a zero-carbon future, (2024) 1–5.

[12] D. Beretta, N. Neophytou, J.M. Hodges, M.G. Kanatzidis, D. Narducci, M. Martin-Gonzalez, M. Beekman, B. Balke, G. Cerretti, W. Tremel, A. Zevalkink, A.I. Hofmann, C. Müller, B. Dörling, M. Campoy-Quiles, M. Caironi, Thermoelectrics: From history, a window to the future, Mater. Sci. Eng. R Reports. 138 (2019) 210–255. https://doi.org/10.1016/j.mser.2018.09.001.

[13] I. Chikina, C. Goupil, S.G. Sharapov, A.A. Varlamov, Thermoelectricity: from the iron arc of Alessandro Volta to radioisotope thermoelectric generators, Phys. Educ. 59 (2024) 015028. https://doi.org/10.1088/1361-6552/ad0a06.

[14] X. Zhang, L.D. Zhao, Thermoelectric materials: Energy conversion between heat and

electricity, J. Mater. 1 (2015) 92–105. https://doi.org/10.1016/j.jmat.2015.01.001.

[15] P. Borchert, D.M. Zellmer-Bruhn, Reproduced with permission of the copyright owner. Further reproduction prohibited without, J. Allergy Clin. Immunol. 130 (2010) 556. http://dx.doi.org/10.1016/j.jaci.2012.05.050.

[16] H.J. Goldsmid, The Seebeck and Peltier effects, Phys. Thermoelectr. Energy Convers. (2017) 1-1-1–3. https://doi.org/10.1088/978-1-6817-4641-8ch1.

[17] E.D.M. Rowe, Thermoelectrics handbook macro to nano, D.Sc, CRC press, (2006). https://doi.org/10.1201/9781420049718.

[18] P.P. Pradyumnan, T. Parvathy, 7 - Thermoelectric nanomaterials for temperature gradient sensing (heat nose), in: R.K. Gupta, T.A. Nguyen, M. Bilal, M. Ahmadi (Eds.), Nanotechnology-Based E-Noses, Elsevier ltd, (2023) 165–192. https://doi.org/https://doi.org/10.1016/B978-0-323-91157-3.00009-X.

[19] Kishor Wani, IJSSBT Vol-2 No. 2 May 14, Int. J. Sci. Spirituality, Bus. Technol. 2 (2014) 3–5.

[20] S. Sharma, V.K. Dwivedi, S.N. Pandit, A review of thermoelectric devices for cooling applications, Int. J. Green Energy. 11 (2014) 899–909. https://doi.org/10.1080/15435075.2013.829778.

[21] M.K. Shilpa, M.A. Raheman, A. Aabid, M. Baig, R.K. Veeresha, N. Kudva, A systematic review of thermoelectric peltier devices: applications and limitations, Fluid Dyn. Mater. Process. 19 (2022) 187–206. https://doi.org/10.32604/fdmp.2022.020351.

[22] I. Terasaki, Thermal conductivity and thermoelectric power of semiconductors, Elsevier Ltd., (2016) 326-358. https://doi.org/10.1016/b978-0-12-803581-8.00771-2.

[23] V. Era, S.C. Lyell, A. Prior, The Thomson effect and the ideal equation on thermoelectric coolers, Energy, 56 (2013) 61-69. https://doi.org/10.1016/j.energy.2013.04.049.

[24] G.A. Moore, Modern thermoelectrics, Electron. Power. 30 (1984) 733. https://doi.org/10.1049/ep.1984.0389.

[25] H.S. Kim, W. Liu, G. Chen, C.W. Chu, Z. Ren, Relationship between thermoelectric figure of merit and energy conversion efficiency, Proc. Natl. Acad. Sci. U. S. A. 112 (2015) 8205–8210. https://doi.org/10.1073/pnas.1510231112.

[26] G.J. Snyder, A.H. Snyder, Figure of merit ZT of a thermoelectric device defined from materials properties, Energy Environ. Sci. 10 (2017) 2280–2283. https://doi.org/10.1039/c7ee02007d.

[27] D.M. Rowe, Thermoelecrics and its energy harvesting: materials, preparation, and characterizatin in thermoelectrics, CRC press, 2 (2012). https://doi.org/10.1201/b11869.

[28] O.H. Ando Junior, A.L.O. Maran, N.C. Henao, A review of the development and applications of thermoelectric microgenerators for energy harvesting, Renew. Sustain. Energy Rev. 91 (2018) 376–393. https://doi.org/10.1016/j.rser.2018.03.052.

[29] B. Liao, B. Qiu, J. Zhou, S. Huberman, K. Esfarjani, G. Chen, Significant reduction of lattice thermal conductivity by the electron-phonon interaction in silicon with high carrier concentrations: A first-principles study, Phys. Rev. Lett. 114 (2015) 1–6. https://doi.org/10.1103/PhysRevLett.114.115901.

[30] M. Hong, W. Lyu, Y. Wang, J. Zou, Z.G. Chen, Establishing the golden range of seebeck coefficient for maximizing thermoelectric performance, J. Am. Chem. Soc. 142 (2020) 2672–2681. https://doi.org/10.1021/jacs.9b13272.

[31] L. Qiu, Y. Feng, Micro and nano thermal transport: characterization, measurement, and mechanism, Elsevier Science, (2022). https://doi.org/10.1016/C2019-0-05291-0.

[32] Y. Wang, Fabrication and properties of novel hybrid thermoelectric materials fabrication and properties of novel hybrid thermoelectric materials, (2022).

[33] C. Gayner, K.K. Kar, Recent advances in thermoelectric materials, Prog. Mater. Sci. 83 (2016) 330–382. https://doi.org/10.1016/j.pmatsci.2016.07.002.

[34] X. Zhang, Y. Pei, Manipulation of charge transport in thermoelectrics, Npj Quantum Mater. 2 (2017) 1–5. https://doi.org/10.1038/s41535-017-0071-2.

[35] A. Pandit, R. Haleoot, B. Hamad, Thermal conductivity and enhanced thermoelectric performance of SnTe bilayer, J. Mater. Sci. 56 (2021) 10424–10437. https://doi.org/-10.1007/s10853-021-05926-x.

[36] A. Mehdizadeh Dehkordi, M. Zebarjadi, J. He, T.M. Tritt, Thermoelectric power factor: Enhancement mechanisms and strategies for higher performance thermoelectric materials, Mater. Sci. Eng. R Reports. 97 (2015) 1–22. https://doi.org/10.1016/j.mser.2015.08.001.

[37] S.S. Li, Scattering mechanisms and carrier mobilities in semiconductors, Semicond. Phys. Electron. (1993) 183–211. https://doi.org/10.1007/978-1-4613-0489-08.

[38] L. Zhao, Carriers: the less, the faster, Mater. Lab. 1 (2022) 1–3. https://doi.org/10.54227/mlab.20220004.

[39] A.F. May, G.J. Snyder, Introduction to modeling thermoelectric transport at high temperatures, Thermoelectr. Its Energy Harvest. Mater. Prep. Charact. Thermoelectr. (2018) 11-1-11–18. https://doi.org/10.1201/b11869-15.

[40] X.L. Shi, J. Zou, Z.G. Chen, Advanced thermoelectric design: From materials and structures to devices, Chem. Rev. 120 (2020) 7399–7515. https://doi.org/10.1021/acs.chemrev.0c00026.

[41] M. Dutta, T. Ghosh, K. Biswas, Electronic structure modulation strategies in high-performance thermoelectrics, APL Mater. 8 (2020) 040910. https://doi.org/10.1063/5.0002129.

[42] H. Han, L. Zhao, X. Wu, B. Zuo, S. Bian, T. Li, X. Liu, Y. Jiang, C. Chen, J. Bi, J. Xu, L. Yu, Advancements in thermoelectric materials: optimization strategies for enhancing energy conversion, J. Mater. Chem. A. (2024) 24041–24083. https://doi.org/10.1039/d4ta03666b.

[43] J. Yang, L. Xi, W. Qiu, L. Wu, X. Shi, L. Chen, J. Yang, W. Zhang, C. Uher, D.J.

Singh, On the tuning of electrical and thermal transport in thermoelectrics: An integrated theory-experiment perspective, Npj Comput. Mater. 2 (2016) 15015. https://doi.org/10.1038/npjcompumats.2015.15.

[44] Y. Pei, A.D. Lalonde, N.A. Heinz, X. Shi, S. Iwanaga, H. Wang, L. Chen, G.J. Snyder, Stabilizing the optimal carrier concentration for high thermoelectric efficiency, Adv. Mater. 23 (2011) 5674–5678. https://doi.org/10.1002/adma.201103153.

[45] B. Srinivasan, Novel chalcogenide based glasses, ceramics and polycrystalline materials for thermoelectric application, (2019) 289.

[46] N. Jia, J. Cao, X.Y. Tan, J. Dong, H. Liu, C.K.I. Tan, J. Xu, Q. Yan, X.J. Loh, A. Suwardi, Thermoelectric materials and transport physics, Mater. Today Phys. 21 (2021) 100519. https://doi.org/10.1016/j.mtphys.2021.100519.

[47] T. Parvathy, P.P. Pradyumnan, Impact of mobility and effective mass on the thermoelectric performance of Ni doped Cu_2Se, J. Alloys Compd. 970 (2024) 172615. https://doi.org/10.1016/j.jallcom.2023.172615.

[48] M. Unikoth, G. Varghese, K. Shijina, H. Neelamkodan, Thermoelectric Nano structured Perovskite Materials, in: P. Sharma, A. Kumar (Eds.), Recent Adv. Multifunct. Perovskite Mater., Intech open, Rijeka, (2022). https://doi.org/10.5772/intechopen.106614.

[49] K. Giri, Y.L. Wang, T.H. Chen, C.H. Chen, Challenges and strategies to optimize the figure of merit: Keeping eyes on thermoelectric metamaterials, Mater. Sci. Semicond. Process. 150 (2022) 106944. https://doi.org/10.1016/j.mssp.2022.106944.

[50] C. Han, Q. Sun, Z. Li, S.X. Dou, Thermoelectric Enhancement of Different Kinds of Metal Chalcogenides, Adv. Energy Mater. 6 (2016) 1600498. https://doi.org/10.1002/aenm.201600498.

[51] H. Meng, M. An, T. Luo, N. Yang, Thermoelectric applications of chalcogenides, Elsevier Ltd, (2019) 31-56. https://doi.org/10.1016/B978-0-08-102687-8.00002-6.

[52] Y. Jain, R. Kurchania, Pressure-induced band gap enhancement and temperature-dependent thermoelectric characterization of semiconducting Transition Metal Chalcogenides LiMS (M = Cu, Ag), Mater. Sci. Semicond. Process. 186 (2025) 100532. https://doi.org/10.1016/j.mssp.2024.109030.

[53] S.J. Park, S. Kim, O. Park, S.W. Lee, S. Il Kim, Thermoelectric Transport Properties of $Co_{0.5}Fe_{0.5}Se_2$, $Co_{0.5}Fe_{0.5}Te_2$, and Their Solid-Solution Compositions, Electron. Mater. Lett. 20 (2024) 432–439. https://doi.org/10.1007/s13391-023-00459-8.

[54] A. V. Powell, P. Vaqueiro, Chalcogenide thermoelectric materials, RSC Energy Environ. Ser. 2017-Janua (2017) 27–59. https://doi.org/10.1039/9781782624042-00027.

[55] L. Yang, Z.G. Chen, G. Han, M. Hong, Y. Zou, J. Zou, High-performance thermoelectric Cu_2Se nanoplates through nanostructure engineering, Nano Energy. 16 (2015) 367–374. https://doi.org/10.1016/j.nanoen.2015.07.012.

[56] W. Zhang, C. Zheng, Y. Dong, J.Y. Yang, L. Liu, Anharmonic phonon frequency

and ultralow lattice thermal conductivity in β-Cu_2Se liquid-like thermoelectrics, Phys. Chem. Chem. Phys. 22 (2020) 28086–28092. https://doi.org/10.1039/d0-cp04591h.

[57] N. Ghobadi, E.G. Hatam, Optical band gap, photocatalysis, surface structures and depth profile properties of Cu_2Se nanostructured thin films, Mater. Res. Express. 9 (2022) 0–13. https://doi.org/10.1088/2053-1591/ac5f36.

[58] W. Di Liu, L. Yang, Z.G. Chen, Cu_2Se thermoelectrics: property, methodology, and device, Nano Today. 35 (2020) 100938. https://doi.org/10.1016/j.nantod.2020.1009-38.

[59] S.A. Danilkin, A.N. Skomorokhov, A. Hoser, H. Fuess, V. Rajevac, N.N. Bickulova, Crystal structure and lattice dynamics of superionic copper selenide $Cu_{2-\delta}Se$, J. Alloys Compd. 361 (2003) 57–61. https://doi.org/10.1016/S0925-8388(03)00439-0.

[60] Z. Zhang, K. Zhao, T.R. Wei, P. Qiu, L. Chen, X. Shi, Cu_2Se-Based liquid-like thermoelectric materials: Looking back and stepping forward, Energy Environ. Sci. 13 (2020) 3307–3329. https://doi.org/10.1039/d0ee02072a.

[61] J. Lei, Z. Ma, D. Zhang, Y. Chen, C. Wang, X. Yang, Z. Cheng, Y. Wang, High thermoelectric performance in Cu_2Se superionic conductor with enhanced liquid-like behaviour by dispersing SiC, J. Mater. Chem. A. 7 (2019) 7006–7014. https://doi.org/10.1039/c8ta12210e.

[62] S.M.K. Nazrul Islam, P. Mayank, Y. Ouyang, J. Chen, A.K. Sagotra, M. Li, M.B. Cortie, R. Mole, C. Cazorla, D. Yu, X. Wang, R.A. Robinson, D.L. Cortie, Copper diffusion rates and hopping pathways in superionic Cu_2Se, Acta Mater. 215 (2021) 117026. https://doi.org/10.1016/j.actamat.2021.117026.

[63] J. Zhang, C. Zhang, T. Zhu, Y. Yan, X. Su, X. Tang, Mechanical properties and thermal stability of the high-thermoelectric-performance Cu_2Se compound, ACS Appl. Mater. Interfaces. 13 (2021) 45736–45743. https://doi.org/10.1021/acsami.1c-12533.

[64] M. Mukherjee, A. Srivastava, A.K. Singh, Recent advances in designing thermoelectric materials, J. Mater. Chem. C. 10 (2022) 12524–12555. https://doi.org/10.1039/d2tc02448a.

[65] A. Basit, J. Xin, G. Murtaza, L. Wei, A. Hameed, W. Guoyu, J.Y. Dai, Recent advances, challenges, and perspective of copper-based liquid-like thermoelectric chalcogenides: A review, EcoMat. 5 (2023) 1–34. https://doi.org/10.1002/eom-2.12391.

[66] M.M.R. Al-Fartoos, A. Roy, T.K. Mallick, A.A. Tahir, Advancing Thermoelectric Materials: A Comprehensive Review Exploring the Significance of One-Dimensional Nano Structuring, Nanomaterials. 13 (2023) 13. https://doi.org/10.33-90/nano13132011.

[67] Q. Zhu, S. Wang, X. Wang, A. Suwardi, M.H. Chua, X.Y.D. Soo, J. Xu, Bottom-Up Engineering Strategies for High-Performance Thermoelectric Materials, Springer Singapore, (2021) 119. https://doi.org/10.1007/s40820-021-00637-z.

[68] H. Alam, S. Ramakrishna, A review on the enhencement of the figure of merit from

bulk to nano-thermoelectric materials, Nanoenergy. 2 (2013) 190-212. https://doi.org/10.1016/j.nanoen.2012.10.005.

[69] Z.G. Chen, G. Hana, L. Yanga, L. Cheng, J. Zou, Nanostructured thermoelectric materials: Current research and future challenge, Prog. Nat. Sci. Mater. Int. 22 (2012) 535–549. https://doi.org/10.1016/j.pnsc.2012.11.011.

[70] T. Module, S. Lv, Z. Qian, D. Hu, X. Li, W. He, A Comprehensive Review of strategies and approaches for enhancing the performance of thermoelctric module, Energies. 13 (2020) 3142. https://doi.org/10.3390/en13123142.

[71] Z. Ma, J. Wei, P. Song, M. Zhang, L. Yang, J. Ma, W. Liu, F. Yang, X. Wang, Review of experimental approaches for improving zT of thermoelectric materials, Mater. Sci. Semicond. Process. 121 (2021) 105303. https://doi.org/10.1016/j.mssp.2020.105303.

[72] Y. Qin, L. Yang, J. Wei, S. Yang, M. Zhang, X. Wang, F. Yang, Doping effect on Cu_2Se thermoelectric performance: a review, Materials (Basel). 13 (2020) 1–32. https://doi.org/10.3390/ma13245704.

[73] A. Mehdizadeh Dehkordi, M. Zebarjadi, J. He, T.M. Tritt, Thermoelectric power factor: Enhancement mechanisms and strategies for higher performance thermoelectric materials, Mater. Sci. Eng. R Reports. 97 (2015) 1–22. https://doi.org/10.1016/j.mser.2015.08.001.

[74] B. Liao, G. Chen, Nanocomposites for thermoelectrics and thermal engineering, MRS Bull. 40 (2015) 746–752. https://doi.org/10.1557/mrs.2015.197.

[75] S. Ghosh, H. Naithani, B. Ryu, G. Oppitz, E. Müller, J. de Boor, Towards energy filtering in Mg_2X-based composites: Investigating local carrier concentration and band alignment via SEM/EDX and transient Seebeck microprobe analysis, Mater. Today Phys. 38 (2023) 101244. https://doi.org/10.1016/j.mtphys.2023.101244.

[76] A. Pakdel, Q. Guo, V. Nicolosi, T. Mori, Enhanced thermoelectric performance of Bi-Sb-Te/Sb_2O_3 nanocomposites by energy filtering effect, J. Mater. Chem. A. 6 (2018) 21341–21349. https://doi.org/10.1039/c8ta08238c.

[77] J. Park, M. Dylla, Y. Xia, M. Wood, G.J. Snyder, A. Jain, When band convergence is not beneficial for thermoelectrics, Nat. Commun. 12 (2021) 1–8. https://doi.org/10.1038/s41467-021-23839-w.

[78] K.H. Lee, S. il Kim, H.S. Kim, S.W. Kim, band convergence in thermoelectric materials: theoretical background and consideration on Bi-Sb-Te Alloys, ACS Appl. Energy Mater. 3 (2020) 2214–2223. https://doi.org/10.1021/acsaem.9b02131.

[79] M. Råsander, L. Bergqvist, A. Delin, Density functional theory study of the electronic structure of fluorite Cu_2Se, J. Phys. Condens. Matter. 25 (2013) 125503. https://doi.org/10.1088/0953-8984/25/12/125503.

[80] Y. Zhang, Y. Wang, L. Xi, R. Qiu, X. Shi, P. Zhang, W. Zhang, Electronic structure of antifluorite Cu_2X (X = S, Se, Te) within the modified Becke-Johnson potential plus an on-site Coulomb U, J. Chem. Phys. 140 (2014) 074702. https://doi.org/10.1063/1.4865257.

[81] Y. Xiao, L. Xu, T. Hong, H. Shi, S. Wang, X. Gao, X. Ding, J. Sun, L.D. Zhao, Ultrahigh carrier mobility contributes to remarkably enhanced thermoelectric performance in n-type PbSe, Energy Environ. Sci. 15 (2022) 346–355. https://doi.org/10.1039/d1ee03339e.

[82] L. Su, H. Shi, S. Wang, D. Wang, B. Qin, Y. Wang, C. Chang, L.-D. Zhao, Enhancing carrier mobility and seebeck coefficient by modifying scattering factor, Adv. Energy Mater. 13 (2023) 2300312. https://doi.org/https://doi.org/10.1002/aenm.202300312.

[83] Z. Hou, Y. Xiao, L.D. Zhao, Investigation on carrier mobility when comparing nanostructures and bands manipulation, Nanoscale. 12 (2020) 12741–12747. https://doi.org/10.1039/d0nr02649b.

[84] S. Wang, Y. Qiu, L.D. Zhao, $BiSbSe_3$: A promising Te-free thermoelectric material, Appl. Phys. Lett. 122 (2023) 260503. https://doi.org/10.1063/5.0159352.

Chapter-2

Synthesis and characterization techniques

This chapter outlines the synthesis methods and characterization techniques used in the preparation of Cu_2Se based nanomaterials. It provides an overview of the various techniques employed for characterizing the structural, morphological, optical, electrical, and thermoelectric properties of the synthesized materials.

2.1. Introduction

The development of nanomaterials requires careful control over the synthesis methods, as these directly influence the nanostructure and resulting physical properties [1]. The selection of appropriate synthesis methods is based on their scalability, cost-effectiveness, and ability to produce high quality nanostructured materials. Additionally, these methods must provide the flexibility to control the size, morphology, and composition of the materials, which are essential for enhancing the ZT and ensuring optimal thermoelectric performance. This chapter focuses on the synthesis and characterization techniques employed to produce Cu_2Se based nanostructures. Two primary synthesis methods were used, hydrothermal synthesis and planetary ball milling, both of which are critical for producing nanostructured materials with tailored properties at the nanoscale. In this study, single and dual-doped Cu_2Se were synthesized using the hydrothermal method, while Cu_2Se based nanocomposites were prepared through planetary ball milling. Hydrothermal synthesis was selected for its ability to precisely control doping and dual doping, which enables the fine-tuning of carrier concentration and electrical conductivity. On the other hand, ball milling was used to fabricate Cu_2Se based composites, which are expected to enhance thermoelectric performance by optimizing phonon and electron scattering mechanisms. Following the synthesis processes, the resulting materials were characterized using a range of analytical techniques. This section provides a brief overview of the techniques used for structural, morphological, optical, electrical, and thermoelectric characterization, including thermal conductivity measurements. The chapter offers a detailed explanation of these synthesis methods and characterization principles, crucial for optimizing the physical properties of these materials.

2.2. Synthesis method

2.2.1. Hydrothermal synthesis

The term 'hydrothermal' originated in earth sciences, where it referred to conditions characterized by high temperature and water pressure [2]. The hydrothermal process is a highly esteemed and extensively employed technique for generating

nanostructured materials [3]. This method relies on solution based reactions, enabling the formation of nanomaterials across a broad temperature spectrum, from room temperature to very high temperature. It is now commonly employed for synthesizing oxides, silicates, selenides, and sulfides compounds with distinctive properties. In the synthesis of inorganic compounds, the process typically begins with aqueous solutions of simple salts like metal chlorides, nitrates, or acetates. These solutions may be converted to metal hydroxides by adding a base such as sodium hydroxide (NaOH), potassium hydroxide (KOH), or ammonium hydroxide (NH_4OH), depending on the specific synthesis requirements. Apart from this, different precursors for pH control, reduction, oxidation, or coating can be incorporated before the hydrothermal treatment as needed. The selection of precursors, reducing agent, reaction duration, and temperature are critical phases in the hydrothermal process because they affect particle size, size distribution, purity, and morphology of the final product [4].

The principle of the hydrothermal method involves allowing an insoluble material to crystallize when the temperature is elevated above the solvent's boiling point and the pressure exceeds 1 bar. This method makes ultrafine metal particles by hydrolyzing and condensing metal salts in water at high temperatures and pressure [5]. During the reaction, the metal salt or precursor undergoes hydrolysis leading to the formation of metal hydroxide, which then condenses into metal oxides or metal particles. In the case of metal selenide nanoparticles, the metal hydroxide formed reacts with a selenium source to produce metal selenide nanoparticles. The hydrothermal medium, generally water at a temperature up to 646.95 K and pressure up to 22.064 MPa, offers perfect conditions for the synthesis, development, and stabilization of the desired products, while minimizing the generation of undesirable byproducts [5]. The morphology of the resulting materials can be precisely controlled by adjusting the pressure conditions either low or high based on the vapor pressure of the primary components involved in the reaction [6]. Optimizing the hydrothermal synthesis requires a thorough understanding of the formation and stability of species under specific conditions, including reaction temperature, pressure, reagent concentration, and pH [5,6].

In this method, appropriate chemical precursors are dissolved in water and transferred into a container made of steel or another compatible metal capable of withstanding temperatures up to 300°C and pressures above 100 bars.This vessel called an autoclave, is typically equipped with controls for temperature and pressure, as well as measurement gauges [7]. The autoclave must possess high mechanical strength to endure long-term high-pressure and high-temperature conditions. It should also be highly resistant to acids, alkalis, and oxidants. Additionally, the autoclave needs to be properly sized and shaped to achieve the desired temperature gradient [8]. The design should be simple for ease of operation and maintenance, and it must provide excellent sealing to maintain the required temperature and pressure. Also to prevent corrosion and maintain sample purity, protective liners such as noble metals or Teflon are used. Teflon is particularly suitable for alkaline or neutral conditions under 300°C and 250 bars, as it expands with heat to create a hermetic seal. The Teflon liner must fit precisely inside the autoclave to ensure proper sealing during the reaction. However, Teflon degrades beyond 300°C and its coating tends to wear out, requiring frequent reapplication to maintain effective protection.

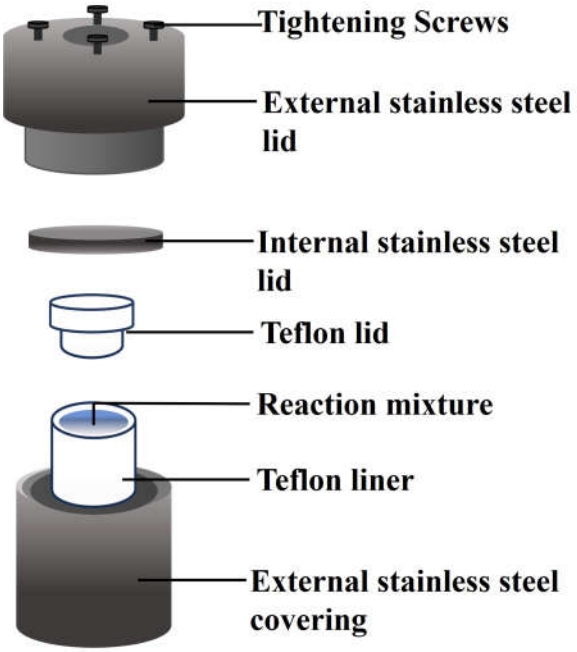

Fig.2.1 Teflon-lined stainless steel autoclave.

2.2.2. Ball milling

Mechanical milling is a cost-efficient technique for creating nanoscale substances from bulk materials. It is also effective for blending different phases, particle size reduction, and producing nanocomposites [3]. The kinetics of mechanical milling are influenced by the energy imparted to the powder by the milling balls. This energy transfer is controlled by several factors, including the type of mill, powder quantity in the milling chamber, milling speed, ball size and distribution, milling conditions (dry or wet), temperature during processing, and milling duration [9]. The kinetic energy of the balls is determined by their mass and velocity, so using dense materials such as steel or tungsten carbide is more effective than using ceramic balls. Furthermore, optimizing the size and distribution of the balls for the particular mill is crucial. Generally, milling reduces particle sizes by breaking down the original grains into smaller fragments. At a macroscopic level, this process increases the surface area of the powder. Typically, as particles break down, the reactivity of the powder increases [10]. High energy ball mills, including tumbler ball mills, vibratory mills, planetary mills, and attritor mills are commonly used [8].

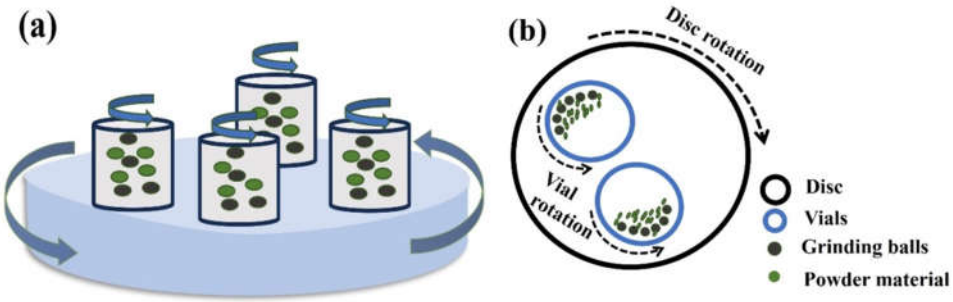

Fig.2.2 Schematics of (a) planetary ball mill, (b) The rotation of the disc and vials, along with the motion of the grinding balls.

Planetary ball milling (PBM) is a widely used ball milling technique for synthesizing nanoparticles. In our work, we utilize planetary ball milling for synthesizing Cu_2Se nanocomposites. The ball mill system consists of four bowls and a turn disc, sometimes known as a turntable. The bowls revolve in the opposite direction from the direction in which the turn disc rotates. The centrifugal forces created by the bowls rotating on their axes, along with the rotation of the turn disc,

act on the powder mixture and milling balls in the bowls. This overall centrifugal force promotes the rotation of the balls inside the mill, leading to the sample's fragmentation through friction and impact [11]. The centrifugal forces are alternately synchronized due to the opposing rotational directions of the turntable and the bowl. This results in friction as the powder mixture and the hardened milling balls roll alternately on the inner wall of the bowl and collide with its outer wall. Gravitational acceleration can enhance the impact energy of the milling balls in the normal direction by up to 40 times. As a result, the planetary ball mill is highly suitable for high speed grinding [12].

Fig.2.3 Planetary ball mill.

2.3. Densification process for powder sample consolidation

The densification processes used in the fabrication of thermoelectric materials are crucial for determining their microstructure, which has a significant effect on their thermoelectric properties and overall performance [13]. After the nanomaterials are synthesized, densification methods will be used, followed by sintering to prepare the samples for thermoelectric measurements. Sintering is the process of compacting and shaping materials into dense bulk forms using pressure or heat at temperatures lower than their melting point. This process effectively minimizes porosity and improves key material properties, such as thermal and electrical conductivity [14]. In

this work, Cu_2Se pellets were consolidated using a conventional sintering process. The synthesized powder was compacted into a circular pellet with a diameter of 13 mm and a thickness of 3 mm using a hydraulic pelletizer, applying a force of approximately 10 tons under ambient conditions. The resulting densified pellet was then subjected to a sintering process at 573 K for 3 hours. The sintered samples were subsequently prepared for comprehensive characterization. Detailed analyses were performed to evaluate the material's structural, morphological, optical, and thermoelectric properties, providing insights into their performance and potential applications.

Fig.2.4 Hydraulic pelletizer and the die set.

2.4. Characterisation techniques

2.4.1. Powder X-ray diffraction techniques

The Debye and Scherrer methods, commonly known as powder X-ray diffraction (XRD), offer a non-destructive and rapid approach for both qualitative and quantitative analysis of a broad range of materials, including minerals, polymers, plastics, metals, semiconductors, ceramics, etc [15]. XRD is utilized to analyze and characterize the atomic positions, their arrangement within each unit cell, and the spacing between atomic planes. According to Hull (1919), every crystalline substance produces a distinct diffraction pattern; the same substance consistently yields the same pattern; and in a mixture of substances, each one generates its

pattern independently of the others. XRD offers insights into the average properties of a large number of particles, unlike direct imaging methods like electron microscopy, which only analyze a small sample of particles [16]. The atomic structure of a crystal is unveiled through the diffraction pattern generated when X-rays interact with it. A crystal is made up of countless repeating structural units, each featuring an identical atomic arrangement that extends uniformly in three dimensions, resembling a three-dimensional wallpaper pattern. The pattern of each crystal includes specific symmetry elements that create a three-dimensional framework for the arrangement of atoms. These symmetry elements are integral to the crystal's structure and can be uniquely identified through X-ray diffraction, providing a detailed understanding of the crystal's atomic arrangement. The diffraction of X-rays is influenced by the spacing between these repeating units, determining the directions in which the X-rays are scattered. Meanwhile, the intensity of the diffracted beams is decided by the specific arrangement of atoms within each unit cell [17].

When periodic structures with a specific spacing are illuminated by a radiation of comparable wavelengths, such as X-rays with wavelengths around 1Å, they scatter off the electrons surrounding the atomic nuclei. These scattered waves, which are emitted in various directions, interact and interfere with one other. The type of interference may be either constructive or destructive, depending on the waves direction and properties. Bragg's Law, first formulated by W.H. Bragg in 1912, states the condition for the diffraction of an incident beam of monochromatic X-rays by the successive atomic planes in a crystal. When a collimated beam of monochromatic X-rays with a wavelength λ interacts with a crystal, penetrating its structure and being partially scattered by successive atomic planes. For a specific interplanar spacing d, there is a distinct angle θ where the scattered X-rays from consecutive planes align in phase, creating a coherent wavefront as they exit the crystal. Ie, If the path difference between waves reflected from successive planes is an integer multiple of the wavelength, these waves will constructively interfere, producing a strong reflected beam. This condition for constructive interference is given by Bragg's law,

$$n\lambda = 2d\sin\theta \qquad \text{....2.1}$$

where n is an integer representing the order of the reflection, λ is the wavelength of the X-rays, d is the interplanar spacing, and θ is the angle of incidence that satisfies the condition for constructive interference. Different materials have unique interplanar distances in three dimensions, which means that the angles at which they diffract X-rays are specific to each material [17,18]. By determining the peak positions and intensities of a specimen's diffraction pattern and calculating the corresponding interplanar spacings using Bragg’s law, we can identify the constituent phases of an unknown sample. This identification is achieved by comparing the recorded interplanar spacing values and strongest peak intensities with those in the international centre for diffraction data (ICDD) database.

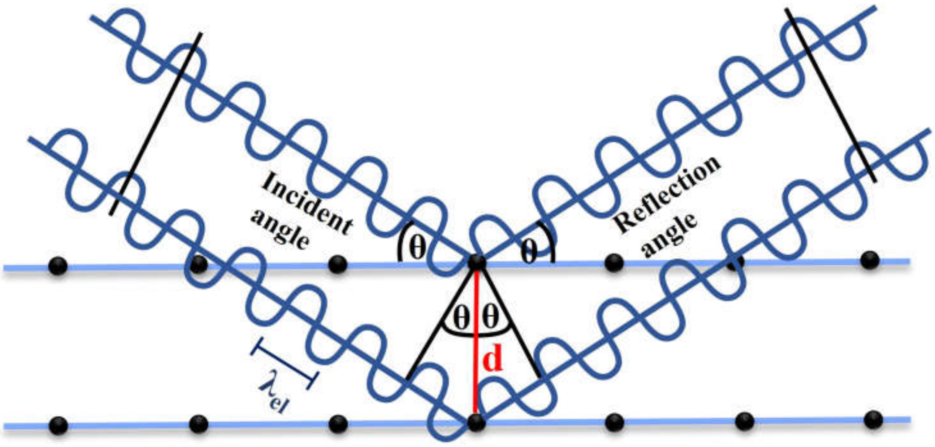

Fig.2.5 Schematic of X-ray diffraction based on Bragg's law.

The average crystallite sizes (D) for all the samples were determined using the well-established Scherrer formula

$$D = \frac{K\lambda}{\beta\cos\theta} \qquad \text{(2.2)}$$

where K -Scherrer constant, λ -incident ray wavelength (= 0.15408nm), β - FWHM in radian, and θ - diffraction angle.

The effect of dopant can cause a strain in the lattice of Cu_2Se which can be calculated using the formula,

$$\text{Microstrain } \varepsilon = \frac{\beta \cos\theta}{4} \quad \ldots\ldots\ldots\ldots\ldots\ldots\ldots\ldots\ldots\ldots\ldots\ldots (2.3)$$

$$\text{and} \quad \text{Dislocation density } \delta = \frac{1}{D^2} \ldots\ldots\ldots\ldots\ldots\ldots\ldots\ldots\ldots\ldots (2.4)$$

In addition to sample dependent effects, XRD peaks can also broaden due to instrumental factors, known as instrumental broadening. It is crucial to account for instrumental broadening to obtain accurate diffraction patterns and properly discern the physical broadening contribution. Instrumental full width at half maximum (FWHM) (β_i) was calculated using a standard silicon sample with exactly the same measuring parameters as those used for the sample. Then the Gaussian correction is used to obtain the true broadening by using the equation 2.5.

$$\beta_i^2 + \beta_S^2 = \beta_T^2 \ldots\ldots\ldots\ldots\ldots\ldots\ldots\ldots\ldots\ldots\ldots\ldots\ldots (2.5)$$

where β_S is the broadening related to the sample and β_T is the total broadening. Then the instrumental broadening is subtracted from the total broadening to get the actual sample value. These β_s values are then used for the calculation of all other structural parameters like microstrain crystallite size, dislocation density, etc.

2.4.1.1. Instrumentation

X-ray diffractometer consists of three primary components: an X-ray tube, a sample holder, and an X-ray detector. X-rays are produced in a cathode ray tube through the heating of a filament, which releases electrons. A high voltage is applied to accelerate these electrons toward the target material. When the accelerated electrons collide with the target material, they have enough energy to dislodge inner-shell electrons from the atoms of the target. This displacement of inner-shell electrons leads to the emission of characteristic X-ray spectra, which are specific to the target material. Copper is the most common target material for single crystal diffraction, producing CuK_α radiation with a wavelength of 1.5408 Å. These X-rays are collimated and directed onto the sample. As both the sample and detector rotate, the intensity of the reflected X-rays is recorded. When the incident X-rays meet the sample at an angle that satisfies Bragg's law, constructive interference occurs, resulting in a peak intensity [19]. The detector captures and processes the X-ray

signal, converting it into a count rate, which is then displayed on an output device such as a computer monitor or printer. In an X-ray diffractometer, the sample is positioned in the path of a collimated X-ray beam and rotates at an angle θ, while the detector, mounted on a movable arm, rotates at 2θ to detect the diffracted X-rays. The goniometer is the instrument used to maintain these angles and rotate the sample, ensuring precise alignment for accurate measurement.

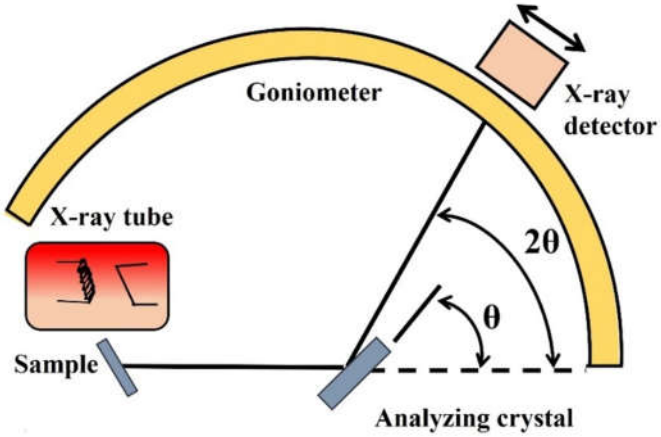

Fig.2.6 Diagram illustrating the diffractometer system.

Fig.2.7 Rigaku-Miniflex 600 X-ray diffractometer.

We have used a Rigaku-Miniflex X-ray diffractometer, equipped with CuK_{α} radiation (λ = 1.5408 Å), to investigate the structure of materials within the angular range of 20° to 80°. The diffractometer has a maximum power output of 600 W (40 kV and 15 mA) for X-ray generation. The analysis is generally conducted at room temperature using the continuous mode of the X-ray diffraction method. X-ray diffractograms are then analyzed by comparing them with standard diffraction data to identify and characterize the materials.

2.4.2. Raman spectroscopy

Raman spectroscopy, named after its inventor C.V. Raman, is a versatile tool extensively used for the determination and identification of molecular structure. It overcomes many limitations of other techniques and can be used for both qualitative analysis, by measuring scattered radiation frequency, and quantitative analysis, by assessing the intensity of scattered radiation [20]. The technique involves measuring the frequency shift of light that has been inelastically scattered by a sample. Raman spectra are generated from the inelastic collision between incident monochromatic radiation and the molecules in a sample [20]. When incident photons interact with the molecules in the sample, they are scattered with changed frequencies. The majority of this scattered radiation maintains a frequency equal to that of the incident radiation, constituting Rayleigh scattering. The scattered light can either have a lower frequency than the incident light, known as Stokes Raman scattering, or a higher frequency, referred to as anti-Stokes Raman scattering. In the case of anti-Stokes scattering, the photon gains energy from the molecular bond when the bond is initially in an excited vibrational state. Stokes-shifted Raman bands involve transitions from lower to higher energy vibrational levels, making them more intense than anti-Stokes bands. Therefore, Stokes bands are typically measured in conventional Raman spectroscopy. In contrast, anti-Stokes bands are used with fluorescing samples, as fluorescence interferes with the measurement of Stokes bands [20]. This frequency shift reveals information about the vibrational modes of the molecules, facilitating the analysis of the sample's molecular composition and structure. According to the Raman selection rule, a change in molecular

polarizability occurs when the constituent atoms are displaced from their equilibrium positions due to molecular vibrations [21].

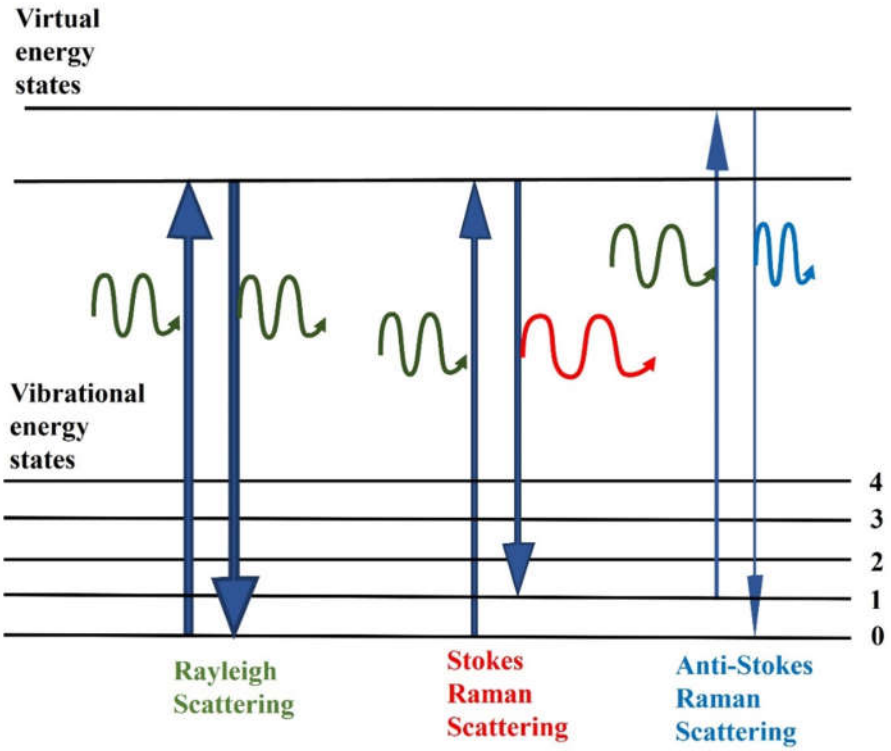

Fig.2.8 Energy diagram illustrating Raman scattering (Rayleigh, Stokes, and anti-Stokes).

When a photon strikes a molecule, it interacts with the molecule's electric dipole. The induced dipole moment occurs as a result of the molecular polarizability, α which represents the deformability of the electron cloud around the molecule in response to an external electric field [22,23].

The intensity of the Raman scattered radiation (I_R) can be expressed as:

$$I_R \propto \upsilon^4 I_0 N \left(\frac{\partial \alpha}{\partial Q}\right)^2 \quad \text{.....(2.6)}$$

Where I_0 represents the incident laser intensity, N denotes the number of scattering molecules in a given state, υ is the frequency of the exciting laser, and Q signifies the vibrational amplitude. Only molecular vibrations that result in a change in polarizability during vibration or rotation are Raman active. In this context, the

change in polarizability with respect to variations in the vibrational amplitude, Q, must be greater than zero.

$$\frac{\partial \alpha}{\partial Q} \neq 0 \text{……..……..(2.7)}$$

The scattering intensity is proportional to the square of the induced dipole moment, which is equivalent to the square of the derivative of the polarizability.

2.4.2.1. Instrumentation

A Raman micro-spectrometer consists of an optical microscope coupled with a Raman spectrometer [23,24]. A Raman spectrophotometer comprises several essential components for its operation. The primary component is a monochromatic light source, typically a 532 nm green laser, used to excite the sample. An optical arrangement directs the laser beam onto the sample and collects the resulting scattered light. This scattered light is then analyzed by the spectrophotometer, which acts as a wavelength selector to differentiate between the various wavelengths present in the scattered light. In Raman imaging, the principle involves scanning the surface with a laser tuned to a specific wavenumber characteristic of a specific component in the mixture. As the focused laser beam interacts with a specific element in the sample, the corresponding Raman response is measured, while signals from unrelated elements are filtered out. Finally, a charge-coupled device (CCD) detector collects the data, allowing for the detailed analysis and interpretation of the Raman spectra. The precise focusing of the incident laser light through the microscope's objective concentrates the laser energy onto a highly confined region. To prevent damage from thermal and photo-induced effects on the samples, it is essential to use low laser energy. Therefore, improving signal collection requires an objective with a wide solid angle and a short focal length [25]. In this study, the Raman spectra of the samples were measured using a Jasco NRS 4100 micro-Raman spectrometer with a 532 nm green laser at room temperature.

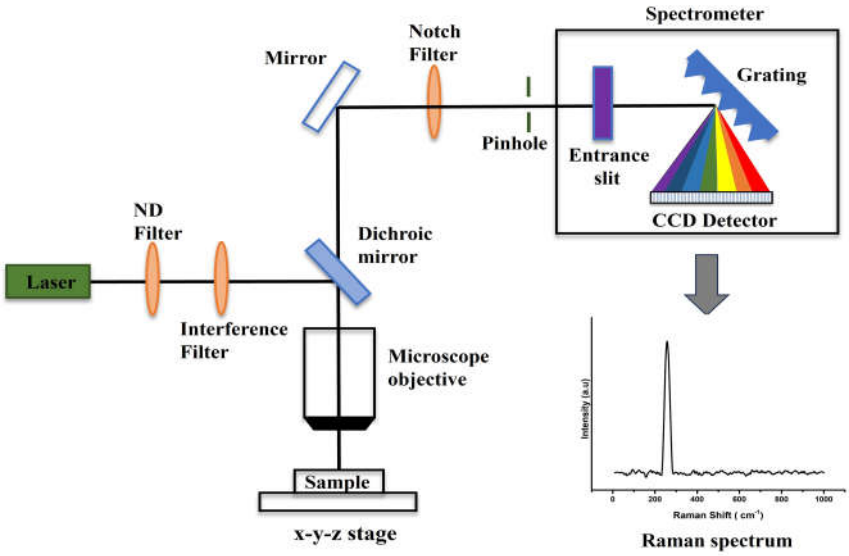

Fig.2.9 Diagrammatic representation of a micro-Raman spectrometer.

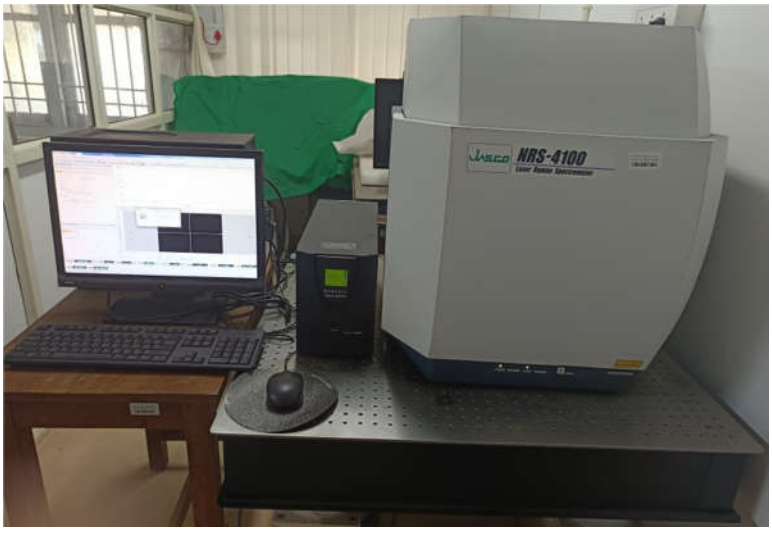

Fig.2.10 Jasco NRS 4100 micro-Raman spectrometer.

2.4.3. Scanning electron microscopy

The scanning electron microscope (SEM) is a highly flexible tool used for examining and analyzing microstructural morphology and chemical composition [26]. The SEM is commonly employed to examine the surface structure and chemistry of various biological and synthetic materials at micrometer to nanometer scales. Its user-friendly nature, typically simple sample preparation, and clear image interpretation along with high resolution, extensive depth of field, and capabilities

for microchemical and crystallographic analysis make this as one of the most effective and versatile characterization techniques [26]. Another key feature of this technique is the 3D appearance of the specimen, which is a direct consequence of its large depth of field [27]. SEM operates on the principle of directing a focused beam of high energy electrons onto a specimen. The interactions between the incident electrons and the specimen can be categorized into elastic and inelastic scattering. Elastic scattering involves the deflection of electrons by atomic nuclei or outer shell electrons, resulting in backscattered electrons (BSEs) that provide compositional and topographic information. Inelastic scattering transfers significant energy to specimen atoms, leading to the emission of secondary electrons (SEs) with energies less than 50 eV, which are primarily used for imaging surface features. These secondary electrons, which are slowed upon striking the specimen's surface, are collected by a detector. The resulting secondary electron signal is used to create a magnified image of the specimen, revealing its morphology and topology. The SEM can also detect other signals such as characteristic X-rays and Auger electrons for additional analysis.

2.4.3.1. Instrumentation

The primary components of the SEM include the electron column, specimen chamber, and computer control system, as depicted in Fig. 2.11. The SEM instrumentation may include secondary and backscattered electron detectors, an energy-dispersive X-ray spectrometer (EDS), a low vacuum detector, and an electron backscattered diffraction (EBSD) detector, among other components. While some of these components are not necessary for basic imaging, they become increasingly important for advanced microscopy applications. An electron beam is generated by an electron source and accelerated toward the specimen using a positive electrical potential. The accelerating voltage, which ranges from 2 to 30 kV depending on the sample and analysis requirements, controls the force of the electrons. Early SEM systems typically utilized tungsten "hairpin" or lanthanum hexaboride (LaB_6) cathodes. However, modern SEMs increasingly favour field emission sources, which offer improved current and reduced energy dispersion. A

high vacuum is essential for the operation of a field emission gun, making it costly. However, this setup provides greater brightness and higher resolution. The beam emitted from the gun is too broad to generate a clear and well-defined image, so the SEM is equipped with lenses to compress the spot and direct the focused electron beam onto the specimen. The beam is then focused and confined by metal apertures and magnetic lenses, creating a thin, monochromatic beam that is directed onto the specimen. The condenser lenses, situated after the beam passes the anode, converge the beam to a focal point and along with the accelerating voltage, control the intensity of the beam on the specimen. Deflection coils within the objective lens direct the electron beam across the specimen, producing a clear image. Secondary electrons emitted from the specimen are drawn toward a detector because of its positive charge. Detectors in the SEM capture signals resulting from the interaction between the electron beam and the specimen. These signals are converted into digital images by electronic detectors. Commonly collected signals include secondary electrons detected by the Everhart–Thornley detector, backscattered electrons detected by a solid-state detector, and X-ray signals captured by an energy dispersive spectrometer (EDS) [28].

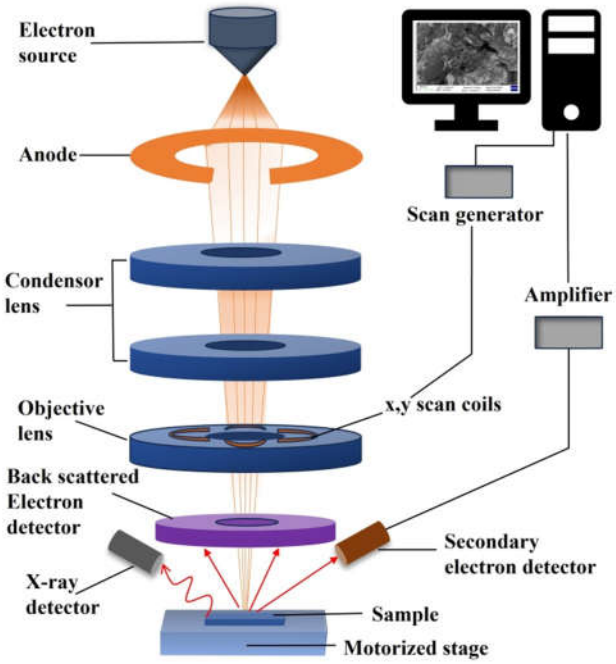

Fig.2.11 Diagrammatic representation of a scanning electron microscope.

In this work, the morphology of the synthesized samples was examined using a Gemini SEM 300 field emission scanning electron microscope (FESEM).

Fig.2.12 Gemini SEM 300 field emission scanning electron microscope (FESEM).

2.4.4. EDS spectroscopy

Most scanning electron microscopes (SEMs) are equipped with energy-dispersive X-ray spectrometers (EDS) for chemical analysis, which detect characteristic X-rays produced by the incident electron beam [26]. EDS utilizes the X-ray spectrum emitted by a solid sample when it is bombarded with a focused electron beam for the identification and quantification of chemicals present at detectable concentrations. When the primary electron beam interacts with the specimen material, it generates characteristic X-rays and background X-rays, together forming an X-ray signal. This signal is collected by an X-ray detector, which measures its energy and intensity distribution. The detector, typically an EDS spectrometer, analyses these X-rays to identify the elements present and determine their concentrations within the examined region of the specimen [27]. It can detect elements from Beryllium (Be) (atomic number 4) to Uranium (U) (atomic number 92), though some instruments may miss lighter elements [29].

The inelastic interaction of the electron beam within the specimen generates two types of X-rays. Characteristic X-rays are produced when incident electrons eject inner shell electrons from the atoms, and electrons from higher energy levels fill these vacancies, emitting X-rays with energy corresponding to the difference between the shells involved (e.g., K_{α}, K_{β}). These X-rays appear as distinct peaks in the energy spectrum. Continuum (Bremsstrahlung) X-rays arise from interactions between the incident electrons and the nuclei of the specimen atoms, creating a broad background in the spectrum. The EDS spectrometer detects these X-rays, measures their energy and intensity, and generates a spectrum that reveals peaks corresponding to the characteristic X-rays of the elements in the specimen. This analysis facilitates both qualitative and quantitative determination of the specimen's elemental composition.

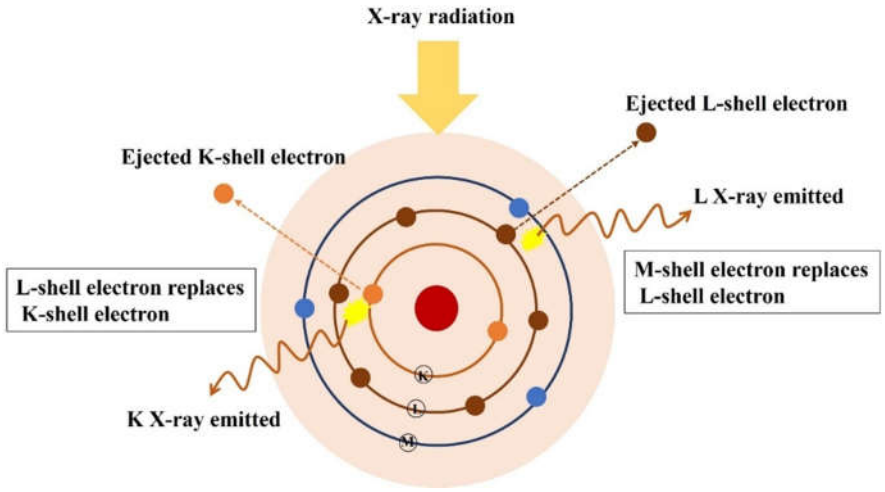

Fig.2.13 Schematic representation of the working principle of energy dispersive X-ray spectroscopy (EDS).

2.4.4.1. Instrumentation

Typically, SEM instrumentation includes an EDS system for chemical analysis. The primary component of the EDS system are: an X-ray detector that detects and transforms X-rays into electrical signals. A pulse processor examines electrical signals to estimate the energy of each detected X-ray and, a multi-channel analyzer (MCA) shows and interprets X-ray data. When an X-ray photon is absorbed by the detector, it generates a photoelectron that creates electron-hole pairs in a single

crystal. This process results in a charge pulse, which is then converted into a voltage pulse by a preamplifier. The voltage pulse, which is proportional to the energy of the incoming X-ray photon, is subsequently amplified and shaped by a linear amplifier. Each atom emits a distinct amount of energy during the transition process, enabling element identification by measuring the energy of emitted X-rays. The processed signal is then analyzed by the MCA, which displays the data as a histogram of intensity versus voltage. X-ray spectra are shown with energy (in keV) on the x-axis and the number of counts on the y-axis as shown in the Fig.2.14.

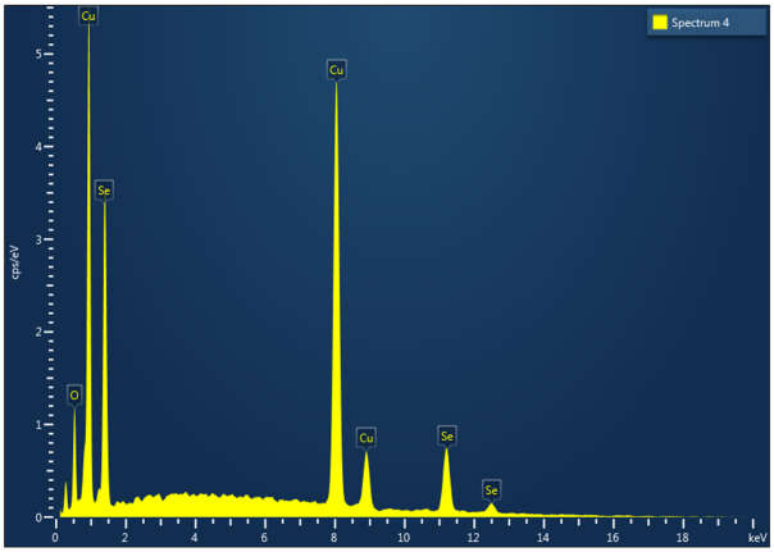

Fig.2.14 EDS spectra of Cu_2Se.

2.4.5. Transmission electron microscopy

Transmission electron microscopy (TEM) is an advanced technique that provides detailed information about the microstructural properties of materials, including atomic orientations through crystal diffraction patterns [30]. TEM can magnify objects up to 50 million times, offering atomic-scale resolution far beyond the capabilities of optical microscopes, which are limited by the visible light spectrum [31]. This exceptional resolution is due to the much shorter wavelengths of electrons, which are approximately 100,000 times smaller than those of visible light. A focused electron beam passes through an ultrathin sample, typically less than 100nm thick, with the transmitted electrons being detected to generate high-resolution images. These images reveal intricate details of the sample's internal

structure, crystal arrangement, atomic configuration, and the positions of individual atoms [32]. However, since electrons have limited penetration ability, the specimen must be extremely thin, usually no thicker than a few 100 Å. In some cases, slightly thicker samples can be used in high-voltage electron microscopes. In contrast to scanning electron microscopy, which only provides information about a specimen's morphology, TEM can reveal detailed insights into its structure, crystallization, morphology, and strain in the lattice planes. However, preparing specimens for TEM can be more time-consuming, as it requires samples to be thin and semi-transparent to electrons.

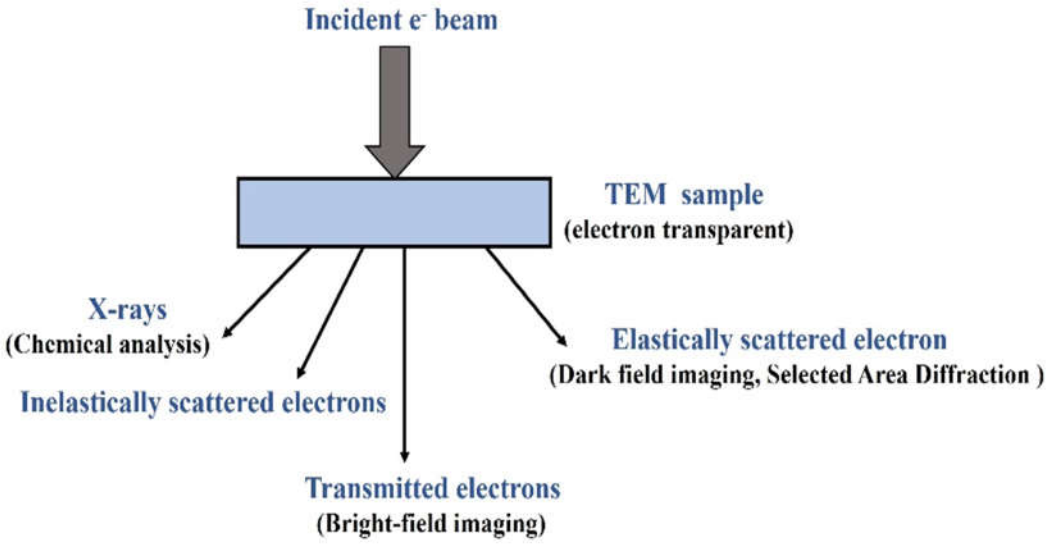

Fig.2.15 Interactions of the incident electron beam with the TEM sample.

There are two modes of operation for a standard TEM microscope: image mode and diffraction mode [33]**.** In image mode, a high-resolution image of the sample is generated by projecting the transmitted electrons onto a camera once the electron beam has passed through the sample. Conventional TEM employs three imaging modes: bright-field, dark-field, and high-resolution electron microscopy, also referred to as phase-contrast mode. In diffraction mode, the interaction of the electron beam with the sample generates a diffraction pattern, which is displayed on a fluorescent screen. This pattern is similar to an X-ray diffraction pattern. A single crystal produces a distinct spot pattern, a polycrystalline material forms concentric rings or a powder pattern, and an amorphous or glassy material shows diffuse halos.

2.4.5.1. Instrumentation

The TEM operates through a high-resolution imaging system consisting of three main components: the electron gun, the image-producing system, and the image-recording system [34]. The electron gun generates the electron beam by emitting electrons from a heated tungsten filament (cathode), which is controlled by a Wehnelt cylinder and focused towards an anode with high voltage. The electron beam passes through an aperture and is refined by a condenser lens system that focuses it onto the specimen. Two condenser lenses are employed to produce a smaller, high-magnification image, which is then directed to the objective lens. The image-producing system includes the objective, intermediate, and projector lenses, as well as a movable stage that holds the specimen. The objective lens, with a short focal length, creates an intermediate image from the transmitted electrons, which is further magnified by the projector lens to produce high resolution imaging. These lenses require stable, high power supplies to ensure optimal resolution. The image-recording system features a fluorescent screen to display the image and a digital camera for permanent recording. To maintain the integrity of the electron beam, a vacuum system is used to prevent air molecules from interfering. The resulting image is typically monochromatic (black and white) but can be digitally processed to produce colour images for better visualization, identification, and characterization of the specimen. As the electron beam passes through the thin specimen, it is scattered and transmitted by the atomic structure, creating contrast in the image based on the degree of electron scattering. In our study, HRTEM images of the samples were captured using a Jeol/JEM 2100 high-resolution transmission electron microscope.

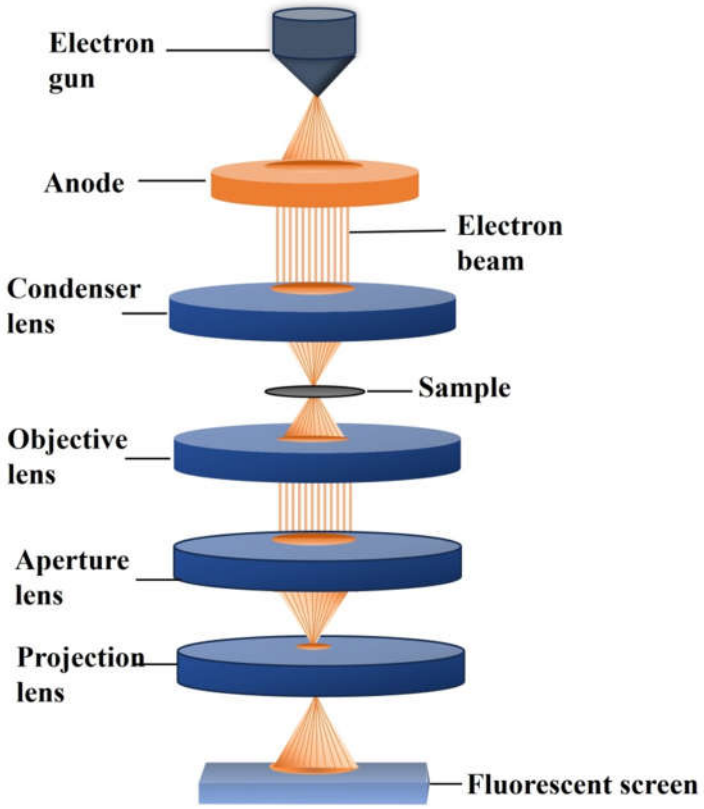

Fig.2.16 Schematic diagram of a transmission electron microscope.

Fig.2.17 Jeol/JEM 2100 high-resolution transmission electron microscope.

2.4.6. Ultraviolet-Visible spectrophotometer

In ultraviolet-visible (UV-Vis) spectroscopy, the absorption of light as a function of wavelength provides insights into electronic transitions within a material. For semiconductors, this technique is useful for estimating the optical band gap by examining electronic transitions between the valence band and the conduction band. During the measurement, the sample is illuminated with electromagnetic rays of various wavelengths, covering the visible (Vis) range as well as the adjacent ultraviolet (UV) and lower infrared (near IR) regions of the spectrum. The substance partially absorbs this light, and the remaining transmitted light is recorded as a function of wavelength by a suitable detector. This process generates the sample's UV-Vis spectrum. The spectral range of a UV-Vis spectrometer typically spans from 190 nm to 900 nm. High-end commercial spectrophotometers can extend this range into the near-infrared (NIR) region, reaching up to 3300 nm, allowing for the measurement of the NIR properties of the material under investigation.

The interaction of light from the UV-Vis-NIR region with solids is considered complex due to absorption and scattering phenomena. Many of these challenges are effectively overcome by utilizing methods such as diffuse reflectance spectroscopy (DRS). In the current research work, the DRS technique is employed to estimate the optical band gap of the synthesized samples. This method relies on the reflection of light from a powdered sample, where the size of the individual particles is similar to the wavelength of the light, typically ranging from 0.2 to 3 μm [35,36]. Diffuse reflection results from single, multiple, and dependent scattering, with the dependent scattering involving multiple scattering events where the phase coherence of the scattered photons is preserved [37]. The reflectance R is defined as the ratio of the total intensity J_0 of light reflected from a sample to the total intensity I_0 of the incident light. Mathematically, it is expressed as

$$R = \frac{J_0}{I_0} \qquad \text{.....(2.8)}$$

In the presence of both scattering and absorption, the amount of light backscattered in a unit volume of the illuminated material is described by the scattering coefficient

S(λ) while the light absorbed in the unit volume of the specimen is characterized by the absorption coefficient K(λ) These effects are combined in the Schuster-Kubelka-Munk (SKM) equation.

$$F(R_\infty) = \frac{(1-R_\infty)^2}{2R_\infty} = \frac{K}{S} \quad \text{.....(2.9)}$$

where R_∞ represents the reflectance of an "infinitely" thick sample. The SKM function replaces the Bouguer-Lambert-Beer law, facilitating the determination of absorbed radiation loss in materials with strong scattering properties.

The correlation between the energy band gap (E_g) and the absorption coefficient (α) for direct band transitions is given by Tauc's relation,

$$(\alpha h\upsilon)^n = A\left(h\upsilon - E_g\right) \quad \text{.....(2.10)}$$

Here A and n represent a constant, and the nature of the electronic transition, respectively. For direct allowed transitions, n=1/2, for direct forbidden transitions, n=3/2, for indirect allowed transitions, n=2, and for indirect forbidden transitions, n=3. The optical band gap of the material can be estimated by extending the straight-line portion of the graph plotted between (hν) versus $(\alpha h\nu)^2$ to the energy axis [38].

2.4.6.1. Instrumentation

In DRS, the instrumentation involves measuring the ratio of light scattered from an infinitely thick layer of the sample to that from an ideal non absorbing reference sample (Teflon) as a function of wavelength. When powdered samples are illuminated by incident radiation, the material experiences diffuse illumination. This incident light is then partially absorbed and partially scattered diffusively by the catalyst particles. The UV-visible spectrophotometer essentially comprises four key components: a light source, a sample holder, a diffraction grating, and a detector. A double-beam UV-Visible-NIR spectrophotometer operates with two light sources: a deuterium lamp for UV light (160-375 nm), and a tungsten halogen lamp for visible and near-infrared (NIR) light (350-2500 nm), providing a continuous spectrum across these ranges. The light from these sources is first separated into its component wavelengths using a monochromator. The resulting spectrum is then

split into two equal intensity beams by a beam splitter. One beam is directed through the sample under investigation, while the other is directed through a reference sample. The two beams are then recombined, and the differences in their intensities are measured. The reflected light is detected using different detectors: a photomultiplier tube (PM) for the UV-Vis region (200-800 nm) and a lead sulfide (PbS) detector for the NIR region (750-3000 nm). Additionally, modern DRS instruments may employ photodiode arrays (PDA) and charge-coupled device (CCD) detectors, which cover the 200-1100 nm range, enabling simultaneous acquisition of the entire spectrum. In this thesis work, DRS spectra of the samples were obtained using a Cary 5000 high-performance UV-Vis-NIR spectrophotometer, covering a wavelength range from 200 to 1100 nm.

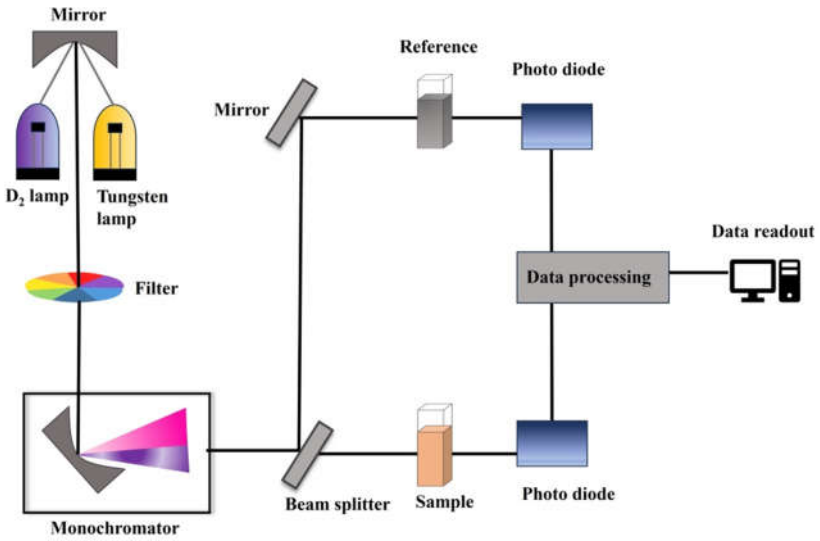

Fig.2.18 Schematic diagram of a UV-Visible spectrophotometer.

Fig.2.19 Carry 5000 high-performance UV-Vis-NIR spectrophotometer.

2.4.7. Hall measurement

The Hall effect, discovered by Edwin Hall in 1879, is a key tool for studying the transport properties of charge carriers in semiconductors such as carrier concentration and mobility [39]. It occurs when a magnetic field is applied perpendicular to the current flow through a material, generating a voltage across the material that is perpendicular to both the magnetic field and the current, due to the Lorentz force acting on moving charge carriers. In 1906, Gans provided the first successful explanation of the Hall effect, demonstrating that the Hall coefficient (R_H) is inversely proportional to the free-carrier concentration (n). The relationship is given by the equation

$$R_H = \frac{r_H}{en} \qquad (2.11)$$

where e is the elementary charge and r_H is the Hall scattering factor. This inverse dependence forms the basis for using the Hall effect to measure the carrier concentration in materials, particularly in semiconductors [40]. The Hall effect arises when a magnetic field is applied perpendicular to the direction of current flow in a conductor. In the absence of this magnetic field, the current flows evenly along the length of the sample. However, when the magnetic field is introduced, the charge carriers in the conductor experience a Lorentz force, which deflects them towards the edges of the sample. This deflection causes a buildup of charge on the edges, creating an electric field that opposes the magnetic force. The system reaches equilibrium when the electric field force counteracts the Lorentz force, resulting in a measurable voltage known as the Hall voltage [41]. It is schematically represented in the Fig. 2.20. This voltage is detected across the sides of the sample that are oriented parallel to the current flow, providing valuable information about the carrier concentration and the nature of the material.

The Hall coefficient (R_H) is a material property that indicates how its free charge carriers react to a magnetic field. It is defined as the ratio of the transverse electric field (E_H) to the product of the current density (J) and the magnetic field strength (B).

$$R_H = \frac{E_H}{R \times B} \quad \text{.....(2.12)}$$

E_H is the Hall electric field, which is the electric field perpendicular to both the current density and the magnetic field strength. J is the current density, representing the current per unit area of the conductor's cross-section and B is the magnetic field strength. The Hall coefficient is positive for p-type semiconductors and negative for n-type semiconductors.

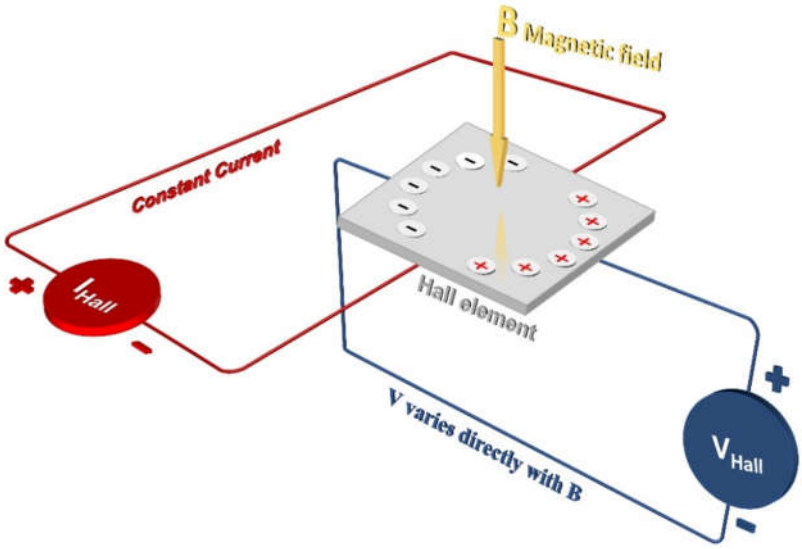

Fig.2.20 Schematic illustration of the Hall effect.

2.4.7.1. Instrumentation

The core of the setup includes a sample holder with precise contact points, often using spring-loaded probes or other types of contacts, to ensure accurate electrical measurements. Gold-coated contacts are ideal for measuring very low voltages and currents. A permanent magnet or electromagnet is employed to create a magnetic field of known strength, which is essential for inducing the Hall voltage. It utilizes a four-point probe configuration in the Van der Pauw arrangement to accurately measure electrical transport properties such as carrier concentration and mobility. The measurements require four ohmic contacts to be placed on the sample, ideally positioned at the sample's boundary. For optimal accuracy, these contacts should be as small as possible to minimize their impact on the measurement results. In this study, the carrier concentration was estimated using the Ecopia HMS 5500. The

measurements were conducted on pellet sample with dimensions of 13 mm diameter, using spring-loaded gold probes with silver dot contacts positioned at equidistant corners. A permanent magnet, providing a flux density of 0.51 Tesla, was used to apply the magnetic fields necessary for the Hall effect measurements. The system uses a constant current source to supply current, with the ability to adjust according to the sample's resistance. It can provide direct current in a range from 1 nA to 20 mA, ensuring compatibility with various sample resistivities and allowing for precise Hall effect measurements.

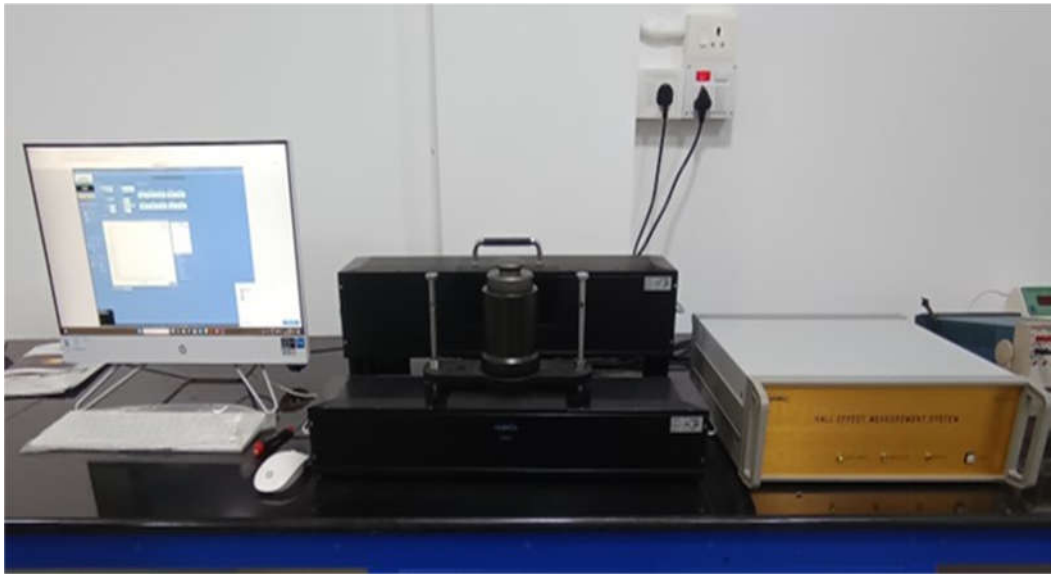

Fig.2.21 Ecopia HMS 5500.

2.4.8. Thermoelectric measurement

In thermoelectric measurement systems, while the ZT is difficult to measure directly in experiments, it can be calculated using the measured Seebeck coefficient (S), electrical conductivity (σ), and thermal conductivity (κ). Both S and σ can be measured simultaneously using a thermoelectric measurement system. The fundamental aspect of Seebeck measurement involves determining the voltage difference (ΔV) across a sample subjected to a constant temperature gradient (ΔT) at a specific average temperature (T). The Seebeck coefficient (S) is then calculated as the ratio of ΔV to ΔT.

$$S = \frac{\Delta V}{\Delta T} \text{……..……..(2.13)}$$

Both voltage and temperature are measured at the same nominal points on the sample [42]. For a specimen under a temperature gradient, temperatures at points A and B are measured using two thermocouples to determine the temperature difference ($\Delta T = T_B - T_A$). The voltage difference (ΔV) between points A and B is measured using the positive (or negative) wires of the two thermocouples. Typically, at least three pairs of ΔV and ΔT are collected to plot the curve [43]. The slope of the curve represents the measured Seebeck coefficient (S_M), at the average temperature $(T_A + T_B)/2$. The metal wires themselves have their own Seebeck coefficients (S_W), which must be subtracted from S_M to determine the material's Seebeck coefficient (S). While commercial instruments automatically apply this correction, it is often overlooked in homemade setups. Electrical resistivity is measured using the standard four-probe method. This approach calculates the electrical resistivity with the formula

$$\rho = \frac{R \times A}{d} \sigma \text{……(2.14)}$$

where R represents the electrical resistance between points A and B, A is the cross-sectional area of the sample, and d denotes the distance between the probes. The measurement system automatically selects the optimal current value for measuring the resistivity of the sample.

2.4.8.1. Instrumentation

In this study, a ULVAC ZEM 3-M8 instrument was employed to simultaneously measure the Seebeck coefficient and electrical conductivity of thermoelectric materials. This instrument is capable of evaluating the thermoelectric properties of a diverse range of materials, including semiconductors, ceramics, and metals. Electrical resistivity is determined using the four-probe technique. The system utilizes an ADCMT-6146 DC source for supplying current and a KEITHLEY-2010 multimeter for voltage measurement. The sample is placed between electrodes fixed to the upper and lower blocks, which are used to apply the temperature. A

microheater at one end of the sample maintains the temperature gradient across it. The system utilizes an infrared gold image furnace known for its superior temperature control, along with a micro heater to manage temperature differences precisely. Temperature measurements are taken using thermocouple probes made of platinum rods positioned on the sample's side. To avoid oxidation, the sample is kept in a helium atmosphere at a low pressure of 10^{-3} Torr. The measurement range extends from room temperature (RT) to 900°C measurements are controlled by a computer, enabling precise control over temperature differences at specific temperatures and automating the process to eliminate dark electromotive forces. Additionally, it features a standard ohmic contact self-check function, which is monitored through a voltage-current (V-I) plot to ensure accurate measurements.

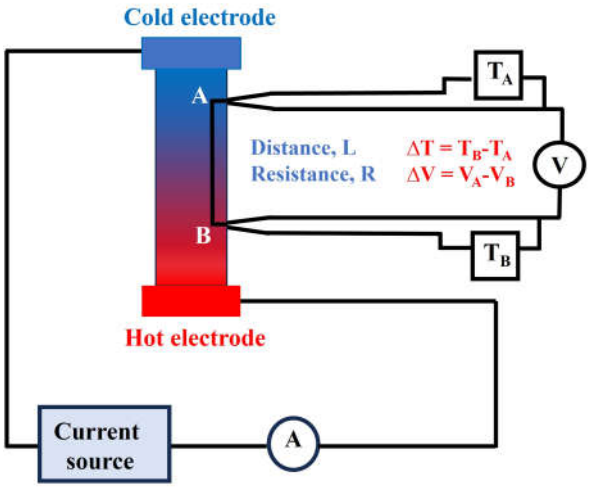

Fig.2.22 Schematic illustration of S and σ measurements.

Fig.2.23 ULVAC ZEM 3-M8 thermoelectric measurement system.

2.4.9. Thermal conductivity measurement

Thermal conductivity (κ) is a material property that quantifies the rate at which heat is conducted through a material. It is defined as the amount of heat (Q) transferred per unit time (t) through a unit cross-sectional area (A) of the material, given a unit temperature gradient (dT) perpendicular to that area [44]. Whenever a thermal gradient exists within a material, heat transport occurs in an attempt to equalize the gradient. This process of heat transfer is characterized by the thermal conductivity coefficient (κ), which is defined as

$$Q = -\kappa A\left(\frac{dT}{dx}\right)\ldots\ldots\ldots\ldots\ldots\ldots\ldots\ldots\ldots\ldots\ldots(2.15)$$

Where dT represents the differential temperature across the sample, while dx denotes the differential thickness of the test sample. It predicts the rate of energy loss through a material and is typically measured in units of $Wm^{-1}K^{-1}$.

In a crystal, heat is transported by phonons, which are the fundamental excitations of the system. The thermal conductivity can be described as [45]

$$\kappa = \left(\frac{1}{3}\right) C_v\, \upsilon\, \lambda\ldots\ldots\ldots\ldots\ldots\ldots\ldots\ldots\ldots\ldots(2.16)$$

Where C_v is the specific heat at constant volume, υ and λ represent the mean velocity and mean free path of the carriers, respectively.

To determine the thermal conductivity of metals, early methods involved heating a rod at one end and measuring the temperature gradient with thermocouples placed along its length [46]. Experimental techniques for measuring thermal conductivity are divided into two main types: steady-state and transient methods. Steady-state methods involve assessing heat flow and temperature gradients along a sample by taking temperature readings at various points. While these methods are accurate, they require lengthy equilibration periods and are not ideal for high temperatures. They also necessitate precise heat insulation or compensation systems. On the other hand, transient methods, like the hot-wire and flash techniques, use advanced instruments to monitor quick temperature changes, often aided by computer

analysis. The hot-wire method calculates thermal conductivity by measuring the temperature increase caused by a consistent heat source embedded in the material.

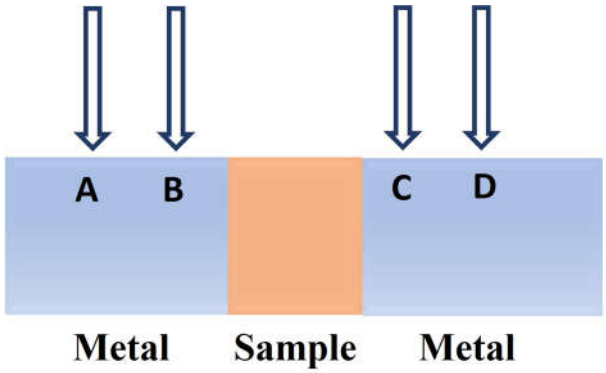

Fig.2.24 Schematics showing divided-bar method.

2.4.9.1. Instrumentation

Several methods exist for determining thermal conductivity, one of which is the divided bar method which is a steady state technique [47]. In this approach, a sample is sandwiched between two metal rods, with the sample cross-section matching that of the metal rods. Heat is introduced at one end of the setup, passing through the first metal rod, then through the sample, and finally exiting through the second metal rod. Conditions are adjusted to ensure a steady state is reached. Temperatures are measured at specific points, labeled as A, B, C, and D, in the setup. These temperature readings are used to calculate the thermal gradient $\left(\frac{dT}{dx}\right)_m$ within the two metal rods. By extrapolating the temperature gradients from lines AB and DC to the interfaces between the sample and the metal rods, the thermal conductivity of the sample $\left(\frac{dT}{dx}\right)_s$ can be determined.

If the entire apparatus is placed in a chamber with minimal heat loss due to radiation, the thermal conductivity can be accurately determined by equating the heat flow through the metal blocks to that through the sample.

we can derive, $$\kappa_m A \left(\frac{dT}{dx}\right)_m = \kappa_s A \left(\frac{dT}{dx}\right)_s \quad \text{.....(2.17)}$$

$$\kappa_s = \frac{\kappa_m \left(\frac{dT}{dx}\right)_m}{\left(\frac{dT}{dx}\right)_s} \text{.....(2.18)}$$

κ_s, the thermal conductivity of the sample is then calculated using this equation 2.18.

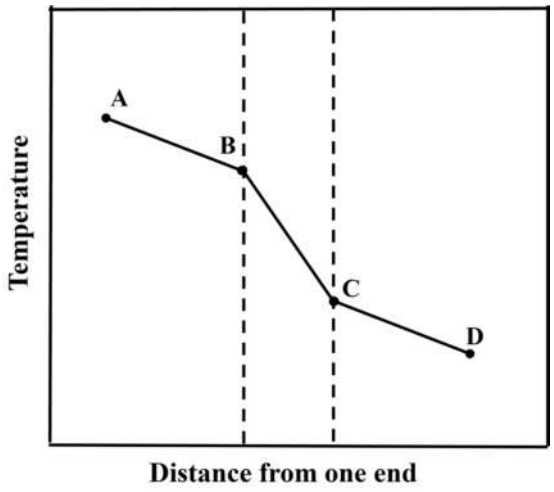

Fig.2.25 Variation of temperature with distance from one end of the block.

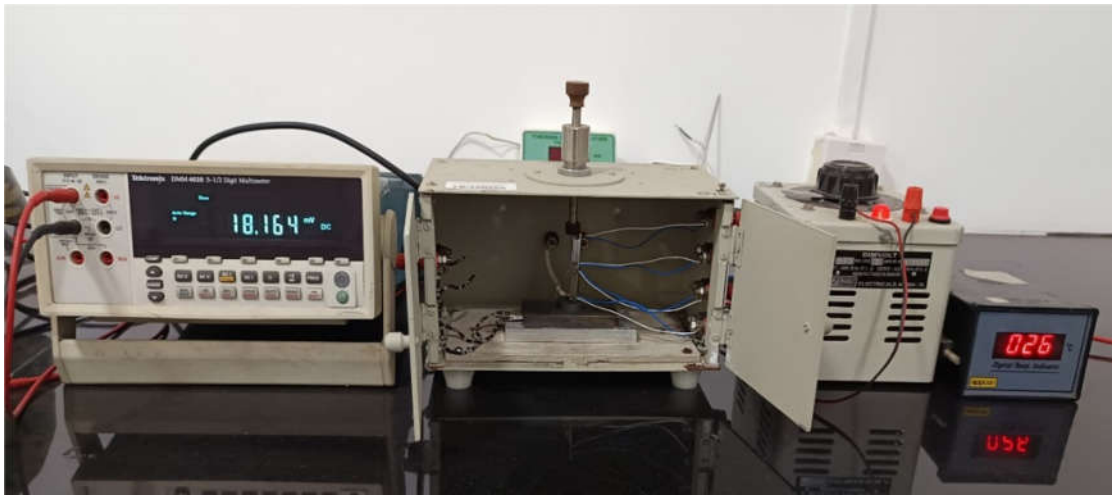

Fig.2.26 Thermal conductivity measurement system.

References

[1] Z.G. Chen, G. Hana, L. Yanga, L. Cheng, J. Zou, Nanostructured thermoelectric materials: Current research and future challenge, Prog. Nat. Sci. Mater. Int. 22 (2012) 535–549. https://doi.org/10.1016/j.pnsc.2012.11.011.

[2] S. Sōmiya, R. Roy, Hydrothermal synthesis of fine oxide powders, Bull. Mater. Sci. 23 (2000) 453–460. https://doi.org/10.1007/BF02903883.

[3] N. Baig, I. Kammakakam, W. Falath, I. Kammakakam, Nanomaterials: A review of synthesis methods, properties, recent progress, and challenges, Mater. Adv. 2 (2021) 1821–1871. https://doi.org/10.1039/d0ma00807a.

[4] A. Sobhani, M. Salavati-Niasari, Transition metal selenides and diselenides: Hydrothermal fabrication, investigation of morphology, particle size and their applications in photocatalyst, Adv. Colloid Interface Sci. 287 (2021) 102321. https://doi.org/10.1016/j.cis.2020.102321.

[5] N.K.V. Nadimpalli, R. Bandyopadhyaya, V. Runkana, Thermodynamic analysis of hydrothermal synthesis of nanoparticles, Fluid Phase Equilib. 456 (2018) 33–45. https://doi.org/10.1016/j.fluid.2017.10.002.

[6] Y.X. Gan, A.H. Jayatissa, Z. Yu, X. Chen, M. Li, Hydrothermal synthesis of nanomaterials, J. Nanomater. (2020) 8917013. https://doi.org/10.1155/2020/89170-13.

[7] S.K. Kulkarni, Nanotechnology : Principles and practices, Springer Cham. (2014). https://doi.org/10.1007/978-3-319-09171-6.

[8] S.H. Feng, G.H. Li, Hydrothermal and solvothermal syntheses, Modern Inorganic Synthetic Chemistry (Second Edition) (2017) 73-104. https://doi.org/10.1016/B978-0-444-63591-4.00004-5.

[9] T. Prasad Yadav, R. Manohar Yadav, D. Pratap Singh, Mechanical Milling: a Top Down Approach for the Synthesis of Nanomaterials and Nanocomposites, Nanosci. Nanotechnol. 2 (2012) 22–48. https://doi.org/10.5923/j.nn.20120203.01.

[10] M. Pentimalli, M. Bellusci, F. Padella, High-energy ball milling as a general tool for nanomaterials synthesis and processing, Handb. Mech. Nanostructuring. 2 (2015) 663–679. https://doi.org/10.1002/9783527674947.ch28.

[11] C. Pohshna, D.R. Mailapalli, Modeling the particle size of nanomaterials synthesized in a planetary ball mill, OpenNano. 14 (2023) 100191. https://doi.org/10.10-16/j.onano.2023.100191.

[12] W. Cao, Understanding Nano Ball Milling Method for Synthesis of Nanomaterials, (1960) 2–5.

[13] H. Khan, A.S. Yerramilli, A. D'Oliveira, T.L. Alford, D.C. Boffito, G.S. Patience, Experimental methods in chemical engineering: X-ray diffraction spectroscopy, XRD, Can. J. Chem. Eng. 98 (2020) 1255–1266. https://doi.org/10.1002/cjce.23747.

[14] B. Ingham, X-ray scattering characterisation of nanoparticles, Crystallogr. Rev. 21 (2015) 229–303. https://doi.org/10.1080/0889311X.2015.1024114.

[15] D. Theprattanakorn, T. Kaewmaraya, S. Pinitsoontorn, Boosting thermoelectric efficiency of Ag_2Se through cold sintering process with Ag nano-precipitate formation, Int. J. Miner. Metall. Mater. 31 (2024) 2760–2769. https://doi.org/10.1-007/s12613-024-2973-x.

[16] D.R. Munazat, D.S. Razaq, B. Soegijono, B. Kurniawan, S. Budiawanti, D. Nanto, Influence of sintering temperature on structural and morphology of $La_{0.7}Ba_{0.25}Nd_{0.05}MnO_3$, J. Electron. Mater. 54 (2020) 1085–1095. https://doi.org/10.-4108/eai.2-10-2018.2295291.

[17] A. Ali, Y.W. Chiang, R.M. Santos, X-Ray diffraction techniques for mineral characterization: A Review for Engineers of the Fundamentals, Applications, and research directions, Minerals. 12 (2022). https://doi.org/10.3390/min12020205.

[18] L.D. Whittig, W.R. Allardice, X-ray diffraction techniques, Methods soil anal. part 1 phys. mineral. methods. 9 (2018) 331–362. https://doi.org/10.2136/sssabookser 5.1.2ed.c12.

[19] A.A. Bunaciu, E. gabriela Udristioiu, H.Y. Aboul-Enein, X-Ray diffraction: instrumentation and applications, Crit. Rev. Anal. Chem. 45 (2015) 289–299. https://doi.org/10.1080/10408347.2014.949616.

[20] G.S. Bumbrah, R.M. Sharma, Raman spectroscopy–Basic principle, instrumentation and selected applications for the characterization of drugs of abuse, Egypt. J. Forensic Sci. 6 (2016) 209–215. https://doi.org/10.1016/j.ejfs.2015.06.001.

[21] P. Rostron, S. Gaber, D. Gaber, Ijetr042430 (1), Int. J. Eng. Tech. Res. 6 (2016) 50–64.

[22] P.J. Larkin, Chapter 1 - Introduction: Infrared and Raman spectroscopy, in: P.J. Larkin (Ed.), Infrared Raman spectrosc. Elsevier (2018) 1–5. https://doi.org/ /10.1016/B978-0-12-804162-8.00001-X.

[23] Raman Instrumentation, in: Pract. Raman Spectrosc. An Introd., John Wiley & Sons, Ltd, (2013) 61–100. https://doi.org/https://doi.org/10.1002/978111996128-4.ch4.

[24] J. Coates, Vibrational Spectroscopy: Instrumentation for Infrared and Raman Spectroscopy, Appl. Spectrosc. Rev. 33 (1998) 267–425. https://doi.org/10.1080/ 05704929808002060.

[25] P. V. Huong, New possibilities of Raman micro-spectroscopy, Vib. Spectrosc. 11 (1996) 17–28. https://doi.org/10.1016/0924-2031(95)00057-7.

[26] W. Zhou, Z.L. Wang, Scanning microscopy for nanotechnology: Techniques and applications, Springer New York, NY (2007). https://doi.org/10.1007/978-0-387-39620-0.

[27] A. Ul-Hamid, A Beginners' Guide to Scanning Electron Microscopy, Springer Cham. (2018). https://doi.org/10.1007/978-3-319-98482-7.

[28] D.M. Kannan, Scanning electron microscopy: principle, components and applications, Textb. Fundam. Appl. Nanotechnol. (2018) 82–92.

[29] University of California Riverside, Introduction to energy dispersive X-ray

spectrometry (EDS), (2013) 1–11. http://micron.ucr.edu/public/manuals/EDS-intro.pdf.

[30] B.J. Inkson, 2 - Scanning electron microscopy (SEM) and transmission electron microscopy (TEM) for materials characterization, in: G. Hübschen, I. Altpeter, R. Tschuncky, H.-G. Herrmann (Eds.), Mater. Charact. Using Nondestruct. Eval. Methods, Woodhead Publishing, (2016) 17–43. https://doi.org/https://doi.org/10.10-16/B978-0-08-100040-3.00002-X.

[31] S. Zaefferer, A critical review of orientation microscopy in SEM and TEM, Cryst. Res. Technol. 46 (2011) 607–628. https://doi.org/10.1002/crat.201100125.

[32] R.F. Egerton, Choice of operating voltage for a transmission electron microscope, Ultramicroscopy. 145 (2014) 85–93. https://doi.org/https://doi.org/10.1016/ j.ultram-ic.2013.10.019.

[33] B. Fultz, J.M. Howe, The TEM, and its optics, in: Transm. electron microsc. diffractometry mater., Springer Berlin Heidelberg, Berlin, Heidelberg, (2001) 63–121. https://doi.org/10.1007/978-3-662-04516-9_2.

[34] M. Kannan, Transmission electron microscope-principle, components and applications, A Textb. Fundam. Appl. Nanotechnol. (2018) 93–102.

[35] Vogt, C., Wondergem, C.S., Weckhuysen, B.M., Ultraviolet-Visible (UV-Vis) Spectroscopy. In: Wachs, I.E., Bañares, M.A. (eds) Springer handbook of advanced catalyst characterization. Springer Handbooks. Springer, Cham. (2023). https://doi.org/10.1007/978-3-031-07125-6_11.

[36] R.D. Prabu, S. Valanarasu, V. Ganesh, M. Shkir, S. Alfaify, A. Kathalingam, S.R. Srikumar, R. Chandramohan, Materials Science in Semiconductor Processing An e ff ect of temperature on structural , optical , photoluminescence and electrical properties of copper oxide thin fi lms deposited by nebulizer spray pyrolysis technique, Mater. Sci. Semicond. Process. 74 (2018) 129–135. https://doi.org/10.1016/j.mssp.2017.10.023.

[37] C. Kole, Preface to the series, Genet. Genomics, Breed. Banan. (2012) vii–xi. https://doi.org/10.1201/b11776.

[38] T. Parvathy, N.A. Muhammed Sabeer, N. Mohan, P.P. Pradyumnan, Effect of dopant gas pressure on the growth of magnetron sputtered CuO thin films for electrical and optical applications, Opt. Mater. (Amst). 125 (2022) 112031. https://doi.org/10.10-16/j.optmat.2022.112031.

[39] R. Green, Hall Effect Measurements in Materials Characterization Who Needs to Measure Hall Effect ? Growing Interest in the Use of Hall Effect Measurements, Keithley White Pap. 3111 (1990) 1–12.

[40] K. Ellmer, Hall effect and conductivity measurements in semiconductor crystals and thin films, Charact. Mater. (2012) 1–16. https://doi.org/10.1002/0471266965.com-035.pub2.

[41] O. Lindbergt, Hall Effect, Proceedings of the IR. 40 (1952) 1414–1419. https://-doi.org/ 10.1109/JRPROC.1952.273972.

[42] T. Seebeck, C.T. Group, Chapter 3 Seebeck metrology, 24–43.

[43] T.R. Wei, M. Guan, J. Yu, T. Zhu, L. Chen, X. Shi, How to Measure Thermoelectric Properties Reliably, Joule. 2 (2018) 2183–2188. https://doi.org/10.1016/j.joule.2018.10.020.

[44] A. Palacios, L. Cong, M.E. Navarro, Y. Ding, C. Barreneche, Thermal conductivity measurement techniques for characterizing thermal energy storage materials – A review, Renew. Sustain. Energy Rev. 108 (2019) 32–52. https://doi.org/10.1016/j.rser.2019.03.020.

[45] A.C. Anderson, Thermal conductivity, Topics in Current Physics, Springer, Berlin, Heidelberg. 24 (1981) 2-3. https://doi.org/10.1007/978-3-642-81534-8_5.

[46] M.A. Llavona, R. Zapico, F. Blanco, L.F. Verdeja, J.P. Sancho, Methods for measuring thermal conductivity, RDM Rev. Minas. 6 (1991) 89–98.

[47] D.B. Sirdeshmukh, K.G. Subhadra, Experiments in solid state physics, South Asian Publishers Ltd., (2008). https://books.google.co.in/books?id=aB1MPgAAC-AAJ.

Chapter-3

Impact of Ni doping on the thermoelectric performance of Cu_2Se crystallites

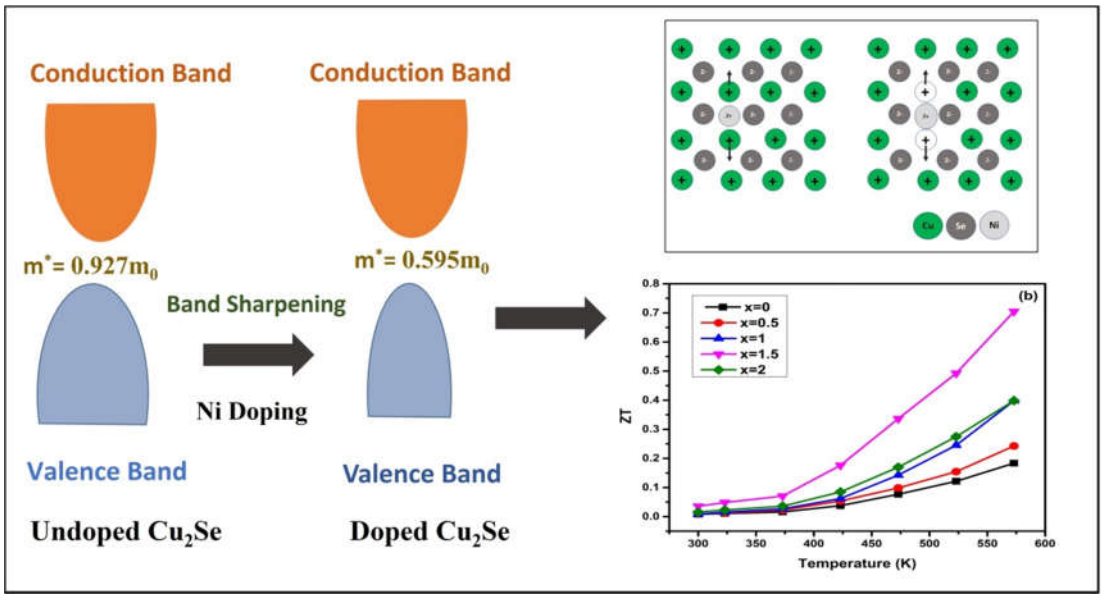

This chapter investigates the enhancement obtained in the thermoelectric performance of Cu_2Se through the strategy of doping. The inclusion of nickel in the Cu_2Se lattice has a substantial influence on its structural, morphological, optical, electrical, and thermal transport properties. The strategy of modifying electronic band structures has been examined to enhance carrier transport by optimizing the balance between carrier mobility and effective mass, aiming to achieve advancements in thermoelectric applications

3.1. Introduction

Cu_2Se has emerged as a highly promising thermoelectric material due to its exceptional electrical properties and naturally low thermal conductivity. Its unique structure, where copper ions exhibit liquid-like mobility within a crystalline selenium lattice, plays a critical role in its thermoelectric behavior. This dynamic interaction between charge carriers and copper ions aligns with the phonon liquid electron crystal (PLEC) concept, offering an innovative approach to improving thermoelectric efficiency. Achieving high thermoelectric performance requires optimizing both electrical transport properties, such as the Seebeck coefficient and electrical conductivity, and phonon transport properties, like thermal conductivity. However, this is a challenging task because these parameters are interdependent. For example, increasing charge carrier concentration can improve electrical conductivity but may also reduce carrier mobility due to scattering, ultimately limiting thermoelectric performance. To overcome this, researchers are employing various strategies, including doping, composite engineering, energy filtering, nanostructuring, and advanced band engineering techniques such as band sharpening and band convergence, to decouple and optimize these interdependent transport characteristics for enhanced thermoelectric performance. Among these, doping is particularly effective which involves introducing controlled alterations to the material's electronic and structural characteristics. By precisely adjusting the charge carrier concentration and scattering mechanisms, doping helps to decouple these interdependent properties, enabling significant enhancements in thermoelectric performance.

Doping is a widely employed technique to optimize thermoelectric performance by introducing acceptors or donors to modulate the type and concentration of charge carriers. The interaction between the dopant and charge carriers strongly influences the electronic transport properties, often enhancing electrical conductivity by increasing charge carrier concentration [1,2]. However, this approach poses challenges, as increasing carrier concentration often induces scattering, which diminishes carrier mobility. Since carrier mobility is intrinsically linked to both the

Seebeck coefficient and electrical conductivity, this reduction can hinder the overall enhancement of thermoelectric performance [3,4]. So, researchers are becoming more aware of the significance of maintaining carrier mobility in high performance thermoelectric materials. Band engineering techniques, such as band sharpening, band flattening, and band convergence, have emerged as effective strategies to achieve this balance [5–8]. Due to the inherent relationship between carrier mobility and effective mass, the electrical transport characteristics exhibit different behaviors in these band modification methods [9]. Band sharpening is a band structure modification approach that increases the mobility of charge carriers by lowering their effective mass [10]. This reduction in carrier effective mass improves the carrier mobility, resulting in high electrical conductivity. So, to obtain good electrical transport properties, we must rationally optimize these transport parameters.

The selection of an appropriate dopant requires thorough investigation and characterization to optimize a material's properties for specific applications. In this study, we focus on modifying the thermoelectric properties of Cu_2Se by incorporating Ni as a dopant. Ni is considered a potential dopant for Cu_2Se due to its ability to integrate into the lattice without affecting structural stability, suggesting suitability for long-term thermoelectric applications. Its smaller atomic size compared to Cu may introduce lattice strain, which could influence material properties depending on concentration. Ni doping is expected to impact carrier concentration, potentially altering electrical conductivity and thermal transport through phonon interactions. Additionally, its presence might influence the electronic band structure, hinting at possible changes in optical and electrical characteristics. These factors indicate that Ni doped Cu_2Se could exhibit improved thermoelectric performance.

To validate these, we systematically investigated the effect of Ni doping on the structural, morphological, optical, electrical, thermoelectrical, and thermal transport properties of Cu_2Se. By varying the Ni concentration, we were able to fine-tune both carrier density and mobility. The incorporation of Ni into the interstitial sites of the

Cu_2Se lattice led to a simultaneous enhancement of carrier concentration and mobility. This doping strategy introduced defects and disorders within the lattice, boosting the thermoelectric properties of Cu_2Se. The synergistic effect of nanostructuring and band modification further enhanced the thermoelectric performance by reducing thermal conductivity while improving electrical transport properties, thereby achieving a notable increase in ZT [11].

3.2. Experimental details

Cu_2Se nanoparticles were synthesized through a low temperature hydrothermal route as detailed in section 2.2.1. All experimental reagents of analytical purity were purchased and used for the synthesis of materials. Copper chloride dihydrate ($CuCl_2.2H_2O$, > 99%), nickel chloride hexahydrate ($NiCl_2.6H_2O$, > 98%), selenium metal powder (> 99.5%), sodium hydroxide (NaOH > 98%), sodium borohydride ($NaBH_4$, > 96 %) purchased from sigma aldrich were used. To synthesize pristine Cu_2Se, $CuCl_2.2H_2O$ was mixed in 150 ml of deionized water at 50^0C. To maintain the pH at 10, NaOH is added dropwise to this solution. Se metal powder is used as a selenium precursor and sodium borohydride is chosen as the reducing agent to convert Se to Se^{2-} ion. $NaBH_4$ is a widely used reducing agent in various chemical processes, including the reduction of metal ions to create nanoparticles [12-14]. During this reaction, $NaBH_4$ provides hydride ions (H^-) to selenium (Se), initiating a reduction process that leads to the creation of a reduced selenium compound (Na_2Se). This reaction can be represented as follows:

$$Se + 4NaBH_4^- + 7H_2O \rightarrow Na_2Se^{2-} + 15H_2 + Na_2B_4O_7 \ldots\ldots\ldots\ldots (3.1)$$

Simultaneously, hydrogen gas (H_2) is produced as a secondary product, and sodium metaborate ($NaBO_2$) is generated as well during the reaction. The overall reaction results in the formation of Cu_2Se can be written as

$$CuCl_2 \cdot 2H_2O + 4NaOH + Se + 4NaBH_4^- + 7H_2O \rightarrow Cu_2Se + 4NaCl + Na_2B_4O_7 + 15H_2 \ldots\ldots\ldots\ldots (3.2)$$

To synthesize undoped Cu_2Se, the stoichiometry between Cu and Se is fixed at 2:1. Here we choose 1.875g of $CuCl_2$ $2H_2O$, 0.4342g of Se metal powder, and 0.8493g

of sodium borohydride for the synthesis of pristine Cu_2Se. The resultant solution was mixed thoroughly with a magnetic stirrer at 50°C for 1 hour. After the reaction is over the solution is transferred to an autoclave which is maintained at 150°C for 24 hours. After heating it was allowed to cool down to room temperature. Then the precipitate was collected, separated by centrifugation, washed several times with deionized water and ethanol, and dried at 80°C under a vacuum overnight. For Ni-doped samples, the concentration of $CuCl_2.2H_2O$ and $NiCl_2.6H_2O$ is varied. Nickel was introduced at different weight percentages (x=0.5, 1.0, 1.5, and 2.0 wt%) for doping, and, the same synthesis procedures were followed. All the synthesized powder was then densified by pressing into a circular pellet of 13mm diameter with 3mm thickness using a hydraulic pelletizer with a force of about 10 tons in air. The densified pellet was sintered at 300°C for 3 hours were taken for further characterization. The structural, morphological, optical, and thermoelectric properties of the sintered pellets were thoroughly analyzed. Chapter 2 provides a detailed explanation of the synthesis procedures and the characterization methods utilized for this work.

3.3. Results and discussion

3.3.1. Phase and structure analysis

Powder X-ray diffraction (PXRD) patterns of the Cu_2Se samples doped with different nickel concentration (x= 0 wt%, 0.5 wt%, 1 wt%, 1.5 wt%, 2 wt%) are shown in Fig.3.1. The diffraction peak at 26.79°, 30.98°, 44.44°, 52.63°, 64.70°, and 71.23° can be indexed to cubic planes of the Cu_2Se phase (ICDD-03-065-2982) without the presence of any secondary phases, suggesting that Ni is incorporated into the Cu_2Se lattice. The average crystallite size (D), Microstrain (ε), and dislocation density (δ) for all the samples were determined using the equations (equation 2.2-2.4) described in chapter 2.

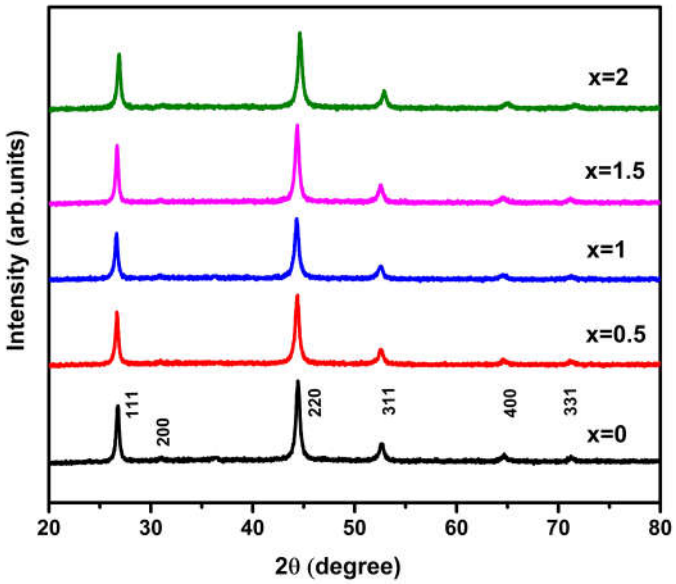

Fig.3.1 PXRD pattern of undoped and Ni doped samples.

The PXRD spectra show that the diffraction peaks of doped samples are somewhat displaced towards lower angles in comparison to undoped Cu_2Se when the concentration of Ni^{2+} increases up to 1 wt%. According to Vegard's law, a shift to a higher angle side is expected for Ni^{2+} as it is slightly smaller than Cu^{+}. But Fig.3.2 shows that the impact of Ni inclusion in Cu_2Se results in a lower angle shift when the doping % increases to 1 wt%. Furthermore, it has been reported that relatively small atoms may cluster at interstitial sites and cause lattice distortions and strain [15,16]. Therefore, to determine the impact of Ni on the lattice, we calculated the microstrain and d-spacing, and Fig.3.3 illustrates how these variables changed with respect to Ni concentration. As the Ni content increases to 1 wt% there is an increase in both d-spacing and microstrain which indicates an expansion of the lattice. This implies that when the doping percentage increases up to 1 wt%, Ni^{2+} occupies the interstitial site rather than the substitutional site. Because Ni^{2+} ions (0.55Å) are typically smaller than Cu^{+} ions (0.60 Å), they have a strong tendency to occupy the interstitial sites of the Cu_2Se lattice [17]. The lattice will slightly expand as cations are added to interstitial sites to occupy them, which increases the d-spacing. Some Ni^{2+} dopant ions reside as interstitial ions rather than directly replacing Cu^{+} in the lattice up to a doping percentage of 1 wt%. This interstitial occupancy of Ni in the

Cu_2Se lattice can cause microstrain, which results in the expansion of the lattice [18]. With further increases in Ni content, the peak position shifts by a very small angle toward higher 2θ, and microstrain and d-spacing decrease. Following Bragg's law, when smaller dopant atoms substitute at host sites, the d-spacing in the lattice is expected to decrease and diffraction peaks shift to higher 2θ [19]. This suggests that as the Ni content increases from 1 wt % Ni^{2+} will substitute at the Cu^{+} site. The presence of Ni in the Cu_2Se lattice can be confirmed by calculating the lattice parameters. A shift to the lower angle side signifies an increase in the lattice parameter. To confirm this, we calculated the lattice parameters from the PXRD data which are shown as a function of Ni content in Fig.3.3 (b). Lattice parameters first increase up to a nickel content variation of 1 wt% and subsequently decrease. The increase in the lattice parameter is due to lattice expansion, which supports the presence of Ni in the interstitial site of Cu_2Se since ionic radii of Ni^{2+} are smaller than Cu^{+}. At higher doping content the lattice parameters decrease which indicates the substitution of Ni^{2+} in the Cu^{+} sites.

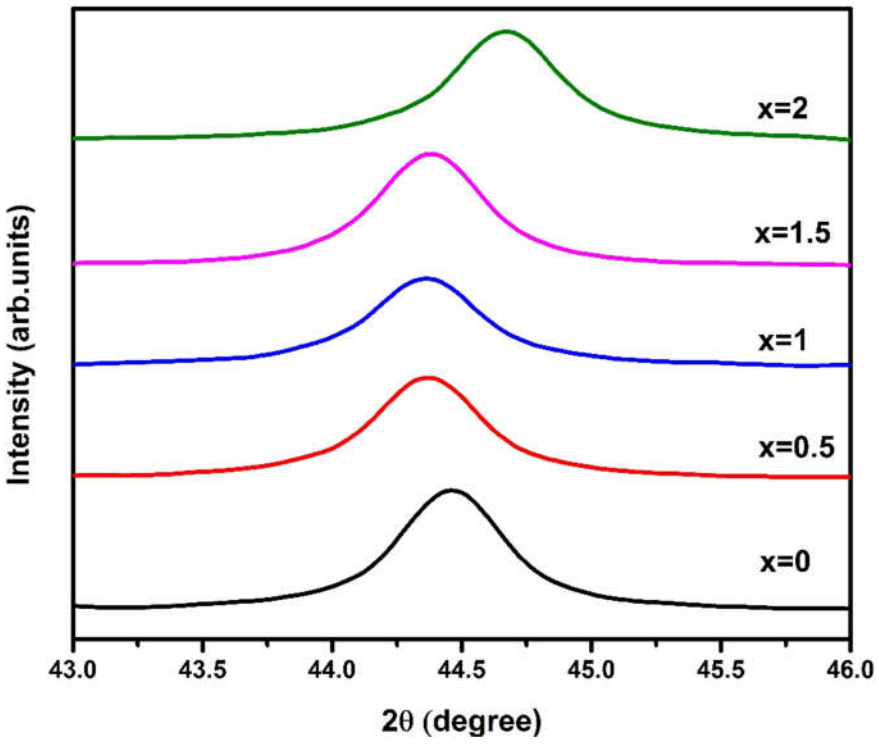

Fig.3.2 Shift observed in the 220-reflection peak with increasing nickel concentration.

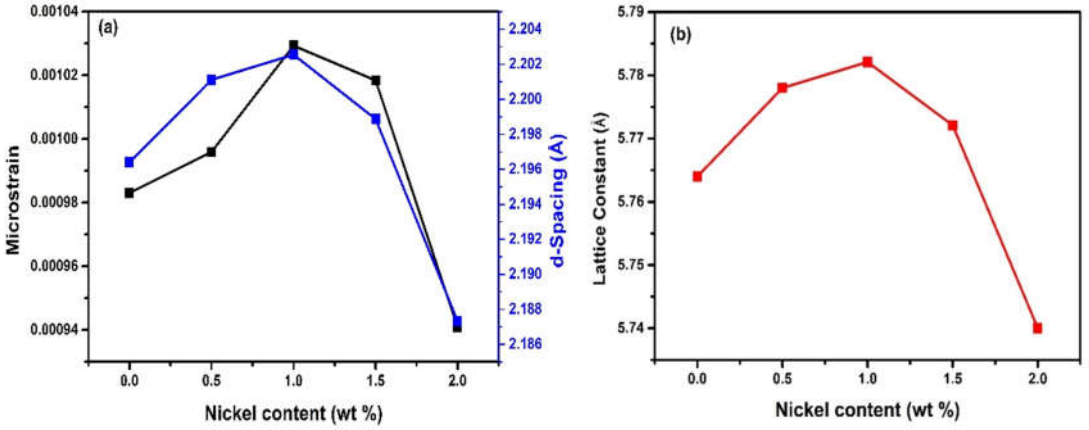

Fig.3.3 Variation of (a) microstrain and d-spacing (b) lattice constant with nickel concentration.

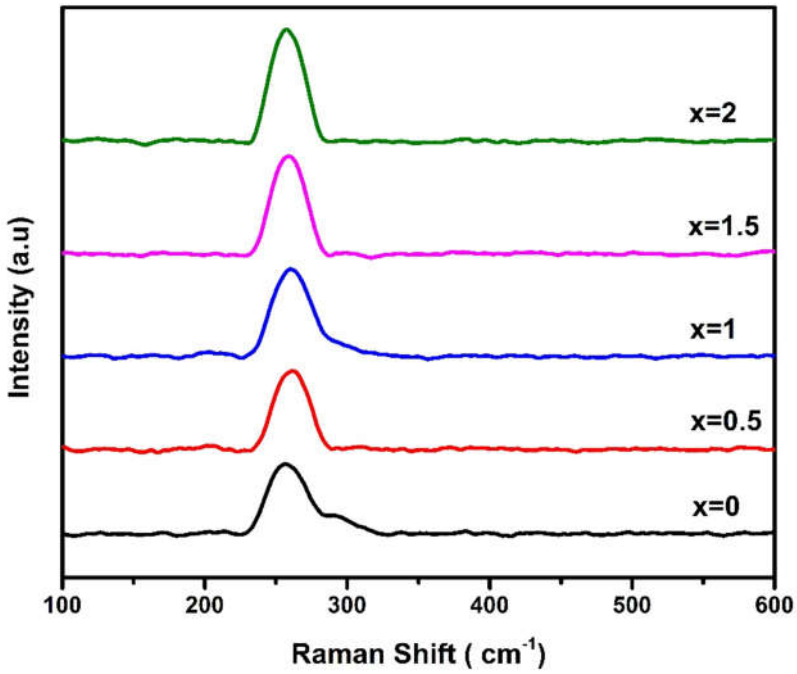

Fig.3.4 Raman spectra of undoped and Ni doped samples.

Fig.3.4 shows the Raman spectra of pristine and Ni doped Cu_2Se samples recorded at room temperature. The observed Raman modes for all samples are consistent with the previously reported values [20,21]. There was only one prominent peak cantered ~ 259 cm^{-1}, (1LO phonon frequency of Cu_2Se) which can be attributed to Cu-Se stretching vibration in Cu_2Se [22,23]. There is no vibrational mode corresponding to nickel in any of the spectra, confirming the phase purity of the doped samples. The

absence of a peak at 237.3 cm^{-1} also shows that there is no residual amount of selenium present in the samples [24]. Raman investigations reveal that the Ni atoms were effectively incorporated in the Cu_2Se lattice during hydrothermal growth and hence no substantial influence on the final composition is detected. The increase in the intensity of the Raman peaks is observed as the doping % of nickel is increased. Similar to PXRD results, when the doping percentage increases to 1 wt%, we can observe a shift in the Raman spectra to a higher frequency, followed by a shift to a lower frequency which is consistent with the PXRD results. This higher frequency shift corresponds to decreased bond length with increased doping, and vice versa. The occurrence of dopants at the interstitial site or substitution causes lattice distortion which might affect the bond length of Cu-Se. The nickel incorporation leads to a modest Raman shift with changes in peak width, as seen in Fig.3.4 indicating that the nickel inclusion is responsible for the improvements in the thermoelectric properties.

The peak shift observed relative to pristine Cu_2Se, resulting from the strain induced by Ni doping in the Cu_2Se lattice, is determined using the following equation 3.3 [21].

$$\epsilon = \frac{\omega - \omega_0}{\Gamma} \qquad (3.3)$$

Γ is the FWHM of the Raman peak measured in cm^{-1}, ω denotes the Raman frequency for the doped samples, and ω_0 is the reference Raman frequency of pristine Cu_2Se.

Phonon relaxation time τ can be calculated using the equation 3.4.

$$\frac{1}{\tau} = \frac{\Delta E}{h} = 2\pi c\Gamma \qquad (3.4)$$

ΔE represents the uncertainty in the energy of the phonon mode, while h is the Planck constant, and c denotes the velocity of light. The Raman peak position, FWHM, along with the calculated strain (ϵ) and phonon relaxation time (τ) for the various doped samples, are presented in table 3.1.

Table 3.1: Variation of Raman frequency (ω), FWHM (Γ), strain (ϵ), and phonon relaxation time (τ).

Sample	ω (cm^{-1})	Γ(cm^{-1})	ϵ (cm^{-1})	τ (ps)
x=0	259.23	34.35	0.00	0.15
x=0.5	261.01	32.07	0.06	0.17
x=1	261.52	26.93	0.02	0.19
x=1.5	258.79	26.18	-0.12	0.20
x=2	257.88	26.90	-0.23	0.19

The strain values indicate that as the doping level increases to 1.5 wt% Ni, the strain initially decreases. However, with further doping, the strain increases, suggesting lattice expansion, possibly due to the substitution of Ni in the Cu_2Se lattice. This change in strain influences phonon behavior, with τ increasing from 0.15 ps to 0.20 ps and then decreasing, which in turn impacts the thermal conductivity of the samples.

3.3.2. Morphological studies

Fig.3.5 shows the morphology of synthesized materials using high-resolution FESEM. Fig.3.5 (a) shows that the pristine Cu_2Se have an irregular nanoflakes like morphology. The inset in Fig.3.5 (a) clearly reveals a dense array of well-formed nanoflakes. The dopant has a substantial influence on the morphology of samples, it deviates with the addition of Ni, as seen in Fig.3.5. As the dopant is introduced into the pristine lattice the structure is transformed into an agglomerated one. The flake-like morphology breaks down as the dopant concentration increases, resulting in dense particle agglomerations. The change in morphology shows that doping Ni^{2+} brings more defects and disorders which may affect the thermoelectric performance of the system.

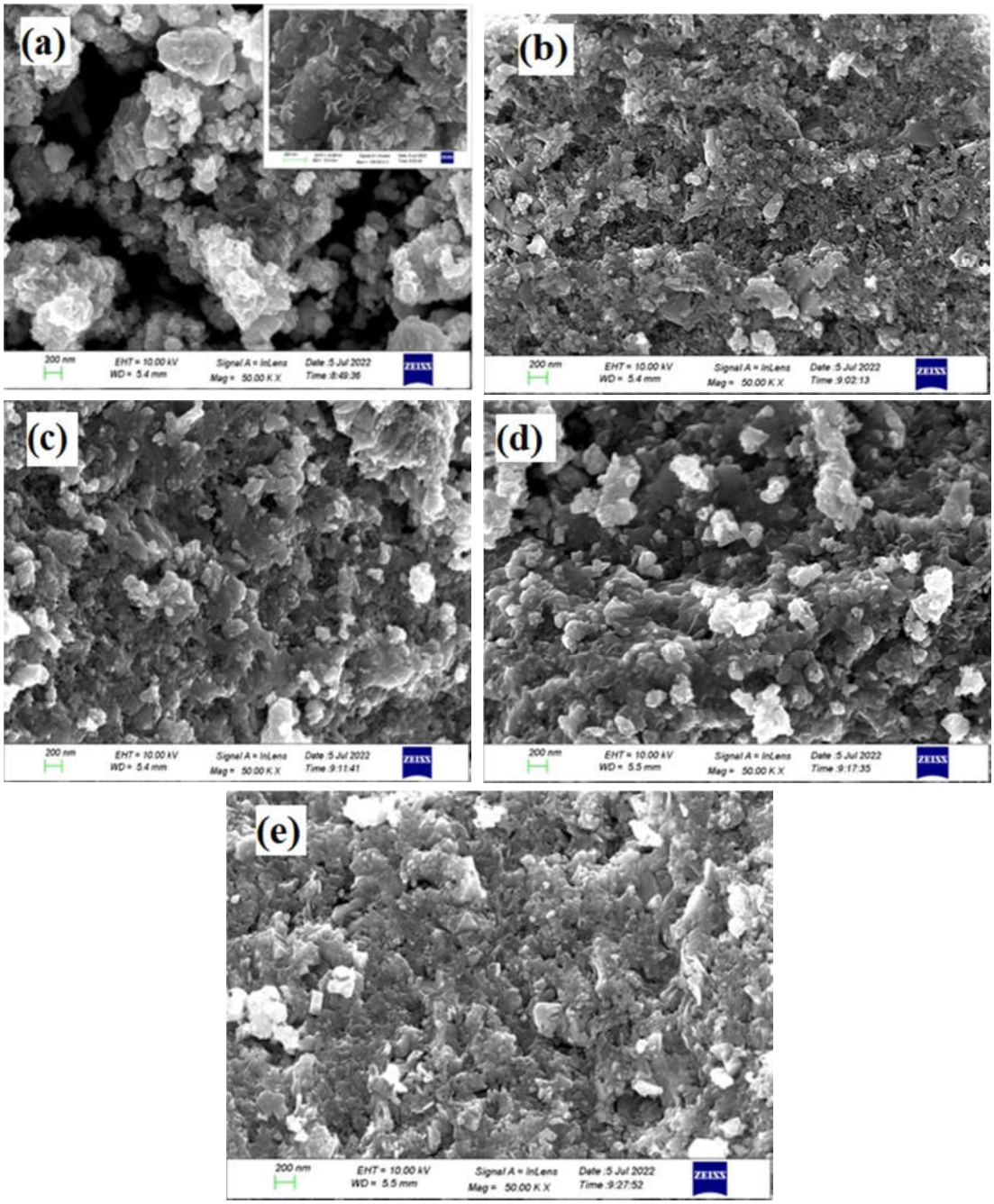

Fig.3.5 FESEM images of (a) undoped Cu_2Se, and samples doped at (b) 0.5 wt% Ni, (c) 1 wt% Ni, (d) 1.5 wt% Ni, (e) 2 wt% Ni**.**

The composition of the synthesized samples was identified using the EDS analytical technique as shown in Fig.3.6. Only the peak corresponding to Cu and Se is detected in pristine samples. For all the doped samples no peaks associated with elements other than Cu, Se, and Ni are observed, revealing the pure phase formation of Cu_2Se which is compatible with the XRD and micro Raman results. EDS mapping in

Fig.3.7 (a-d) illustrates the distribution of Cu, Se, and Ni in the Cu_2Se matrix for the 1.5 wt% Ni-doped sample. The maps confirm the successful incorporation of Ni, showing its random and uniform distribution throughout the matrix.

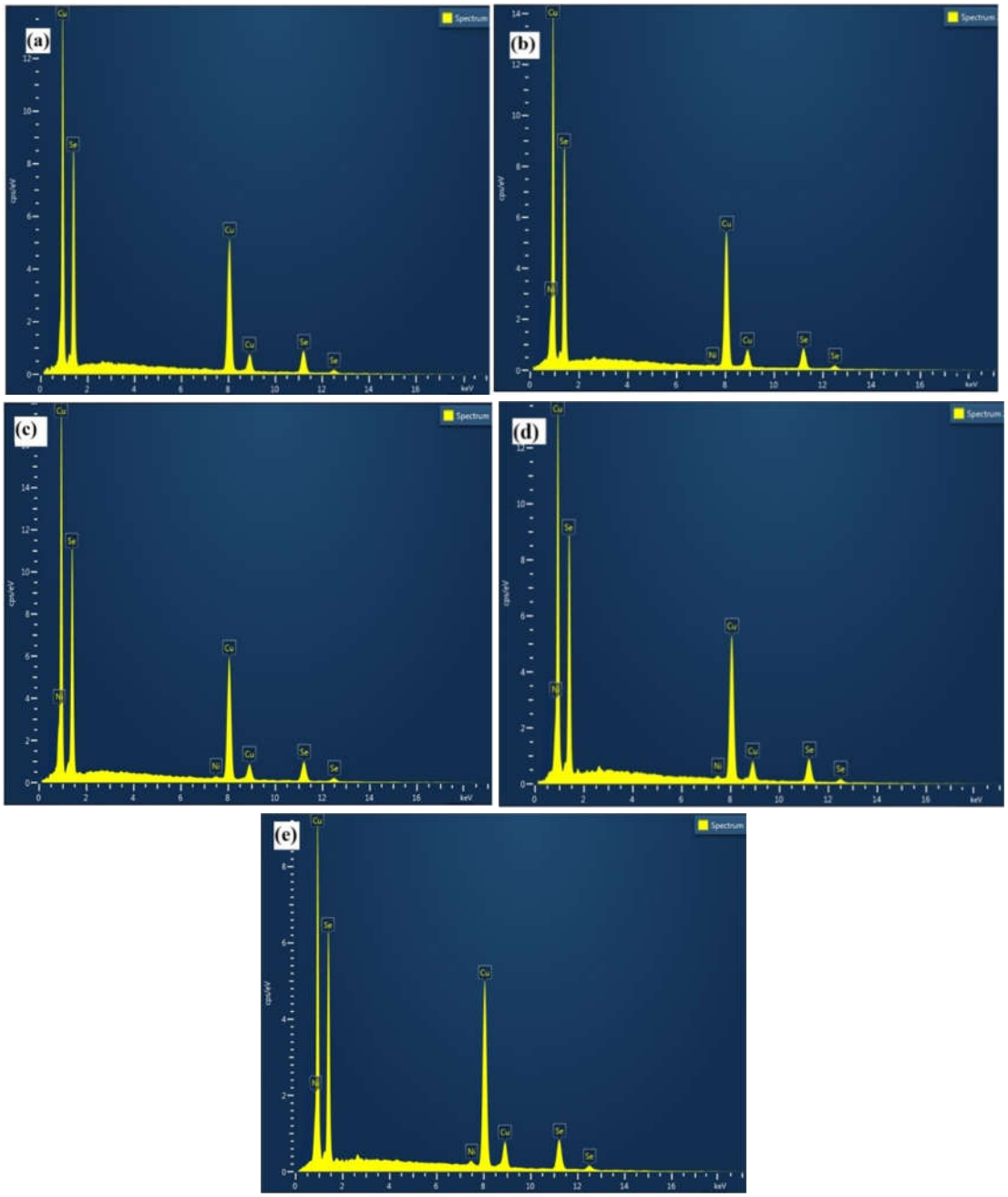

Fig.3.6 EDS spectra of (a) undoped Cu_2Se, and samples doped at (b) 0.5 wt% Ni, (c) 1 wt% Ni, (d) 1.5 wt% Ni, (e) 2 wt% Ni**.**

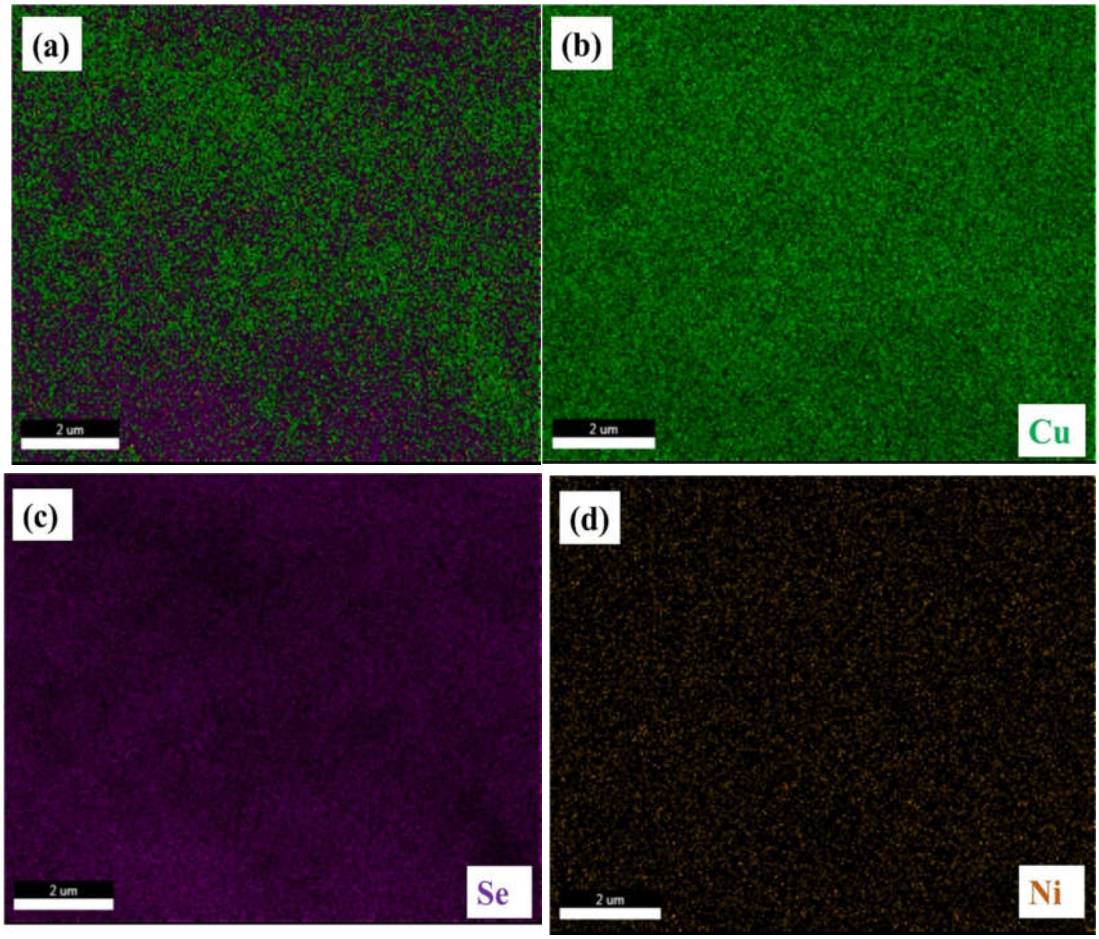

Fig.3.7 EDS elemental mapping for the Cu_2Se sample with 1.5 wt% Ni showing (a) the combined distribution of all elements, (b) the distribution of Cu, (c) Se, and (d) Ni.

3.3.3. Thermoelectric measurement studies

Temperature dependence on the Seebeck coefficient, electrical conductivity, and power factor are shown in Fig.3.8. The positive sign of the Seebeck coefficient confirms the p-type nature of the doped samples. With increasing dopant concentration, the electrical conductivity increases, while the Seebeck coefficient decreases concurrently for up to 1 wt% of dopant concentration. At higher doping concentrations Seebeck coefficients of the sample increase and approach near the value of pristine Cu_2Se. Impurity doping is a typical approach for tuning the semiconductor properties by adding impurities with acceptor (positively charged) or donor (negatively charged) charge carriers. Normally, Ni^{2+} substitution at the Cu^{+} site reduces p-type conductivity [25]. Here, we can see an increment in the electrical conductivity with Ni doping as compared to pristine Cu_2Se. The results showed that

electrical conductivity increased in low-doping regions as Ni content increased while the conductivity decreased as the doping content increases from 1 wt%. Due to increased degeneracy and intervalley scattering, mobility should typically decline as carrier concentration rises. This is a real concern for TE performance optimization in most TE materials [26].

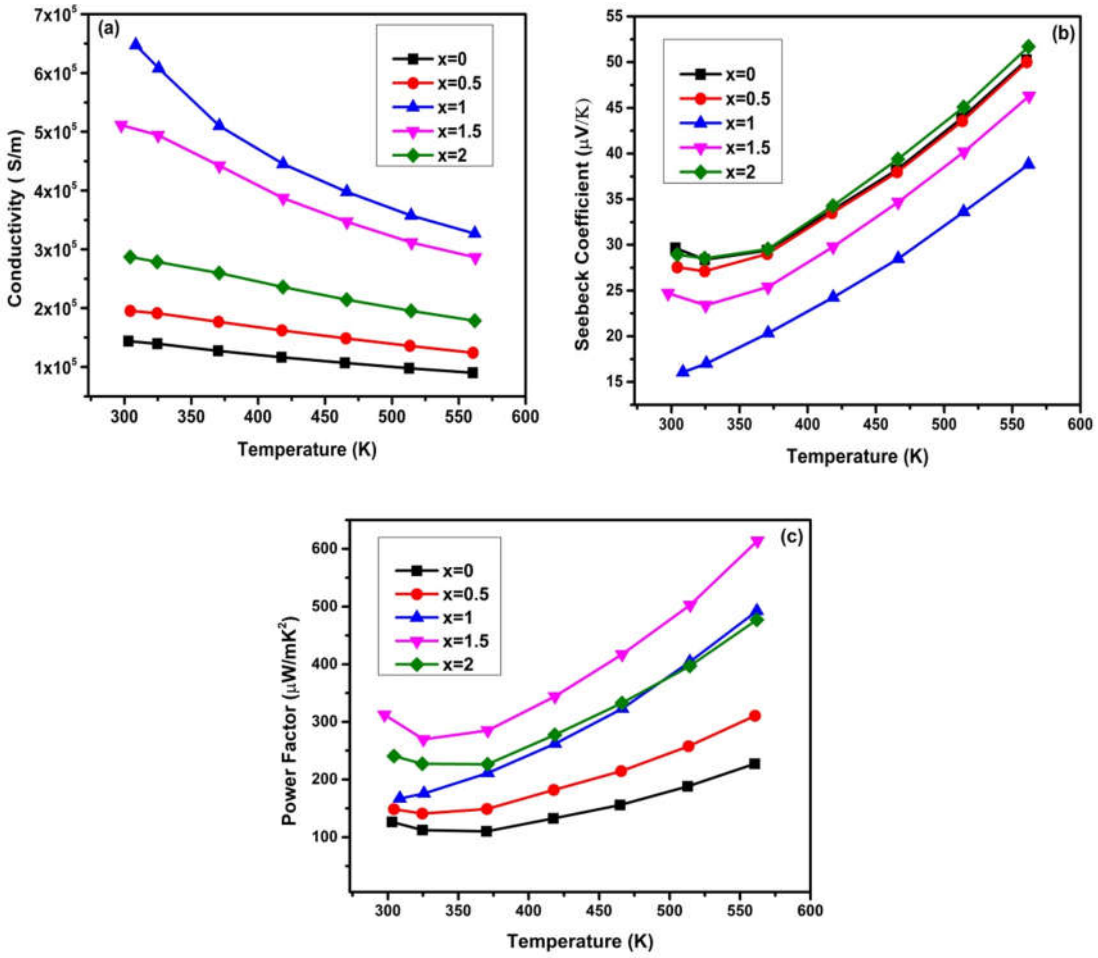

Fig.3.8 Temperature dependence of (a) electrical conductivity (b) and Seebeck coefficient (c) power factor of the synthesized samples.

The temperature dependence of carrier concentration and mobility are shown in Fig.3.10. Here simultaneous enhancement of carrier concentration and mobility can be observed for doping concentration up to 1 wt%. Such an increment is reported by Lou et al. in $In_4Se_{2.5}$ with iodine doping [27]. According to the PXRD studies, at this doping %, Ni ions may choose to occupy interstitial positions rather than substitution. Similarly, up to that doping %, we can see an improvement in both

carrier concentration and mobility resulting in an increase in electrical conductivity. The interstitial Ni ion causes a simultaneous increase in carrier concentration and mobility in these samples, which makes TE performance significantly improved. Here the Ni^{2+} is a donor type dopant in the Cu_2Se lattice. So it should obviously decrease the electrical conductivity. We observed a reduction in conductivity when the nickel level increased over 1 wt% due to the substitution of Ni^{2+} in Cu^{+} sites. However, an anomaly is observed at low Ni doping content. We were able to demonstrate through structural analyses that, at these doping percentages, Ni occupies interstitial sites rather than Cu^{+} sites. Therefore, we must verify how Ni interstitial improves conductivity in Cu_2Se. This can be explained by the possibility of 3d and 3d interaction between Cu^{+} and Ni^{2+} in the Cu_2Se samples. The mechanical impact of introducing an impurity causes strain, which further redistributes the conduction electron around the impurity ion [28]. When Ni^{2+} occurs at the interstitial sites of Cu_2Se, there will be electrical coulomb repulsion between the Ni and nearby Cu ions. The valence orbital (3d) of Ni $^{2+}$ may interact with the valence orbital (3d) of Cu^{+} ion results in a d-d orbital repulsion, which forces the Cu atoms out of their positions, resulting in the formation of numerous acceptor-type copper vacancies as shown in Fig.3.9. This increases the total p-type carrier concentration and, as a result, the p-type conductivity [29]. The conductivity increases with increasing doping density up to 1 wt% Ni, but beyond that, the conductivity begins to decrease due to the substitution of Ni^{2+} in the Cu^{+} sites. This is supported further by the carrier's temperature-dependent behavior. We can observe that when the temperature increases, the concentration of carriers decreases. This is because the repulsion between the 3d orbitals becomes minimal as temperatures increase. The change in conductivity is caused by a change in carrier concentration as the nickel content increases. At higher doping % holes in the valence band decrease whereas the mobility increases which enhances the conductivity. The interstitial site may be the ideal site to dope in order to control the electrical transport properties in the p-type Cu_2Se system since the distortion caused by Ni atoms occupying the interstitial sites of Cu_2Se has no significant effect on the carrier transport. These Ni interstitial presents a dynamic doping behavior that

concurrently increases the carrier density and the carrier mobility. The mobility increases as the doping % increases up to 1.5 wt % and thereafter decreases. At this stage of doping, the neutralization of holes by electrons due to the substitution of Ni^{2+} in the Cu^{+} site decreases the carrier concentration, increasing electrical resistance when compared to the other samples. A corresponding increase in the power factor can be seen in Fig.3.8 (c) and a maximum power factor of 614 $\mu W/mK^2$ is observed for the sample doped at 1.5 wt% Ni at 573 K. The electron transport in the conduction band results in an increase in the conductivity. The decreases in mobility at a doping concentration of 2 wt% are attributable to increased carrier scattering caused by Ni^{2+} inclusion in the Cu_2Se lattice, which lowers the carrier concentration, as seen in Fig.3.10. A high level of doping results in the creation of many scattering sites (defect centers) for the charge carriers [30]. This increases the Seebeck coefficient while decreasing electrical conductivity, consequently lowering the power factor at a higher doping of 2 wt%.

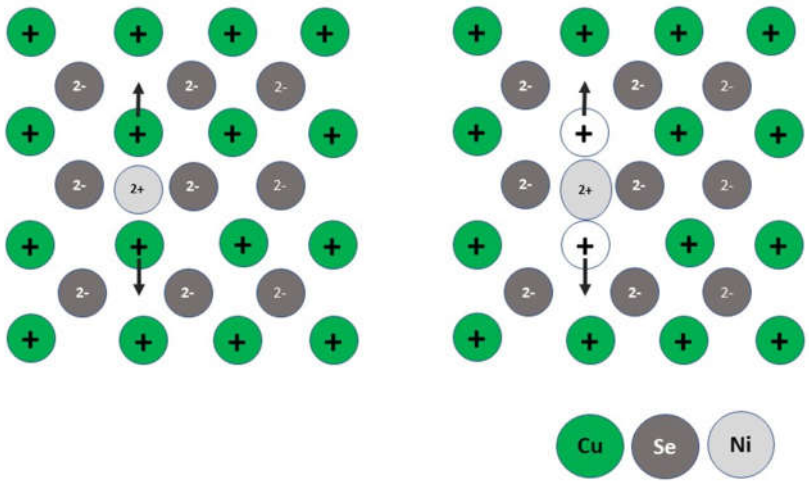

Fig.3.9 Schematic representation of electronic defects due to the presence of Ni in the lattice of Cu_2Se.

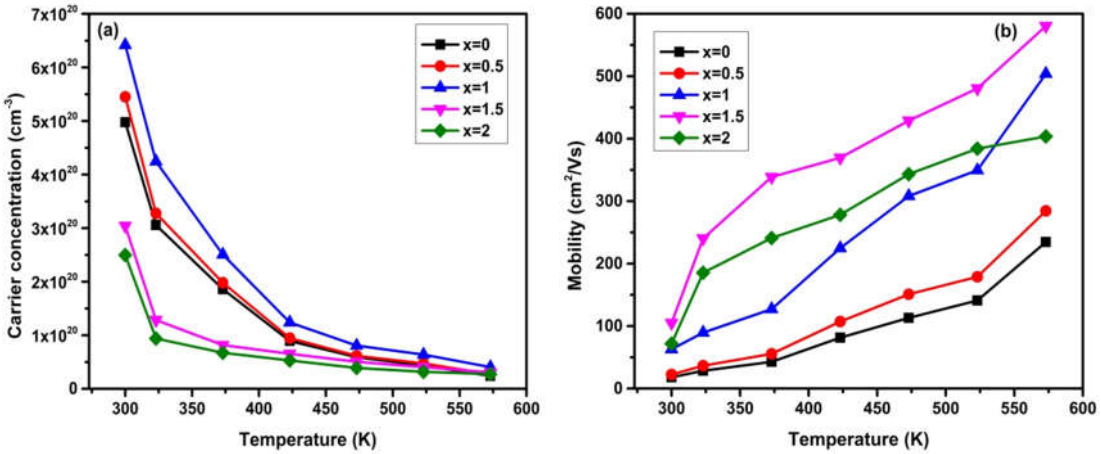

Fig.3.10 Temperature dependence of (a) carrier concentration and (b) mobility of the synthesized samples.

3.3.4. Optical studies

The electronic structure of the material is directly investigated by measuring the optical characteristics, which yields a great deal of information essential for developing thermoelectric materials [31]. The optical properties of the samples were studied to assess the influence of Ni^{2+} insertion on the band gap tuning of the doped samples. We employed the Tauc relation,

$$\alpha h\upsilon = A(h\upsilon - E_g)^{1/n} \quad \text{.....(3.5)}$$

where α is the absorption coefficient and n=2 for direct band gap semiconductor to calculate the direct band gap [32]. The value of the optical band gap is obtained by extrapolating the linear portion until they intercept the photon energy axis as shown in Fig.3.11. The value of the band gap for pristine Cu_2Se was found to be 2.29 eV is in good agreement with the literature values. The doping of Ni in Cu_2Se can cause band sharpening and the band gaps of the 0.5 wt%, 1 wt%, 1.5 wt%, and 2 wt% Ni doped Cu_2Se are 2.18, 2.10, 2.11, and 2.19 eV, respectively which is smaller than the undoped Cu_2Se. The structural modification may be responsible for the reduction in the optical band gap of Cu_2Se upon Ni doping. The sharpening of band gaps was expected to have a substantial impact on electrical transport properties thereby enhancing the thermoelectric performance of doped samples. The presence of interstitial or substitutional Ni^{2+} ions causes structural deformation in the lattice,

which increases the energy level in the Cu_2Se band gap near the valence band edge and decreases the energy associated with the direct transition [33]. The decrease in bond length as nickel doping percentage increases to 1wt%, enhancing hybridization between Cu and Se orbitals, reducing band gap, and increasing carrier concentration [34]. When Cu vacancies are introduced into the lattice through Ni doping there will be a shift of the electronic states with respect to the Fermi level. The transport properties will vary when the Fermi level is shifted from the valence band maximum into the valence band despite a similar electron configuration. The existence of additional carriers reduces electron conductivity and the Seebeck coefficient decreases due to the metallic nature of the states at the Fermi level [35].

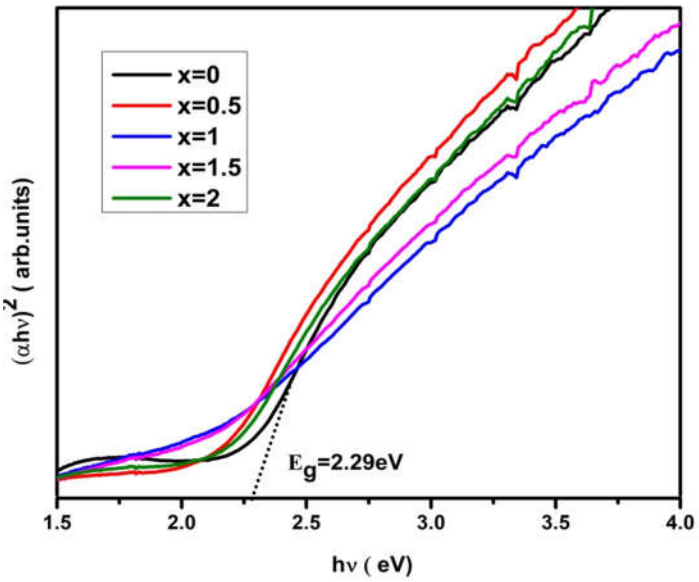

Fig.3.11 Optical band gap variation of undoped and doped samples.

The bandgap in Cu_2Se decreases continuously as the nickel concentration increases to 1.5 wt %, accompanied by a process of band shape sharpening in both the valence and conduction bands [3,10,36]. The carrier effective mass is intrinsically related to band shape and bandgap. The effective mass and Seebeck coefficient are related to the equation,

$$S=\frac{8\Pi^2 k_B^{\,2}}{3eh^2}\, m^*T\left(\frac{\Pi}{3n}\right)^{2/3} \qquad \text{.....(3.6)}$$

where m* is the effective mass of holes (electrons), μ is the mobility of the charge carriers, k_B is the Boltzmann constant, e is the electronic charge = 1.6 $\times 10^{-19}$ C, h is the Planck's constant = 6.626×10^{-34} J Hz^{-1} and T is temperature.

For degenerate semiconductors with Kane-type band dispersion, the effective mass of carriers (m*) is proportional to the band gap (E_g) through the relation [37],

$$\frac{\hbar^2 k^2}{2m^*} = E\left(1 + \frac{E}{E_g}\right) \quad \text{.....(3.7)}$$

where ħ is the reduced Planck's constant, k is the crystal momentum, and E is the energy of electron states. The band sharpening due to Ni doping can lower the carrier effective mass which exhibits high carrier mobility to maintain high carrier transport properties. Thus, a reduced carrier effective mass and a sharp band shape will result from a decreased bandgap. The temperature-dependent carrier effective mass of the samples was calculated by using equation 3.6 and shown in Fig.3.12. As the doping content of Ni increases there is a reduction in the carrier effective mass up to 1.5 wt % and increases thereafter, consistent with the band gap studies. The considerable decrease in m* from 0.927 m_0 (m_0 is the free electron mass) for the undoped sample to 0.556 m_0 for the 1.5 wt% of Ni sample at RT clearly shows that either Ni-doping has a large impact on the dispersion at the valence band top or there is a significant band nonparabolicity [36]. Such a reduction in the effective mass suggests that the band structure is affected by the doping of Ni in the Cu_2Se lattice. According to the relationship,

$$\mu \, \alpha \frac{1}{m^*} \quad \text{.....(3.8)}$$

this decreased carrier effective mass theoretically results in a high carrier mobility, which significantly benefits a high thermoelectric performance. With increasing the Ni content, the valence band of Cu_2Se gets sharper which reduces the carrier's effective mass and promotes high carrier mobility [9]. As shown in the Fig.3.10 (b) the mobility increases as the doping % increases up to 1.5 wt % and thereafter decreases. Thus, band sharpening can reduce the bandgap while concurrently lowering the carrier effective mass, allowing for increased carrier mobility which

results in high electrical conductivity. At higher doping content due to enhanced carrier-carrier and ionized impurity scattering, the high population of free carriers in strongly doped semiconductors causes a reduction in carrier mobility [38].

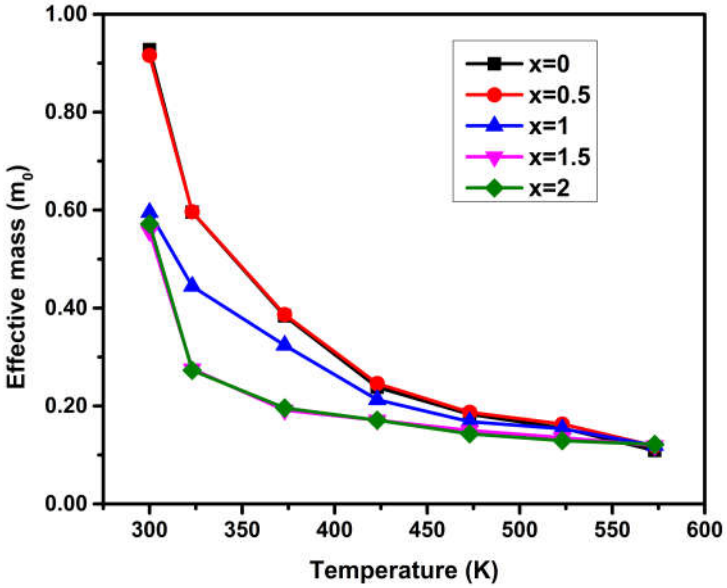

Fig.3.12 Temperature variation of carrier effective mass of samples.

3.3.5. Thermal transport measurements

Fig.3.13 (a) shows the total thermal conductivity as a function of temperature for the samples. Initially, there is an increase in the thermal conductivity of the samples as the doping % increases to 1 wt% which is due to the simultaneous increase in both carrier concentration and mobility. An enhancement in the electrical conductivity at these doping concentrations, results in an increment in the total thermal conductivity of the samples. While at 1.5 wt% Ni, a reduction in the carrier concentration causes a decrease in electrical conductivity, which in turn causes a decrease in the samples' thermal conductivity. Raman studies also reveal that the phonon relaxation time (τ) increases with increasing Ni content, indicating reduced phonon scattering. However, at 2 wt% Ni, τ decreases, suggesting enhanced phonon scattering, which likely contributes to a reduction in thermal conductivity. A very low thermal conductivity of 0.49 W/mK at 573 K is obtained for the sample doped at 2 wt% of Ni. From the PXRD and Raman studies, we found that when the doping percentage exceeds 1 wt% Ni^{2+} will occupy the substitutional sites, hence carrier concentration

of holes reduces. So, the reduction of electrical conductivity favours the enhancement of the Seebeck coefficient which concurrently reduces the thermal conductivity.

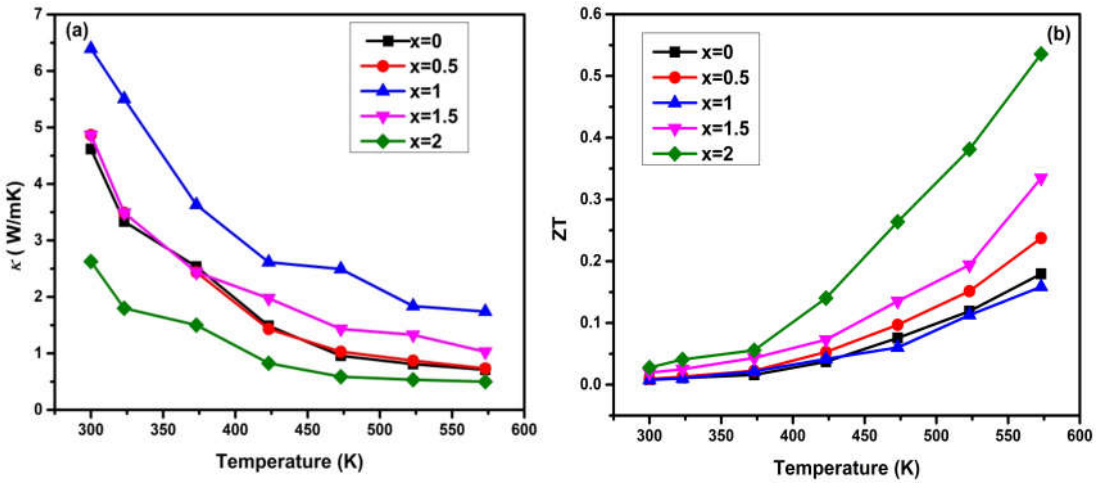

Fig.3.13 Temperature dependence of (a) total thermal conductivity and (b) Figure of merit (ZT) of the samples.

The temperature dependent figure of merit (ZT) was calculated using the measured thermoelectric parameters as shown in Fig.3.13 (b). The ZT values show an increasing trend with temperature which is undeniably due to the tremendous improvement in its electrical transport properties due to Ni doping. The maximum ZT value of 0.535 is obtained at 573 K for the sample doped at 2 wt% of Ni, which is almost 3 times higher than that of pristine Cu_2Se which is due to the optimized electronic and thermal transport parameters. ZT obtained in this study is compared with the literature. Chalermpol Rudradawong et al reported a maximum figure of merit of 0.47 at 523 K for Cu_2Se samples through Sb doping [39]. $Cu_2Se_{0.75}Te_{0.25}$ synthesized through mechanical alloying and solid-state reaction method shows a ZT value of ~ 0.55 at 573 K [40]. A ZT value of 0.25 at 473 K is reported by Adam et al for Ag-doped Cu_2Se [41]. However, we synthesized the sample using the hydrothermal method, and sintering was processed using the conventional cold pressing technique, obtained values are comparable to Cu_2Se samples synthesized through spark plasma sintering or hot press method. This study shows that optimizing the carrier concentration and carrier mobility simultaneously through band modification is an effective method to augment the thermoelectric properties of Cu_2Se.

3.4. Conclusion

In this study, the strategy of Ni doping was employed to improve the thermoelectric performance of Cu_2Se. The hydrothermal route is utilized for the synthesis of Cu_2Se and the effect of nickel doping on the structural, morphological, optical, electrical, and thermoelectric properties were discussed. Benefiting from the doping advantages, such as better electrical conductivity and low thermal conductivity, Cu_2Se exhibits dramatically enhanced thermoelectric performance in comparison to pristine sample. The PXRD and micro-Raman studies confirm the phase purity with the presence of Ni in the lattice of Cu_2Se. FESEM micrographs shows that the dopant has a significant influence on the agglomeration of particles and EDS spectra confirm the presence of Ni in the Cu_2Se lattice. The presence of Ni in the interstitial and substitutional sites of Cu_2Se augments the electrical and thermal transport properties. The inclusion of Ni^{2+} in the interstitial sites of Cu_2Se results in a simultaneous improvement in carrier concentration and mobility. Here the nickel doping causes band sharpening which lower the carrier effective mass and a high mobility of ~ 600 cm^2/Vs is achieved for the sample doped at 1.5 wt% Ni at 573 K. Tuning the mobility and carrier concentration through doping helps to achieve a maximum power factor of 614 $\mu W/mK^2$ at 573K for the Cu_2Se sample doped at 1.5 wt% Ni. These synergistic effects enable the 2 wt% Ni added sample to reach a peak ZT of 0.535 at 573 K through the conventional sintering method. Our results show that Ni doping may successfully modify Cu_2Se's thermoelectric characteristics and enhance its power generation as well as sensor performance, widening the possibilities for technological applications in the medium-temperature range.

References

[1] C. Soumya, P.P. Pradyumnan, Enhancement of thermoelectric properties of transition metals, nickel and copper dually doped ZnO, Mater. Today Commun. 35 (2023) 106197. https://doi.org/10.1016/j.mtcomm.2023.106197.

[2] A. Paulson, N.A. Muhammed Sabeer, P.P. Pradyumnan, Enhancement of optical and thermoelectric properties in dysprosium doped ZnO thin films as an impact of non-parabolic band structure, Mater. Sci. Eng. B Solid-State Mater. Adv. Technol. 262 (2020) 114745. https://doi.org/10.1016/j.mseb.2020.114745.

[3] Y. Xiao, L. Xu, T. Hong, H. Shi, S. Wang, X. Gao, X. Ding, J. Sun, L.D. Zhao, Ultrahigh carrier mobility contributes to remarkably enhanced thermoelectric performance in n-type PbSe, Energy Environ. Sci. 15 (2022) 346–355. https://doi.org/10.1039/d1ee03339e.

[4] Y.L. Pei, H. Wu, D. Wu, F. Zheng, J. He, High thermoelectric performance realized in a BiCuSeO system by improving carrier mobility through 3D modulation doping, J. Am. Chem. Soc. 136 (2014) 13902–13908. https://doi.org/10.1021/ja507945h.

[5] X. Zhang, Y. Pei, Manipulation of charge transport in thermoelectrics, Npj Quantum Mater. 2 (2017) 1–5. https://doi.org/10.1038/s41535-017-0071-2.

[6] J. Yang, L. Xi, W. Qiu, L. Wu, X. Shi, L. Chen, J. Yang, W. Zhang, C. Uher, D.J. Singh, On the tuning of electrical and thermal transport in thermoelectrics: An integrated theory-experiment perspective, Npj Comput. Mater. 2 (2016) 15015. https://doi.org/10.1038/npjcompumats.2015.15.

[7] S. Wei, B. Wang, Z. Zhang, W. Li, L. Yu, S. Wei, Z. Ji, W. Song, S. Zheng, Achieving high thermoelectric performance through carrier concentration optimization and energy filtering in Cu_3SbSe_4-based materials, J. Mater. 8 (2022) 929–936. https://doi.org/10.1016/j.jmat.2022.04.007.

[8] S.K. Kihoi, J.N. Kahiu, H. Kim, U.S. Shenoy, D.K. Bhat, S. Yi, H.S. Lee, Optimized Mn and Bi co-doping in SnTe based thermoelectric material: A case of band engineering and density of states tuning, J. Mater. Sci. Technol. 85 (2021) 76–86. https://doi.org/10.1016/j.jmst.2020.12.063.

[9] Z. Hou, Y. Xiao, L.D. Zhao, Investigation on carrier mobility when comparing nanostructures and bands manipulation, Nanoscale. 12 (2020) 12741–12747. https://doi.org/10.1039/d0nr02649b.

[10] Q. Yang, T. Lyu, Y. Dong, B. Nan, J. Tie, X. Zhou, B. Zhang, G. Xu, Anion exchanged Cl doping achieving band sharpening and low lattice thermal conductivity for improving thermoelectric performance in SnTe, Inorg. Chem. Front. 8 (2021) 4666–4675. https://doi.org/10.1039/d1qi00727k.

[11] X. Zhang, Y. Zhou, Y. Pei, Y. Chen, B. Yuan, S. Zhang, Y. Deng, S. Gong, J. He, L.D. Zhao, Enhancing thermoelectric performance of SnTe via nanostructuring particle size, J. Alloys Compd. 709 (2017) 575–580. https://doi.org/10.1016/j.jallcom.2017.02.283.

[12] N. Moloto, M.J. Moloto, M. Kalenga, S. Govindraju, M. Airo, Synthesis and characterization of MnS and MnSe nanoparticles: Morphology, optical and magnetic properties, Opt. Mater. (Amst). 36 (2013) 31–35. https://doi.org/10.1016/j.optmat.2013.06.023.

[13] B. Pejjai, V.R. Minnam Reddy, K. Seku, M.R. Pallavolu, C. Park, Eco-friendly synthesis of SnSe nanoparticles: Effect of reducing agents on the reactivity of a Se-precursor and phase formation of SnSe NPs, New J. Chem. 42 (2018) 4843–4853. https://doi.org/10.1039/c7nj04547f.

[14] N. Moloto, M.J. Moloto, N.J. Coville, S. Sinha Ray, Optical and structural characterization of nickel selenide nanoparticles synthesized by simple methods, J. Cryst. Growth. 311 (2009) 3924–3932. https://doi.org/10.1016/j.jcrysgro.2009.06.006.

[15] A. Paulson, N.A.M. Sabeer, P.P. Pradyumnan, A synergetic approach of band gap engineering and reduced lattice thermal conductivity for the enhanced thermoelectric property in Dy ion doped ZnO, J. Alloys Compd. 786 (2019) 581–587. https://doi.org/10.1016/j.jallcom.2019.01.336.

[16] N.R. Panda, B.S. Acharya, Impurity induced crystallinity and optical emissions in ZnO nanorod arrays, Mater. Res. Express. 2 (2015) 15011. https://doi.org/10.1088/2053-1591/2/1/015011.

[17] P. Peng, Z.N. Gong, F.S. Liu, M.J. Huang, W.Q. Ao, Y. Li, J.Q. Li, Structure and thermoelectric performance of β-Cu_2Se doped with Fe, Ni, Mn, In, Zn or Sm, Intermetallics. 75 (2016) 72–78. https://doi.org/10.1016/j.intermet.2016.05.012.

[18] R. Karmakar, S.K. Neogi, A. Banerjee, S. Bandyopadhyay, Structural; Morphological; optical and magnetic properties of Mn doped ferromagnetic ZnO thin film, Appl. Surf. Sci. 263 (2012) 671–677. https://doi.org/10.1016/j.apsusc.2012.09.133.

[19] B. Feng, W. Mao, The mechanism of the effect of V doping on the thermoelectric properties of ZnO ceramics, J. Solid State Chem. 305 (2022) 122645. https://doi.org/10.1016/j.jssc.2021.122645.

[20] F. Lin, G.Q. Bian, Z.X. Lei, Z.J. Lu, J. Dai, Solvothermal growth and morphology study of Cu_2Se films, Solid State Sci. 11 (2009) 972–975. https://doi.org/10.1016/j.solidstatesciences.2009.02.017.

[21] B. Minceva-Sukarova, M. Najdoski, I. Grozdanov, C.J. Chunnilall, Raman spectra of thin solid films of some metal sulfides, J. Mol. Struct. 410–411 (1997) 267–270. https://doi.org/10.1016/S0022-2860(96)09713-X.

[22] X. Han, F. Liao, Y. Zhang, Z. Yuan, H. Chen, C. Xu, CTAB-assisted hydrothermal synthesis of Cu_2Se films composed of nanowire networks, Mater. Lett. 210 (2018) 62–65. https://doi.org/10.1016/j.matlet.2017.08.124.

[23] N.S. Babu, M. Abdul Khadar, Deposition of nanocrystal thin films of Cu2Se and their optical and electrical characterization, Appl. Surf. Sci. 474 (2019) 34–41. https://doi.org/10.1016/j.apsusc.2018.06.158.

[24] L. Ren, H. Zhang, P. Tan, Y. Chen, Z. Zhang, Y. Chang, J. Xu, F. Yang, D. Yu, Hexagonal Selenium Nanowires Synthesized via Vapor-Phase Growth, J. Phys. Chem. B. 108 (2004) 4627–4630. https://doi.org/10.1021/jp036215n.

[25] N. Wongcharoen, T. Gaewdang, Thermoelectric properties of Ni-doped CuAlO2, Phys. Procedia. 2 (2009) 101–106. https://doi.org/10.1016/j.phpro.2009.06.016.

[26] Q. Song, P. Qiu, H. Chen, K. Zhao, M. Guan, Y. Zhou, T.R. Wei, D. Ren, L. Xi, J. Yang, Z. Chen, X. Shi, L. Chen, Enhanced carrier mobility and thermoelectric performance in $Cu_2FeSnSe_4$ diamond-like compound via manipulating the intrinsic lattice defects, Mater. Today Phys. 7 (2018) 45–53. https://doi.org/10.1016/j.mtphys.2018.10.005.

[27] Z. Wei, Z. Li, P. Luo, J. Zhang, J. Luo, Simultaneously increased carrier concentration and mobility in p-type $Bi_{0.5}Sb_{1.5}Te_3$ throng Cd doping, J. Alloys Compd. 830 (2020) 154625. https://doi.org/10.1016/j.jallcom.2020.154625.

[28] J.S. Galsin, Physical Effects of Impurities in Metals, Impurity Scatt. Met. Alloy. (2002) 93–123. https://doi.org/10.1007/978-1-4615-1241-7_5.

[29] Novel carrier doping in p-type semiconductors enhances photovoltaic device performance by increasing hole concentration. ScienceDaily. Retrieved June 27, 2023, from www.sciencedaily.com/releases/2022/09/220919103157.htm

[30] J.D. Musah, X. Yanjun, A.M. Ilyas, T.G. Novak, S. Jeon, C. Arava, S. V. Novikov, D.S. Nikulin, W. Xu, L. Liu, A. Md, K.H. Lam, X. Chen, C.M.L. Wu, V.A.L. Roy, Simultaneous Enhancement of Thermopower and Electrical Conductivity through Isovalent Substitution of Cerium in Bismuth Selenide Thermoelectric Materials, ACS Appl. Mater. Interfaces. 11 (2019) 44026–44035. https://doi.org/10.1021/acsami.9b11344.

[31] Z.M. Gibbs, A. Lalonde, G.J. Snyder, Optical band gap and the Burstein-Moss effect in iodine doped PbTe using diffuse reflectance infrared Fourier transform spectroscopy, New J. Phys. 15 (2013) 075020. https://doi.org/10.1088/1367263-0/15/7/07-5020.

[32] T. Parvathy, N.A. Muhammed Sabeer, N. Mohan, P.P. Pradyumnan, Effect of dopant gas pressure on the growth of magnetron sputtered CuO thin films for electrical and optical applications, Opt. Mater. (Amst). 125 (2022) 112031. https://doi.org/10.1016/j.optmat.2022.112031.

[33] R.K. Gupta, F. Yakuphanoglu, F.M. Amanullah, Band gap engineering of nanostructure Cu doped CdO films, Phys. E Low-Dimensional Syst. Nanostructures. 43 (2011) 1666–1668. https://doi.org/10.1016/j.physe.2011.05.019.

[34] B. Feng, G. Li, Y. Hou, C. Zhang, C. Jiang, J. Hu, Q. Xiang, Y. Li, Z. He, X. Fan, Enhanced thermoelectric properties of Sb-doped BiCuSeO due to decreased band gap, J. Alloys Compd. 712 (2017) 386–393. https://doi.org/10.1016/j.jallcom.2017.04.121.

[35] B. Hamawandi, S. Ballikaya, M. Råsander, J. Halim, L. Vinciguerra, J. Rosen, M. Johnsson, M. Toprak, Composition tuning of nanostructured binary copper selenides through rapid chemical synthesis and their thermoelectric property evaluation, Nanomaterials. 10 (2020) 854. https://doi.org/10.3390/nano10050854.

[36] Z. Long, Y. Wang, X. Sun, Y. Li, Z. Zeng, L. Zhang, H. Chen, Band engineering of the second phase to reach high thermoelectric performance in Cu_2Se-based composite material. Adv Mater. 35 (2023) 2210345. https://doi:-10.1002/adma.202210345.

[37] G. Tan, X. Zhang, S. Hao, H. Chi, T.P. Bailey, X. Su, Enhanced density-of-states effective mass and strained endotaxial nanostructures in Sb-Doped $Pb_{0.97}Cd_{0.03}Te$ thermoelectric alloys, ACS Appl Mater Interfaces 11 (2019) 9197-9204. https://doi: 10.1021/acsami.8b21524.

[38] G.K. Ren, S.Y. Wang, Y.C. Zhu, K.J. Ventura, X. Tan, W. Xu, Y.H. Lin, J. Yang, C.W. Nan, Enhancing thermoelectric performance in hierarchically structured BiCuSeO by increasing bond covalency and weakening carrier-phonon coupling, Energy Environ. Sci. 10 (2017) 1590–1599. https://doi.org/10.1039/c7ee00464h.

[39] C. Rudradawong, S. Khammuang, K. Kotmool, T. Bovornratanaraks, P. Limsuwan, N. Somdock, R. Sakdanuphab, A. Sakulkalavek, Enhanced thermoelectric properties of Cu_2Se via Sb doping: An experimental and computational study, J. Eur. Ceram. Soc. 43 (2023) 401–406. https://doi.org/10.1016/j.jeurceramsoc.2022.09.021.

[40] T.K. Mac, T.T. Ta, H.T. Nguyen, V. Du Nguyen, T.L.H. Pham, V.T. Duong, T.D. Thanh, B.T. Phan, A.T. Duong, Influence of structure phase transition on the thermoelectric properties of $Cu_2Se_{1-x}Te_x$ liquid-like compounds, RSC Adv. 12 (2022) 26383–26389. https://doi.org/10.1039/d2ra04268a.

[41] A M Adam, Transport and thermoelectric properties of crystalline $Cu_{2-x}Ag_xSe$ alloys prepared by facile method, Phys. Scr.98 (2023) 0-8. https://doi.org/10.10-88/1402-4896/acbcfb.

Chapter-4

Synergistic effect in the thermoelectric properties of Ni and Zn dual doped Cu_2Se

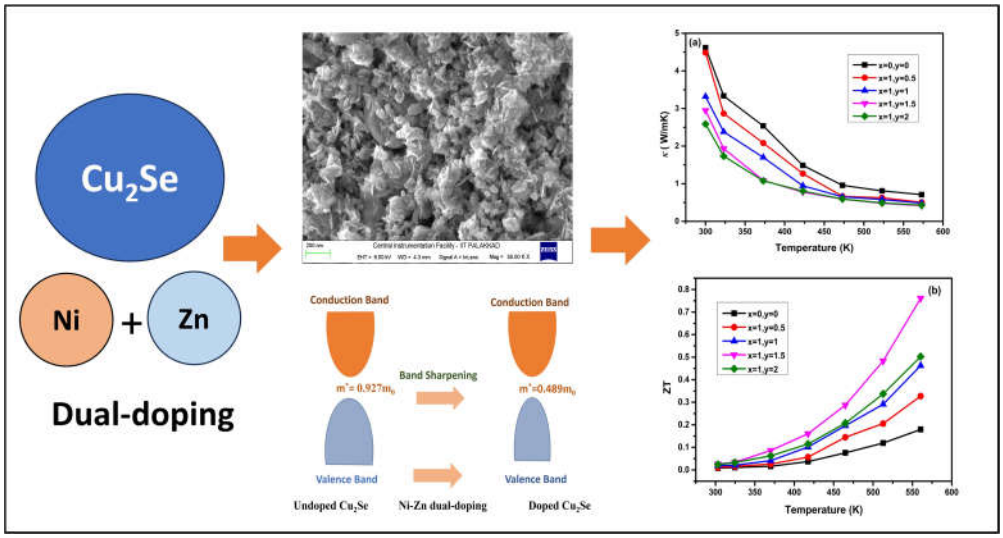

This chapter presents a novel method for enhancing the thermoelectric properties of Cu_2Se by concurrently optimizing the electronic and thermal transport properties through Ni and Zn co-doping strategy, which has not been explored previously. Integrating both Ni and Zn into the lattice of Cu_2Se affects the electrical and thermal properties by enhancing carrier mobility and increasing phonon scattering due to lattice defects. This dual doping strategy notably reduced thermal conductivity, owing to enhanced point-defect scattering and lattice anharmonicity.

4.1. Introduction

In our previous chapter, we investigated the modification of electronic band structures to enhance the carrier transport in Cu_2Se through doping technique. By doping Cu_2Se with Ni, we aimed to optimize the balance between carrier mobility and effective mass, leading to an improvement in the thermoelectric properties. This approach resulted in a notable achievement of a ZT value of 0.535 at 573 K. Further improvement in thermoelectric performance can be attained by employing the dual doping strategy. Dual doping involves the simultaneous incorporation of two different dopant elements into the crystal lattice, offering the potential for synergistic effects that could enhance the thermoelectric performance. This helps in reducing thermal conductivity by introducing defects and perturbations in the crystal lattice, which act as scattering centres for phonons and induce lattice anharmonicity, thereby impeding phonon transport. Effective phonon scattering is particularly crucial for achieving low thermal conductivity. Improving phonon scattering at grain boundaries through nanostructuring and utilizing point defect scattering via extrinsic doping are effective methods for enhancing phonon scattering by inducing lattice anharmonicity [1,2]. The introduction of nanostructures and suitable dopants enhances phonon scattering, leading to modifications in thermal transport properties and potential improvements in thermoelectric performance. These scattering mechanisms result in a decrease in the total phonon relaxation time (τ_{tot}) at a characteristic frequency ω, thereby lowering the thermal conductivity [3].

To date, various research groups have employed different techniques to achieve the highest power factor in Cu_2Se. However, the approach of dual doping in Cu_2Se remains unexplored to the best of our knowledge. Inspired by the findings from recent literature on thermoelectric materials, we adopted a co-doping approach to enhance the thermoelectric performance of Cu_2Se [4-7]. This co-doping approach aims to optimize the material's electronic structure, carrier concentration, and thermal conductivity, thereby improving its power factor and overall thermoelectric efficiency. In this study, we introduced Ni and Zn, simultaneously into the lattice of Cu_2Se using a hydrothermal route which synergistically manipulates the electrical

and thermal behaviour by enhancing carrier mobility and scattering phonons through lattice defects. Here the impact of dual Ni and Zn doping on the structural, morphological, optical, electrical, and thermoelectric properties of Cu_2Se is examined. The Ni concentration was optimized and fixed at 1 wt% based on prior studies and the Zn concentration was varied. It was observed that at this Ni concentration, co-doping effectively enhanced electrical conductivity without significantly compromising the Seebeck coefficient. The incorporation of Ni and Zn point defects reduces the thermal conductivity and increases electrical conductivity in Cu_2Se, ultimately resulting in an enhanced ZT value.

4.2. Experiment details

The pristine Cu_2Se and Ni and Zn dual doped Cu_2Se samples were prepared by hydrothermal method. The experimental techniques for synthesis and characterization utilized in this study are based on methodologies established in chapter 2. High-quality reagents were employed in the synthesis of Cu_2Se nanoparticles. Copper chloride dihydrate ($CuCl_2.2H_2O$), nickel chloride hexahydrate ($NiCl_2.6H_2O$), zinc chloride ($ZnCl_2$), selenium metal powder, sodium hydroxide (NaOH), and sodium borohydride ($NaBH_4$) from sigma aldrich were used. The synthesis involved dissolving $CuCl_2.2H_2O$ in deionized water, adjusting the pH with NaOH, and using Se powder with $NaBH_4$ as a reducing agent. Following thorough mixing with a magnetic stirrer at 50°C for 1 hour, the solution was transferred to an autoclave, where it was held at 150°C for 24 hours. After the solution was heated, it was left to cool to RT. The resulting precipitate was gathered and subjected to centrifugation for separation. Following this, the precipitate underwent multiple washes with deionized water and ethanol to remove impurities. For dual doping, Ni concentration was maintained at a fixed weight percentage of 1 wt%, while the wt% of Zn was systematically varied at 0.5 wt%, 1 wt %, 1.5 wt%, and 2 wt% respectively (x=1, y=0.5, 1, 1.5 and 2). The powder was compacted into a circular pellet measuring 13mm in diameter and 3mm in thickness using a hydraulic pelletizer under a force of approximately 10 tons in ambient air. These densified pellets were subsequently sintered at 300°C for 3 hours before being utilized for characterization.

4.3. Results and discussion

4.3.1. Phase and structure analysis

The structural characteristics, including purity, crystallinity, and the orientation of phases in the compounds, were assessed through powder X-ray diffraction (PXRD) measurements. These measurements were conducted in the 20°–80° range at a rate of 2°/min, and X-ray CuK_{α} (1.5408 Å) radiation. The Fig.4.1 shows prominent XRD peaks for pristine Cu_2Se at 26.79°, 30.98°, 44.44°, 52.63°, 64.70°, and 71.23° corresponding to the (111), (200), (220), (311), (400), and (331) cubic planes of the Cu_2Se phase (ICDD-03-065-2982) respectively. The XRD spectra indicate the absence of additional peaks corresponding to nickel, zinc, or any associated secondary or impurity phases. This absence suggests that any incorporation of $Ni^{2+}$and Zn^{2+} likely occurs within the lattice sites of Cu_2Se, indicating that the dopants have been effectively integrated into these sites.

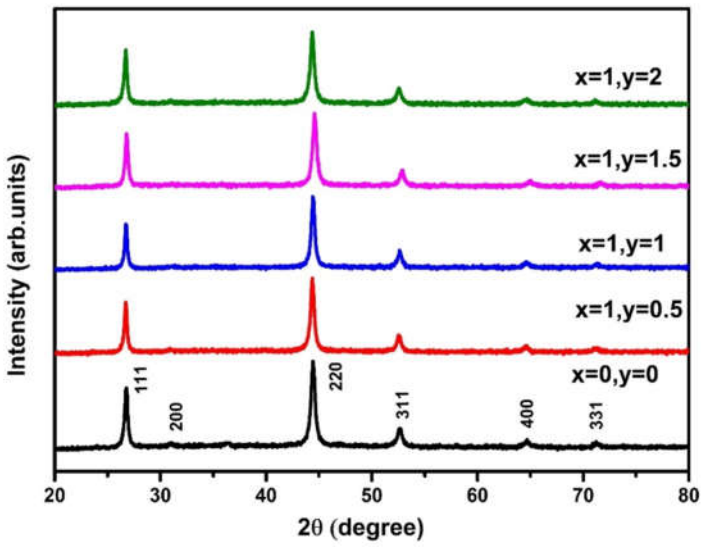

Fig.4.1 PXRD pattern of pristine and Ni and Zn dual doped Cu_2Se.

Typically, introducing impurities through doping can indeed create additional defects such as interstitials and vacancies within the lattice structure [8]. In general, factors such as the concentration of foreign atoms, external strain, differences in ionic radii compared to the substituted matrix ion, and the presence of defects in the system significantly alter the lattice parameters [9]. All the structural parameters

were computed using the formula outlined in the chapter 3. Microstrain was calculated and shown in the Fig.4.3. It is found that strain increases with increasing dual doping content. Introducing both nickel and zinc, with ionic radii of 0.55 Å for Ni^{2+} and 0.60 Å for Zn^{2+}, into the Cu_2Se lattice (where Cu^{+} has a radius of 0.60 Å) could potentially induce defects that influence the lattice's crystalline structure [10-13]. Fig.4.2 illustrates the shift in the lattice due to increasing doping content. As the Zn concentration increases, the XRD peak gradually shifts towards higher angle side up to a doping level of 1.5 wt%, indicating an increase in lattice strain. This shift suggests that the incorporation of Zn^{2+} ions initially compress the lattice. However, at higher Zn concentrations beyond 1.5 wt%, the peak shifts toward a lower angle, which may be attributed to significant Zn^{2+} substitution within the host lattice. This substitution likely causes lattice expansion despite the increased strain [14]. The observed trend shows a balance between strain causing the lattice to compress and Zn^{2+} substitution causing expansion, which affects the material's structure at different dual doping levels.

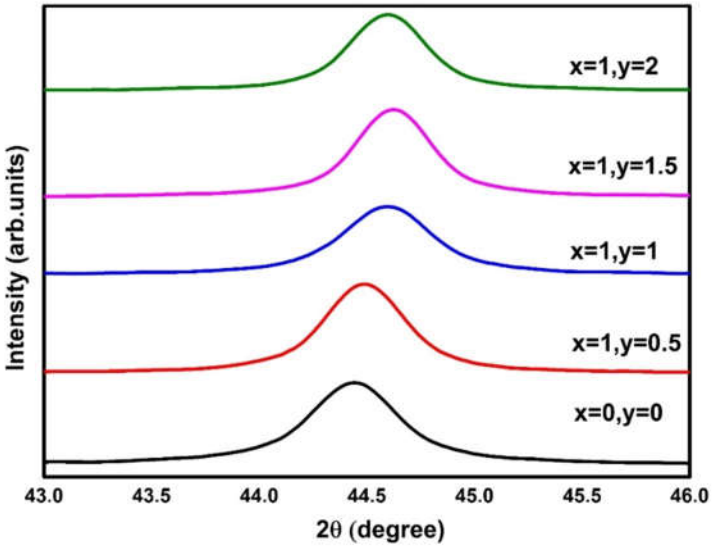

Fig.4.2 Shift observed in the 220-reflection peak with increasing doping concentration.

The average crystallite sizes for all the dual doped samples were determined using the well-established Scherrer formula [15]. As the concentration of dual doping increases, FWHM increases, indicating a reduction in the crystallite size. The crystallite size decrease as the doping content increases which indicates that the

grain growth is inhibited due to the presence of dopant ions. Reducing the crystallite size to the nano level leads to alterations in lattice dimensions, subsequently impacting the chemical and physical properties of the materials [16]. The estimated dislocation density (δ), in the order of magnitude of 10^{15} m^{-2}, is shown in the table 4.1 and is found to increase with rising doping content suggesting a reduction in the thermal conductivity with doping [17]. To assess the impact of defects and dislocations on thermal transport properties, further measurements of thermal conductivity have been done.

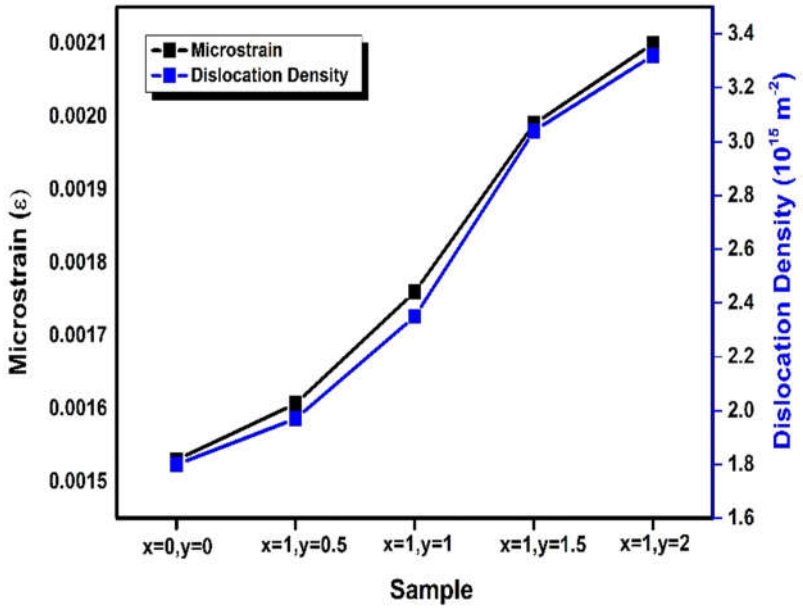

Fig.4.3 Variation of microstrain and dislocation density with increasing doping content.

Table 4.1: Variation of crystallite size, microstrain, dislocation density of pristine and Ni and Zn dual doped Cu_2Se.

Sample	Crystallite size (nm)	Microstrain	Dislocation density (10^{15} m^{-2})
x=0, y=0	23.57	0.00153	1.80
x=1, y=0.5	22.54	0.00161	1.97
x=1, y=1	20.62	0.00176	2.35
x=1, y=1.5	18.13	0.00199	3.04
x=1, y=2	17.33	0.00210	3.32

Raman spectroscopy proves invaluable for comprehending the molecular vibrations within a crystal lattice and their correlations with structural parameters, quantization effects, lattice contractions and expansions etc [18]. This is achieved through the observation of broadening and shifts in the peak positions of Raman bands [19]. The presence and phase of pristine and dual doped Cu_2Se were confirmed by typical vibrational peaks observed at 257 cm^{-1} in Fig.4.4 consistent with findings reported in the literature [1]. The single dominant peak centered at 257 cm^{-1}, corresponding to the 1LO phonon frequency associated with Cu-Se stretching vibration in the lattice. No Raman bands indicative of impurities was detected in the samples, indicating the high purity of the prepared samples. A minor upward shift of the Raman modes towards higher frequencies was observed in the samples as the doping percentage of Zn increased to 1.5 wt%, followed by a subsequent shift towards lower frequencies. Introducing dual doping of Ni and Zn into the Cu_2Se lattice, a notable peak broadening of 1LO modes occurs. The broadening of Raman peaks provides clear evidence of phonon dispersion broadening [19]. This is due to the strain induced by dual doping within the Cu_2Se matrix. Lattice strains induce variations in atomic spacing, consequently altering interaction forces. These changes ripple through the system, leading to fluctuations in phonon frequencies and broadening of phonon dispersion. This phenomenon leads to a reduction in phonon relaxation time and ultimately lowers the thermal conductivity [20].

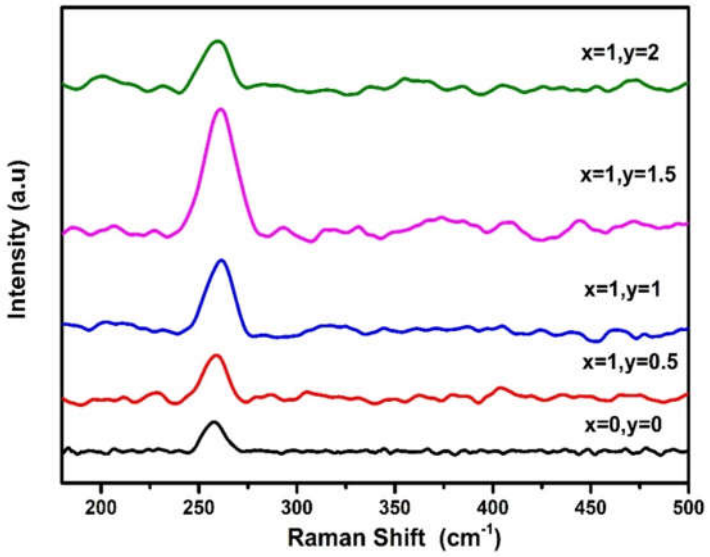

Fig.4.4 Raman spectra of pristine and Ni and Zn dual doped Cu_2Se.

The blue shift in the peaks, compared to pristine Cu_2Se, results from the compressive strain field effect induced by dual doping of Ni and Zn in the Cu_2Se lattice [21]. The observed strain (ϵ) and phonon relaxation time (τ) were determined using equations 3.3 and 3.4 from chapter 3. The Raman peak position, full width at half maximum (FWHM), along with the calculated strain (ϵ) and phonon relaxation time (τ) for the doped samples, are summarized in table 4.2.

Table 4.2: Variation of Raman frequency (ω), FWHM (Γ), strain (ϵ) and phonon relaxation time (τ).

Sample	ω (cm^{-1})	Γ(cm^{-1})	ϵ (cm^{-1})	τ (ps)
x=0, y=0	257.70	13.14	0.000	0.40
x=1, y=0.5	258.09	14.57	0.027	0.36
x=1, y=1	260.43	16.29	0.168	0.33
x=1, y=1.5	260.95	19.28	0.169	0.28
x=1, y=2	258.56	16.57	0.052	0.32

The observed variation in FWHM in the samples, primarily depends on two key contributions: (1) phonon-phonon interaction due to lattice anharmonicity (Γ_{an}) and (2) electron-phonon coupling (Γ_{EPC}) [22]. As depicted in Fig.4.8, the electrical conductivity decreases as temperature increases. This suggests that electron-phonon coupling (EPC) increases with temperature. At lower temperatures, the contribution of Γ_{EPC} to FWHM can be disregarded. The fundamental aspect of phonon scattering lies in the rate of change in its distribution function, which characterizes the strength of interaction among phonons (exchange of energy within the lattice waves) [23]. Here there is broadening in the phonon distribution function, it expedites the rate of change, resulting in a reduced relaxation time for phonons to revert to equilibrium in response to perturbations induced by dual doping of Ni and Zn in the lattice of Cu_2Se. Here as the doping % increases, shift observed in the peak signifies the emergence of deep-level defects within the material [24]. This induced lattice anharmonicity acts as a primary mechanism for scattering phonons, thereby diminishing their relaxation time (τ) as the doping percentage increases. When the relaxation time of phonons decreases, it indicates increased phonon scattering, which in turn results in diminished thermal conductivity.

4.3.2. Morphological studies

The microstructure of the samples analysed using FESEM techniques are shown in Fig.4.5. The Fig.4.5 (a-e) shows that the substitution of Ni and Zn in Cu_2Se result in significant morphological changes.

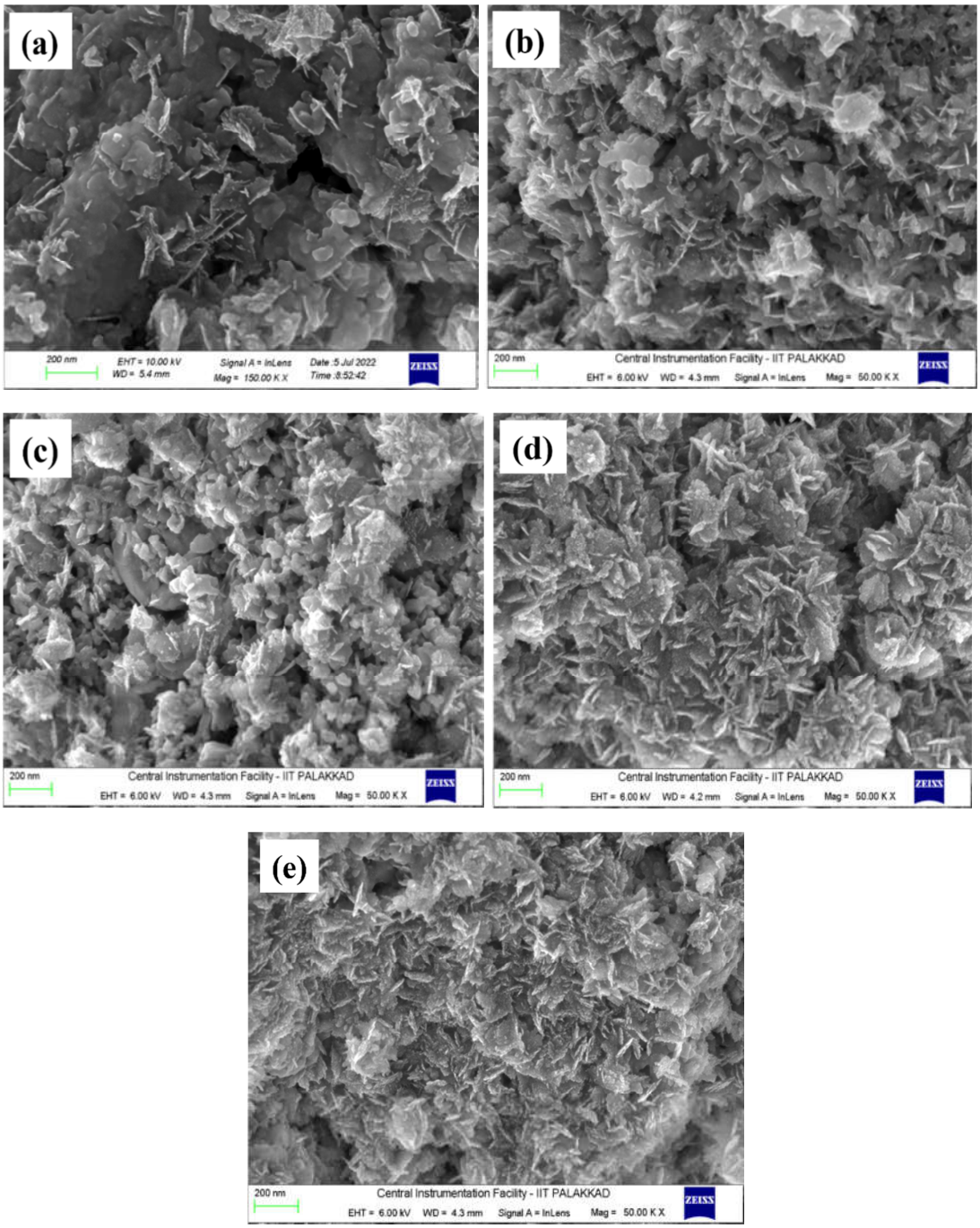

Fig.4.5 FESEM images of (a) undoped and Ni and Zn dual doped Cu_2Se with (b) x=1,y=0.5, (c) x=1,y=1, (d) x=1,y=1.5, (e) x=1,y=2.

The morphology of pristine Cu_2Se features a surface composed of irregular, nanoflake-like, less dense particles. As the dual doping content increases, the shape of the particles becomes more uniform, transitioning from a mix of granular and flaky to predominantly flaky. Additionally, aggregation increases with doping concentration, resulting in a more densely packed structure. The morphological changes due to increased doping content, lead to the formation of additional scattering centers and interfaces. These defects can act as scattering centres for phonons, increasing phonon scattering rates and thereby reducing the phonon relaxation time.

The composition of the synthesized samples was determined using the EDS analytical technique, as shown in Fig.4.6. The EDS analysis confirms the presence of Cu, Se, Ni, and Zn without any other elements in the synthesized samples. Additionally, the spectrum shows no impurity elements, verifying the successful incorporation of Ni and Zn into the Cu_2Se lattice. EDS mapping in Fig.4.7 (a-d) illustrates the distribution of Cu, Se, Ni, and Zn, respectively. These maps were obtained from the SEM image of sample doped with 1 wt% Ni and 1.5 wt% Zn (x=1,y=1.5). The maps clearly depict the distribution and concentration of the dopant elements, thereby confirming their successful incorporation into the sample matrix.

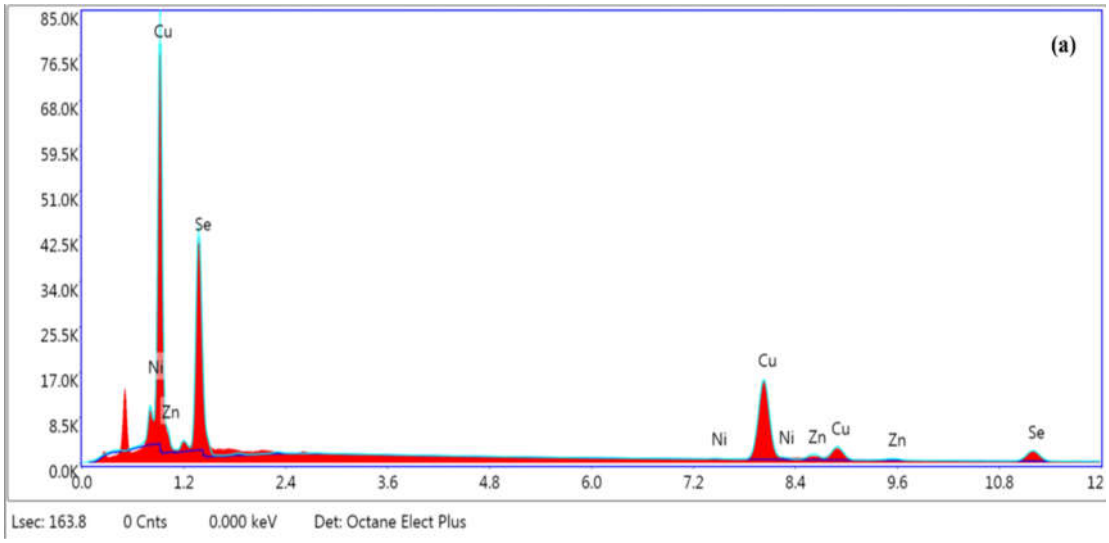

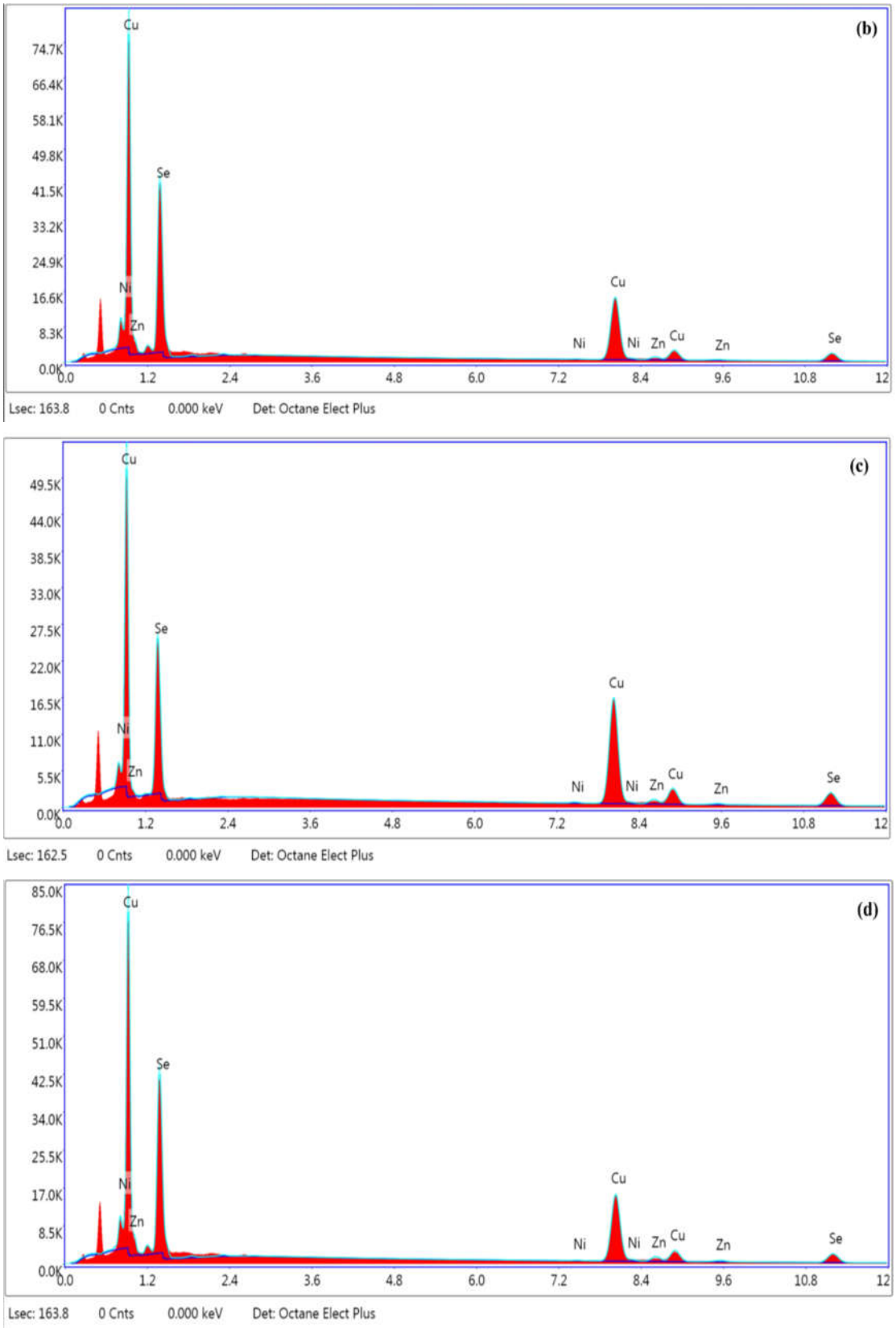

Fig.4.6 EDS spectra of Ni and Zn dual doped Cu_2Se with (a) x=1,y=0.5, (b) x=1,y=1, (c) x=1,y=1.5, (d) x=1,y=2.

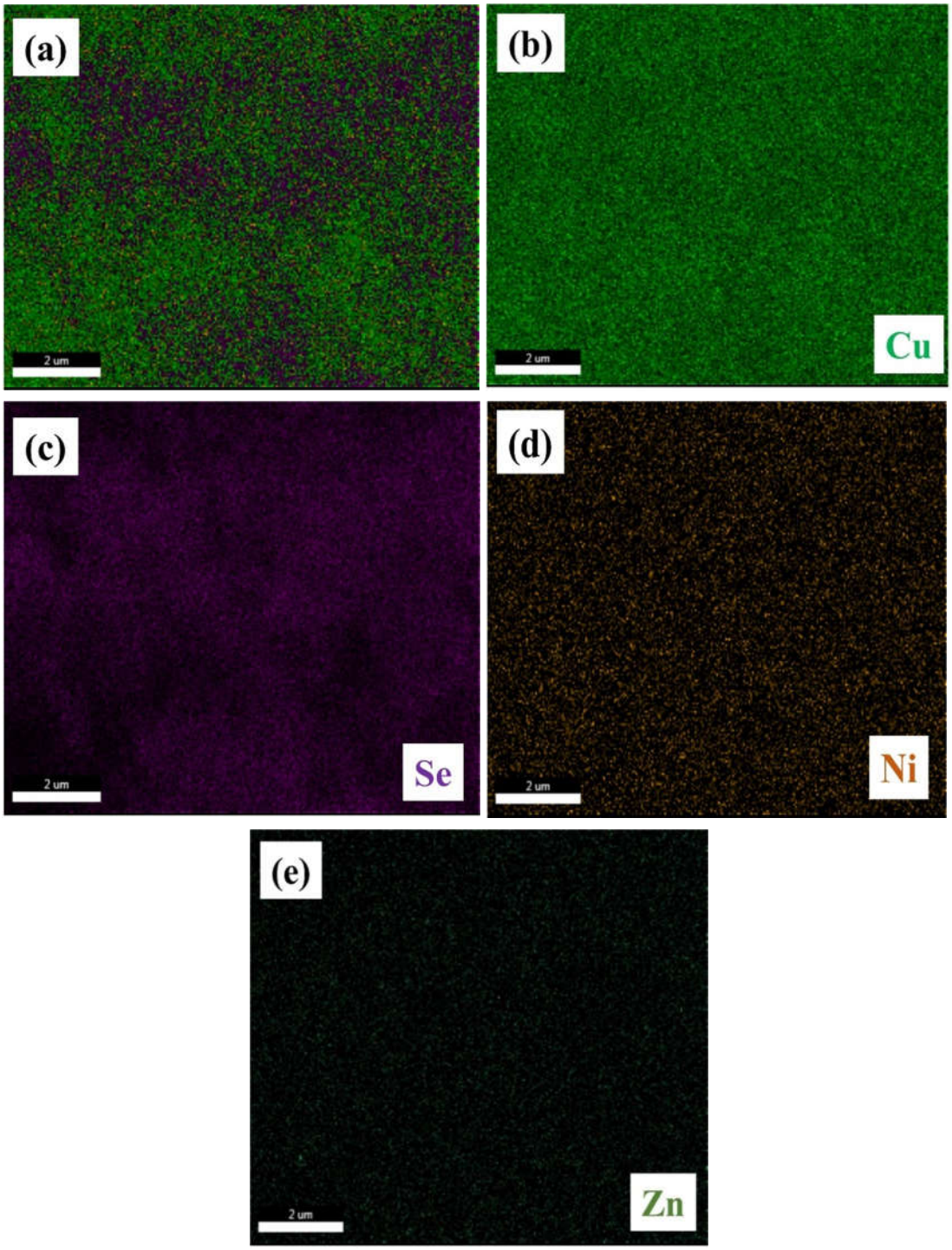

Fig.4.7 EDS elemental mapping of (a) the combined distribution of all elements, (b) Cu, (c) Se, (d) Ni and (e) Zn for the sample 1 wt% Ni and 1.5 wt% Zn (x=1,y=1.5).

4.3.3. Thermoelectric measurement studies

The thermoelectric properties of the Ni and Zn dual doped samples are depicted in the Fig.4.8 highlighting the synergistic optimization achieved through dual doping.

As depicted in Fig.4.8 (a), the electrical conductivity of all samples shows a decreasing trend with increasing temperature, indicative of a metal-like conduction behaviour, proving that all the samples are heavily doped degenerate semiconductors. All dual substituted samples exhibit greater electrical conductivity compared to pristine Cu_2Se, as shown in the Fig.4.8 (a). In our previous chapter 3, we reported that introducing Ni doping into Cu_2Se significantly enhances σ while maintaining a minimal reduction in the Seebeck coefficient [22]. We observed that doping Ni in Cu_2Se increases electrical conductivity due to its presence in the interstitial sites. This increases p-type conductivity due to interactions between Cu^+ and Ni^{2+} ions in their 3d orbitals. Ni^{2+} occupies interstitial spaces in the Cu_2Se lattice, causing electrical coulomb repulsion between Ni and neighbouring Cu ions. This contact induces strain in the lattice, which reorganizes conduction electrons around the Ni impurity. The valence orbitals (3d) of Ni^{2+} and Cu^+ ions interact, resulting in d-d orbital repulsions. This repulsion displaces copper atoms from their positions, leading to the creation of numerous acceptor-type copper vacancies. In the Ni and Zn dual doping, Hall measurement studies indicate a similar influence on the lattice of Cu_2Se. Initially at lower dopant concentrations, an increase in the dopant content of Zn to 0.5 wt%, there is a corresponding rise in carrier concentration, thereby enhancing the p-type conductivity. This dopant concentration generates Cu vacancies acting as acceptors, similar to the behaviour observed in single Ni doping. However, with a further increase in Zn content from 0.5 wt% to 2 wt% while maintaining the Ni content at 1 wt%, the carrier concentration tends to decrease. This trend appears reasonable because the introduction of Zn atoms adds more electrons to the system, as evidenced by the decreasing carrier concentration depicted in Fig.4.9 (a). The reduction in the concentration of charge carriers leads to decreased carrier conductivity, yet σ increases owing to enhanced carrier mobility. In Ni doped Cu_2Se, the increase in carrier mobility is attributed to the decrease in carrier effective mass due to band sharpening [22]. The mobility of carriers correlates closely with both the effective mass and the curvature of conduction valleys [25]. Reducing the effective mass or augmenting the conduction valleys could lead to an improved mobility. The effective mass, as calculated and illustrated in the Fig.4.10, indicates that, similar to single doping, the augmentation in carrier mobility results from a reduction in the effective mass of the carriers. Moreover, the effective mass of a conduction valley primarily depends on the covalency of the

associated chemical bonds. In other words, an increase in bond covalency promotes greater overlap of adjacent electron densities and diminishes periodic potential fluctuations, resulting in more dispersed bands and consequently lowering the effective mass of carriers [26]. The significant bond ionicity, stemming from the considerable electronegativity contrast between Cu (χ_{Cu} ~1.90) and Se (χ_{Se} ~ 2.55), may result in pronounced lattice scattering of charge carriers [27]. This, coupled with the frail interlayer bonding and the distortion of the $CuSe_4$ tetrahedra, could further exacerbate the scattering effect. The diminishing trend of the effective mass (m*) with decreasing carrier concentration underscores the notable band nonparabolicity present in Cu_2Se, a phenomenon commonly observed in narrow-gap thermoelectric materials [28]. Reduced m* in dual doped samples will lessen carrier-phonon scattering, consequently boosting carrier mobility.

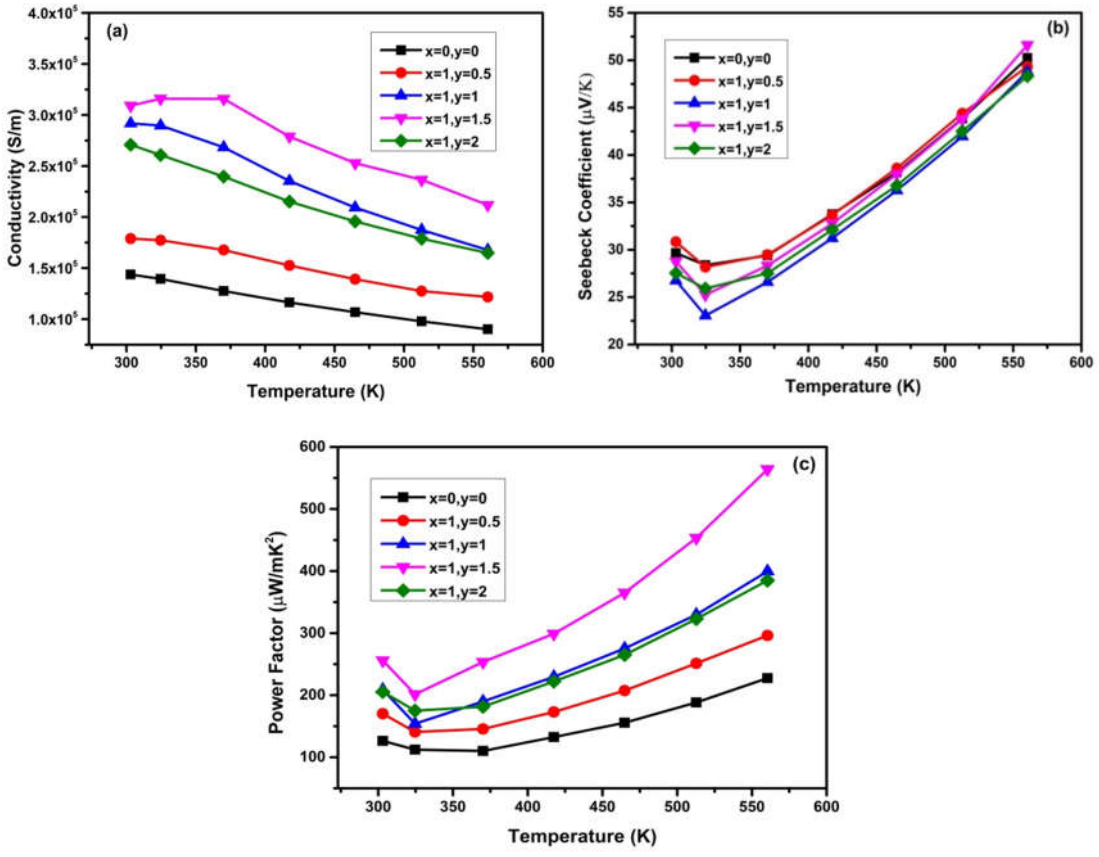

Fig.4.8 Variation of (a) electrical conductivity, (b) Seebeck coefficient and (c) power factor with temperature in pristine and Ni and Zn dual doped Cu_2Se.

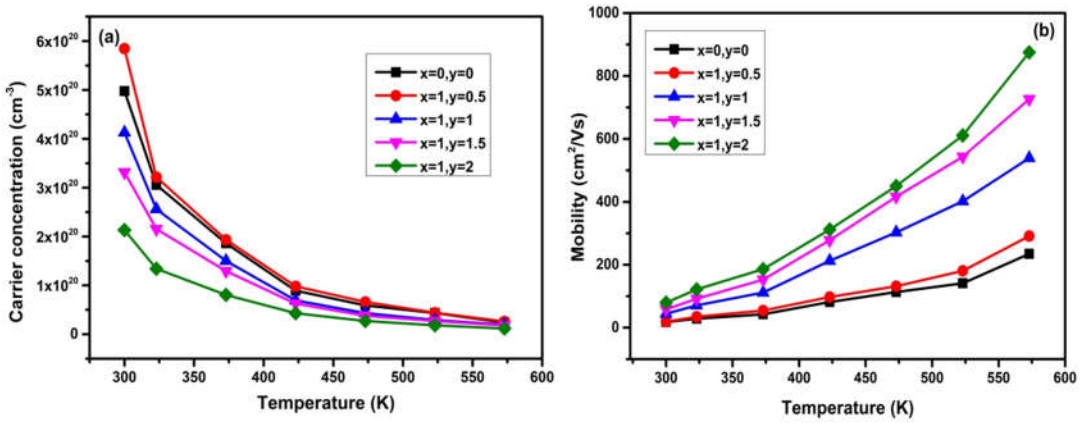

Fig.4.9 Temperature dependence of (a) carrier concentration, (b) mobility of pristine and Ni and Zn dual doped Cu_2Se.

The positive Seebeck coefficient observed in all samples depicted in the Fig.4.8 (b) indicates p-type conduction, aligning with the results obtained from Hall effect measurements. The relationship between the Seebeck coefficient (S) and the effective mass (m^*) is described by the equation

$$S=\frac{8\Pi^2 k_B{}^2}{3eh^2} m^*T \left(\frac{\Pi}{3n}\right)^{2/3} \quad \text{.....(4.1)}$$

where m* is the effective mass of holes (electrons), μ is the mobility of the charge carriers, k_B is the Boltzmann constant, e is the electronic charge = 1.6×10^{-19} C, h is the Planck's constant = 6.626×10^{-34} J Hz^{-1} and T is temperature. The temperature-dependent carrier effective mass of the samples was calculated by using equation 4.1 and shown in Fig.4.10. Equation 4.1 shows that the Seebeck coefficient varies inversely with concentration of charge carriers and directly with the effective mass of the carriers. The effective mass m^* can also be expressed as

$$m^* = N_v^{\frac{2}{3}} m_b^* \quad \text{.....(4.2)}$$

Where m_b^* is the band effective mass of a single parabolic band. Enhancing valley degeneracy and adjusting the band effective mass can lead to an improvement in the Seebeck coefficient, even with an increase in carrier concentration. This approach disrupts the typical trade-off between the Seebeck coefficient and carrier concentration, allowing for an improvement in σ with minimal reduction in the

Seebeck coefficient. Reducing the carrier concentration typically leads to an increase in the Seebeck coefficient, which often results in a decrease in electrical conductivity. Here as the doping content of Zn increases, we observe a decrease in both carrier concentration and Seebeck coefficient. However, the electrical conductivity significantly increases and the reduction in Seebeck coefficient is minimal as compared to single Ni doped samples. This increase is primarily attributed to the high mobility of the charge carriers. Enhancing carrier mobility typically leads to a higher Seebeck coefficient, particularly as the carrier concentration decreases [30]. In a conventional semiconductor, the mobility of charge carriers is influenced by various factors, including the relaxation time (τ) between scattering events, which involve interactions such as phonon-electron, ionized-impurity, and electron-electron scattering. Additionally, the carrier effective mass plays a significant role in determining mobility [31]. For a semiconductor featuring a simple parabolic band structure undergoing elastic scattering, the mobility (μ) can be expressed as follows [32],

$$\mu = \frac{e<\tau>}{m^*} \qquad (4.3)$$

The significantly decreased effective mass of the hole could serve as a primary factor contributing to the exceptionally high mobility at RT [33]. Band engineering studies have shown that the mobility can be enhanced by adjusting m*. The Fig.4.10 illustrates that m* decreases with increasing dual doping content. This leads to a substantial enhancement in hall mobility, increasing it from 234 $cm^2V^{-1}s^{-1}$ to 875 $cm^2V^{-1}s^{-1}$ at 573 K resulting in an improvement in the power factor. Consequently, through the utilization of improved electrical conductivity and Seebeck coefficient, the power factor experiences a notable increase across a wide temperature spectrum, achieving an exceptional peak power factor of approximately 564 $\mu W/mK^2$ at 573 K for Cu_2Se dual doped with 1 wt% Ni and 1.5 wt% Zn.

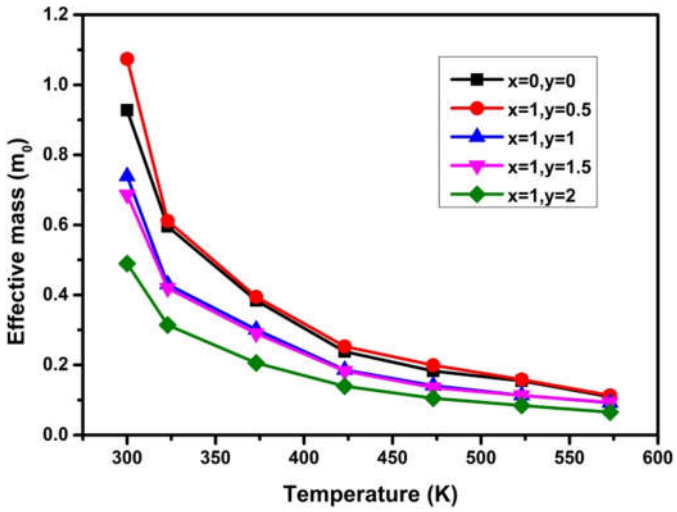

Fig.4.10 Temperature dependence of carrier effective mass of pristine and Ni and Zn dual doped Cu_2Se.

4.3.4. Optical studies

A decrease in the effective mass of charge carriers in a semiconductor is typically associated with a decrease in the energy band gap. The method for calculating the optical band gap (E_g) using the Tauc plot was detailed in the previous chapter 3. For the present doping concentrations, the direct band gap was derived from the Tauc plot of $(\alpha h\upsilon)^2$ versus photon energy ($h\upsilon$), with the band gap value extrapolated from the linear region, as shown in the inset of Fig.4.11. In the case of Ni doped Cu_2Se, we observed a decrease in the band gap as the Ni content increased, attributed to band sharpening. The band gap for pure Cu_2Se is found to be nearly 2.29 eV, closely aligning with the literature. For dual doped samples, the band gaps are 2.22 eV, 2.19 eV, 2.10 eV, and 2.04 eV as the Zn doping content increases from 0.5 wt%, 1 wt%, 1.5 wt%, and 2 wt%, respectively. This slight decrease in band gap compared to the pure sample indicates that dual doping also results in a reduction of the sample's band gap. Here, we observe a reduction in effective mass upon the introduction of dopants. A reduction in effective mass means that charge carriers can more easily respond to lattice vibrations, leading to enhanced mobility. As a result, the energy required for charge carriers to transition between energy bands within the material decreases, effectively narrowing the band gap. The introduction of dopants can induce strain in the lattice, influence the molecular band gap structure, affecting

the arrangement of valence and conduction bands [34].

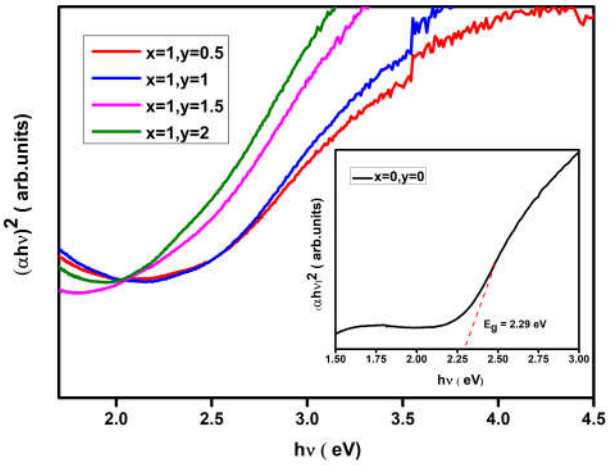

Fig.4.11 Tauc's plot of pristine and Ni and Zn dual doped Cu_2Se.

4.3.5. Thermal transport measurements

Defects not only impact disrupt carrier transport but also phonon dynamics, thereby influencing thermal conductivity [35]. Fig.4.12 (a) depicts the temperature-dependent behaviour of the total thermal conductivity for dual doped samples spanning temperatures from 300 to 573 K. The κ values for all samples diminish as doping content increases and as temperature rises. The introduction of point defects through Ni and Zn co-doping in the lattice of Cu_2Se leads to an additional decrease in thermal conductivity. The thermal conductivity of all dual doped samples is lower than that of the pristine samples. In our previous study, we achieved a notably low thermal conductivity of 0.49 W/mK at 573 K for the sample doped with 2 wt% of Ni. However, through simultaneous introduction of Ni and Zn at carefully adjusted concentrations, we were able to achieve a further reduction in thermal conductivity, reaching a value of 0.41 W/mK at 573 K. Dopants induce phonon scattering through point defects, resulting from fluctuations in mass and variations in size. This generates differences in the interatomic coupling forces, creating fluctuations in the strain field between the host and dopant atoms [36]. Lattice strain causes a widening of the phonon dispersion (ω), which accelerates changes in the phonon distribution function, ultimately leading to a reduction in the relaxation time for phonons to reach equilibrium [37]. Raman studies confirm that the relaxation time of phonons

decreases as a result of phonon scattering induced by the strain in the lattice caused by the presence of dual dopants through point defects. The equation 4.4 derives the effect of phonon scattering by point defects generated by dual dopants on the relaxation time of phonons relative to their concentration is given by [38]

$$\tau_{PD}^{-1} = V_a C_i \left(\frac{m_i - m_{avg}}{m_{avg}}\right)^2 \frac{\omega^4}{4\pi v^3} \quad \text{.....(4.4)}$$

where the mass of the defect and the average mass of the atoms are represented by the variables m_i and m_{avg} respectively, the atomic volume is indicated by the variable V_a , and the defect concentration is indicated by the variable C_i. The XRD measurements confirms the increase in the density of dislocations with doping content. The increase in the concentration of dual dopants results in the creation of defects, thereby reducing phonon scattering relaxation time, as evidenced by our Raman measured values. The increased dislocation density enhances phonon scattering, leading to a significant reduction in total thermal conductivity.

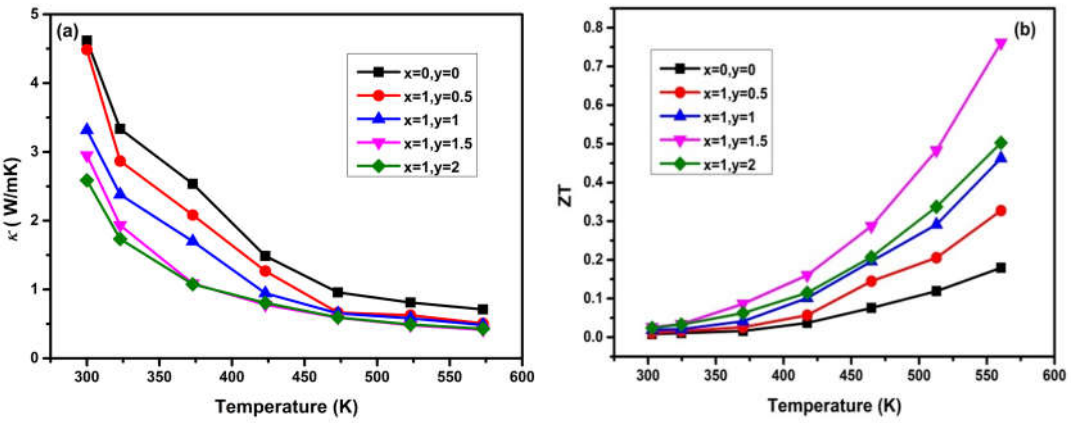

Fig.4.12 Variation of (a) total thermal conductivity and (b) ZT with temperature in pristine and Ni and Zn dual doped Cu_2Se.

The exceptionally low thermal conductivity results in a high figure of merit (ZT), as illustrated in Fig.4.12 (b). Due to the optimized carrier concentration maintaining a high power factor and the effective suppression of total thermal conductivity resulting from multiple defects, the thermoelectric properties of the dual doped system were notably enhanced. This enhancement was particularly evident in achieving a peak ZT of 0.761 at 573 K for the dual doped sample with 1 wt% Ni and

1.5 wt% Zn which is 4.2 times as large as that for undoped Cu_2Se and higher than that for single Ni doped Cu_2Se (ZT~ 0.535 for 1.5 wt% Ni doped Cu_2Se at 573 K). These findings suggest that dual doping enhances the power factor and reduces the thermal conductivity in Cu_2Se. The findings illustrate that Ni and Zn dual doping yields synergistic effects on the thermoelectric characteristics of Cu_2Se, effectively optimizing both electrical and thermal transport properties simultaneously. The enhancement observed in dual doped Cu_2Se is highly desirable for energy harvesting from waste heat in the intermediate temperature range.

4.4. Conclusion

A novel and effective method has been devised to reduce the thermal conductivity and enhance the power factor of Cu_2Se by co-doping its lattice with Ni and Zn, synthesized via hydrothermal route. An extensive investigation into the structural, morphological, electrical, optical, and thermoelectric properties of p-type Cu_2Se samples has been performed. The PXRD and micro-Raman studies confirm the phase purity and the presence of Ni and Zn in the lattice. Incorporating both Ni and Zn into the lattice of Cu_2Se synergistically manipulates its electrical and thermal transport behaviour by enhancing carrier mobility and scattering phonons through lattice defects. Dual doping significantly improves Hall mobility, increasing it from 234 $cm^2V^{-1}s^{-1}$ to 875 $cm^2V^{-1}s^{-1}$ at 573 K, thereby enhancing electrical conductivity with minimal reduction in the Seebeck coefficient. A maximum power factor of approximately 564 $\mu W/mK^2$ at 573 K was achieved for Cu_2Se dual doped with 1 wt% Ni and 1.5 wt% Zn. The increased scattering of phonons through lattice defects reduces the total phonon relaxation time, resulting in an ultra-low thermal conductivity of 0.41 W/mK at 573 K. This reduction in thermal conductivity is attributed to stronger point-defect scattering and the lattice anharmonicity introduced by the dual dopants. As a result, a peak ZT of 0.761 at 573 K was obtained for the co-doped sample with 1 wt% Ni and 1.5 wt% Zn, which is 4.2 times higher than that of undoped Cu_2Se. The substantial improvement in thermoelectric properties highlights the potential of dual doping with specific ions as an effective strategy to improve the performance of Cu_2Se in thermoelectric applications.

References

[1] T. Parvathy, P.P. Pradyumnan, Impact of mobility and effective mass on the thermoelectric performance of Ni doped Cu_2Se, J. Alloys Compd. 970 (2024) 172615. https://doi.org/10.1016/j.jallcom.2023.172615.

[2] V. Karthikeyan, C.M. Arava, M.Z. Hlaing, B. Chen, C.H. Chan, K.H. Lam, V.A.L. Roy, Dislocation-induced ultra-low lattice thermal conductivity in rare earth doped β-Zn_4Sb_3, Scr. Mater. 174 (2020) 95–101. https://doi.org/10.1016/j.scriptamat.2019.08.037.

[3] Q. Meng, L. Wu, Y. Zhu, Phonon scattering of interfacial strain field between dissimilar lattices, Phys. Rev. B - Condens. Matter Mater. Phys. 87 (2013) 1–9. https://doi.org/10.1103/PhysRevB.87.064102.

[4] Y.-H. Zhao, Z.-H. Shan, W. Zhou, R. Zhang, J. Pei, H.-Z. Li, J.-F. Li, Z.-H. Ge, Y.-B. Wang, B.-P. Zhang, Enhanced thermoelectric performance of Bi–Se Co-doped $Cu_{1.8}S$ via carrier concentration regulation and multiscale phonon scattering, ACS Appl. Energy Mater. 5 (2022) 5076–5086. https://doi.org/10.1021/acsaem.2c00414.

[5] J.-D. Musah, L. Linlin, C. Guo, A. Novitskii, A.O. Ilyas, I. Serhiienko, V. Khovaylo, V.A.L. Roy, C.-M. Lawrence Wu, enhanced thermoelectric performance of bulk bismuth selenide: synergistic effect of indium and antimony co-doping, ACS Sustain. Chem. Eng. 10 (2022) 3862–3871. https://doi.org/10.1021/acssuschemeng.1c07256.

[6] K. Rani, V. Gupta, Ranjeet, A. Pandey, Enhanced thermoelectric performance of Mg and Se co-doped Bi_2Te_3 nanostructures, J. Solid State Chem. 330 (2024) 124486. https://doi.org/https://doi.org/10.1016/j.jssc.2023.124486.

[7] M.R. Shankar, A.N. Prabhu, T. Srivastava, Materials Advances bismuth and tellurium co-doping : a route to improve thermoelectric efficiency in, (2024) 9823–9837. https://doi.org/10.1039/d4ma01011f.

[8] M. Ashokkumar, S. Muthukumaran, Microstructure, optical and FTIR studies of Ni, Cu co-doped ZnO nanoparticles by co-precipitation method, Opt. Mater. (Amst). 37 (2014) 671–678. https://doi.org/10.1016/j.optmat.2014.08.012.

[9] M. Jamshidijam, P. Thangaraj, A. Akbari-Fakhrabadi, M.A. Niño Galeano, J. Usuba, M.R. Viswanathan, Influence of rare earth (RE=Nd, Y, Pr and Er) doping on the microstructural and optical properties of ceria nanostructures, Ceram. Int. 43 (2017) 5216–5222. https://doi.org/10.1016/j.ceramint.2017.01.046.

[10] C. Soumya, P.P. Pradyumnan, Enhancement of thermoelectric properties of transition metals, nickel and copper dually doped ZnO, Mater. Today Commun. 35 (2023) 106197. https://doi.org/10.1016/j.mtcomm.2023.106197.

[11] C. Soumya, P.P. Pradyumnan, Enhancement of thermoelectric power factor of zinc oxide by nickel and indium dual doping, Int. J. Energy Res. 46 (2022) 19574–19584. https://doi.org/10.1002/er.8529.

[12] T. Parvathy, N.A. Muhammed Sabeer, N. Mohan, P.P. Pradyumnan, Effect of dopant gas pressure on the growth of magnetron sputtered CuO thin films for electrical and

optical applications, Opt. Mater. (Amst). 125 (2022) 112031. https://doi.org/10.101-6/j.optmat.2022.112031.

[13] T. Munawar, S. Fatima, M.S. Nadeem, F. Mukhtar, U.A. Akbar, A.S. Hakeem, F. Iqbal, Tunability of physical properties of NiO by the introduction of rare earth metal (Y, Ho) dual doping for natural sunlight-driven photocatalysis, J. Mater. Sci. Mater. Electron. 34 (2023) 1–24. https://doi.org/10.1007/s10854-023-10095-5.

[14] S. Debnath, R. Das, Cobalt doping on nickel ferrite nanocrystals enhances the micro-structural and magnetic properties: Shows a correlation between them, J. Alloys Compd. 852 (2021) 156884. https://doi.org/10.1016/j.jallcom.2020.156884.

[15] K. Jayasankar, A. Pandey, B.K. Mishra, S. Das, Evaluation of microstructural parameters of nanocrystalline Y_2O_3 by X-ray diffraction peak broadening analysis, Mater. Chem. Phys. 171 (2016) 195–200. https://doi.org/10.1016/j.matchemphys.20-16.01.005.

[16] C. Li, H. Song, Y. Cheng, R. Qi, R. Huang, C. Cui, Y. Wang, Y. Zhang, L. Miao, highly suppressed thermal conductivity in diamond-like Cu_2SnS_3 by dense dislocation, ACS Appl. Energy Mater. 4 (2021) 8728–8733. https://doi.org/10.1021/acsaem.1c01859.

[17] T. Parvathy, K. V. Nabeela, P.P. Pradyumnan, Raman structural transition studies and optical band calculation on the multiphase of tin selenides, Mater. Chem. Phys. 301 (2023) 127622. https://doi.org/10.1016/j.matchemphys.2023.127622.

[18] L.K. Gaur, M. Chandra Mathpal, P. Kumar, S.P. Gairola, V. Agrahari, M.A.R. Martinez, F.F.H. Aragon, M.A.G. Soler, H.C. Swart, A. Agarwal, Observations of phonon anharmonicity and microstructure changes by the laser power dependent Raman spectra in Co doped SnO_2 nanoparticles, J. Alloys Compd. 831 (2020) 154836. https://doi.org/10.1016/j.jallcom.2020.154836.

[19] S. Chen, J. Wei, Z. Kang, X. Miao, D. An, W. Fan, C. Dun, Enhancement of thermoelectric performance in $Mg_3(Sb,Bi)_2$ through engineered lattice strain and controlled carrier scattering, Chem. Eng. J. 490 (2024) 151404. https://doi.org/10.1016/j.cej.2024.151404.

[20] Y.J. Fan, K.L. Peng, Y.L. Huang, H.J. Liao, Z.Y. Huang, J. Li, Y.C. Yan, H.S. Gu, B. Zhang, Y.M. Hu, X. Lu, X.Y. Zhou, Enhanced thermoelectric performance of Cu_2SnSe_3 via synergistic effects of Cd-doping and $CuGaTe_2$ alloying, Rare Met. 41 (2022) 3466–3474. https://doi.org/10.1007/s12598-022-02043-9.

[21] V. Lourdhusamy, J.L. Chen, I. Paulraj, L.C. Hsu, Y.Y. Li, T.S. Yang, K.V. Prabu, C.J. Liu, Enhanced thermoelectric performance of polycrystalline $InSb_{1-x}Bi_x$ by using isoelectronic substitution on the Sb site, J. Alloys Compd. 920 (2022). https://doi.org/10.1016/j.jallcom.2022.165949.

[22] R.S.C. Bose, K. Ramesh, Study of anisotropic thermal conductivity in textured thermoelectric alloys by Raman spectroscopy, RSC Adv. 11 (2021) 24456–24465. https://doi.org/10.1039/d1ra04886d.

[23] Y. Wu, Z. Chen, P. Nan, F. Xiong, S. Lin, X. Zhang, Y. Chen, L. Chen, B. Ge, Y. Pei, Lattice Strain Advances Thermoelectrics, Joule. 3 (2019) 1276–1288. https://doi.org/10.1016/j.joule.2019.02.008.

[24] J. Liu, M. Wang, J. Lin, G. Chen, B. Liu, J. Huang, M. Zhang, G. Liang, L. Lu, P. Xu, B. Tian, H.S. Kwok, G. Li, Mitigating deep-level defects through a self-healing process for highly efficient wide-bandgap inorganic $CsPbI_{3-x}Br_x$ perovskite photovoltaics, J. Mater. Chem. A. 10 (2022) 17237–17245. https://doi.org/10.1039/d2ta02022j.

[25] B. Feng, G. Li, Y. Hou, C. Zhang, C. Jiang, J. Hu, Q. Xiang, Y. Li, Z. He, X. Fan, Enhanced thermoelectric properties of Sb-doped BiCuSeO due to decreased band gap, J. Alloys Compd. 712 (2017) 386–393. https://doi.org/10.1016/j.jallcom.2017.04.121.

[26] G.K. Ren, S.Y. Wang, Y.C. Zhu, K.J. Ventura, X. Tan, W. Xu, Y.H. Lin, J. Yang, C.W. Nan, Enhancing thermoelectric performance in hierarchically structured BiCuSeO by increasing bond covalency and weakening carrier-phonon coupling, Energy Environ. Sci. 10 (2017) 1590–1599. https://doi.org/10.1039/c7ee00464h.

[27] C. Barreteau, D. Bérardan, E. Amzallag, L.D. Zhao, N. Dragoe, Structural and electronic transport properties in Sr-doped BiCuSeO, Chem. Mater. 24 (2012) 3168–3178. https://doi.org/10.1021/cm301492z.

[28] Y. Du, S.Z. Shen, W. Yang, R. Donelson, K. Cai, P.S. Casey, Simultaneous increase in conductivity and Seebeck coefficient in a polyaniline/graphene nanosheets thermoelectric nanocomposite, Synth. Met. 161 (2012) 2688–2692. https://doi.org/10.1016/j.synthmet.2011.09.044.

[29] H. Namiki, M. Kobayashi, K. Nagata, Y. Saito, N. Tachibana, Y. Ota, Relationship between the density of states effective mass and carrier concentration of thermoelectric phosphide $Ag_6Ge_{10}P_{12}$ with strong mechanical robustness, Mater. Today Sustain. 18 (2022) 100116. https://doi.org/10.1016/j.mtsust.2022.100116.

[30] J. Gao, C. Liu, L. Miao, X. Wang, C. Li, R. Huang, Y. Chen, S. Tanemura, Power factor enhancement via simultaneous improvement of electrical conductivity and Seebeck coefficient in tellurium nanowires/reduced graphene oxide flexible thermoelectric films, Synth. Met. 210 (2015) 342–351. https://doi.org/10.1016/j.synthmet.2015.10.018.

[31] Y. Liu, P. Sahoo, J.P.A. Makongo, X. Zhou, S.J. Kim, H. Chi, C. Uher, X. Pan, P.F.P. Poudeu, Large enhancements of thermopower and carrier mobility in quantum dot engineered bulk semiconductors, J. Am. Chem. Soc. 135 (2013) 7486–7495. https://doi.org/10.1021/ja311059m.

[32] J. Shuai, J. Mao, S. Song, Q. Zhu, J. Sun, Y. Wang, R. He, J. Zhou, G. Chen, D.J. Singh, Z. Ren, Tuning the carrier scattering mechanism to effectively improve the thermoelectric properties, Energy Environ. Sci. 10 (2017) 799–807. https://doi.org/10.1039/c7ee00098g.

[33] T. Irisawa, M. Myronov, O.A. Mironov, E.H.C. Parker, K. Nakagawa, M. Murata, S. Koh, Y. Shiraki, Hole density dependence of effective mass, mobility and transport time in strained Ge channel modulation-doped heterostructures, Appl. Phys. Lett. 82 (2003) 1425–1427. https://doi.org/10.1063/1.1558895.

[34] N.A. Hamizi, M.R. Johan, Z.Z. Chowdhury, Y.A. Wahab, Y. Al-Douri, A.M. Saat, O.A. Pivehzhani, Optical structure modification induced by lattice strain in Mn-

doped CdSe QDs, Opt. Mater. (Amst). 86 (2018) 441–448. https://doi.org/10.1016/j.optmat.2018.10.041.

[35] J. Dong, F.H. Sun, H. Tang, J. Pei, H.L. Zhuang, H.H. Hu, B.P. Zhang, Y. Pan, J.F. Li, Medium-temperature thermoelectric GeTe: Vacancy suppression and band structure engineering leading to high performance, Energy Environ. Sci. 12 (2019) 1396–1403. https://doi.org/10.1039/c9ee00317g.

[36] J. Yang, G.P. Meisner, L. Chen, Strain field fluctuation effects on lattice thermal conductivity of ZrNiSn-based thermoelectric compounds, Appl. Phys. Lett. 85 (2004) 1140–1142. https://doi.org/10.1063/1.1783022.

[37] Y. Wu, P. Nan, Z. Chen, Z. Zeng, R. Liu, H. Dong, L. Xie, Y. Xiao, Z. Chen, H. Gu, W. Li, Y. Chen, B. Ge, Y. Pei, Thermoelectric Enhancements in PbTe Alloys Due to Dislocation-Induced Strains and Converged Bands, Adv. Sci. 7 (2020). https://doi.org/10.1002/advs.201902628.

[38] V. Vijay, S. Harish, J. Archana, M. Navaneethan, Synergistic effect of grain boundaries and phonon engineering in Sb substituted Bi_2Se_3 nanostructures for thermoelectric applications, J. Colloid Interface Sci. 612 (2022) 97–110. https://doi.org/10.1016/j.jcis.2021.12.027.

Chapter-5

Thermoelectric performance of Cu_2Se with ZnSe nanoinclusions

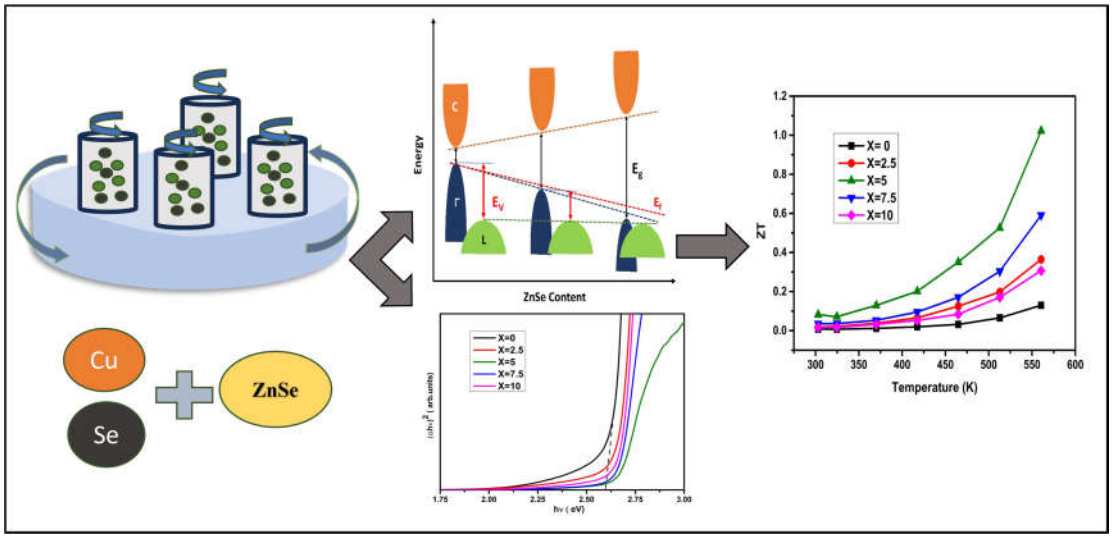

This chapter explores the impact of the nanocomposite approach to enhance the thermoelectric performance of Cu_2Se through ZnSe inclusions via planetary ball milling. By simultaneously engineering the electronic structure and suppressing phonon transport, ZnSe alloying plays a crucial role in optimizing charge carrier dynamics. Our study reveals that ZnSe addition effectively tunes the Fermi level, promotes valence band convergence, and increases the density of states, thereby enabling the decoupling of electrical transport parameters. This synergy leads to a remarkable enhancement in both the Seebeck coefficient and electrical conductivity, thereby boosting the overall thermoelectric performance.

5.1. Introduction

The thermoelectric generators commonly used in industrial applications are typically made from telluride-based alloys, which are suitable for room temperature operations, and silicon germanium, which is designed for high temperature operations. In practical scenarios, achieving an optimal ZT requires a delicate balance between maximizing the power factor and minimizing thermal conductivity (κ). These two factors are linked through variables such as carrier concentration (n) and electronic structure. To improve the overall thermoelectric performance and efficiency of materials, it is crucial to simultaneously optimize the power factor and reduce thermal conductivity. However, optimizing one parameter often negatively impacts the other two. Therefore, developing strategies or concepts that can decouple these parameters to enable concurrent optimization of electron and phonon transport is highly desirable and represents a critical advancement for the thermoelectric research community. In the preceding two chapters, we utilized the strategy of doping and dual doping to enhance the TE performance of Cu_2Se. Our findings revealed that both electrical conductivity and thermal conductivity exhibited significant improvements. However, this enhancement came at the cost of a reduction in the Seebeck coefficient. This trade-off highlights the complex interplay between these parameters and underscores the challenge of optimizing thermoelectric materials.

Strategies to enhance the power factor have been explored through band structure engineering, while efforts to reduce thermal conductivity have focused on creating nano and microstructures designed to scatter phonons. These approaches aim to independently optimize electrical and thermal transport properties, thereby improving overall thermoelectric performance [1,2]. The development of composites is expected to enhance the thermoelectric conversion efficiency by decoupling the transport parameters [3]. By carefully designing composite structures, it may be possible to optimize electron transport for improved electrical properties while simultaneously suppressing phonon transport to reduce thermal conductivity. This decoupling strategy could lead to significant advancements in thermoelectric

performance without compromising the mechanical strength and durability of the materials. Many investigators highlight the scientific benefits of the nanocomposite approach, which enables the simultaneous enhancement of the power factor and reduction of thermal conductivity [4]. Nanocomposites can effectively scatter phonons at the newly created interfaces without reducing the electrical conductivity significantly when an optimum amount of second phase is incorporated into the host matrix [5]. The main approach for improving the electrical transport properties of these materials mostly depend on valence band convergence, which can be achieved through alloying with different substitutions to minimize the energy offset between the light and heavy valence bands [8].

The utilization of Cu_2Se based composites has consistently been considered as the most effective approach for mid temperature power generation due to their remarkably high ZT values [6,7]. The primary strategies for improving the electrical transport properties of these materials often focus on valence band convergence. This can be attained through alloying with various substitutions, which reduces the energy offset between the light and heavy valence bands. Studies indicate that adjusting the energy offset between these valence bands enables charge transport across multiple band valleys, thereby improving conductivity without significantly compromising the Seebeck coefficient. Recent literature shown that this leads to better thermoelectric performance. These techniques have been successfully implemented to SnTe, MnTe, PbTe and PbSe based alloys by alloying them with suitable compounds to modify their electronic structure and improve their thermoelectric performance [9-12]. This motivated to the initiation of the current study, which seeks to enhance the thermoelectric (TE) properties of p-type Cu_2Se by introducing zinc selenide (ZnSe) nanoparticles through the process of ball milling. This work reveals that the addition of ZnSe not only optimises the carrier concentration but also significantly lowers the offset energy of the valence band which improves the overall thermoelectric performance. Simultaneously manipulating the carrier concentration through nanostructuring, coupled with the introduction of a compatible second phase in the form of synthesized composites, will be an effective strategy for achieving a high ZT. Here secondary phase

integration is utilised extensively as a feasible intrinsic technique to increase the density of states (DOS) effective mass, hence increasing the Seebeck coefficient [13]. The research indicates that these secondary phases aid in the merging of valence bands, resulting in the development of intricate electronic structures. This in turn can lead to a high electrical transport properties while concurrently maintaining low thermal conductivity [14].

5.2. Experimental details

5.2.1. Synthesis of ZnSe nanoparticles

Zinc selenides nanoparticles were synthesised using hydrothermal method. All experimental reagents of analytical purity were purchased and used for synthesis of ZnSe. Zinc Acetate dihydrate ($Zn(CH_3COO)_2(H_2O)_2$ > 99%), selenium metal powder (> 99.5%), sodium hydroxide (NaOH > 98%), hydrazine hydrate purchased from sigma aldrich were used. In a typical synthesis of ZnSe, the original molar ratio between zinc and selenium were selected to be 1:1. Zinc acetate and selenium powder were added to 150 ml of distilled water in a beaker, and the mixture was stirred vigorously for 30 minutes at room temperature. NaOH was added drop wise to maintain a constant pH value10. Hydrazine hydrate (8 ml) which is a reducing agent was added drop-wise to the mixture and the colourless solution changed to grey colour. After the reaction is over the solution was transferred to an autoclave which was maintained at 180°C for 6 hours. Then, the autoclave was allowed to cool to room temperature naturally. The products were obtained and collected by centrifugation, washed with deionized water, and then dried at 80°C under vacuum overnight.

5.2.2. Synthesis of Cu_2Se-ZnSe composites

Cu_2Se-ZnSe nanocomposites were synthesized through planetary ball milling technique. To synthesize pristine Cu_2Se, copper (99.99%, Alfa Aesar) and selenium (99.99%, Alfa Aesar) powders taken in a stochiometric ratio were milled in a high energy planetary ball-mill for an optimised time period of 12 hours. The ball to powder ratio was set at 10:1 with a milling speed of 200 rpm. To synthesise Cu_2Se-

ZnSe composites, appropriate ratio of Cu, Se and x wt% (2.5 wt%, 5 wt%, 7.5 wt% and 10 wt%) of ZnSe were taken for milling (x: weight percent ratio of ZnSe particles in the composites). These raw materials are combined in a planetary ball mill and the composite samples are synthesized in the same route as pristine Cu_2Se. The powder was compressed into a circular pellet of 13 mm diameter and 3 mm thickness using a hydraulic pelletizer with a force of roughly 10 tonnes in air. The densified pellet was sintered at 300°C for 3 hours in vacuum before being characterised. The structural, morphological, optical, and thermoelectric properties of the sintered pellets were comprehensively examined. A detailed description of the synthesis procedures and characterization techniques utilized in this study is provided in chapter 2.

5.3. Results and discussion

5.3.1. Phase and structure analysis

Powder X-ray diffraction studies (PXRD) were carried out to investigate the nanostructured features are shown in Fig.5.1. For the pristine sample, six diffraction peaks can be found at 2θ values of 26.73°, 30.91°, 44.40°, 52.53°, 64.51°, and 71.13°, which can be indexed to (111), (200), (220), (311), (400), and (331) of cubic Cu_2Se phase respectively (ICDD-03-065-2982). This suggests the successful formation of Cu_2Se by planetary ball milling. The primary peaks of ZnSe and Cu_2Se have the same diffraction angles, making it much more challenging to discern the peak at extremely low ZnSe concentration. Therefore, the major peak of Cu_2Se-ZnSe composites with varying ZnSe ratios appear to be close or overlapping at very low content of ZnSe and found to be increasing with increasing content of ZnSe. But at 5 wt% of ZnSe, new reflections of ZnSe noticed along with Cu_2Se phase which indicates the independent existence of ZnSe in the Cu_2Se matrix. There is an appearance of smaller new peak at 24.97° and 28.58° which can be attributed to the ZnSe phase (1CDD-00-015-0105). With increasing ZnSe content, the intensity of these peak increases and new small peak of ZnSe ascribed at 29.07° and 49.85° which suggest the increased proportion of ZnSe in the samples. At 7.5 wt% ZnSe, along with ZnSe and Cu_2Se, there are some diffraction peaks correspond to

tetragonal Cu_3Se_2 phase (ICDD-03-065-1656). Copper selenide can occur in several phases, including cubic, monoclinic, orthorhombic, and tetragonal [15]. The contribution of copper and selenium has a significant influence on phase selection in the copper selenide phase. Depending on the stoichiometry, copper in the solid can exist as Cu^{+} or Cu^{2+}, resulting in the formation of Cu_2Se, CuSe, or Cu_3Se_2 [16]. Here, we can observe that tetragonal Cu_3Se_2 phase exists at higher ZnSe content. The results suggest that ball milling may cause partial oxidation of Cu^{+} to Cu^{2+}, as the atomic ratio of Cu to Se changes from 2:1 with increasing ZnSe content, leading to the formation of Cu_3Se_2 phase [17].

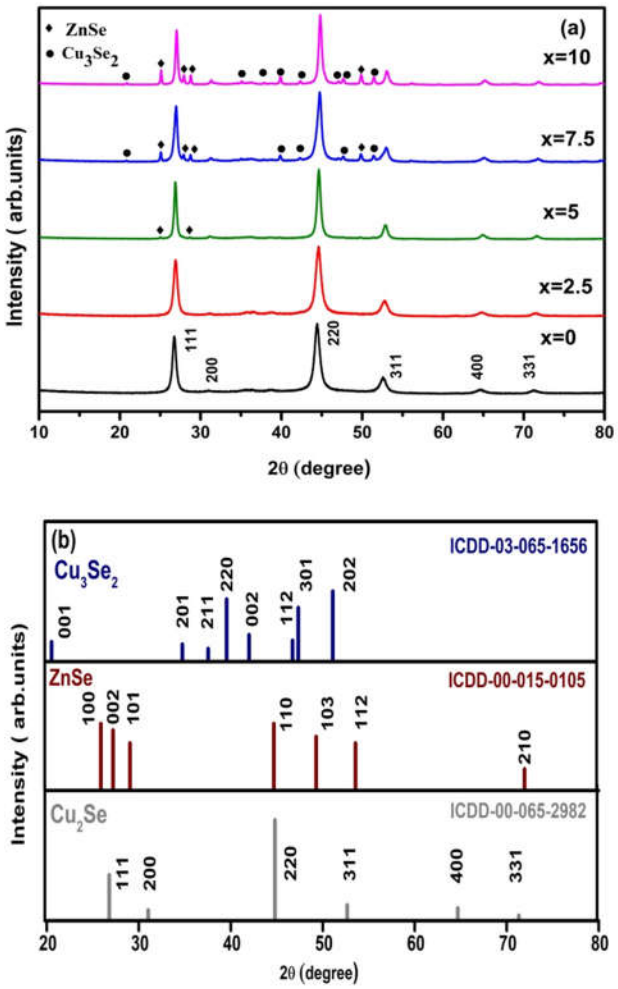

Fig.5.1 (a) PXRD patterns showing Cu_2Se + x % ZnSe (x = 0, 2.5, 5, 7.5, and 10) samples and (b) ICDD database of Cu_2Se, ZnSe and Cu_3Se_2.

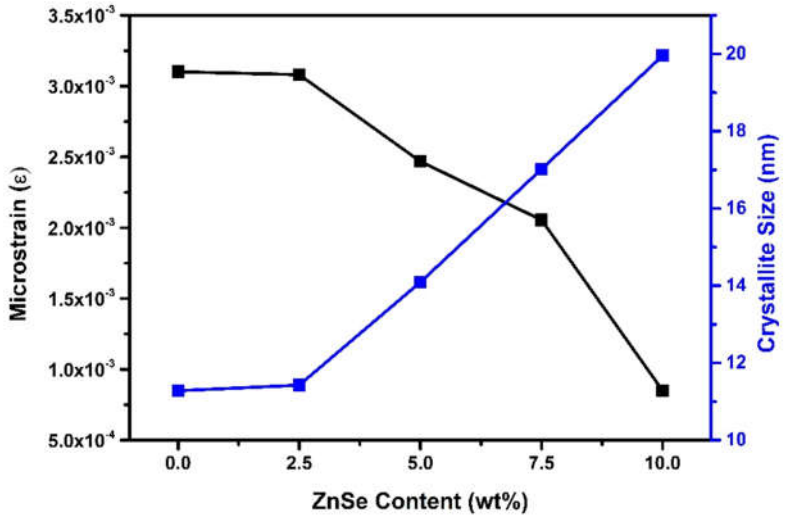

Fig.5.2 Variation of microstrain and crystallite size with ZnSe content.

As it is evident from the Fig.5.1 (a) that the diffraction peak corresponding to both Cu_2Se and ZnSe are present in the PXRD pattern which suggest the successful formation of Cu_2Se-ZnSe composites. The most prominent peaks in the XRD patterns were utilised to determine all diffraction related metrics such as FWHM, crystallite size, dislocation density, and microstrain. Here, the crystallite size, microstrain, and dislocation density were calculated using the equations outlined in chapter 3. As the concentration of ZnSe increases the crystallite size increased, going from 11.27 nm to a maximum value of 19.95 nm whereas the microstrain decreases. The increase in crystallite size might be due to ZnSe attaching themselves to the Cu_2Se particles that form throughout the matrix with increase in the ZnSe concentration. Dislocations, which are regarded as a type of imperfections and disorder in the lattice, are a highly important attribute that directly influences the electrical properties of the material [19]. The dislocation density was determined, resulting in values of 0.008 nm^{-2}, 0.0079 nm^{-2}, 0.0049 nm^{-2}, 0.0033 nm^{-2}, and 0.0023 nm^{-2} corresponding to x values of 0, 2.5 wt%, 5 wt%, 7.5 wt%, and 10 wt% of ZnSe, respectively. As the amount of ZnSe increases, the dislocation density is observed decreasing. The incorporation of ZnSe into the Cu_2Se matrix catalyzes the growth of larger crystallites. This enlargement in crystallite size results in a reduction in the number of grain boundaries available as potential sites for dislocation initiation. As the size of the crystallites grows, there is a corresponding reduction in the abundance

of grain boundaries where dislocations, which are structural irregularities within the crystal lattice, tend to accumulate. Consequently, the net effect is a decrease in dislocation density within the material.

5.3.2. Morphological studies

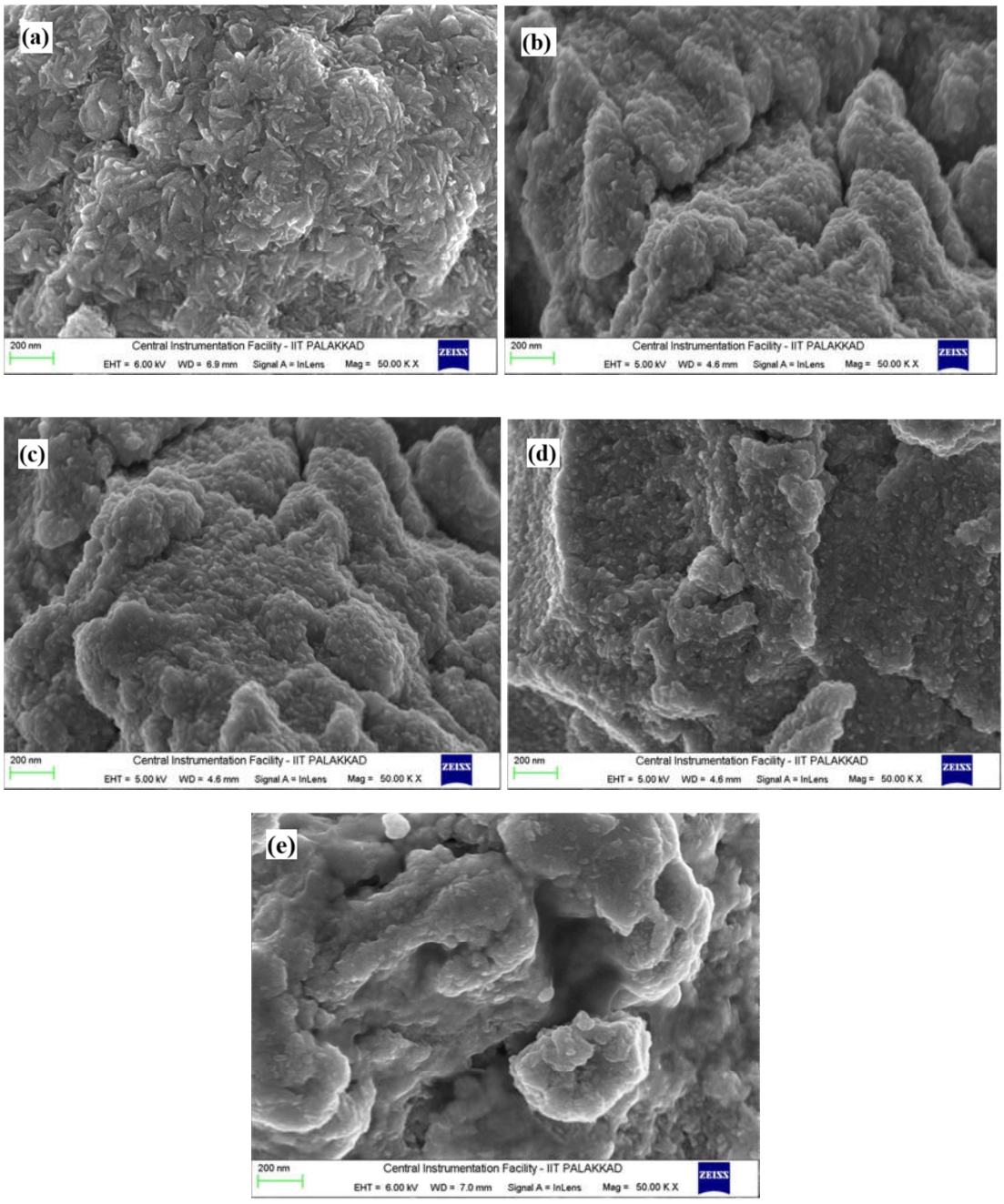

Fig.5.3 SEM images of Cu_2Se + x % ZnSe composites with (a) x=0, (b) x=2.5, (c) x=5, (d) x=7.5, and (e) x=10.

Fig.5.3 displays the morphology of the synthesized samples, as observed through high-resolution FESEM. Fig.5.3 (a) depicts the pristine Cu_2Se sample, which features a nanoflake-like surface with distinct grains and a porous structure, characterized by small voids between the grains, resulting in an uneven, irregular texture. As the ZnSe content increases, the surface roughness also increases, with the grains becoming more agglomerated compared to the pristine sample. The sheet-like structures become less noticeable, and the overall surface becomes more irregular. As the ZnSe content rises from 2.5 wt% to 10 wt%, the surface morphology becomes more granular and agglomerated. At lower ZnSe concentrations (2.5 and 5 wt%), moderate roughening and clustering occur, indicating partial dispersion of ZnSe within the Cu_2Se matrix. However, at higher concentrations (7.5 and 10 wt%), the surface roughness increases significantly, with greater agglomeration and more distinct grain boundaries. The SEM images also reveal an increase in particle size with rising ZnSe content, as higher concentrations lead to larger, more agglomerated clusters which aligns with the findings from PXRD studies.

The compositional analysis of the samples was conducted using EDS technique, as shown in Fig.5.4 (a-e). In the pristine sample, only peaks corresponding to Cu and Se are detected. For all other samples, no peaks related to elements other than Cu, Se, and Zn are observed, which aligns with the PXRD results. EDS mapping in Fig.5.5 (a-d) illustrates the distribution of Cu, Se, and Zn in the Cu_2Se sample with 5 wt% ZnSe content. The EDS mapping clearly shows the distribution of ZnSe with in the Cu_2Se matrix.

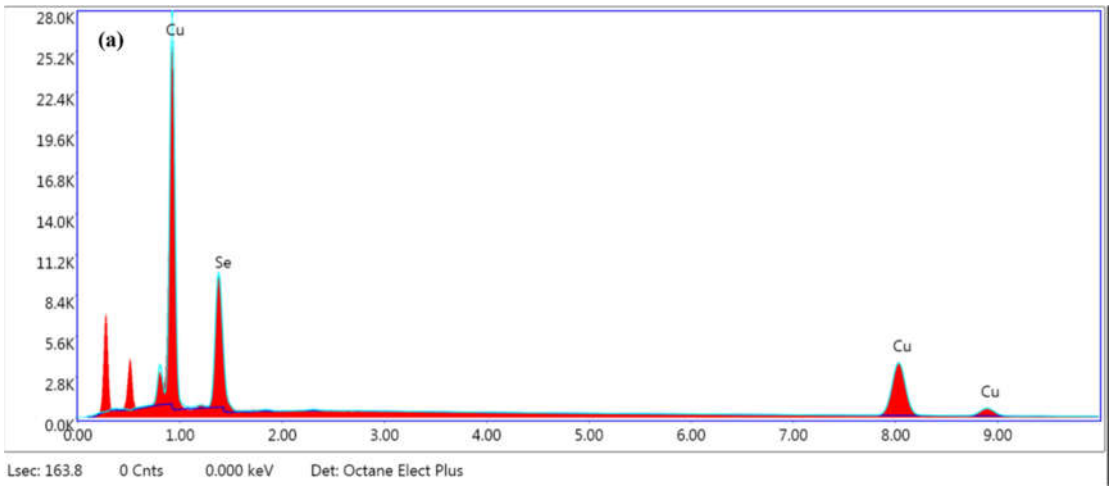

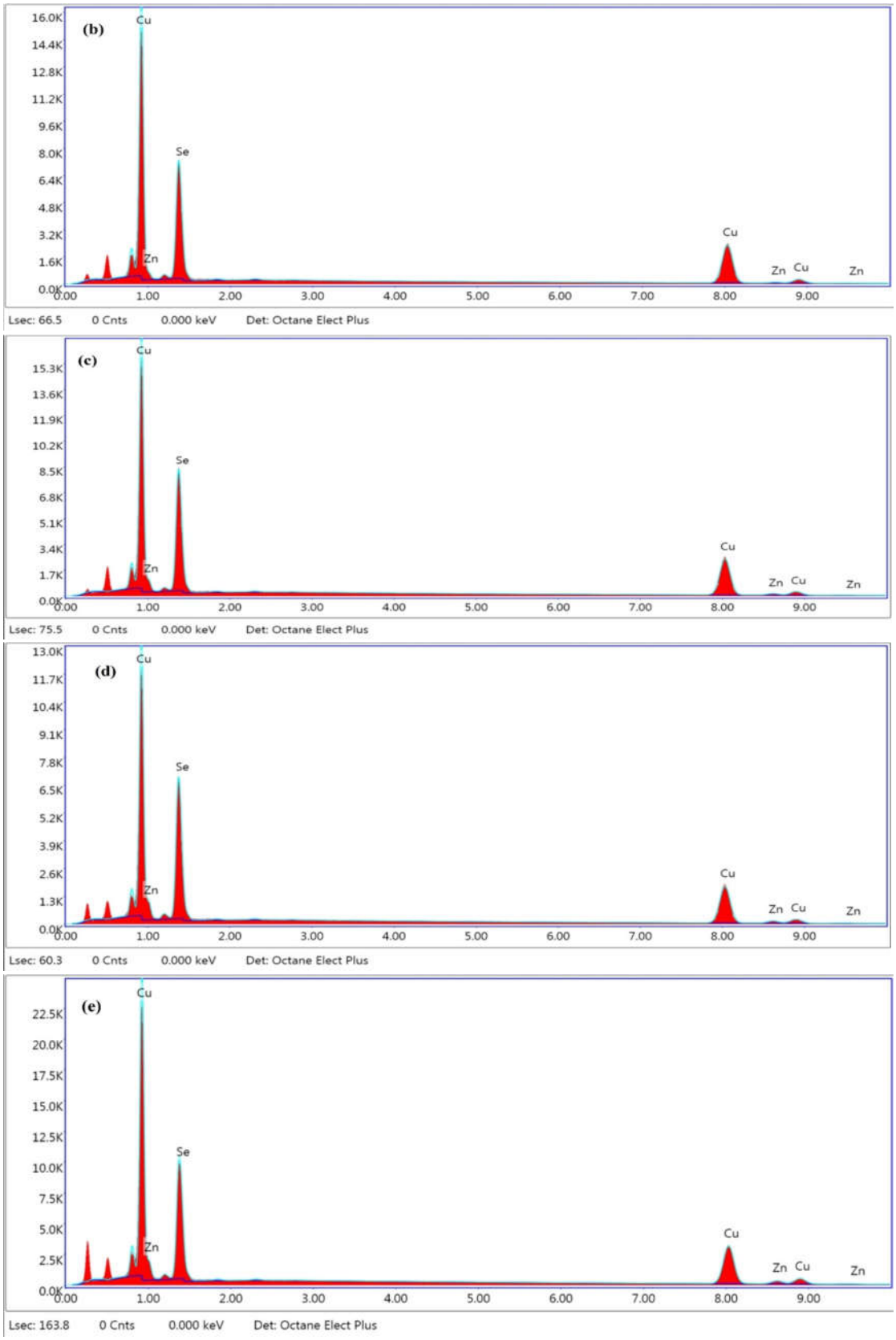

Fig.5.4 EDS spectrum of Cu_2Se + x % ZnSe composites with (a) x=0, (b) x=2.5, (c) x=5, (d) x=7.5, and (e) x=10.

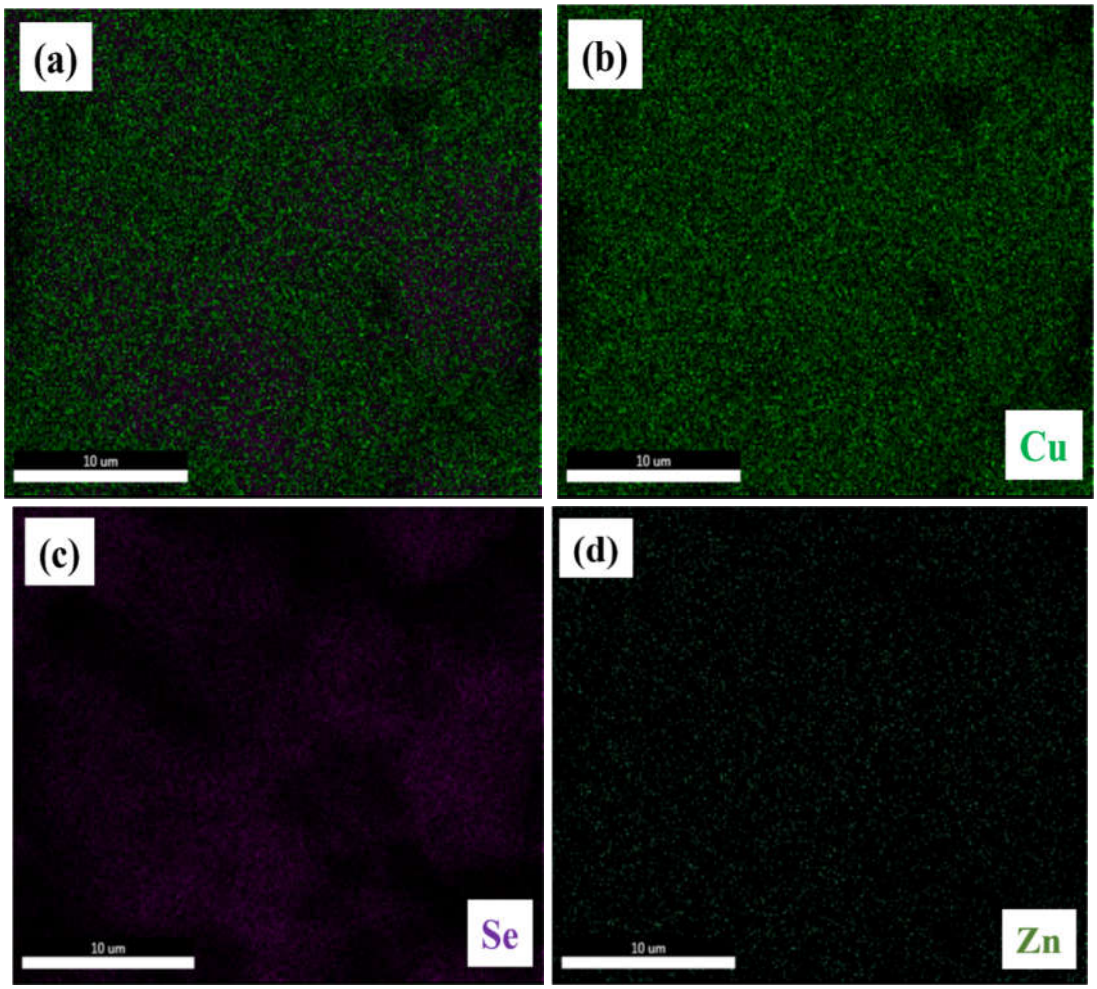

Fig.5.5 EDS elemental mapping for the Cu_2Se sample with 5 wt% ZnSe showing (a) the combined distribution of all elements, (b) the distribution of Cu, (c) Se and (d) Zn.

HRTEM was utilized to examine the microstructure of the samples containing 5 wt% ZnSe, as depicted in Fig.5.6. The darker regions in Fig.5.6 (a) likely indicate denser areas, such as clusters of Cu_2Se with embedded ZnSe inclusions, which form irregular, aggregated particles. In Fig.5.6 (b) the measured distances, ranging from 2 nm to 7 nm, likely correspond to the size of the ZnSe nanoinclusions or the spacing between particles, illustrating the scale of these inclusions within the Cu_2Se matrix. The lattice fringes seen in Fig.5.6 (c) correspond to the (220) crystallographic planes of Cu_2Se and (110) planes of ZnSe confirming the coexistence of mixed phases, as verified by PXRD data. The lattice d-spacing values were calculated using ImageJ software are shown in Fig.5.6 (d). The figure shows d-spacing values of 0.24 nm and 0.25 nm, corresponding to the (220) planes of Cu_2Se and the (110) planes of ZnSe phase, respectively. Notably, both Cu_2Se (220) and ZnSe (110) planes exhibit nearly

identical d-spacing values as indicated by the PXRD studies based on ICDD data. The SAED pattern of the sample shown in Fig.5.6 (e), confirms the polycrystalline nature and high crystallinity of the sample. Distinct diffraction spots corresponding to the (220) and (311) planes of cubic Cu_2Se, as well as the (110) plane of ZnSe, are clearly visible, in agreement with the PXRD diffraction peaks for these phases. The d-spacing values derived from the SAED pattern, specifically 0.244 nm, 0.183 nm, and 0.248nm, precisely align with the interplanar spacings of the (220) and (311) planes of Cu_2Se and the (110) planes of ZnSe, respectively. This confirms the presence of ZnSe nanoparticles within the Cu_2Se matrix which serves as effective phonon scattering centers, leading to a significant reduction in the thermal conductivity of the material.

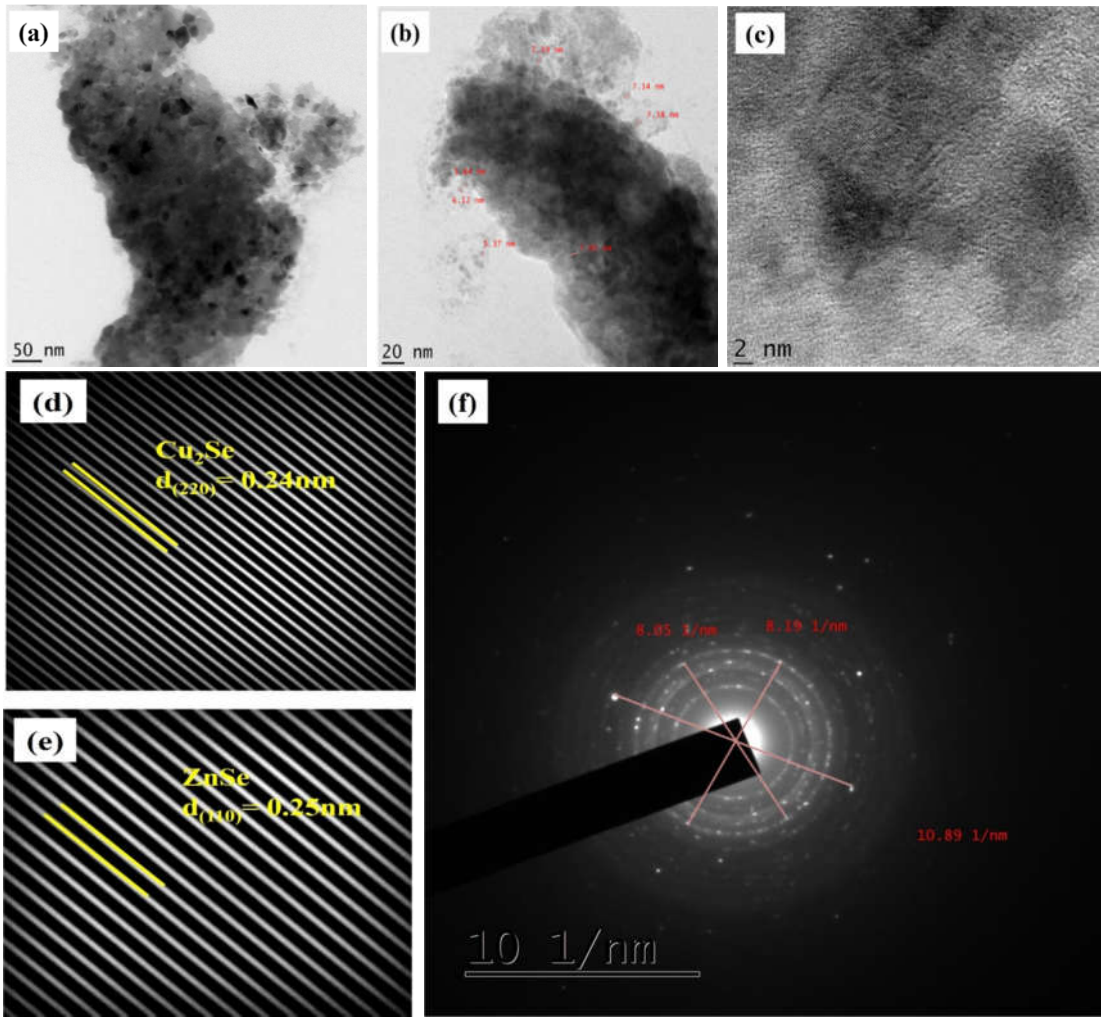

Fig.5.6 (a-c) HRTEM image, (d,e) d-spacing of lattice planes of Cu_2Se and ZnSe and (f) selected area electron diffraction (SAED) pattern of Cu_2Se sample with 5 wt% ZnSe content.

5.3.3. Thermoelectric measurement studies

The thermoelectric properties of the Cu_2Se-ZnSe composite as a function of temperature were investigated, and the results are shown in Fig.5.7.

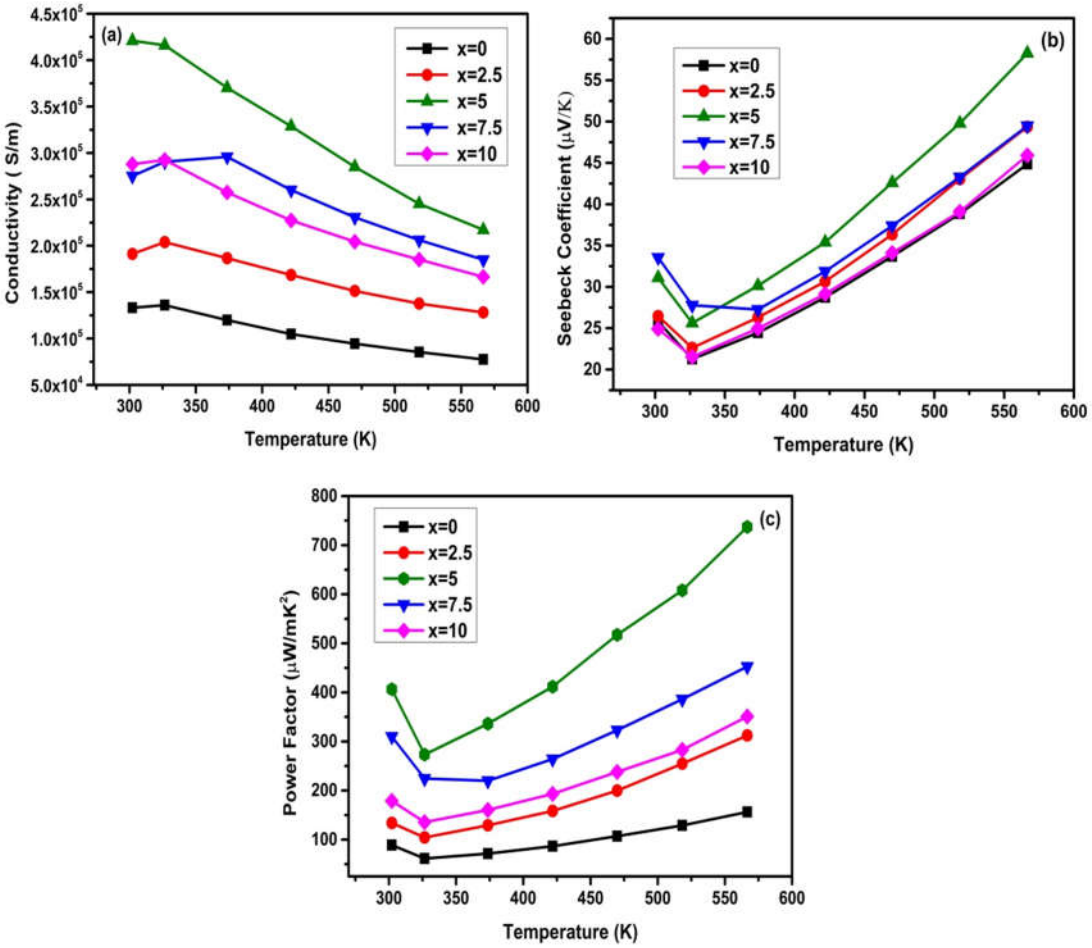

Fig.5.7 Variation of (a) electrical conductivity (b) Seebeck coefficient (c) power factor of Cu_2Se + x % ZnSe (x = 0, 2.5, 5, 7.5, and 10) samples.

Increasing the concentration of ZnSe leads to a simultaneous enhancement in both electrical conductivity and the Seebeck coefficient. The electrical conductivity of all samples decreases with rising temperature, indicating semimetallic transport behavior [20]. Typically, the Seebeck coefficient tends to decrease as electrical conductivity increases and vice versa. However, an intriguing deviation from this conventional trend is observed upon the incorporation of ZnSe into the Cu_2Se matrix. Strikingly, the inclusion of ZnSe in Cu_2Se can result in a simultaneous boost in both the Seebeck coefficient and electrical conductivity. This exceptional

occurrence challenges established norms and highlights the distinctive attributes and prospective uses of ZnSe as a promising material for thermoelectric applications. When incorporating material such as ZnSe into a system, it has the potential to impact the electronic band structure and density of states within that system. Depending on the unique characteristics of ZnSe, it may lead to an augmentation in the density of states within the energy bands, potentially resulting in an enhancement of the Seebeck coefficient. To gain a comprehensive understanding of the mechanisms driving this augmentation, it would be imperative to conduct an in-depth examination of the electronic band structure, charge carrier concentration, and mobility within the particular Cu_2Se-ZnSe system.

In order to comprehensively explore the electrical transport characteristics of Cu_2Se + x wt% ZnSe samples, a series of Hall measurement studies were conducted. The accompanying Fig.5.8 illustrates the intriguing interplay between carrier concentration and mobility at different temperatures. It's evident from the data that both carrier concentration and mobility decrease as the temperature rises. Within this dataset, a discernible pattern emerges as ZnSe is incorporated into the Cu_2Se matrix: a gradual and consistent rise in carrier concentration, paralleled by a persistent decline in mobility. This intriguing behaviour underscores the significant influence of ZnSe on the charge carriers within the material. With an increasing content of ZnSe, carriers become more abundant, leading to an enhancement in carrier concentration. In composite samples with lower ZnSe content ($\leq$ 5 wt%), this increase is linked to the presence of more interfacial defects. However, as ZnSe content exceeds 5 wt%, hole concentration decreases, likely because of particle agglomeration. Interestingly, this increment in carrier concentration coincides with a corresponding reduction in carrier mobility, signifying a restriction in their effective movement within the material. Notably, when compared to pristine Cu_2Se, these samples consistently exhibit higher carrier concentrations and lower carrier mobilities across all weight percentages of introduced ZnSe. The observed decrease in carrier mobility with increasing ZnSe content in the composite material can be attributed to enhanced nanoinclusion interface scattering [21]. When ZnSe is introduced into the material, it creates interfaces or boundaries that impede the

smooth movement of charge carriers, causing them to scatter. This scattering effect results in a reduction in carrier mobility because the carriers experience increased resistance to their motion. However, the simultaneous increase in carrier concentration, which is the number of charge carriers present, compensates for the reduction in mobility. As ZnSe content continues to increases beyond a certain threshold, the enhanced carrier concentration becomes dominant, leading to a remarkable enhancement in electrical conductivity. In essence, the trade-off between reduced mobility due to scattering and increased carrier concentration is a key factor influencing the electrical properties of the composite material.

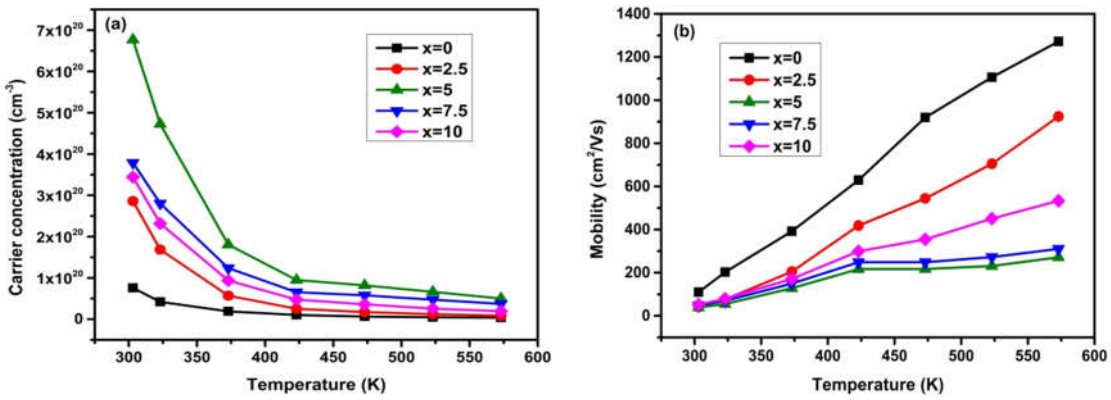

Fig. 5.8 Variation of (a) carrier concentration and (b) mobility of Cu_2Se + x % ZnSe (x = 0, 2.5, 5, 7.5, and 10) samples.

Fig.5.7 (b) shows the temperature dependent Seebeck coefficient for the Cu_2Se + x % ZnSe (0-10 wt%). The fact that all samples exhibit a positive Seebeck coefficient suggests that holes are the prevailing carriers, aligning with the results of Hall measurements. With increasing ZnSe content, the Seebeck coefficient in the composite material shows a clear and significant improvement compared to pristine Cu_2Se. This suggests that the addition of ZnSe has a positive impact on the thermoelectric properties of the composite material, and this effect becomes more pronounced as the ZnSe content increases to 5 wt%. The notable observation is that, in contrast to the anticipated behavior dictated by the well established Mott formula, the Seebeck coefficient does not decrease [22]. Instead, it exhibits a slight increase with the gradual incorporation of ZnSe and the corresponding rise in carrier concentration within the composite materials. The fact that the hole concentration

increases with increasing ZnSe content but does not reduce S over the whole temperature range. This unexpected phenomenon challenges the conventional understanding, which suggests an inverse proportional relationship between the Seebeck coefficient and carrier concentration as described by the Mott formula [22,23]. A detailed explanation of this equation is provided in chapter 3.

$$S = \frac{8\Pi^2 {k_B}^2}{3eh^2} m^* T \left(\frac{\Pi}{3n}\right)^{2/3} \quad \text{.....(5.1)}$$

and the electronic density of states

$$g(E) = \frac{(m^*)^{3/2}\ \sqrt{2E}}{\hbar^3 \Pi^2} \quad \text{.....(5.2)}$$

It is known that the secondary lower VBM of Cu_2Se is situated at the L point with a high degeneracy of 8, and the valence band maximum (VBM) is located at the Γ point with a low degeneracy of 3. This finding implies that in p-type Cu_2Se, thermoelectric performance can be enhanced by the application of band structure modification [24]. Introduction of ZnSe can induce pronounced band convergence within the electronic structure of Cu_2Se, which may ultimately result in a remarkable increase in the Seebeck coefficient. To provide a more detailed insight into these findings, a thorough grasp of the band structure within the samples is essential. It is necessary to compute the effective mass (m*) in order to justify the interaction between the electronic structure and transport properties in order to comprehend the thermoelectric performance, which is often dependent on the characteristics of the band structure around the Fermi level. Alterations in the electronic configuration manifest in the effective mass of carriers, and this, in turn, has a direct impact on the Seebeck coefficient of the materials [25]. So, to explore the increment in Seebeck coefficient, the effective mass (m*) is calculated and shown in the Fig.5.9. Figure shows that the m* increases when ZnSe is introduced, rising from 0.230 m_0 for pristine Cu_2Se (m_0 is the free electron mass) to 1.194 m_0 for Cu_2Se with 5 wt% ZnSe suggests that addition of ZnSe modify the band structure of Cu_2Se. The addition of ZnSe in Cu_2Se lattice leads to an enhancement in the effective mass and the effective mass of charge carriers is closely linked to the curvature of the energy

bands near the Fermi level. An increase in effective mass implies a change in the band structure, often associated with variations in the DOS suggesting a possible rise in the electronic density of states near the Fermi level. This could be due to the overlapping or hybridization of the energy levels of ZnSe with the valence band of pristine Cu_2Se [26]. Such band convergence boosts the DOS near the Fermi level, which is crucial for promoting the excitation of holes and electrons into available states. With this enhanced DOS and increased effective mass, the energy levels become more densely populated, allowing a greater number of carriers to occupy these states. Consequently, we observe a significant rise in carrier concentration. This suggests that the manipulation of the inverse connection between S and n is, in fact, caused by the greater effective mass of carrier [27]. However, as the ZnSe content is further increased m* subsequently decreases to 0.610 m_0 which was consistent with the decrease in the Seebeck coefficient and carrier concentration. The variation in effective mass leads to the participation of new energy levels or electronic states that affect the charge transport properties [28].

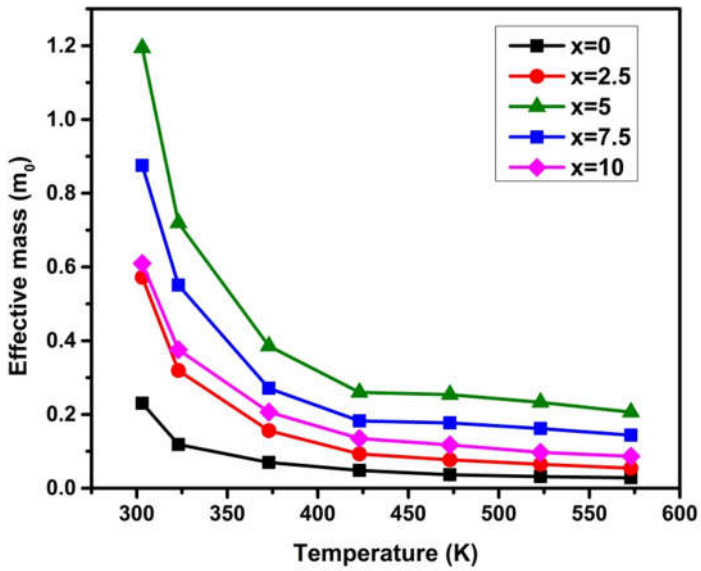

Fig.5.9 Temperature dependence of carrier effective mass of Cu_2Se + x % ZnSe (x = 0, 2.5, 5, 7.5, and 10) samples.

The correlation proposed by Fritzsche suggests that the magnitude of an individual gain in the Seebeck coefficient is approximately proportional to the distance from the Fermi energy (E_f) in terms of energy units. Fritzsche's model illustrates the

connection between the Seebeck coefficient and the energy difference between the conduction band and Fermi level. This correlation is particularly relevant when the density of states edge permits carrier motion exclusively in either the conduction band or the valence band [28]. The addition of ZnSe may introduce energy levels that modify the Fermi level. The (E_c-E_f) value has been determined by analyzing the slope of the graph, where 1/T is plotted on the x-axis and S on the y-axis and shown in table 5.1.

Table 5.1: Computed values of Fermi level, optical band gap and thermal band gap.

Sample	E_c-E_f (eV)	Optical band gap, E_g (eV)	Thermal band gap, ϵ_g (eV)
x=0	-0.0178 ± 0.0023	2.598	0.051
x=2.5	-0.0204 ± 0.0028	2.627	0.056
x=5	-0.0247 ± 0.0033	2.702	0.066
x=7.5	-0.0242 ± 0.0025	2.674	0.056
x=10	-0.0181 ± 0.0025	2.655	0.052

The Fermi level normally lies inside the band gap but closer to the valence band in p-type semiconductors, where positively charged holes are the dominating carriers. For all p-type samples, the negative values of (E_c-E_f) indicate that the Fermi level (E_c-E_f) is located closer to the valence band (E_v) than it is to the conduction band (E_c). This energy difference increases with the increases in ZnSe content up to 5 wt% which indicates that the fermi level is shifting even closer to the valence band which causes an increase in carrier concentration.

Thermal band gap was calculated using sharp goldsmith relation [29].

$$\epsilon_g = 2eS_{max}T_{max} \quad \text{.....(5.3)}$$

Where, ϵ_g is the thermal bandgap, e charge of an electron, S_{max} is the maximum Seebeck coefficient and T_{max} is the consistent temperature, respectively. The calculated thermal band gap of the samples is shown in the table 5.1. Thermal band gap of the sample increases as the ZnSe content increases to 5 wt% which indicates a supress in bipolar diffusion. The fermi level is shifting deep into the valence band

as the ZnSe concentration increases. This increases the energy gap between the Fermi level and the conduction band, decreasing the likelihood of electrons being thermally stimulated into the conduction band and suppressing bipolar diffusion [30].

Schematics showing the variation in band structures with ZnSe addition is shown in Fig.5.10. The Cu_2Se valence band edge is characterised by a significant p-d hybridization that stems from the small energy difference between the Cu-d and Se-p atomic orbitals [24]. It can be seen that as the ZnSe is introduced, VB at the L point shifts upward closer to the VBM. So, the energy gap between VB and the VBM, which improves degeneracy and increases DOS close to the Fermi level. Addition of ZnSe in Cu_2Se alter the band structure in 2 ways. First, according to the results, ZnSe addition to Cu_2Se is thought to facilitate charge carrier injection by bringing the two valence bands (Γ and L) closer together in energy (ΔE_v), or valance band convergence. Second, ZnSe addition may also widen the band gap that separates the conduction band (C) from the valance band (Γ and L), preventing minority carriers (electron) from crossing the gap, thus Seebeck increases. Additionally, when the doping level increases, it tends to maintain the Fermi level's location near the VBM, which is beneficial for electrical conductivity. Also, strong band convergence between the valence maxima would imply a high DOS and a high S values.

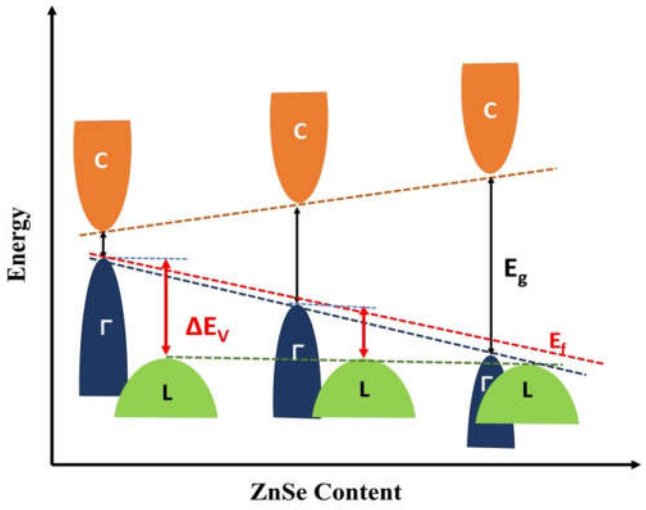

Fig.5.10 Schematics showing the variation in band structures with increasing ZnSe content.

5.3.4. Optical studies

The optical studies of the synthesized samples were done using UV-Vis spectroscopy. The band gap of the synthesized samples was determined using the Tauc plot method, as outlined in the preceding chapters. The obtained values of band gap are shown in table 5.1. The determined band gap value of pristine Cu_2Se is consistent with the literature [32]. As the concentration of ZnSe increased up to 10 wt%, the electronic absorption spectra of the composite samples exhibited a noticeable shift in the absorption edge towards higher energy, in comparison to the pristine sample. We expect an increase in the band gap based on our results from the electrical transport parameters when ZnSe is added to Cu_2Se. The widening of the band gap with increasing ZnSe concentration, attributed to the rise in carrier concentration, aligns well with the Burstein-Moss shift [33]. Therefore, the optical measurements align with and substantiate the observed changes in the electrical transport properties. The increase in the optical band gap implies a reduction in the energy separation between the valence bands [Γ and L], facilitating more controllable band convergence [34]. The convergence of the valence band in composites, substantiated by electrical transport parameters and linked to an increase in the bandgap as per the Kane dispersion model, is likely responsible for the upsurge in the effective mass of DOS [35]. It has been experimentally shown in several similar TE materials that the theoretically predicted widening of the band gap accounts for the observed increase in DOS effective mass [36]. Since there is an increase in the density of states near the Fermi energy, such valence band convergence is expected to contribute to amplification of the Seebeck coefficient due to contribution from both bands. In our work, we note a concurrent change in both the carrier concentration and the Seebeck coefficient upon the introduction of ZnSe into the Cu_2Se lattice, a phenomenon that contradicts the Mott relation. This observation suggests that the elevated DOS effective mass plays a significant role in influencing the inverse relationship between S and n. The significant improvement in the Seebeck coefficient, combined with a notably enhanced carrier concentration, leads to a sharp increase in the power factor.

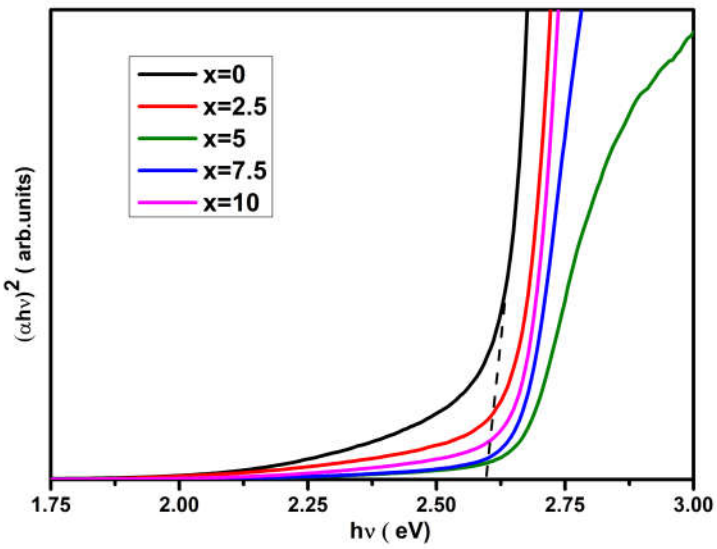

Fig.5.11 Variation in the optical band gap of Cu_2Se + x % ZnSe (x = 0, 2.5, 5, 7.5, and 10) samples.

5.3.5. Thermal transport measurements

Fig.5.12 (a) shows the temperature-dependent total thermal conductivities of all of the samples. Composite materials have the benefit of mixing two different components in order to enhance the thermal transport characteristics. As seen in Fig.5.12 (a), the addition of ZnSe to the Cu_2Se matrix may effectively lower the overall thermal conductivity of Cu_2Se. In comparison to pristine Cu_2Se, all of the samples showed low thermal conductivity. In addition, the total thermal conductivity of all composite phases follows a consistent trend with increasing wt% of ZnSe, with the lowest value of 0.404 W/mK at 573 K obtained for sample containing 5 wt% ZnSe. The obtained values are comparable with literature. Farooq et al reported a thermal conductivity of 0.5 W/mK at 773 K for composite phases of Cu_2Se/Cu_2S, with the composite containing 15% Cu_2S [37]. Qiujun_Hu et al reported a lowest thermal conductivity of 0.45 W/mK at 973 K for Cu_2Se/CDs hybrid materials [38]. Ruiming Lu observed a significant enhancement in the total thermal conductivity at room temperature, reaching 0.65 W/mK, with the incorporation of 0.5 mol% $CuFeSe_2$ into the Cu_2Se matrix [39]. The thermal conductivity reduces with increasing ZnSe concentration, possibly due to point-defect scattering. This decrease in thermal conductivity suggests that the phonon scattering efficiency of the well-dispersed nanostructured ZnSe is quite high. Optical studies shows that ZnSe

addition effectively widen the bandgap and simultaneously bring two valence bands closer together. The improvement in the Seebeck coefficient is facilitated by this band convergence, and the larger bandgap can inhibit the bipolar diffusion that favours the reduction in total thermal conductivity. The results reveal that the inclusion of ZnSe leads to the convergence of valence bands, which modifies the electrical transport characteristics and thermal conductivity.

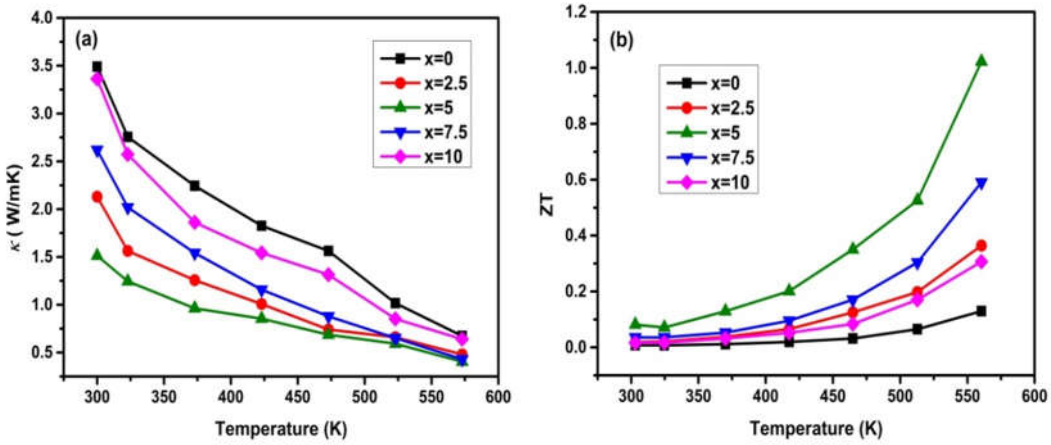

Fig.5.12 Temperature dependence of (a) total thermal conductivity and (b) Figure of merit (ZT) of Cu_2Se + x % ZnSe (x = 0, 2.5, 5, 7.5, and 10) samples.

Benefiting from the superior electrical transport property and the great reduction of thermal conductivity by tuning ZnSe content in Cu_2Se lattice, enhancement in the ZT value is obtained. The Fig.5.12 (b) shows the temperature dependence of ZT for all the samples. It can be shown that the ZT value increases with increasing temperature for pristine and composite samples. The highest ZT value recorded was 1.02 at 573K for Cu_2Se with 5 wt% ZnSe, which is over 8 times higher than that of pristine Cu_2Se. Obviously, the exceptional TE performance of our nanocomposites stems from the high PF value as well as the substantially decreased thermal conductivity. Employing concepts of nanostructuring and band convergence to modify the electronic structure of Cu_2Se by tuning the concentration of ZnSe, one may easily enhance ZT compared to pristine Cu_2Se. These results confirm that introducing ZnSe secondary phase to the Cu_2Se matrix can improve thermoelectric performance for intermediate temperature applications.

5.4. Conclusion

This study introduces the concept of utilizing nanostructured composite materials to enhance the dimensionless thermoelectric figure of merit (ZT). It highlights significant improvement obtained in the thermoelectric performance of p-type Cu_2Se through band structure engineering by the incorporation of ZnSe. By simultaneously modulating the electronic structure and suppressing phonon transport, the study demonstrates how ZnSe boosts the thermoelectric properties of Cu_2Se. The addition of ZnSe effectively tunes the Fermi level, promotes the convergence of light and heavy valence bands, and enhances the density of states, facilitating the decoupling of electrical transport parameters. ZnSe plays a critical role in optimizing p-type charge carriers while simultaneously increasing the Seebeck coefficient due to the strong convergence of valence bands. In this study Cu_2Se-ZnSe nanocomposites were synthesized through mechanical alloying via a planetary ball-milling technique. Structural and morphological studies confirmed the successful formation of Cu_2Se-ZnSe nanocomposites. By carefully optimising the ZnSe concentration, a simultaneous enhancement in electrical conductivity and Seebeck coefficient is achieved, leading to a maximum power factor of 736 $\mu W/mK^2$ at 573 K for the sample with 5 wt% ZnSe. Furthermore, the optical band gap widens with increasing ZnSe content, which suppresses bipolar transport by reducing minority carrier contributions to the Seebeck effect and inhibiting carrier thermal excitation across the band gap. These combined effects result in a remarkable ZT value of 1.02 at 573 K for Cu_2Se with 5 wt% ZnSe. This work presents a controlled strategy for synthesizing Cu_2Se-based thermoelectric nanocomposites and offers an effective approach to designing materials with exceptional thermoelectric performance.

References

[1] C. Bi, T. Se, Enhanced thermoelectric performance of n-type $Cu_{0.008}Bi_2Te_{2.7}Se_{0.3}$ by band engineering, 3 (2015) 10604–10609. https://doi.org/10.1039/c5tc01731a.

[2] Z.H.I. Peng, D. He, X.I.N. Mu, H. Zhou, C. Li, W. Zhu, X. Nie, W. Zhao, Preparation and enhanced thermoelectric performance of Cu_2Se–SnSe composite materials, 47 (2018) 3350–3357. https://doi.org/10.1007/s11664-018-6218-5.

[3] H. Wang, G. Han, B. Zhang, Y. Chen, X. Liu, K. Zhang, X. Lu, G. Wang, X. Zhou, Acta Materialia $AgSbSe_2$ inclusions enabling high thermoelectric and mechanical performance in n-type Ag_2Se-based composites, 248 (2023). https://doi.org/10.1016/j.actamat.2023.118753

[4] M.S. Dresselhaus, G. Chen, Z.F. Ren, G. Dresselhaus, A. Henry, J. Fleurial, New composite thermoelectric materials for energy Harvesting Applications, 8 (2009) 1043-1053. https://doi.org/10.1002/adma.200600527.

[5] S. Yadav, S. Chaudhary, D.K. Pandya, Applied Surface Science, Incorporation of MoS_2 nanosheets in $CoSb_3$ matrix as an efficient novel strategy to enhance its thermoelectric performance, Appl. Surf. Sci. 435 (2018) 1265–1272. https://doi.org/10.1016/j.apsusc.2017.11.262.

[6] Y. Jin, J. Hwang, M.-K. Han, W. Shon, J.S. Rhyee, S. Kim, Size controlled Au-Cu_2Se core-shell nanoparticles and their thermoelectric properties., ACS Appl. Mater. & Interfaces. 12 (2020) 36589-63599. https://doi.org/10.1021/acsami.0c08149.

[7] G.R. Nigmatullina, D.Y. Kovalev, A. V. Karpov, self-propagating high-temperature synthesis of SiC-Doped Cu_2Se compound: thermoelectric properties, Int. J. Self-Propagating High-Temperature Synth. 33 (2024) 319–323. https://doi.org/10.3103/S1061386224700304.

[8] Y. Pei, X. Shi, A. Lalonde, H. Wang, L. Chen, G.J. Snyder, Convergence of electronic bands for high performance bulk thermoelectrics, Nature. 473 (2011) 66–69. https://doi.org/10.1038/nature09996.

[9] J. Tang, Z. Yao, Z. Chen, S. Lin, X. Zhang, F. Xiong, W. Li, Y. Chen, Y. Pei, Maximization of transporting bands for high-performance SnTe alloy thermoelectrics, 9 (2019) 10091. https://doi.org/10.1016/j.mtphys.2019.03.005.

[10] Q. Sun, Z. Chen, M. Li, X. Shi, S. Xu, Y. Yin, M. Dargusch, J. Zou, R. Ang, Z. Chen, Structural evolution of high-performance Mn-alloyed thermoelectric materials : A case study of SnTe, 2100525 (2021) 1–10. https://doi.org/10.1002/smll.202100525.

[11] Y. Pei, A.D. Lalonde, N.A. Heinz, G.J. Snyder, High thermoelectric figure of merit in PbTe alloys demonstrated in PbTe–CdTe, 2 (2012) 1–6. https://doi.org/10.1002/aenm.201100770.

[12] H. Wang, Z.M. Gibbs, Y. Takagiwa, G.J. Snyder, Tuning bands of PbSe for better thermoelectric efficiency, Energy Environ. Sci. 7 (2014) 804–811. https://doi.org/10.1039/c3ee43438a.

[13] C. Soumya, P.P. Pradyumnan, Enhancement of thermoelectric properties of transition metals, nickel and copper dually doped ZnO, Mater. Today Commun. 35 (2023) 106197. https://doi.org/10.1016/j.mtcomm.2023.106197.

[14] M.S. El-asfoury, M.N.A. Nasr, K. Nakamura, Enhanced thermoelectric performance of Bi_{85} Sb_{15} -graphene composite by modulation carrier transport and density of state effective mass, J. Alloys Compd. 745 (2018) 331–340. https://doi.org-/10.1016/j.jallcom.2018.02.040.

[15] M. Lakshmi, K. Bindu, S. Bini, K.P. Vijayakumar, C.S. Kartha, T. Abe, Reversible $Cu_{2-x}Se \leftrightarrow Cu_3Se_2$ phase transformation in copper selenide thin films prepared by chemical bath deposition, 386 (2001) 127–132. https://doi.org/10.1016/S0040-6090(00)01783-1.

[16] A. Marlot, J. Vedel, Electrodeposition of copper-selenium compounds onto gold using a rotating electrochemical quartz crystal microbalance, 146 (1999) 177–183. https://doi.org/10.1016/j.electacta.2022.140676.

[17] L. Zhu, Y. Zhao, W. Zheng, N. Ba, G. Zhang, J. Zhang, X. Li, H. Xie, L. Bie, One-step room temperature rapid synthesis of Cu_2Se nanostructures, phase transformation, and formation of p-Cu_2Se/p-Cu_3Se_2 heterojunctions, CrystEngComm. 18 (2016) 5202–5208. https://doi.org/10.1039/c6ce00370b.

[18] H. Xie, X. Su, G. Zheng, T. Zhu, K. Yin, Y. Yan, C. Uher, M.G. Kanatzidis, X. Tang, The role of Zn in chalcopyrite $CuFeS_2$: Enhanced thermoelectric properties of $Cu_{1-x}Zn_xFeS_2$ with In Situ nanoprecipitates, 10 (2016) 1–14. https://doi.org/10.1002/aenm.201601299.

[19] T.A. Hameed, S.H. Moustafa, H. Shaban, B.A. Mansour, The effect of selenium on the structural , morphology , optical , electrical properties of Cu 2 Te thin films for thermoelectric and photovoltaic applications, Opt. Mater. (Amst). 109 (2020) 110308. https://doi.org/10.1016/j.optmat.2020.110308.

[20] J. Li, Q. Tan, J. Li, D. Liu, F. Li, Z. Li, M. Zou, K. Wang, BiSbTe-Based nanocomposites with high zt : the effect of sic nanodispersion on thermoelectric properties, Adv. Funct. Mater., 23 (2013) 4317-4323. https://doi.org/10.10-02/adfm.201300146.

[21] H. Deng, X. Lou, W. Lu, J. Zhang, D. Li, S. Li, Q. Zhang, X. Zhang, X. Chen, D. Zhang, Y. Zhang, G. Tang, nano energy high-performance eco-friendly MnTe thermoelectrics through introducing SnTe nanocrystals and manipulating band structure, 81 (2021) 105649. https://doi.org/10.1016/j.nanoen.2020.105649.

[22] B. Madavali, D. Shin, D. Kim, S. Hong, Intermetallics Enhanced thermoelectric properties by e ff ective decoupling of electrical , thermal properties and seebeck coe ffi cient through the addition of rare earth sesquioxides in p-type BiSbTe alloys, Intermetallics. 105 (2019) 139–145. https://doi.org/10.1016/j.intermet.2018.11.017.

[23] T. Parvathy, P.P. Pradyumnan, Impact of mobility and effective mass on the thermoelectric performance of Ni doped Cu_2Se, J. Alloys Compd. 970 (2024) 172615. https://doi.org/10.1016/j.jallcom.2023.172615.

[24] X. Cai, H. Jing, H. Wuliji, H. Zhu, Xiaomeng Cai, § Huirong Jing, Hexige Wuliji, Valence Band Structure Degeneracy Enhanced Thermoelectric Performance in β-Cu_2Se and Hong Zhu, J. Phys. Chem. C 127 (2023) 5576-5583. https://doi.org/10.1021/acs.jpcc.2c08797.

[25] A. Pakdel, Q. Guo, V. Nicolosi, T. Mori, Enhanced thermoelectric performance of Bi-Sb-Te/Sb_2O_3 nanocomposites by energy filtering effect, J. Mater. Chem. A. 6 (2018) 21341–21349. https://doi.org/10.1039/c8ta08238c.

[26] Y. Chen, Y. Zhang, P.F.P. Poudeu, R. Lu, T.P. Bailey, Nanoscale Advances $CuInSe_2$ hierarchical composites, 13 (2022) 4279–4290. https://doi.org/10.1039/d2na00230b.

[27] Y. You, X. Su, S. Hao, W. Liu, Y. Yan, Ni and Se co-doping increases the power factor and thermoelectric performance of CoSbS, 6 (2018) 15123–15131. https://doi.org/10.1039/c8ta05572f.

[28] A. Paulson, N.A.M. Sabeer, P.P. Pradyumnan, A synergetic approach of band gap engineering and reduced lattice thermal conductivity for the enhanced thermoelectric property in Dy ion doped ZnO, J. Alloys Compd. 786 (2019) 581–587. https://doi.org/10.1016/j.jallcom.2019.01.336.

[29] V. Vijay, S. Harish, J. Archana, M. Navaneethan, Journal of Colloid and Interface Science Realization of an ultra-low lattice thermal conductivity in $Bi_2Ag_xSe_3$ nanostructures for enhanced thermoelectric performance, J. Colloid Interface Sci. 637 (2023) 340–353. https://doi.org/10.1016/j.jcis.2023.01.042.

[30] H. Wu, C. Chang, D. Feng, Y. Xiao, X. Zhang, Y. Pei, Environmental Science Synergistically optimized electrical and thermal transport properties of SnTe via alloying high- solubility MnTe, (2015) 8 3298–3312. https://doi.org/10.1039/c5ee02423d.

[31] T. Parvathy, K. V. Nabeela, P.P. Pradyumnan, Raman structural transition studies and optical band calculation on the multiphase of tin selenides, Mater. Chem. Phys. 301 (2023) 127622. https://doi.org/10.1016/j.matchemphys.2023.127622.

[32] M. Petrovi, M. Gili, Ć. Jovana, M. Rom, N. Rom, J. Traji, I. Yahia, Optical properties of CuSe thin films – band gap determination, 49 (2017) 167–174. https://doi.org/10.2298/SOS1702167P.

[33] P. Shyni, P.P. Pradyumnan, Fermi level tuning in modified Bi_2Te_3 system for thermoelectric applications, RSC Adv. 11 (2021) 4539–4546. https://doi.org/10.1039/d0ra09278a.

[34] A. Banik, U.S. Shenoy, S. Anand, U. V Waghmare, K. Biswas, Mg alloying in SnTe facilitates valence band convergence and optimizes thermoelectric properties, 27 (2014) 581-587. https://doi.org/10.1021/cm504112m.

[35] T. Parashchuk, B. Wiendlocha, O. Cherniushok, R. Knura, K.T. Wojciechowski, high thermoelectric performance of p-type PbTe enabled by the synergy of resonance scattering and lattice softening, ACS Appl. Mater. Interfaces. 13 (2021) 49027–49042. https://doi.org/10.1021/acsami.1c14236.

[36] S. Das, P. Singha, R. Daou, O.I. Lebedev, S. Hébert, A. Maignan, A. Banerjee, Physical review materials 6, 035401 (2022) Improvement of thermoelectric

performance in Sb_2Te_3/Te composites, 035401 (2022) 1–11. https://doi.org/10.1103/PhysRevMaterials.6.035401.

[37] M.U. Farooq, S. Butt, K. Gao, X. Sun, X. Pang, S.U. Khan, Enhanced thermoelectric ef fi ciency of Cu $_2$ À $_x$ Se – Cu_2S composite by incorporating Cu_2S nanoparticles, 42 (2016) 8395–8401. https://doi.org/10.1016/j.ceramint.2016.02.055.

[38] Q. Hu, Y. Zhang, Y. Zhang, X. Li, H. Song, High thermoelectric performance in Cu_2Se /CDs hybrid materials, J. Alloys Compd. 813 (2020) 152204. https://doi.org/10.1016/j.jallcom.2019.152204.

[39] R. Lu, T.P. Bailey, C. Uher, P.F.P. Poudeu, Ultrafine interwoven dendritic Cu_2Se-$CuFeSe_2$ composites with enhanced thermoelectric performance, 9 (2020) 9133-9142. https://doi.org/10.1021/acsaem.0c01525.

Chapter-6

Modification of the thermoelectric properties of Cu_2Se through MgO inclusions

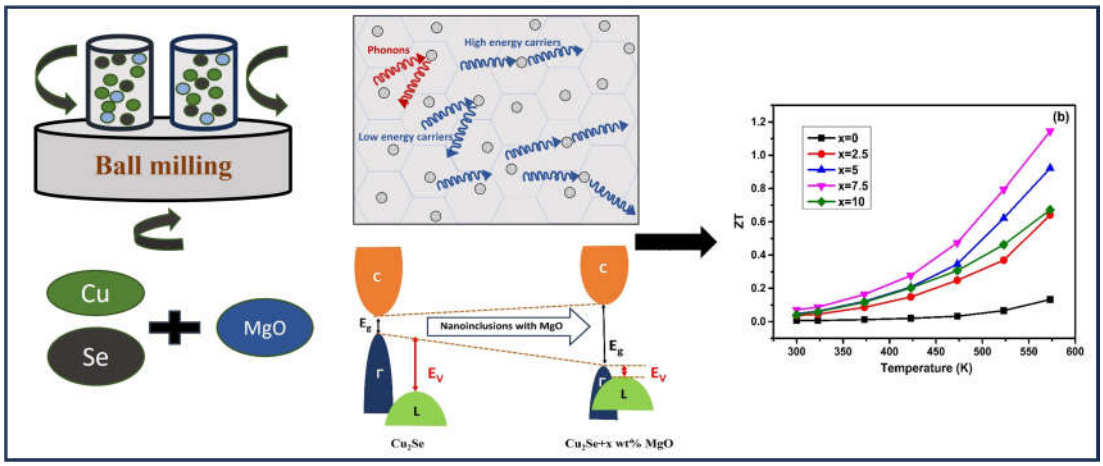

This chapter investigates the enhancement obtained in the thermoelectric properties of Cu_2Se through MgO nanoinclusions. MgO introduces energy filtering, addressing challenges like bipolar carrier transport, which typically reduces the Seebeck coefficient and increases thermal conductivity. Through the ball milling technique, Cu_2Se-MgO composites with well-defined interfaces are created, enhancing the Seebeck coefficient via valence band convergence and interface energy filtering. Additionally, controlling the Cu vacancies optimizes the carrier concentration, leading to an improvement in the overall thermoelectric performance.

6.1. Introduction

Recently, researchers have identified thermoelectric (TE) nanocomposites as a promising approach to simultaneously enhance both TE efficiency and mechanical properties [1,2]. This strategy improves TE efficiency mainly by reducing thermal conductivity through scattering mechanisms that affect both phonons and charge carriers. It also increases the power factor by employing an energy filtering mechanism, which selectively regulates the carrier energy [2]. To enhance the Seebeck coefficient, a crucial parameter in thermoelectric materials, it is essential to precisely optimize the carrier concentration. This optimization ensures an optimal balance between electrical conductivity and thermal conductivity. The Seebeck coefficient (S) depends on the difference between the average energy of charge carriers (E_J) and the Fermi level (E_f), expressed as [3]

$$S = \frac{|E_J - E_f|}{KT} \quad \text{.....(6.1)}$$

S is enhanced when high-entropy carriers contribute significantly to conductivity, as their presence promotes greater energy transport. By controlling the scattering behavior of these carriers, their mobility can be increased while concurrently lowering thermal conductivity. Moreover, increasing the effective mass of charge carriers can further boost the Seebeck coefficient by increasing the density of states near the Fermi level. One effective approach to significantly increase the Seebeck coefficient without reducing conductivity is through energy filtering, which selectively enhances the contribution of high-entropy carriers to electrical conductivity. To facilitate energy filtering, a material with a distinct Fermi level is usually incorporated into a thermoelectric material. The interface between these two materials creates an energy barrier that selectively scatters low energy charge carriers, thus raising the average energy of the remaining charge carriers. This process improves the S and consequently, the thermoelectric conversion efficiency [4]. Additionally, phonon scattering at the newly formed interfaces can substantially reduce thermal conductivity.

Recent strategies to improve the thermoelectric efficiency of Cu_2Se include adding secondary phases to lower thermal conductivity, optimizing carrier concentration to

boost the Seebeck coefficient, using band engineering to tune the electronic properties, doping to enhance charge carrier mobility, and nanostructuring to increase phonon scattering and electrical conductivity [5,6]. However, while these strategies appear promising, recent research highlights the effectiveness of inducing the energy filtering effect via matrix energy barriers. Oxide nanoinclusions, known for their chemical inertness, simplicity, and cost-effectiveness, enhance thermoelectric efficiency by improving thermal and phase stability, reducing thermal conductivity (κ), and strengthening mechanical properties. This enables a controlled enhancement of the ZT in any thermoelectric material [7]. Incorporating oxide nanoparticles into a Cu_2Se matrix has proven effective in enhancing the thermoelectric properties. Ma et al. demonstrated significant thermoelectric enhancement in nano Y_2O_3 dispersed Cu_2Se [8]. Incorporating a nanosecond phase like Y_2O_3 into the Cu_2Se matrix effectively alters grain size, enhancing phonon scattering and reducing thermal conductivity through increased interface scattering. However, this modification does not alter the Seebeck coefficient. Selecting suitable secondary phases can enhance the Seebeck coefficient by inducing the energy filtering effect through potential energy barriers within the matrix [9]. Mani et al. reported that incorporating CuO nanoparticles into a Cu_2S matrix significantly reduces the thermal conductivity by enhancing phonon scattering through embedded nanoparticles and phase boundaries [10]. Additionally, the Seebeck coefficient increases due to the filtration of low energy carriers at CuO potential barriers, resulting in an overall increase in conversion efficiency [11]. This motivated the present study, which investigates the enhancement of thermoelectric conversion efficiency in Cu_2Se by incorporating magnesium oxide (MgO) into the host matrix using the planetary ball milling technique. Incorporating thermally, chemically, and physically stable MgO naninclusions into the superionic host matrix of Cu_2Se can effectively balance the relationship between carrier concentration, Seebeck coefficient, and electrical and thermal conductivity. This approach helps to achieve high electrical conductivity while reducing thermal conductivity, thereby enhancing the overall thermoelectric performance of the material. The Seebeck coefficient of the composite experiences notable enhancement through optimizing the carrier concentration and the energy filtering effect at phase interfaces, effectively scattering low-energy carriers. Additionally, the study elucidated the potential for an energy filtering effect on the Seebeck coefficient, along with the mechanism of

carrier or phonon scattering that affects thermal conductivity at newly formed interfaces.

6.2. Experimental details

Cu_2Se-MgO nanocomposites were synthesized using the ball milling technique. All chemicals were purchased from Alfa Aesar, with copper (99.5%), selenium (99.9%), and MgO (99.9%) obtained in powder form and used without further purification. To synthesize pristine Cu_2Se, Cu and Se powders taken in a stochiometric ratio were milled in a planetary ball mill for an optimized time period of 12 hours. The ball to powder ratio was set at 10:1 with a milling speed of 200 rpm. For the synthesis of Cu_2Se-MgO composites, we used varying weight percentages (2.5 wt%, 5 wt%, 7.5 wt%, and 10 wt%) of MgO relative to Cu and Se. The composite samples are synthesized in the same route as pristine Cu_2Se. The synthesized samples were then pressed into a circular pellet (13mm diameter, 3mm thickness) using a hydraulic pelletizer with an applied force of approximately 10 tonnes in air. The densified pellet was then sintered at 300°C for 3 hours in a vacuum before undergoing characterization. The structural, morphological, optical, and thermoelectric properties of the sintered pellets were analyzed. A detailed explanation of the synthesis process and characterization techniques were provided in chapter 2.

6.3. Results and discussion

6.3.1. Phase and structure analysis

The crystal structures and phase purities of Cu_2Se + x wt% MgO (x = 0, 2.5, 5, 7.5 and 10 wt%) composites were analyzed via powder X-ray diffraction (PXRD) technique with CuK_α radiation (λ = 1.5408 Å) at room temperature, scanning at 10°/min from 10° to 80° in 2θ. Fig.6.1 shows that the diffraction peaks align with the primary peaks of Cu_2Se, exhibiting Bragg angles at 26.73°, 30.91°, 44.40°, 52.53°, 64.51°, and 71.13°, which correspond to the (111), (200), (220), (311), (400), and (331) crystallographic planes of the cubic Cu_2Se phase (ICDD-03-065-2982). As the MgO content increases, no noticeable changes are observed in the diffraction peaks for MgO content up to 2.5 wt%. However, distinct changes become apparent when the concentration exceeds 2.5 wt%. For composites containing MgO concentration >

2.5 wt%, an additional diffraction peak appears at 42.4°, corresponding to the (200) crystallographic planes of the cubic MgO phase (ICDD-01-087-0653). As the MgO content increases to 7.5 wt%, the diffraction peak of MgO becomes distinctly visible. At a MgO content of 10 wt%, along with Cu_2Se and MgO, peaks corresponding to the tetragonal Cu_3Se_2 phase (ICDD-03-065-1656) are also visible in the diffraction pattern. The introduction of higher wt% of MgO can significantly alter the chemical environment, influencing the formation energies and stability of various phases, which can promote the formation of Cu_3Se_2 along with the Cu_2Se phase [11].

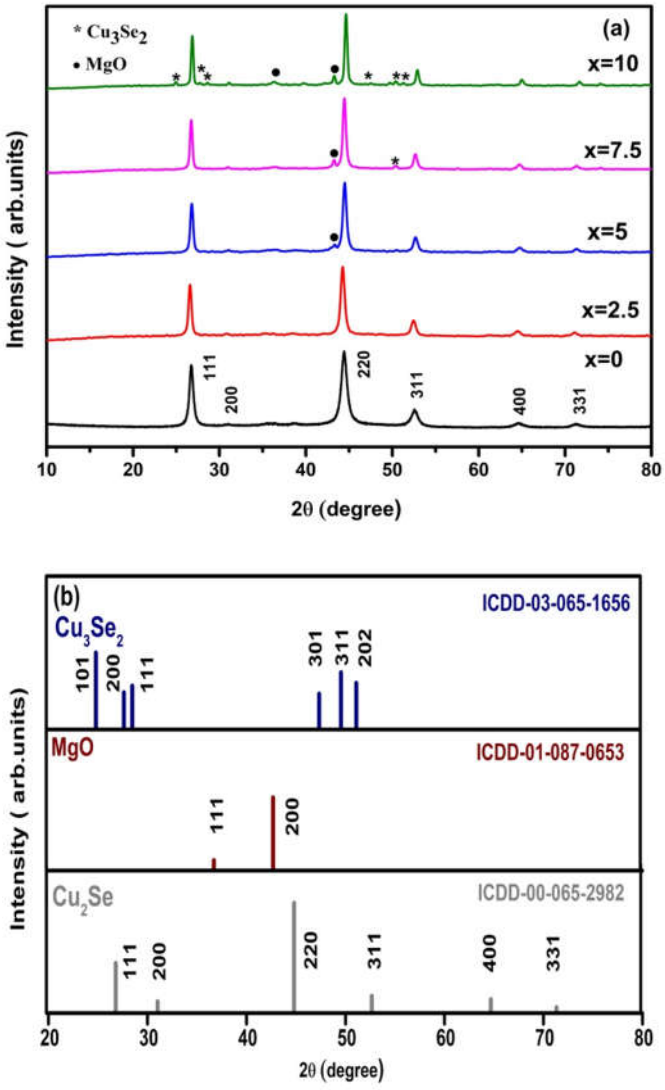

Fig.6.1 (a) PXRD patterns showing Cu_2Se + x % MgO (x = 0, 2.5, 5, 7.5, and 10) samples and (b) ICDD database of Cu_2Se, MgO and Cu_3Se_2.

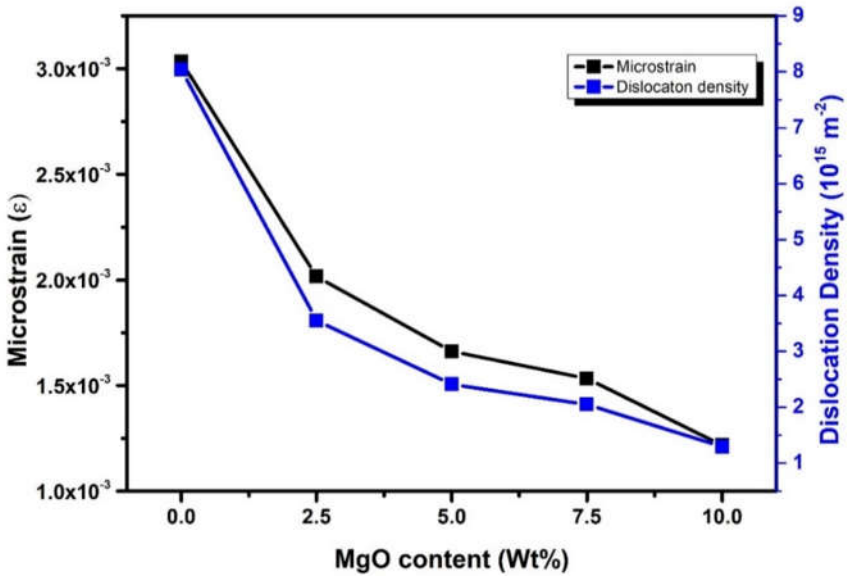

Fig.6.2 Variation of microstrain and dislocation density with increasing MgO content.

The inclusion of MgO in the Cu_2Se matrix alters the microstructural parameters by affecting the crystallite size (D). This, in turn, influences the microstrain (ε) and dislocation density [12,13]. The average crystalline size, dislocation density, and microstrain for all samples have been calculated using the formulas reported in the previous chapter 2. Fig.6.2 illustrates the variations in microstrain, and dislocation density of all samples as the MgO content increases. The Full width half maximum (FWHM) of the sample decreases with an increase in MgO content which shows an increase in the crystallinity. The calculated crystalline size ranges from 11.15 nm to 27.79 nm for pristine and composite samples. The larger crystallite sizes observed in samples with higher MgO content highlight MgO's role in promoting grain growth and inhibiting the formation of smaller crystallites. MgO particles act as grain growth promoters, allowing the smaller crystallites to coalesce into larger grains. This growth mechanism leads to the reduction of grain boundaries and an overall increase in crystallite size. Increasing the concentration of MgO in Cu_2Se suggests a decrease in microstrain and dislocation density compared to pristine sample. This decrease in microstrain with increasing MgO content can be attributed to the effective dispersion of MgO particles within the Cu_2Se matrix. This dispersion helps to alleviate internal stresses and promotes more uniform grain growth.

Additionally, the presence of MgO at grain boundaries can act as a barrier to dislocation movement, thereby reducing dislocation density and enhancing overall structural stability. It was clearly indicated that both the microstrain and the dislocation density decrease with an increase in MgO content, allowing carriers to move more freely within the lattice. This observation aligns with the well-known phenomenon where an increase in crystallite size typically results in reduced microstrain and dislocation density in the material [14,15]. The strain induced by MgO incorporation may facilitate better charge carrier mobility by minimizing potential barriers at grain boundaries. This can enhance the Seebeck coefficient and overall thermoelectric performance. The optimization of microstructure through precise control of MgO content is therefore crucial for tuning the physical properties of Cu_2Se based thermoelectric materials. This strategy underscores the importance of compositional modifications in achieving desirable thermoelectric characteristics by balancing grain size, strain, and defect density.

6.3.2. Morphological studies

The morphology of the synthesized materials was analyzed using high resolution FESEM, as shown in Fig. 6.3. The pristine Cu_2Se sample shows a layered nanoflake-like morphology, characteristic of its structure. As MgO is introduced, the grain boundaries become more distinct, and the surface roughness increases, indicating the dispersion of MgO within the Cu_2Se matrix. These morphological changes indicate that the addition of MgO disrupts the uniform structure of the Cu_2Se matrix, likely affecting its electrical and thermal properties by altering the mechanisms for electron and phonon transport.

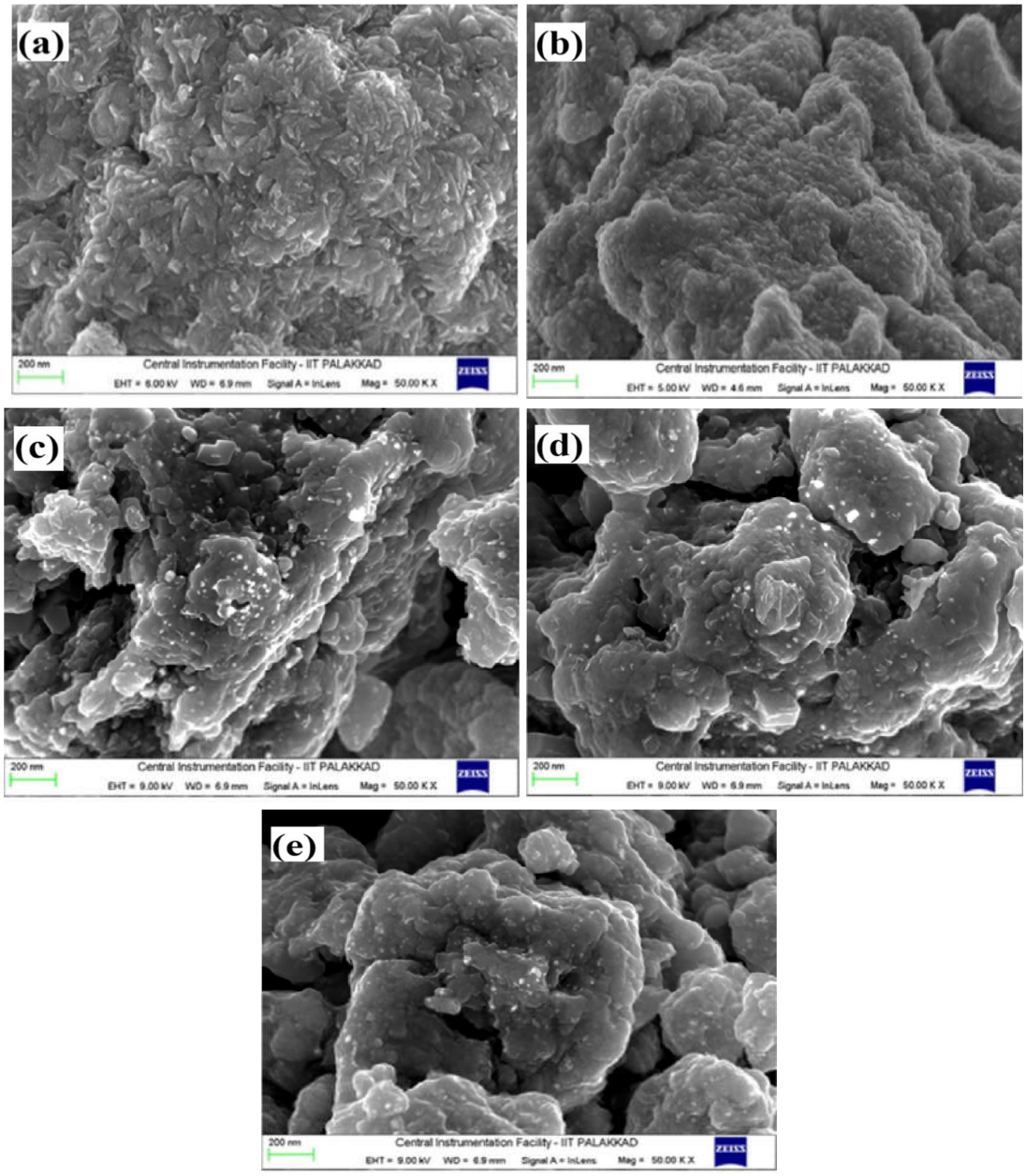

Fig.6.3 FESEM images of Cu_2Se + x wt% MgO composites with (a) x=0, (b) x=2.5, (c) x=5, (d) x=7.5, and (e) x=10.

The compositional analysis of the MgO sample was performed using the EDS technique as shown in Fig.6.4. Figure shows that only the peak corresponding to Cu and Se is detected in pristine samples. For all the composites samples no peaks associated with elements other than Cu, Se, Mg, and O are observed, which is compatible with the PXRD results. Fig.6.5 presents the EDS mapping for the sample with 7.5 wt% MgO, showing the distribution of Cu, Se, Mg, and O.

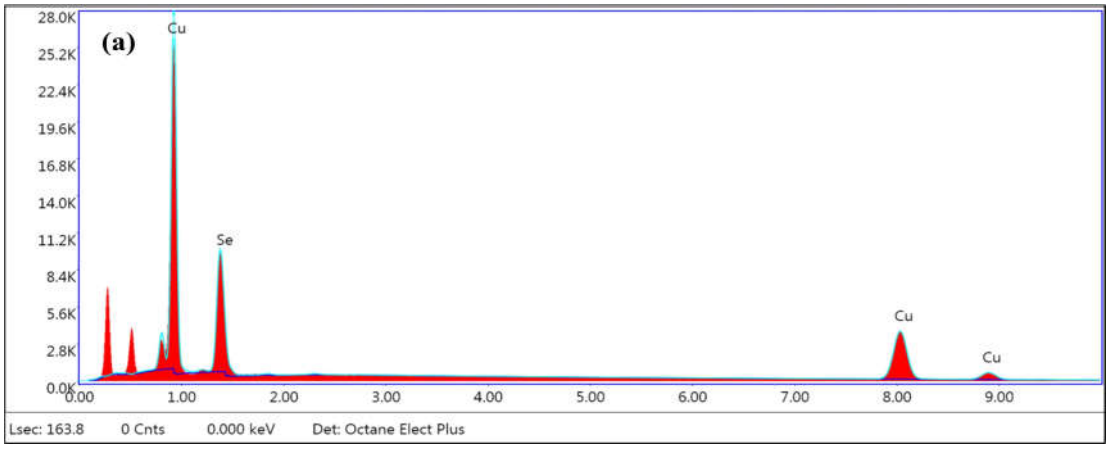
(a)
Cu
Se
Cu
Cu
28.0K
25.2K
22.4K
19.6K
16.8K
14.0K
11.2K
8.4K
5.6K
2.8K
0.0K
0.00 1.00 2.00 3.00 4.00 5.00 6.00 7.00 8.00 9.00
Lsec: 163.8 0 Cnts 0.000 keV Det: Octane Elect Plus

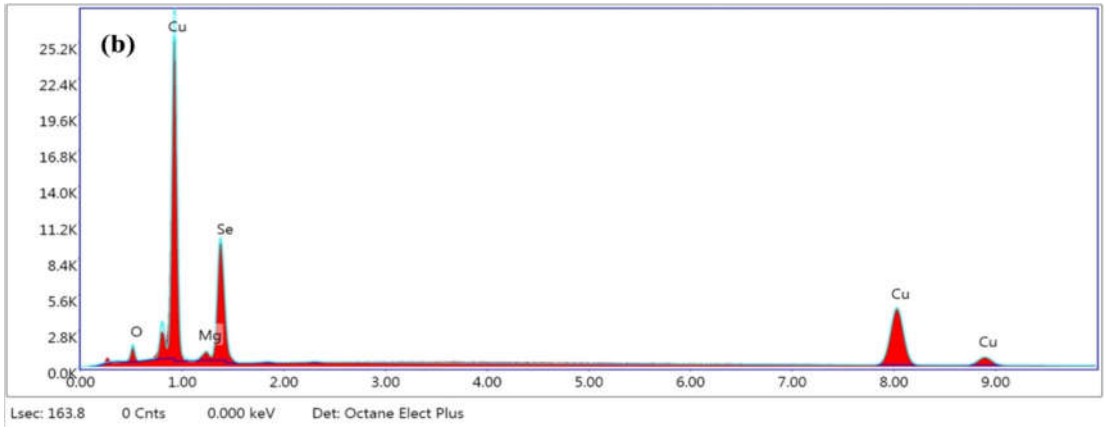
(b)
Cu
Se
O
Mg
Cu
Cu
25.2K
22.4K
19.6K
16.8K
14.0K
11.2K
8.4K
5.6K
2.8K
0.0K
0.00 1.00 2.00 3.00 4.00 5.00 6.00 7.00 8.00 9.00
Lsec: 163.8 0 Cnts 0.000 keV Det: Octane Elect Plus

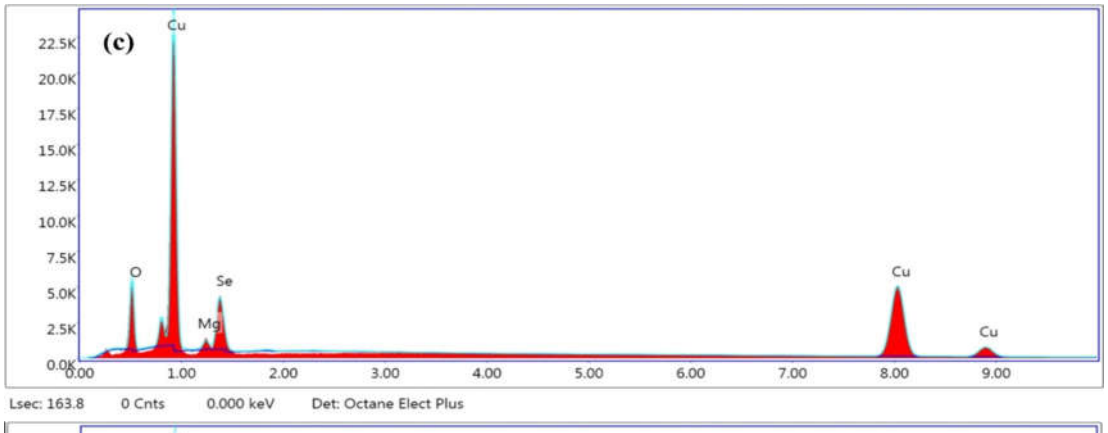
(c)
Cu
O
Se
Mg
Cu
Cu
22.5K
20.0K
17.5K
15.0K
12.5K
10.0K
7.5K
5.0K
2.5K
0.0K
0.00 1.00 2.00 3.00 4.00 5.00 6.00 7.00 8.00 9.00
Lsec: 163.8 0 Cnts 0.000 keV Det: Octane Elect Plus

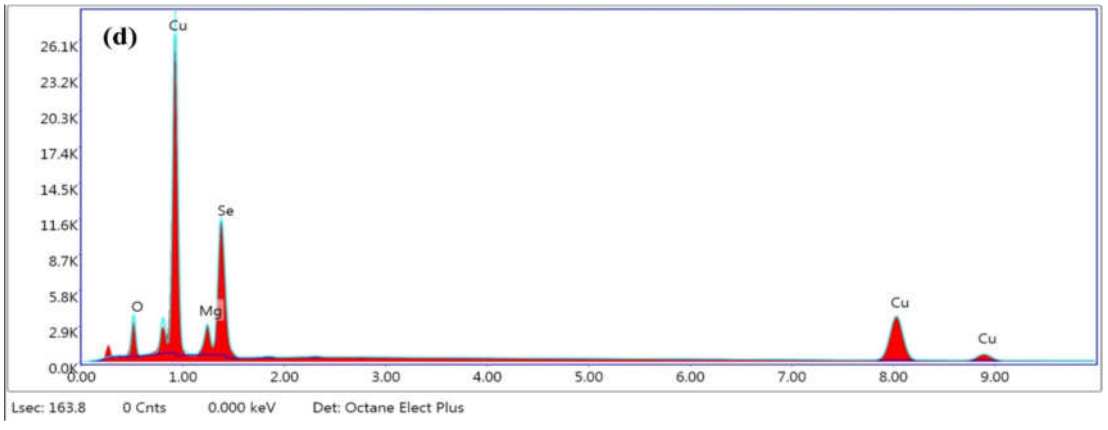
(d)
Cu
Se
O
Mg
Cu
Cu
26.1K
23.2K
20.3K
17.4K
14.5K
11.6K
8.7K
5.8K
2.9K
0.0K
0.00 1.00 2.00 3.00 4.00 5.00 6.00 7.00 8.00 9.00
Lsec: 163.8 0 Cnts 0.000 keV Det: Octane Elect Plus

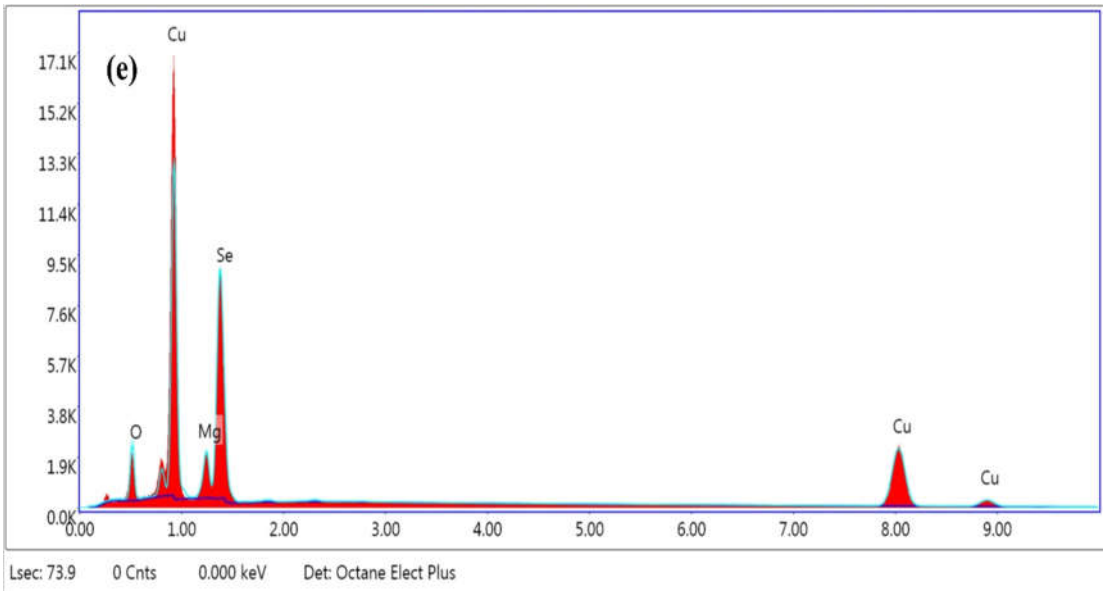

Fig.6.4 EDS spectrum of Cu_2Se + x wt% MgO composites with (a) x=0, (b) x=2.5, (c) x=5, (d) x=7.5, and (e) x=10.

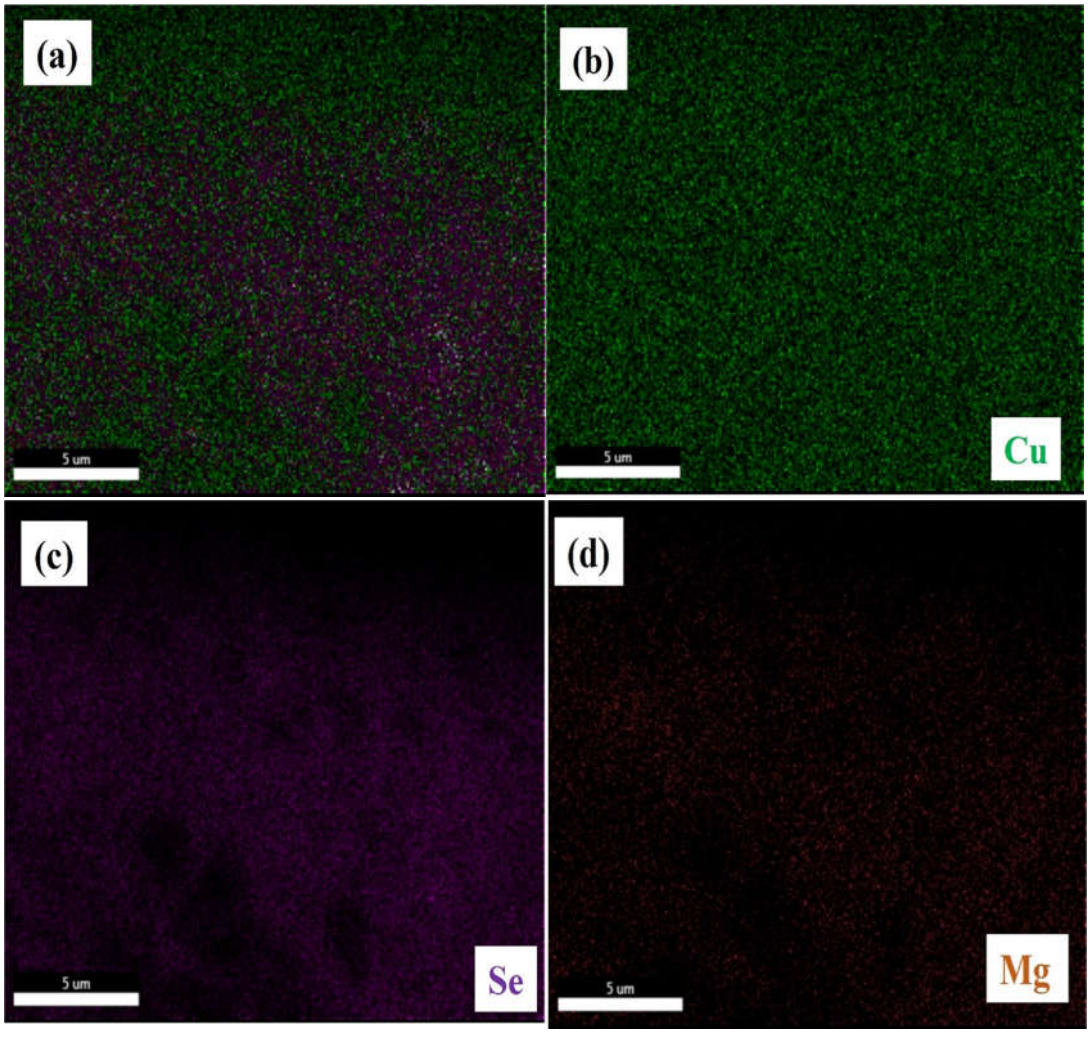

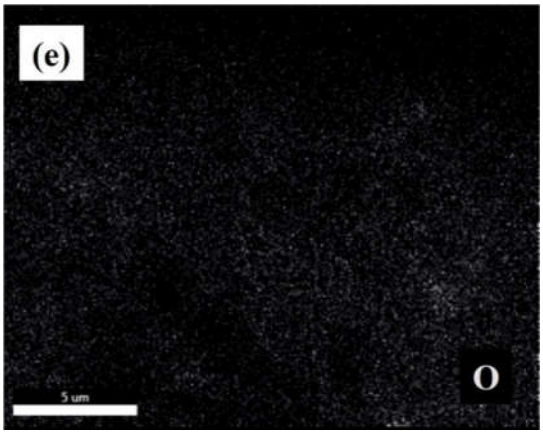

Fig.6.5 EDS elemental mapping for the Cu_2Se sample with 7.5 wt% MgO showing (a) the combined distribution of all elements, (b) the distribution of Cu, (c) Se, (d) Mg, and (e) O.

HRTEM was employed to investigate the microstructure of MgO within the Cu_2Se matrix, aiming to enhance the understanding of how MgO nanoparticles influence the thermoelectric properties. Fig.6.6 presents the HRTEM analysis of the Cu_2Se sample with 7.5 wt% MgO sample, confirming the distribution of MgO nanoparticles within the Cu_2Se matrix. Fig.6.6 (a) and (b) show the formation of Cu_2Se and MgO nanoparticle agglomerates. At lower magnification, the image reveals a broader view of the well dispersed Cu_2Se and MgO nanoparticles, though some agglomeration is observed. The particles exhibit clustering or aggregation, a typical phenomenon when a secondary material, such as MgO, is incorporated into the host matrix. Fig.6.6 (c) presents a closer view of the particle structure, revealing individual Cu_2Se particles or nanocrystals, with MgO nanoparticles interspersed between them. The inclusion of MgO could potentially improve the crystallinity or influence the electronic properties at the interfaces. This high magnification image shown in Fig 6.6 (d) shows the atomic arrangement within the nanocrystals, providing details on the crystal planes and the interface between Cu_2Se and MgO. The image shows a distinct interface characterized by a contrast difference, which may indicate a phase boundary between the Cu_2Se matrix and MgO inclusions. This heterogeneous barrier likely arises from the dispersion of MgO particles within the Cu_2Se matrix, creating a phase boundary that could impede carrier or phonon movement. Such barriers are advantageous in thermoelectric materials, as they can lower thermal conductivity by scattering phonons while preserving electrical transport, thereby enhancing thermoelectric performance.

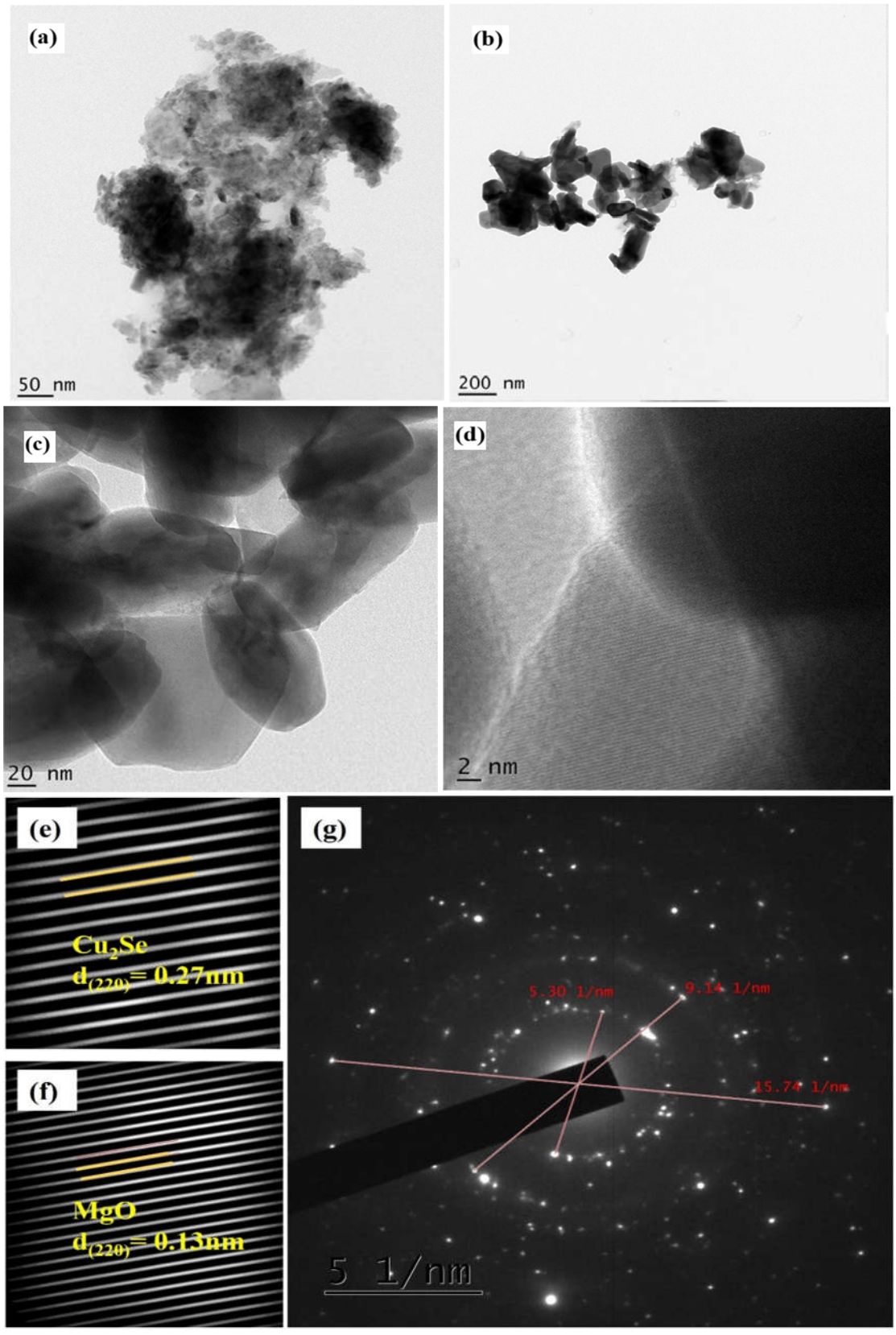

Fig.6.6 (a-d) HR-TEM image, (e,f) d-spacing of lattice planes of Cu_2Se and MgO, and (g) SAED pattern of the Cu_2Se with 7.5 wt % MgO samples.

The lattice d-spacing values were calculated using ImageJ software are shown in Fig.6.6 (e). The figure shows d-spacing values of 0.27 nm and 0.13 nm, corresponding to the (220) planes of cubic Cu_2Se and the (220) planes of cubic MgO phase, respectively. The selected area electron diffraction (SAED) pattern of the sample shown in Fig.6.6 (f), confirms the polycrystalline nature and high crystallinity of the sample. Distinct diffraction spots corresponding to the (111) and (220) planes of cubic Cu_2Se, as well as the (220) planes of cubic MgO, are clearly visible, in agreement with the PXRD diffraction data for these phases. The d-spacing values derived from the SAED pattern, specifically 0.377 nm, 0.219 nm, and 0.127 nm, precisely align with the interplanar spacings of the (111) and (220) planes of Cu_2Se and the (220) planes of MgO, respectively. This confirms the successful formation of a composite structure where MgO is present as a distinct crystalline phase embedded within the Cu_2Se matrix. The symmetrical and well defined diffraction spots further underscore the composite's high degree of crystallinity and structural order.

6.3.3. Thermoelectric measurement studies

The thermoelectric properties of Cu_2Se with varying MgO contents (x = 2.5, 5, 7.5, and 10) were examined over a range of temperatures, as illustrated in Fig.6.7. As shown in Fig.6.7 (a), the electrical conductivity (σ) exhibits a linear monotonic decrease with increasing temperature. This behavior, indicative of metal-like conduction is typical for heavily doped degenerate semiconductors. In TE materials, an increase in S is accompanied by a decrease in σ, and vice versa [16]. As temperature rises, the S of all samples increases as shown in Fig.6.7 (b). In the observed measurement range, the Seebeck coefficient exhibits a trend opposite to that of conductivity. The positive values of the Seebeck coefficient indicate that both pristine Cu_2Se and its composites with MgO exhibit p-type semiconductor behavior, with holes being the majority charge carriers.

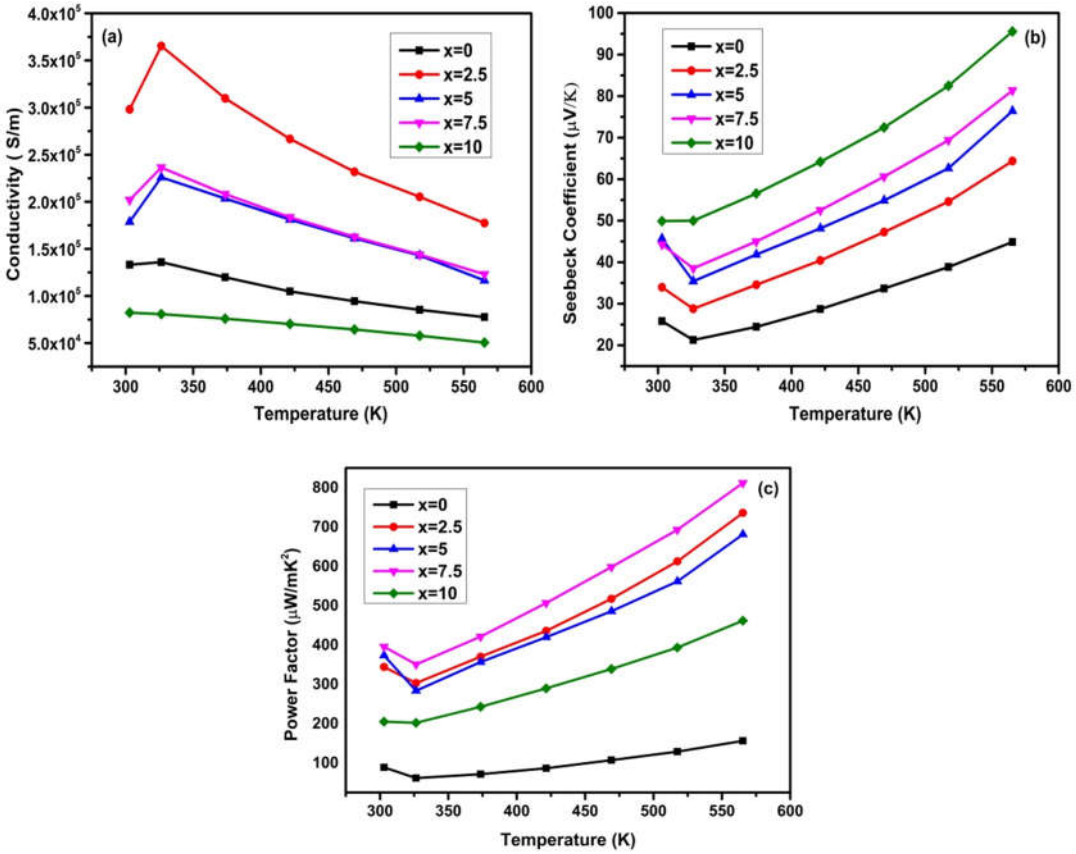

Fig.6.7 Variation of (a) electrical conductivity (b) Seebeck coefficient (c) power factor of Cu_2Se + x % MgO (x = 0, 2.5, 5, 7.5, and 10) samples.

The Seebeck coefficient of the composites exhibited a notable increase compared to the pristine samples. This improvement is due to the efficient energy-filtering effect caused by the incorporation of potential barriers with appropriate bandgap. By incorporating MgO into the lattice of Cu_2Se, numerous phase interfaces are created, further enhancing the energy filtering effect and contributing to the observed increase in the Seebeck coefficient. This effect selectively facilitates the passage of high-energy charge carriers, enhancing the overall Seebeck coefficient [17,18]. To further comprehend the energy filtering mechanism, Hall measurements performed on the samples are depicted in Fig.6.9. The results indicate that the carrier concentration gradually decreased with increasing MgO doping concentration. As the MgO concentration increases, the concentration of charge carriers decreases while the mobility increases compared to the pristine sample. This phenomenon is attributed to a band structure mismatch between the dispersed MgO and the Cu_2Se lattice. The formation of Cu_2Se-MgO composites creates a heterogeneous interface,

leading to changes in the electronic transport properties of the material. These heterogeneous interfaces serve as energy barriers, effectively scattering the charge carriers within the matrix. These potential barriers enhance the energy filtering effect, leading to a more efficient blocking of low-energy carriers from contributing to conductivity. Consequently, only higher energy electrons are able to pass through, resulting in improved energy filtering as shown in Fig.6.8. As a result, the S increases gradually due to the predominance of high-energy carriers in the energy transfer process [19]. Additionally, the Hall mobility increases compared to the pristine sample as the MgO content rises to 7.5 wt%. This increase in mobility is likely due to the formation of asymmetric potentials within the host matrix, which weakens the scattering of the majority carriers.

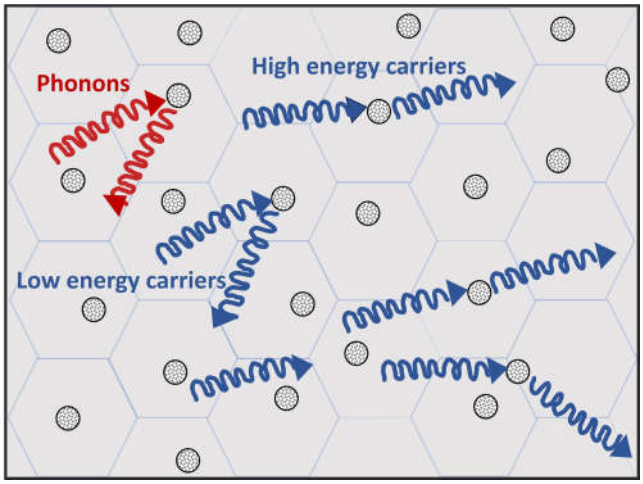

Fig.6.8 The schematic of energy filtering in Cu_2Se-MgO nanocomposites.

Energy filtering usually reduces electrical conductivity at a given fermi level because it obstructs the movement of low energy charge carriers which reduces carrier concentration. As a result, many charge carriers no longer participate in the transport process [20]. However, in this work, the introduction of MgO nanoparticles results in an increase in conductivity as the MgO content increases to 7.5 wt %. This phenomenon can be attributed to carrier channeling, where MgO nanoparticles facilitate more efficient transport pathways for charge carriers, enhancing conductivity. Initially, both the σ and the S of the composite samples increase as the MgO content rises to 2.5 wt%. Subsequently, the conductivity

decreases, but it remains higher than in pristine samples as the MgO content increases to 7.5 wt%. Beyond this point, the conductivity continues to decrease. However, it's essential to note that as the MgO content increases, the Seebeck coefficient of all samples surpasses that of pristine Cu_2Se. Consequently, all these factors collectively contribute to the enhanced power factor observed in the composites. The power factor for all composites was determined, and its variation with temperature is shown in Fig.6.7 (c). The PF values of all the samples clearly indicate that the Seebeck coefficient has a greater influence than the electrical conductivity. A maximum PF of approximately 811 μW/mK² was observed for the sample containing 7.5 wt% MgO. These results demonstrate that the improvement in PF for all the composites is attributed to the monotonic increase in the S with temperature.

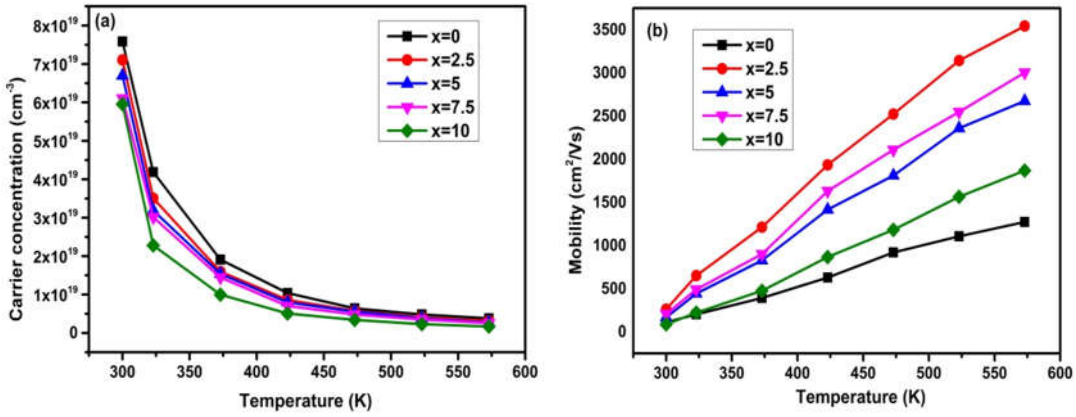

Fig.6.9 Variation of (a) carrier concentration and (b) mobility of Cu_2Se + x % MgO (x = 0, 2.5, 5, 7.5, and 10) samples.

The Seebeck coefficient is commonly defined using the Mott equation which is explained in detail in chapter 3, as follows [21]

$$S=\frac{8\Pi^2 k_B{}^2}{3eh^2}\, m^*T\left(\frac{\Pi}{3n}\right)^{2/3} \quad \ldots\ldots (6.2)$$

The Seebeck coefficient is influenced by both carrier concentration and carrier effective mass. The effective mass (m*) of charge carriers, which plays a crucial role in determining the Seebeck coefficient of composites, is influenced by changes in their electronic structure. The estimated effective mass (m*), calculated using the

measured S and n at different temperatures is shown in Fig.6.10. It can be observed that as x increases from 0 to 10, m* increases from 0.23 m_0 to 0.38 m_0 (m_0 is the free electron mass). It is reasonable to assume that the rise in the S with the addition of MgO is attributed to an increase in the effective mass of the density of states (DOS) [22]. The presence of nanoparticles and interfaces can indeed modify the electronic band structure of a material, leading to changes in the effective mass. When the effective mass increases, it means there are more available electronic states near the Fermi level. This increase in available states enhances the energy dependency of the Seebeck coefficient. With more states available, the probability of high energy carriers contributing to electrical conductivity is higher. These high-energy carriers are less affected by scattering compared to low energy carriers, further emphasizing the importance of the energy dependency of the Seebeck coefficient in thermoelectric materials [23]. Also, such an introduced interface affects the movement of the charge carriers which strongly scatters low energy carriers, leading to lowering the electrical conductivity. This form of energy filtering effectively boosts the Seebeck coefficient.

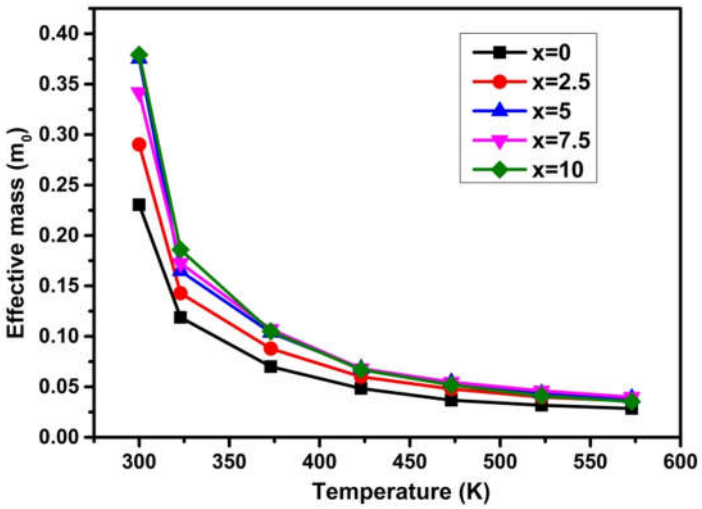

Fig.6.10 Temperature dependence of carrier effective mass of Cu_2Se + x % MgO (x = 0, 2.5, 5, 7.5, and 10) samples.

6.3.4. Optical studies

The absorbance spectra of all the samples were analyzed using a UV-Visible

spectrophotometer to evaluate their optical bandgap. The energy bandgap was estimated utilizing the Tauc plot method as outlined in chapter 3. Fig 6.11 (a) illustrates the trend of increasing energy bandgap with increasing concentrations of MgO. The calculated optical band gaps of the samples are shown in table 6.1. The band gap increases as the MgO content increases. These findings strongly indicate that in composite samples, there is a considerable reduction in the energy gap between the light and heavy hole valence bands, as shown in Fig.6.11 (b) [26]. This reduction enhances the Seebeck coefficient due to contributions from both valence bands. The enhanced m* reveals the contribution of the heavy hole valence band in improving the Seebeck coefficient of composite samples. Specifically, m* increases from $0.23m_0$ (at x = 0) to $0.38m_0$ (at x =10) with rising x, highlighting the significant impact of the heavy hole band on the transport properties. The widened bandgap filters longer wavelength phonons, which contribute partially to thermal conductivity [27]. The rise in the Seebeck coefficient can also be due to the reduction in minority carriers within the conduction band, stemming from the widened bandgap [24]. This widening of the bandgap, which diminishes the bipolar contribution to thermal conductivity, results in a decrease in the n at elevated temperatures [28]. This observation is well aligned with the data obtained from Hall measurements.

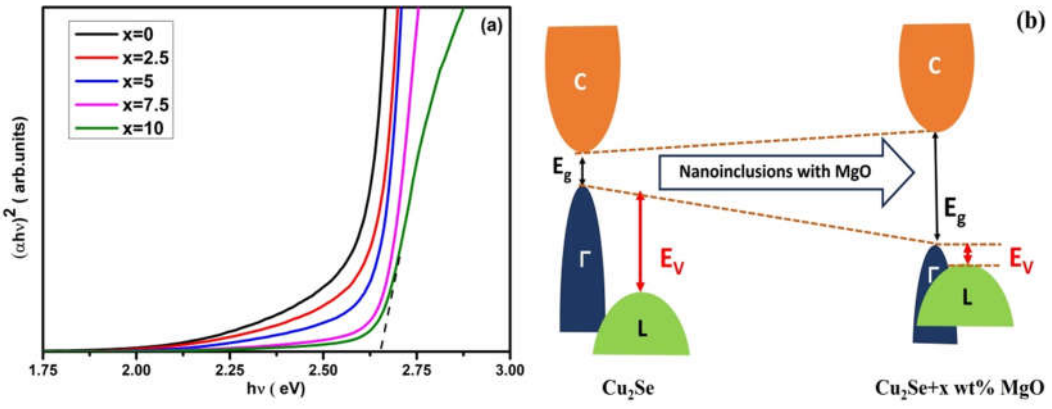

Fig.6.11 (a) Variation in the optical band gap of Cu_2Se + x % MgO (x = 0, 2.5, 5, 7.5, and 10) samples, (b) Schematic showing band gap widening and valence band convergence due to MgO nanoinclusions.

Table 6.1: Computed values of optical band gap and thermal band gap.

Sample	Optical band gap, E_g (eV)	Thermal band gap, ϵ_g (eV)
x=0	2.598	0.051
x=2.5	2.635	0.073
x=5	2.647	0.087
x=7.5	2.655	0.092
x=10	2.679	0.108

We utilized the empirical Goldsmid-Sharp equation

$$\epsilon_g = 2eS_{max}T_{max} \quad \text{.....(6.3)}$$

where T_{max} represents the temperature associated with the maximum Seebeck coefficient (S_{max}) to compute the thermal band gap ϵ_g for the composite samples is shown in table 6.1. The effective band gap for the pristine sample is calculated as 0.051 eV, showing a gradual linear increase with higher MgO content. Notably, the thermal band gap expands to 0.108 eV for the sample with 10 wt% MgO. This trend is substantiated by Hall measurements, indicating that the addition of MgO effectively enlarges the band gap of Cu_2Se. This result suggests that energy filtering of minority carriers delays the onset of bipolar conduction to higher temperatures by selectively hindering their movement, consequently increasing the bandgap. The bipolar effect generally can disrupt electrical and thermal transport by lowering the Seebeck coefficient. In this work, we observed an increase in S as the MgO content increases. Therefore, it is reasonable to suggest that increasing the band gap reduces the impact of minority carriers on the Seebeck coefficient, which leads to achieve a higher Seebeck coefficient.

6.3.5. Thermal transport measurements

Cu_2Se inherently possesses low thermal conductivity due to its distinctive phonon liquid electron crystal structure [29]. When MgO is incorporated into the Cu_2Se matrix, these heterostructures serve as centers for phonon scattering, effectively reducing thermal conductivity as the doping concentration increases. Fig.6.12 (a)

clearly illustrates a significant decrease in total thermal conductivity following the incorporation of MgO into the Cu_2Se matrix. It is evident that the total thermal conductivity (κ) of all composite samples is lower than that of pristine Cu_2Se, and it steadily decreases as the temperature rises. Specifically, for pure Cu_2Se matrix at 573K, the total thermal conductivity is approximately 0.673 W/mK, which progressively decreases as the MgO content increases from 2.5 to 10 wt%. The lowest thermal conductivity value of κ = 0.394 W/mK was achieved with 10 wt% MgO added, representing a 41% reduction compared to pristine Cu_2Se. The decrease in total thermal conductivity can be ascribed to the significant scattering of charge carriers at newly formed Cu_2Se-MgO potential barriers or interfaces, potentially induced by an energy filtering effect [30,31]. Optical studies indicate that the band gap widens with increasing MgO content. This increased band gap filters longer wavelength phonons, which contribute significantly to thermal conductivity. This effect can enhance the Seebeck coefficient without significant impact in the electrical conductivity while reducing its thermal conductivity [24,32].

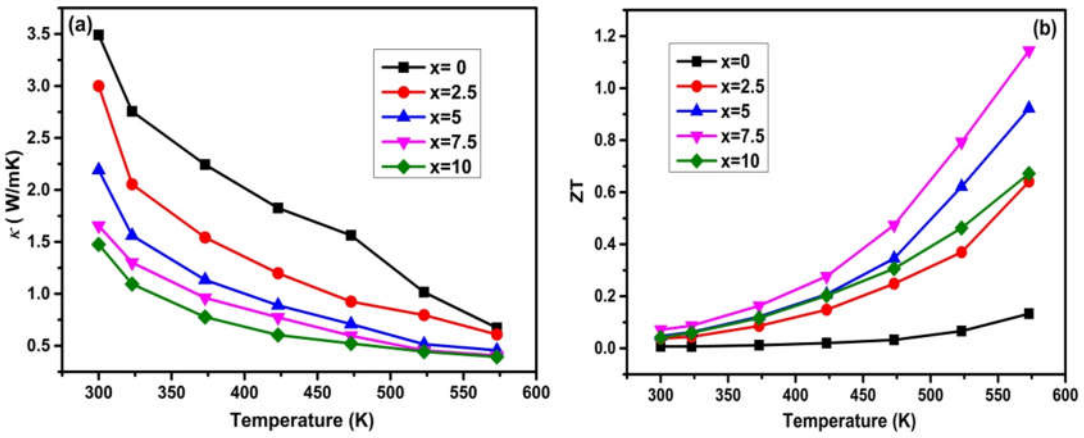

Fig.6.12 Temperature dependence of (a) total thermal conductivity and (b) Figure of merit (ZT) of Cu_2Se + x % MgO (x = 0, 2.5, 5, 7.5, and 10) samples.

The temperature variation of the ZT for both pristine Cu_2Se and the composite samples are depicted in Fig.6.12 (b). The ZT increases significantly with the increase in MgO content up to 7.5 wt% and thereafter decreases. Although κ continues to decrease with MgO content up to 10 wt%, the ZT does not improve further due to a reduction in the power factor, reaching a peak value of 1.14 at 573 K

for 7.5 wt% MgO. The enhanced thermoelectric performance observed in the Cu_2Se-7.5 wt% MgO sample is attributed to two primary factors. The enhanced power factor primarily stems from an elevated Seebeck coefficient, driven by the energy filtering effect on carriers. Additionally, the decreased thermal conductivity results from the effective scattering of phonons and carriers at interfaces and grain boundaries. These mechanisms collectively enhance the TE performance of the Cu_2Se-7.5 wt% MgO composite. The combined effect of an increased Seebeck coefficient and reduced thermal conductivity leads to a higher figure of merit, enhancing the material's thermoelectric conversion efficiency due to the presence of MgO in the Cu_2Se lattice.

6.4. Conclusions

In this work, the thermoelectric properties of Cu_2Se were synergistically regulated by introducing MgO nanoinclusions, which effectively decouple the thermal and electrical transport phenomena. The integration of MgO nanoparticles into the Cu_2Se matrix through ball milling establishes an energy potential barrier at Cu_2Se-MgO interfaces, enhancing the Seebeck coefficient through introducing an energy filtering mechanism. XRD analysis confirmed the cubic crystal structure of the samples and identified MgO as a secondary phase. Although dispersing MgO in Cu_2Se leads to a reduction in carrier concentration, the enhanced carrier mobility compensates for the drop, thereby maintaining the electrical conductivity. The synergistic optimization achieved a maximum observed power factor of approximately 811 $\mu W/mK^2$ for the sample containing 7.5 wt% MgO. The incorporation of MgO nanoinclusions generates heterostructure interfaces and structural lattice defects, which effectively form thermal barriers for scattering phonon transport. Moreover, there is a substantial (>41%) decrease in total thermal conductivity to $\kappa = 0.3947$ W/mK for 10 wt% MgO, attributed to effective scattering of charge carriers at newly formed heterointerfaces induced by the energy filtering effect of MgO. The significant enhancement in the Seebeck coefficient and reduction in thermal conductivity have collectively improved the thermoelectric figure of merit. Specifically, a maximum

ZT value of 1.14 at 573 K is achieved for Cu_2Se with 7.5 wt% MgO composites, marking an approximately 75% increase over the pristine sample. These findings underscore the potential of MgO's presence in Cu_2Se for the development of efficient thermoelectric materials for sustainable energy applications.

References

[1] H. Han, L. Zhao, X. Wu, B. Zuo, S. Bian, T. Li, X. Liu, Y. Jiang, C. Chen, J. Bi, J. Xu, L. Yu, Advancements in thermoelectric materials: optimization strategies for enhancing energy conversion, J. Mater. Chem. A. 12 (2024) 24041–24083. https://doi.org/10.1039/d4ta03666b.

[2] B. Madavali, H.S. Kim, K.H. Lee, S.J. Hong, Enhanced Seebeck coefficient by energy filtering in Bi-Sb-Te based composites with dispersed Y_2O_3 nanoparticles, Intermetallics. 82 (2017) 68–75. https://doi.org/10.1016/j.intermet.2016.11.002.

[3] X. Guan, J. Ouyang, Enhancement of the Seebeck coefficient of organic thermoelectric materials via energy filtering of charge carriers, CCS Chem. 3 (2021) 2415–2427. https://doi.org/10.31635/ccschem.021.202101069.

[4] C. Li, D. Luo, T. Wang, C. Shan, C. Li, K. Sun, A.K.K. Kyaw, J. Ouyang, Great Enhancement in the seebeck coefficient and thermoelectric properties of solid PEDOT:PSS films through molecular energy filtering by zwitterions, Small Struct. 4 (2023) 1-11. https://doi.org/10.1002/sstr.202300245.

[5] Z. Long, Y. Wang, X. Sun, Y. Li, Z. Zeng, L. Zhang, H. Chen, Band engineering of the second phase to reach high thermoelectric performance in Cu_2Se-based composite material, Adv. Mater. 35 (2023) 2210345. https://doi.org/https://doi.org/10.1002/adma.202210345.

[6] J. Yu, X. Liu, H. Hu, Y. Jiang, H.-L. Zhuang, H. Li, B. Su, J.-W. Li, Z. Han, Z. Wang, L. Chen, K. Hayashi, Y. Miyazaki, B.L. Mehdi, J.-F. Li, Ultralow thermal conductivity and high ZT of Cu_2Se-based thermoelectric materials mediated by TiO_2 nanoclusters, Joule. 8 (2024) 2652–2666. https://doi.org/10.1016/j.joule. 2024.06.007.

[7] V.C.S. Theja, V. Karthikeyan, D.S. Assi, V.A.L. Roy, Insights into the classification of nanoinclusions of composites for thermoelectric applications, ACS Appl. Electron. Mater. 4 (2022) 4781–4796. https://doi.org/10.1021/acsaelm.2c00617.

[8] R. Ma, D. Yang, X. Li, H. Song, Y. Zhang, Thermoelectric properties in nano Y_2O_3 dispersed Cu_2Se, Appl. Phys. A Mater. Sci. Process. 128 (2022). https://doi.org/10.1007/s00339-022-06273-7.

[9] Parvathi Krishna, V. Vijay, S. Ponnusamy, M. Navaneethan, Synergistic effect of energy filtering effect and secondary phase formation in Cu substituted SnS for enhanced thermoelectric applications, J. Mater. Sci. Mater. Electron. 35 (2024) 1–12. https://doi.org/10.1007/s10854-023-11615-z.

[10] J. Mani, S. Radha, F.J. Prita, R. Rajkumar, M. Arivanandhan, G. Anbalagan, Enhancing the Thermoelectric performance of Cu_2S/CuO nanocomposites through energy-filtering effect and phonon scattering, J. Inorg. Organomet. Polym. Mater. 34 (2023) 1548–1563. https://doi.org/10.1007/s10904-023-02885-5.

[11] K. Monikapani, V. Vijay, R. Abinaya, J. Archana, S. Harish, M. Navaneethan, Realizing an enhanced Seebeck coefficient and extremely low thermal conductivity in anharmonic Sb-substituted SnSe nanostructures, J. Alloys Compd. 923 (2022) 165961. https://doi.org/10.1016/j.jallcom.2022.16596.

[12] A.G. Manohari, S. Dhanapandian, C. Manoharan, K.S. Kumar, T. Mahalingam, Effect of doping concentration on the properties of bismuth doped tin sulfide thin films prepared by spray pyrolysis, Mater. Sci. Semicond. Process. 17 (2014) 138–142. https://doi.org/10.1016/j.mssp.2013.09.012.

[13] T. Parvathy, P.P. Pradyumnan, Impact of mobility and effective mass on the thermoelectric performance of Ni doped Cu_2Se, J. Alloys Compd. 970 (2024) 172615. https://doi.org/10.1016/j.jallcom.2023.172615.

[14] J. Dona, M. Navaneethan, S. Harish, J. Archana, C. Muthamizhchelvan, K. Hara, Synergistic effect of indium nano-inclusions to enhance interface phonon scattering in polycrystalline SnSe for thermoelectric applications, J. Alloys Compd. 856 (2021) 157358. https://doi.org/10.1016/j.jallcom.2020.157358.

[15] P. Muhammed Shafi, A. Chandra Bose, Impact of crystalline defects and size on X-ray line broadening: A phenomenological approach for tetragonal SnO_2 nanocrystals, AIP Adv. 5 (2015) 057137. https://doi.org/10.1063/1.4921452.

[16] A. Karati, M. Nagini, S. Ghosh, R. Shabadi, K.G. Pradeep, R.C. Mallik, B.S. Murty, U. V. Varadaraju, $Ti_2NiCoSnSb$-a new half-Heusler type high-entropy alloy showing simultaneous increase in Seebeck coefficient and electrical conductivity for thermoelectric applications, Sci. Rep. 9 (2019) 1–12. https://doi.org/10.1038/s41598-019-41818-6.

[17] J. Miao, D. Qian, P. Wang, S. Sun, P. Yuan, P. Zhou, Y. Yuan, R. Lan, Modulated carrier concentration and enhanced seebeck coefficient of $Ge_2Sb_2Te_5$ thin films by Sn doping, Vacuum. 198 (2022) 110881. https://doi.org/10.1016/j.vacuum.2022.1108-81.

[18] H. Li, Y. Liang, Y. Liu, S. Liu, P. Li, C. He, Engineering doping level for enhanced thermoelectric performance of carbon nanotubes/polyaniline composites, Compos. Sci. Technol. 210 (2021) 108797. https://doi.org/10.1016/j.compscitech.2021.10-8797.

[19] Z. Ma, C. Wang, J. Lei, D. Zhang, Y. Chen, Y. Wang, J. Wang, Z. Cheng, Core-shell nanostructures introduce multiple potential barriers to enhance energy filtering for the improvement of the thermoelectric properties of SnTe, Nanoscale. 12 (2020) 1904–1911. https://doi.org/10.1039/c9nr09331a.

[20] C. Li, X. Guan, S. Yue, X. Wang, J. Li, H. Cheng, S. Wang, A.K.K. Kyaw, J. Ouyang, Simultaneous enhancements in the Seebeck coefficient and conductivity of PEDOT:PSS by blending ferroelectric $BaTiO_3$ nanoparticles, J. Mater. Chem. A. 9 (2021) 16952–16960. https://doi.org/10.1039/d1ta04235a.

[21] V. Shalini, S. Harish, H. Ikeda, Y. Hayakawa, J. Archana, M. Navaneethan, Enhancement of thermoelectric power factor via electron energy filtering in Cu doped MoS_2 on carbon fabric for wearable thermoelectric generator applications, J. Colloid Interface Sci. 633 (2023) 120–131. https://doi.org/10.1016/j.jcis.2022.1-0.147.

[22] M.S. El-Asfoury, M.N.A. Nasr, K. Nakamura, A. Abdel-Moneim, Enhanced thermoelectric performance of $Bi_{85}Sb_{15}$-graphene composite by modulation carrier transport and density of state effective mass, J. Alloys Compd. 745 (2018) 331–340.

https://doi.org/10.1016/j.jallcom.2018.02.040.

[23] S. Liang, Y. Shi, D. Hu, H. Zhu, S. Yue, Significantly improved thermoelectric performance of Ag-doped $Bi_{0.5}Sb_{1.5}Te_3$ films deriving from high-efficient carrier filtering effect, Ceram. Int. 49 (2023) 35309–35315. https://doi.org/10.1016/j.ceramint.2023.08.203.

[24] Y. Pei, A.D. Lalonde, N.A. Heinz, X. Shi, S. Iwanaga, H. Wang, L. Chen, G.J. Snyder, Stabilizing the optimal carrier concentration for high thermoelectric efficiency, Adv. Mater. 23 (2011) 5674–5678. https://doi.org/10.1002/adma.201103153.

[25] T. Parvathy, K. V. Nabeela, P.P. Pradyumnan, Raman structural transition studies and optical band calculation on the multiphase of tin selenides, Mater. Chem. Phys. 301 (2023) 127622. https://doi.org/10.1016/j.matchemphys.2023.127622.

[26] A. Banik, U.S. Shenoy, S. Anand, U. V. Waghmare, K. Biswas, Mg alloying in SnTe facilitates valence band convergence and optimizes thermoelectric properties, Chem. Mater. 27 (2015) 581–587. https://doi.org/10.1021/cm504112m.

[27] J. Mani, S. Radha, T.R. Shalini Devi, R. Rajkumar, M. Arivanandhan, G. Anbalagan, Effect of energy filtering on Cu_2NiSnS_4/CuO composites for thermoelectric applications, J. Mater. Sci. 59 (2024) 8911–8929. https://doi.org/10.1007/s10853-024-09689-z.

[28] L. Chen, Q. Zhang, Z. Guo, Z. Yan, K. Song, G. Wu, X. Wang, X. Tan, H. Hu, P. Sun, G.Q. Liu, J. Jiang, Expand band gap and suppress bipolar excitation to optimize thermoelectric performance of $Bi_{0.35}Sb_{1.65}Te_3$ sintered materials, Mater. Today Phys. 21 (2021) 100544. https://doi.org/10.1016/j.mtphys.2021.100544.

[29] L. Li, Y. Zhao, C. Shi, W. Zeng, B. Liao, M. Zhang, X. Tao, Facile synthesis of copper selenides with different stoichiometric compositions and their thermoelectric performance at a low temperature range, RSC Adv. 11 (2021) 25955–25960. https://doi.org/10.1039/d1ra04626h.

[30] J. Zhang, X. Qin, D. Li, H. Xin, C. Song, L. Li, X. Zhu, Z. Wang, G. Guo, L. Wang, Enhanced thermoelectric performance of $CuGaTe_2$ based composites incorporated with nanophase Cu_2Se, J. Mater. Chem. A. 2 (2014) 2891–2895. https://doi.org/10.1039/c3ta15211a.

[31] J.H. Bahk, A. Shakouri, Minority carrier blocking to enhance the thermoelectric figure of merit in narrow-band-gap semiconductors, Phys. Rev. B. 93 (2016) 1–17. https://doi.org/10.1103/PhysRevB.93.165209.

[32] M. Thesberg, H. Kosina, N. Neophytou, On the effectiveness of the thermoelectric energy filtering mechanism in low-dimensional superlattices and nano-composites, J. Appl. Phys. 120 (2016). https://doi.org/10.1063/1.4972192.

Chapter-7

Summary and Conclusions

This chapter offers a comprehensive summary of the research focused on enhancing the thermoelectric properties of Cu_2Se based nanomaterials. It highlights the detailed characterizations of the synthesized materials and significant results obtained from the thermoelectric studies.

7.1. Introduction

In recent years, the field of thermoelectric has grown with significant advancements driven by the increasing demand for sustainable energy solutions and the pursuit of materials that offer improved thermoelectric performance. Indeed, one of the primary challenges in advancing thermoelectric technology lies in enhancing the thermoelectric performance of materials. The primary challenge in designing a highly efficient thermoelectric material lies in the intricate relationship between the Seebeck coefficient (S), electrical conductivity (σ), and thermal conductivity (κ) with the carrier concentration (n). Both the Seebeck coefficient and electrical conductivity are highly influenced by the Fermi level, which is itself dependent on carrier concentration, carrier effective mass, and temperature. To achieve high thermoelectric performance, it is crucial to implement strategies that optimize carrier concentration and carrier effective mass while avoiding negative impacts on thermal conductivity. Key approaches include employing scattering mechanisms and structural modifications to enhance the power factor, alongside leveraging materials with low intrinsic thermal conductivity. The phonon liquid electron crystal strategy, which is particularly effective for superionic conductors, represents a notable advancement in this field. This approach is especially relevant for superionic conductors, where metallic ions exhibit liquid like behavior and can migrate between lattice sites, resulting in extremely low thermal conductivity. Cu_2Se, a superionic conductor, exemplifies this concept and demonstrates exceptional thermoelectric properties as a p-type material. Given these potentials, it is essential to advance its thermoelectric performance through innovative approaches, such as nanostructuring, band engineering, etc to fully harness its capabilities for enhanced efficiency. This thesis explores innovative strategies to enhance the thermoelectric performance of Cu_2Se nanostructures by optimizing electronic and thermal transport properties. The study employs different strategies including doping, dual doping, and the development of Cu_2Se based composite systems, to achieve superior thermoelectric efficiency.

7.2. Summary of the thesis

Cu_2Se inherently exhibits extremely low thermal conductivity and outstanding thermoelectric performance due to its 'phonon liquid electron crystal' nature. To further enhance these thermoelectric properties, several strategies have been employed, including element doping, nanostructure engineering, composite engineering etc. This thesis aims to enhance the thermoelectric performance of Cu_2Se by optimizing both electrical and phonon transport properties to improve overall conversion efficiency. It details a successful synthesis of Cu_2Se based systems using hydrothermal and planetary ball milling techniques and explores the impact of nanostructuring, band engineering, and nanoinclusions on its structural, morphological, optical, electrical and thermoelectric properties, resulting in notable improvements in the thermoelectric performance. The thesis details four series of work, demonstrating that the combination of nanostructuring with defect engineering through doping and nanoinclusions effectively enhances thermoelectric performance. Specifically, two series (chapter 3 and 4) explore doping strategies with Cu_2Se synthesized via the hydrothermal route, while the remaining two series (chapter 5 and 6) investigate the incorporation of nanoinclusions into the Cu_2Se lattice using planetary ball milling techniques. Here, we present the main outcomes of our research, including the thermoelectric power factor, thermal conductivity, and figure of merit for each series of work conducted in this thesis.

7.2.1. Ni doped Cu_2Se

Several optimization methods, such as doping and band engineering, can significantly enhance the thermoelectric performance of p-type Cu_2Se. Although traditional doping increases carrier concentration, it often leads to a decrease in carrier mobility. High carrier mobility is crucial for improving the thermoelectric performance over a broad temperature range. However, conventional doping methods typically reduce carrier mobility. The challenge is to optimize carrier concentration while maintaining high carrier mobility, which requires identifying more effective dopants. To address this, we have fine-tuned defects in Cu_2Se by doping the lattice with Ni, synthesized via a hydrothermal route, to enhance carrier

mobility. In this study, we examined the effect of electronic defects on the thermoelectric properties of Cu_2Se through Ni doping. We systematically varied the Ni concentration (0 wt%, 1 wt%, 1.5 wt%, and 2 wt%) to tune the carrier density and carrier mobility. It is observed that

- The inclusion of nickel in the Cu_2Se lattice at either substitutional or interstitial sites has a substantial influence on its thermal and electrical transport properties.
- The presence of Ni in the interstitial sites results in a simultaneous increase in carrier concentration and carrier mobility, and the theoretical basis for such an increase is described. All the doped samples showed enhanced electrical conductivity compared to that of undoped Cu_2Se.
- Nickel doping causes band sharpening, reducing the carrier effective mass and achieving a high mobility of approximately 600 cm^2/Vs for the 1.5 wt% Ni doped sample at 573 K.
- Tuning the mobility and narrowing band gap help to achieve a maximum power factor of 614 $\mu V/mK^2$ at 573K for the Cu_2Se sample doped at 1.5 wt% Ni by decoupling the thermopower and electrical conductivity.
- The lattice distortion and point defects introduced by Ni substitution create additional phonon scattering centers, leading to a significant reduction in thermal conductivity. The sample doped with 2 wt% Ni exhibits a maximum ZT value of 0.535 at 573 K, approximately three times greater than that of pristine Cu_2Se.

These results indicate that the remarkable thermoelectric performance is due to ultrahigh carrier mobility across the operating temperature range (300 K-573 K), which is attained by effectively modifying transport parameters through Ni doping. This demonstrates that Ni is an innovative and effective dopant capable of significantly improving the thermoelectric performance of Cu_2Se through defect and band engineering.

7.2.2. Ni and Zn dual doped Cu_2Se

In our previous study, we explored how electronic defects influence carrier transport in Cu_2Se, focusing on the effects of Ni doping. Building on this, dual doping, which involves the simultaneous introduction of two different dopants, offers a more precise approach to tailor both electronic and thermal properties. This strategy not only optimizes carrier concentration and mobility but also introduces additional lattice defects and phonon scattering mechanisms, effectively lowering thermal conductivity. In this work, we present a novel approach to enhancing Cu_2Se's thermoelectric performance through co-doping with Ni and Zn, a dual-doping strategy not previously explored for this system. This dual doping strategy enhances electrical conductivity without compromising the Seebeck coefficient, resulting in a higher power factor. By strategically altering the crystal structure and introducing controlled defects, the research aims to improve carrier mobility while simultaneously reducing thermal conductivity through effective phonon scattering at lattice defects. The key results for the Ni and Zn dual doped samples (Ni = 1 wt%, Zn = 0.5 wt%, 1 wt%, 1.5 wt%, 2 wt%) are summarized as follows:

- Structural studies confirm the successful incorporation of Ni and Zn into the lattice of Cu_2Se.
- Phonon scattering by point defects and dislocations has been significantly increased, resulting in reduced thermal conductivity, as confirmed by PXRD and Raman studies.
- Dual doping substantially enhances Hall mobility, increasing it from 234 $cm^2V^{-1}s^{-1}$ to 875 $cm^2V^{-1}s^{-1}$ at 573 K, which boosts electrical conductivity with only a slight reduction in the Seebeck coefficient.
- The power factor significantly increases over a wide temperature range, reaching a value of approximately 564 $\mu W/mK^2$ at 573 K for Cu_2Se dual-doped with 1 wt% Ni and 1.5 wt% Zn, attributed to the enhanced electrical conductivity and Seebeck coefficient.

- Scattering mechanisms induced by lattice defects shorten the total phonon relaxation time, evident from Raman spectra peak broadening, ultimately leading to an ultra low thermal conductivity of 0.41 W/mK at 573 K.
- Reduction in thermal conductivity, coupled with the simultaneous enhancement in the power factor, results in a maximum ZT of up to 0.761 for the Ni 1 wt% Zn 1.5 wt% co-doped sample, representing a fourfold enhancement compared to pristine Cu_2Se.

This co-doping approach results in an improved figure of merit as compared to Ni single doped samples. This substantial enhancement underscores the promising potential of dual doping as a strategic approach for advancing the thermoelectric properties of Cu_2Se for practical applications. The precise control of doping levels and synthesis conditions underscores this study's significant contribution to advancing the commercial potential of Cu_2Se based thermoelectric devices through dual doping.

7.2.3. Cu_2Se-ZnSe composites

Addressing electron and phonon transport both independently and simultaneously, the use of a nanocomposite approach is considered an effective method for improving the thermoelectric properties of bulk materials. Nanoinclusions effectively reduce thermal conductivity by promoting phonon scattering at interfacial boundaries. This study emphasizes the synergistic improvement of both electrical and thermal transport properties in Cu_2Se through ZnSe alloying. To achieve optimal thermoelectric performance, the electronic band structure of Cu_2Se can be fine-tuned by incorporating ZnSe into the host matrix using planetary ball milling. The Cu_2Se-ZnSe composites were synthesized by varying the concentration of ZnSe (0 wt%, 2.5 wt%, 5 wt%, 7.5 wt%, and 10 wt%), and the results are summarized as follows,

- The electrical conductivity increased in conjunction with the Seebeck coefficient, owing to an increase in carrier concentration and density of state effective mass, respectively.

- The incorporation of ZnSe into the Cu_2Se lattice affects its electronic band structure by reducing the energy difference between the light and heavy hole valence bands, widening the band gap, delaying the onset of the bipolar effect, and consequently increasing the Seebeck coefficient.

- The addition of ZnSe to Cu_2Se tunes the Fermi level, promotes the convergence of two valence bands, and simultaneously increases the density of states, which facilitates the decoupling of electrical transport parameters.

- A significant improvement in the thermoelectric properties of Cu_2Se-ZnSe composites was achieved, with a maximum power factor of 736 $\mu W/mK^2$ at 573 K for the sample with 5 wt% ZnSe, which is five times greater than that of pristine Cu_2Se.

- The exceptional ZT value of 1.02 at 573K for Cu_2Se with 5 wt% ZnSe is attributed to the combined effects of alloy scattering, which reduces thermal conductivity (κ), engineering of electronic properties through band structure modification, and reducing the negative impact of minority carriers by widening the bandgap.

This study shows that simultaneously adjusting carrier concentration through nanostructuring and incorporating a compatible second phase through composite engineering can be an effective strategy for achieving a high figure of merit. This study proposes a systematic strategy for synthesizing thermoelectric composites based on Cu_2Se, along with an effective technique for synthesizing materials with considerable thermoelectric performance.

7.2.4. Cu_2Se-MgO composites

Cu_2Se thermoelectric materials hold promise for sustainable energy harvesting but face challenges such as bipolar carrier transport, which reduces the Seebeck coefficient and increases the thermal conductivity. Enhancing the Seebeck coefficient is crucial for optimizing Cu_2Se-based thermoelectric devices. Strategic use of potential barriers can selectively enhance the Seebeck coefficient by allowing the majority carriers while blocking the minority ones. Precise dispersion of

nanoinclusions enhances the Seebeck coefficient and reduces thermal conductivity, thereby improving the thermoelectric figure of merit (ZT) and increasing energy conversion efficiency. Herein, we propose a strategy to enhance the energy filtering effect through nanoinclusion of MgO (0 wt%, 2.5 wt%, 5 wt%, 7.5 wt%, and 10 wt%), in the Cu_2Se matrix synthesized via ball milling technique. It is observed that

- Integrating MgO nanoparticles into the Cu_2Se matrix creates energy potential barriers at the Cu_2Se-MgO interfaces, which enhances the Seebeck coefficient by introducing an energy filtering mechanism.
- MgO alloying enlarges the energy gap of both the conduction and valence bands, effectively suppressing bipolar thermal conductivity by increasing the band gap.
- The increase in the Seebeck coefficient with MgO addition is attributed to an increase in the density of states (DOS) effective mass, which modifies the electronic band structure of Cu_2Se.
- The synergistic optimization resulted in a maximum observed power factor (PF) of approximately 811 $\mu W/mK^2$ for the sample with 7.5 wt% MgO.
- Thermal conductivity was significantly reduced due to the introduction of scattering centers, which weakened the contribution from electrical conductivity and scattered phonons carrying heat at newly established interfaces.
- A maximum thermoelectric figure of merit (ZT) value of 1.14 was achieved at 573 K for Cu_2Se with a 5 wt% MgO sample, which was 8.5 times higher than that of the pristine Cu_2Se.

These results demonstrate that the strategic incorporation of MgO nanoinclusions into Cu_2Se offers a significant pathway for enhancing the thermoelectric performance of these materials.

In summary, this thesis presents a comprehensive exploration of strategies to enhance the thermoelectric performance of Cu_2Se based nanomaterials. The work

focuses on various methods such as doping, dual doping, and nanocomposite engineering to optimize both the electrical and thermal transport properties of Cu_2Se. By fine-tuning carrier concentration, carrier mobility, effective mass, and thermal conductivity through these approaches, significant improvements in the material's thermoelectric efficiency have been achieved. The research also highlights the approach of decoupling transport parameters, demonstrating how strategies that optimize electrical conductivity, Seebeck coefficient, and thermal conductivity collectively can significantly enhance the material's thermoelectric performance. In conclusion, this research offers crucial insights into the design and optimization of thermoelectric materials, setting the stage for the development of high-performance Cu_2Se-based thermoelectric materials for sustainable energy solutions.

Chapter-8

Recommendations for future research

This chapter outlines the recommendations for future research on the materials discussed in this thesis.

8.1. Introduction

Thermoelectric materials are essential for developing devices such as power generators, coolers, and sensors. However, for these devices to operate efficiently in power generation and refrigeration, it is crucial that the materials exhibit high thermoelectric efficiency. This thesis aims to enhance the thermoelectric performance of Cu_2Se by decoupling its electrical and thermal transport properties through the adoption of various strategies to improve overall energy conversion efficiency. Through the application of synthesis methods like hydrothermal and planetary ball milling techniques, this research explores the effects of nanostructuring, band engineering, and nanoinclusions on the structural, morphological, optical, electrical, and thermoelectric properties of Cu_2Se. This research work investigates the effects of Ni doping, dual Ni-Zn co-doping, ZnSe and MgO nanoinclusions on the transport properties of Cu_2Se, highlighting the strategies that most effectively enhance its thermoelectric performance. The study demonstrates that combining nanostructuring with defect engineering through doping and nanoinclusions leads to significant improvements in thermoelectric performance of Cu_2Se. Based on the results of this research, there are several potential avenues exist to extend the study and further optimize thermoelectric materials. Addressing these unexplored areas is essential for developing high-performance thermoelectric materials and driving advancements in energy conversion applications. The following section highlights these promising directions for future research.

8.2. Recommendations for future research

- The enhancement of existing thermoelectric materials through doping has been one of the most widely explored strategies for improving overall thermoelectric performance. Chapters 3 and 4 highlight the impact of Ni doping and dual doping with Ni and Zn on the thermoelectric properties of Cu_2Se. The findings of this study suggest the need to explore additional dopants which could further improve its thermoelectric performance and

provide additional opportunities to fine-tune its properties for enhanced efficiency in energy conversion applications.

- In this study, thermoelectric properties were investigated only for nanomaterials. However, thin films can be fabricated using techniques such as RF sputtering and doctor blade coating, which offer significant advantages in enhancing thermoelectric performance while achieving extremely low thermal conductivity.

- Theoretical studies related to this research can be conducted using advanced techniques such as Density Functional Theory (DFT) to gain deeper insights into the electronic structure and transport properties. Exploring new materials, such as high-entropy materials and chalcogenides, can also help improve thermoelectric performance.

- In this study, only p-type Cu_2Se-based nanomaterials were synthesized. To develop a complete thermoelectric module, it is essential to synthesize an n-type counterpart with comparable performance. Future research could focus on the design and optimization of n-type Cu_2Se-based nanomaterials, enabling the fabrication of an efficient p-n thermoelectric module.

- Future research could explore low-temperature thermoelectric measurements to gain deeper insights into carrier dynamics, phase stability, and thermal transport mechanisms, further expanding the potential applications of Cu_2Se-based materials.

- In this study, we focused on the thermoelectric properties of Cu_2Se. However, future research can be extended to explore other selenide-based materials, which may offer promising thermoelectric performance through structural and compositional modifications.

- Future research could investigate the Peltier effect in these materials, paving the way for the development of cooling modules through applied voltage.

These recommendations paved a pathway for the further progress in Cu_2Se based thermoelectric materials. We can significantly improve the thermoelectric efficiency and overall performance by addressing current challenges and exploring novel strategies. The insight gained from this research provides a strong basis for improving Cu_2Se based TE materials, which will help the development of next-generation thermoelectric devices.